Development of birefringence characterization and compensation techniques for gravitational wave detectors.

Shalika Singh

School of Science

Institute of Science Tokyo

A thesis submitted for the degree of

Graduate Major in Physics

February, 2026

Supervised by Prof. Kentaro Somiya

Abstract

Gravitational wave detectors are high-precision metrological instruments used to detect perturbations in space time fabric. The sensitivity of these instruments determines how often events creating gravitational waves can be detected and how far away we can look in the universe. There are several fundamental noise sources which are rigorously mitigated using novel techniques to improve the performance and sensitivity of the detectors. Hence, one of the objectives in GW community is to lower the thermal noise of mirrors by cooling them down. A GW detector in Japan, KAGRA, is one such instrument. KAGRA has deployed cryogenic technology and as a result, uses crystalline materials for mirrors. However, the current crystalline mirrors are manufactured with reduced quality, i.e., they exhibit non-uniform birefringence. The work presented in this thesis forms a backbone in reducing the effect of non-uniform birefringence in the detector and can be divided into two parts.

Part 1 of this thesis involved the development of a birefringence characterisation setup. The improved setup can now provide more information about birefringence in contrast to past techniques used in GW community. The measurement method enabled characterisation of both transmissive and reflective materials, along with the evaluation of the sign of retardation and diattenuation, which was not accessible using a single measurement setup. Additionally, the characterisation could be done using any arbitrary polarisation, thereby relaxing the requirements on the polarisation optics used in the characterisation systems. The thesis then proceeds to showcase the development of a polarisation actuator operating at MHz speed for fast characterisation and improved sensitivity of birefringence. Additionally, the polarisation actuation at MHz speed enables measurement of birefringence fluctuation and a method to probe birefringence in the GW detector.

Part 2 of this thesis focused on the development of a birefringence-compensation system for GW detectors. The research demonstrates, firstly, uniform birefringence compensation using a pair of polarisation actuators. The thesis then proceeds to identify a low-loss compensator material compatible for use inside the detector. Analysis of several crystals in the pursuit of finding a low-loss crystal optimal for use in the detector is showcased.

Additionally, a possible configuration of a birefringence compensation system for the detector is highlighted.

The results shown in this thesis demonstrate a significant step towards knowing non-uniform birefringence better and the implementation of non-uniform birefringence compensation techniques in gravitational wave detectors. This will help to reduce the performance degradation of the GW detector with non-uniform birefringence.

Acknowledgements

The work presented in this thesis would not have been possible without the support of several people, not all of whom might have been accounted for here.

First of all, thanks to Kentaro Somiya for accepting me as a graduate student at SciTokyo and for being a kind and encouraging supervisor. I appreciate the freedom he has given me in choosing my research topics and encouraging me to meet other researchers and learn from them. He has unhesitatingly supported my research in NAOJ as a visiting student. He has always encouraged me to freely voice my opinions, lent a kind ear towards my complaints, and I am deeply grateful for his support.

Secondly, I extend my gratitude towards Takayuki Tomaru and Yoichi Aso for opening the doors of NAOJ for me. This research would have been impossible if I were not at NAOJ. Yoichi Aso taught me several things, from optics to electronics and has shaped my initial years of research with his vast knowledge.

I will like to thank Marc Eisenmann for actively supervising me and making sure that I am not lost. He kindly welcomed me to work on the project of birefringence, and this thesis is hopefully good enough to be a token of appreciation for his kind gesture. He has often shown a huge amount of patience in listening to my troubles in experiments and simulations and has offered suggestions to overcome them. I have learnt a huge deal from him, ranging from optics to colour for my plots (the latter was one of the most difficult to learn). He has kindly accepted my purchase requests, and this thesis is a result of experiments supported by him.

I would like to thank Kiwamu Izumi for sharing his knowledge on RF electronics and optics. His kind advice enabled the realisation of high voltage driver circuit for the Pockels cell and kept my motivation in the process. I appreciate that he could understand the issues and devise a solution for me by hearing my ill-articulated troubles. I have always been mesmerised by his expertise, and he remains a person to whom I can ask about anything.

I appreciate the kind efforts from Haoyu Wang in teaching me about non-uniform birefringence simulations (more than once), which improved my understanding towards doing simulations for detectors in general. I also thank him and Yuta Michimura for my first trip to KAGRA, showing me around the incredible detector (from PSL room to the

end station in both arms) and for letting me join them during their work onsite. That week somehow felt the most productive in my entire stay in Japan, even though we had 4 hours of lunch break every day. I learnt from Yuta Michimura how not to be stressed, a very important lesson, and I still have to work on that.

I thank all the NAOJ members Yohei Nishino, Munetake Otsuka, Kohei Mitsuhashi, Matteo Leonardi, Tomotada Akutsu, Hiroki Fujimoto, Michael Page, and Chenjie Zhou. I thank Diego Dominguez and Kaido Suzuki for being so welcoming in SciTokyo. Thanks to Ryo Iden for being such an encouraging colleague, for always assisting me with course structure and for deciding to pursue a PhD (I am glad I am not alone). Thanks to visitors Gabirella Chiarini for teaching me how to use Jammt, Frederic Cleva for teaching me a thing or two about optical setups and getting me in touch with Jean-Pierre Coulon, who kindly helped me with questions about transformers.

Thanks to Jerome Degallaix for sending us interesting Sapphire samples and for giving me advice in general on any topic. Thanks to Hiroaki Yamamoto for his useful insights. Thanks to Riku Katsuki and Masumi Taki for the opportunity to measure the hydrogel's birefringence. Thanks to Thomas James Roocke for sharing information and answering my several questions on the Pockels cells driver made in University of Adelaide.

Thanks to Carl Blair and Ju Li for welcoming me to UWA. Thanks to Alex Adams for introducing me to the birefringence measurement setup in UWA and letting me use it to characterise the Sapphire samples, and for all the interesting discussions. Thanks to Koh Baker for teaching me patiently about the CO_2 laser and its alignment on the test mass at GinGin.

Thanks to Naotsu Hirata and Tomio Kanzawa for 3D printing and ideas for the mould design of the inductor. Thanks to Satoru Ikeda for helping with the servers, licenses and all the digital infrastructure.

Thanks to Miki Tsuchiya for help through all the administration work in SciTokyo and for always being kind to me. Thanks, Mizuho Yoshizumi, for the administration work in NAOJ and for sharing Aomori apples with me every year. Thanks to Naho Sakaguchi for assisting me in my trip to KAGRA.

Last but not least, thanks to my family. Thanks to my partner Dibyesh for introducing me to the world of GW back in my undergraduate years. It is truly because of him that I stumbled upon the option to become a researcher, especially in GW field. Thanks to my parents, Indrani and Ram Pyare and my sister Nitika, for always loving me and curiously asking me about GW detector and my research on non-uniform birefringence. It is their curious minds that encourage me to look at problems so differently. I always appreciate their love and patience for me, which helps me get through life.

Contents

List of Figures

List of Tables

Abbreviations

1G 1st Generation

2G 2nd Generation

3G 3rd Generation

AS Anti-Symmetric

BS Beam Splitter

DRFPMI Dual Recycling Fabry-Perot Michelson interferometer

ETM End Test Mass

FEM Finite Element Modelling

FEP Fluorinated Ethylene Propylene

FPMI Fabry-Perot Michelson interferometer

FWHM Full-width half-maximum

GW Gravitational Waves

HWP Half-Wave Plate

iLM The Institute of Light and Matter

ITM Input Test Mass

LC Liquid Crystal

LMA Laboratoire des Matériaux Avancés

LP Linear Polariser

NAOJ National Astronomical Observatory of Japan

Opamp Operational Amplifier

PBS Polarising Beam Splitter

PCB Printed Circuit Board

PD Photodiode

PEM Photoelastic Modulator

PRFPMI Power Recycling Fabry-Perot Michelson interferometer

PRM Power Recycling Mirror

PRT Polarization Ray Tracing
PSA Polarization State Analyser
PSG Polarization State Generator
QWP Quarter-Wave Plate
RF Radio Frequency
SciTokyo Institute of Science Tokyo
SRM Signal Recycling Mirror
TWE Transmitted Wavefront Error
UEC The University of Electro-Communications
UWA The University of Western Australia
VNA Vector Network Analyser

Thesis Structure

The purpose of the work presented in this literature is to develop techniques to tackle issues due to non-uniform birefringence in gravitational wave detectors. The research, hence, showcases the development of birefringence characterisation and compensation systems. The outline of this thesis can be better understood with the following flowchart and descriptions.

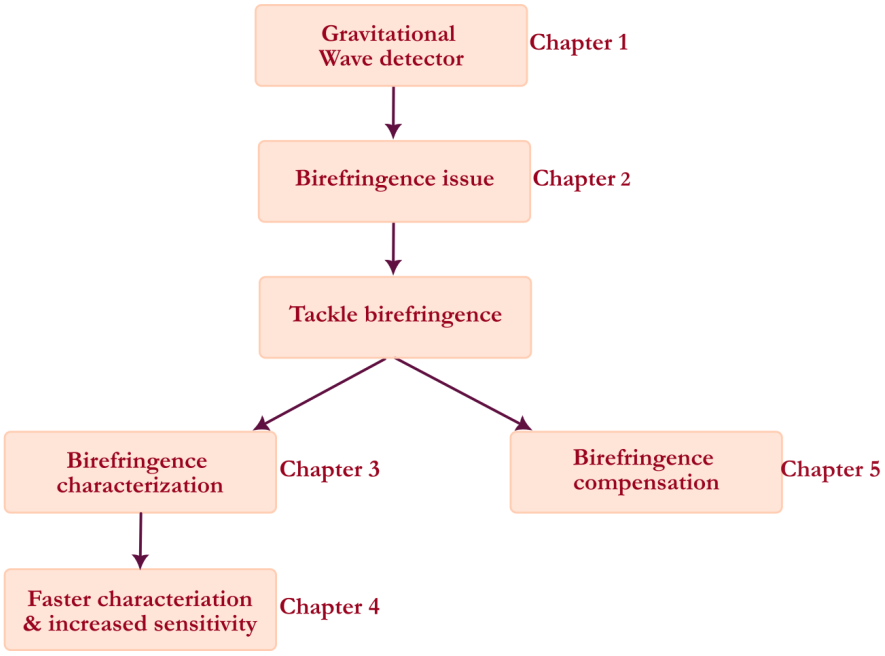

Figure 1: The flow chart gives an overview of the structure of this thesis

Chapter 1 in this thesis gives a brief introduction to gravitational waves and the gravitational wave detector. The author's research focused directly on the improvements required for increasing the sensitivity of the detector that can be implemented for future observation runs. Hence, it was crucial to introduce the general outline of the detector and the science behind it.

Chapter 2 delves deeply into the issue being addressed through the research discussed in this thesis. The chapter explains the basics of birefringence and the issues due to birefringence in the GW detector. The chapter brings into discussion the existing methods to characterise the birefringence of any test mass in the gravitational wave community. The previously

used techniques for birefringence had some cons, which are being addressed here. This chapter also sets the premise for the following chapters by putting forth the theoretical and experimental framework for polarization control.

Chapter 3 highlights the development of a new method to characterise the birefringence and diattenuation of transmissive and reflecting materials. The research demonstrated here is robust against misalignments in polarisation optics (required to characterise any element), or the need for a perfect polarisation for characterisation, in contrast to old measurement techniques. The sections mention the extraction of complete birefringence using Jones calculus. It then shows results from several transmissive and reflective optics. At last, it addresses some developments required to increase precision and sensitivity, and the need for the development of a fast actuator, shown in Chapter 4.

Chapter 4 is about the work on polarisation control at MHz speed to increase our precision of measured birefringence. While measuring birefringent samples for Chapter 3, we realise that the sensitivity has to be improved to measure the birefringence of dielectric materials. Consequently, a follow-up motivation was to be able to measure birefringence noise at the same time. The chapter focuses on the development of polarisation generation and readout at a speed of MHz using Pockels cells. The chapter includes the development of a high voltage circuit to achieve maximum modulation depth of the Pockels cells, and then the characterisation of the Pockels cells.

Chapter 5 focuses on the development of a birefringence compensation system for the GW detector. While birefringence characterisation is one way to understand the effect of the installed test mass, the other is to reduce this non-uniformity. The initial work presented demonstrates compensation at a single spatial point, and the preparation for non-uniform compensation with some realistic actuation compatible for use in GW detector. The chapter highlights investigations into a temperature-controlled actuator and analysis of several materials to achieve a good range of polarisation actuation.

Conclusion summarises the work mentioned in this thesis and highlights some next steps, mainly focusing on the follow-up work from Chapter 4 and Chapter 5.

Appendix A discusses the evaluation of the requirements of impedance matching form Chapter 4. It shows the derivation of the capacitance value required for a resonant circuit to be impedance-matched with the source. Appendix B shows some results for several crystals analysed for thermal actuator in Chapter 5, as results from only one crystal are shown in the Chapter 5.

1 Gravitational wave detector

Contents

1.1 Gravitational waves

Einstein's theory of General Relativity [1] describes gravity as a consequence of the curvature of space and time, which gave rise to the prediction of the theory of gravitational waves from fluctuating mass-energy distribution [2]. In theory, gravitation is considered a distortion in space -time and is expressed by a physical quantity called metric, which evolves as a function of time. A small change in the metric can propagate as a wave through space time fabric and is called a gravitational wave (GW). The distortions in space-time are strong near the source

and reduce as they travel through the space-time fabric. These distortions and their effect can be expressed using Einstein's equation and are discussed in the following section.

1.1.1 As Solution of Einstein's Equation

GW can be derived as a solution of Einstein's equation, which is briefly visualised here [3]. The interval of two separated events in space-time can be described using the metric tensor $g_{\mu\nu}$ as,

$$ds^2 = g_{\mu\nu} dx^\mu dx^\nu \tag{1.1}$$

where μ, ν vary from 0 to 4 (for the four spacetime coordinates), and dx denotes the infinitesimal change in the coordinates. Using this notation, the space-time can be expressed as $x^\mu = (ct, x, y, z)$. The crucial Einstein's equation shows the relation between gravity and the energy of the masses as, [1].

$$R_{\mu\nu}(g_{\mu\nu}) - \frac{1}{2} g_{\mu\nu}(R_{\mu\nu}) = \frac{8\pi G}{c^4} T_{\mu\nu} \tag{1.2}$$

where $g_{\mu\nu}$ is the distortion in space-time (gravity), $R_{\mu\nu}$ is the Ricci tensor, $R = g_{\mu\nu} R_{\mu\nu}$ is the Ricci scalar curvature, and $T_{\mu\nu}$ is the stress-energy-momentum tensor. In this weak field limit, the space-time metric can be approximately written as, [3]

$$g_{\mu\nu} \simeq \eta_{\mu\nu} + h_{\mu\nu}, \quad \text{where} \quad |h_{\mu\nu}| \ll 1 \tag{1.3}$$

where $\eta_{\mu\nu}$ is the Minkowsky metric representing the flat space and $h_{\mu\nu}$ is the perturbation in space-time (gravitational wave). For a spatial coordinate system, where the GW is travelling in the z direction, the plane wave solution can be summarised as, [3]

$$h_{\mu\nu} = \begin{pmatrix} 0 & 0 & 0 & 0 \\ 0 & -h_+ & h_\times & 0 \\ 0 & h_\times & h_+ & 0 \\ 0 & 0 & 0 & 0 \end{pmatrix} e^{i\omega_g \left(t - \frac{z}{c}\right)} \tag{1.4}$$

where ω_g is the frequency of the gravitational wave and the two independent polarisations are $h_\times$ and h_+.

In order to measure gravitational waves, we can look at their measurable effects. This can be understood using two free masses, which are located at a distance $x = L$ apart from each other, with one of the masses at the origin. The separation between the two masses can be measured by sending a plane wave of light originating at the origin. The

light would then bounce off the far-off mass, and consequently, the phase of the returning wave can be expressed as

$$\phi_{rt}(t_{rt}) = \int_0^{t_{rt}} 2\pi f \, dt \tag{1.5}$$

where t_{rt} is the time taken by the light to make one round trip and f is its frequency (corresponding wavelength is λ). In the absence of any radiation, the integration can be done by changing it into an integral over length by using the flat space metric $\eta_{\mu\nu}$ and relating space and time ($t_{rt} = 2L/c$ and $dt = dx/c$).

In the presence of a GW, for instance, a h_+ oriented wave, with a period much longer than the round-trip travel time, the round-trip phase can be calculated using Equation 1.3 as,

$$\phi_{rt}(t_{rt}) = 2\frac{2\pi f}{c}\int_0^L \sqrt{|g_{xx}|}dx \simeq 2\left(1 - \frac{h_+}{2}\right)\frac{2\pi L}{\lambda} \tag{1.6}$$

The integration along y axis will give the round-trip phase for the wave travelling along the y axis as,

$$\phi_{rt}(t_{rt}) \simeq 2\left(1 + \frac{h_+}{2}\right)\frac{2\pi L}{\lambda} \tag{1.7}$$

Therefore, the difference in the phase shift between the two arms gives us

$$\Delta\phi_{rt}(t_{rt}) \simeq \frac{2h_+}{2}\frac{2\pi L}{\lambda} \tag{1.8}$$

This equation helps to see the effect when a gravitational wave passes by. The arms are stretched and compressed as shown in Fig. 1.1. The phase shift can be interpreted as a length measurement indicating the apparent change in length in each arm. The length shift is proportional to the original distance between the masses, and is expressed as,

$$\frac{\Delta L}{L} = \frac{h_+}{2} \tag{1.9}$$

1.1.2 Astrophysical sources of gravitational waves

This section briefly describes the sources that can produce gravitational waves. and highlights the sources that have been detected to date, and also the possible future interests.

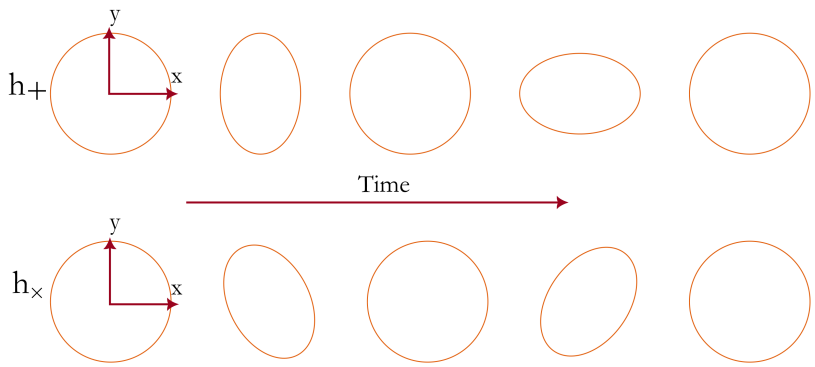

Figure 1.1: The effect of h_+ and $h_\times$ waves propagating in the z direction on a circle of test particles in the x-y plane.

1.1.2.1 Compact Binary Coalescence

A binary system formed by a pair of massive objects such as black holes, neutron stars or white dwarf lose their orbital energy into GWs, and therefore they are the most prominent source of GWs. The orbital radius shrinks, which causes the orbital motion to speed up. During such an event, the gravitational waves keep increasing in both amplitude and frequency as the binary system spirals into its death, resulting in a chirp signal. Such a system (a binary black hole) was the one which produced the first detection of GW event GW150914 [4, 5].

1.1.2.2 Spinning massive objects

Compact spinning objects such as neutron stars are targets for a continuous GW search [6]. Continuous waves comprise a periodic waveform created by slow-changing systems, for instance binary compact object at its early stage or a bumpy rotating neutron star. Those neutron stars whose magnetic axes happen to align with Earth's line of sight and are emitting light pulses are known as pulsars. The spinning pulsars are targets of terrestrial laser interferometric detectors, as the frequency of some pulsars is in the detector's observation band.

1.1.2.3 Stochastic gravitational wave background

The Big Bang is a prime candidate for a stochastic gravitational wave source. A stochastic background of GW is expected to arise from a superposition of a large number of unresolved GW sources of astrophysical and cosmological origin. They should carry signatures from the earliest epochs in the evolution of the universe. Such detections will help develop new insights into the evolution of the universe and fundamental physics. [7]

1.1.2.4 Core-collapse Supernovae

It is natural to expect a GW emission during a supernova explosion. Core-collapse Supernovae are among the lesser-known and crudely modelled burst sources. However the prediction of the waveform is difficult due to a lack of understanding of the explosion mechanism. Most of the explosion modes suggest that the frequency of such GW signals is widely spread and within the observation band of terrestrial interferometers. [7]

1.2 Gravitational wave detector

The gravitational waves from the sources mentioned can be detected by measuring the differential length change in two directions, as described by Equation 1.9. This can be achieved by using a laser interferometer. Over the years, the laser interferometers have observed several configuration changes to improve their sensitivity. The details from basic to advanced configuration are briefly discussed in the upcoming sections.

1.2.1 Michelson Configuration

The Michelson interferometer is a configuration as shown in Fig. 1.2. The setup consists of a light source (laser), a 50/50 beam splitter (BS), and two mirrors or end test mass (ETM, having a substrate and reflective coating) positioned in two orthogonal directions. The laser is split equally using a BS and travels an equal length along the two arms. The laser bounces off the two ETM and recombines at the BS again. The laser interferes destructively at the detector port, which is called the anti-symmetric (AS) port. For perfect destructive interference, no laser will reach this port, and therefore, it is also called the dark port [8].

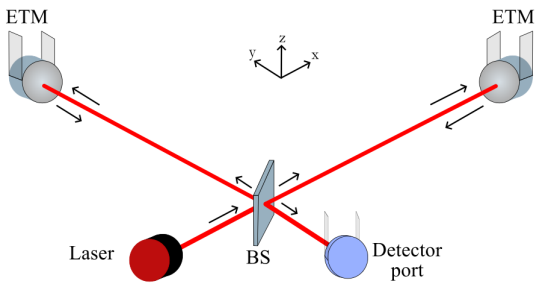

Figure 1.2: The Michelson interferometer configuration for gravitational wave detection.

The laser interferes constructively in the transmission of the beam splitter, and all the light is reflected in the direction of the incoming laser. When GW of a certain frequency

passes, it modulates the microscopic optical length of the arm by ΔL at the same frequency. The microscopic length change is differential in the two arms, *i.e.*, one arm shrinks (expands) while the other expands (shrinks) respectively, as shown in Fig. 1.1. The GW will manifest as intensity variation at the AS port. If the wavelength of the GW of amplitude h is much longer than the arm lengths, the amount of change is proportional to the macroscopic arm length L, so that [8]

$$\Delta L \sim hL \tag{1.10}$$

If a GW polarised in plus mode passes along the z axis, through the Michelson interferometer, placed in the $x-y$ plane, the phase change can be derived using the equations discussed below. First of all, the interval Equation 1.1 can be expressed as [3, 8],

$$ds^2 = -(cdt)^2 + (1+h(t))dx^2 + (1-h(t))dy^2 + dz^2 \tag{1.11}$$

Since the light travels along the world line of $ds^2 = 0$, the light travelling on the x axis satisfies [3, 8],

$$cdt = (1+h(t))\,dx \tag{1.12}$$

Integrating dx over the round-trip path from the BS to ETM, the following is obtained [3, 8],

$$\int_{t-\tau_x}^{t} \frac{t'}{\sqrt{1+h(t')}} dt \approx \int_{t-\tau_x}^{t} \left(1 - \frac{1}{2}h(t')\right) dt' = \frac{2L_x}{c} \tag{1.13}$$

where τ_x represents the duration the light takes to make a round trip in the x arm of length L_x. Therefore, the duration can be represented as [3, 8],

$$\tau_x = \frac{2L_x}{c} + \frac{1}{2}\int_{t-\tau_x}^{t} h(t')dt' \approx \frac{2L_x}{c} + \frac{1}{2}\int_{t-L_x/c}^{t} h(t')dt' \tag{1.14}$$

where, τ_x is approximated by $2L_x/c$ in the last expression as $h \ll 1$. This can be used to evaluate the net change in the optical phase. The light (of wavelength λ and ω_0 as the angular frequency) travelling in x and y direction will acquire phase as represented by following equation [3, 8],

$$\phi_x = \omega_0\tau_x = \underbrace{\frac{2\omega_0 L_x}{c}}_{\substack{\text{static phase rotation due to} \\ \text{light traveling a length of } 2L_x}} + \underbrace{\frac{\omega_0}{2}\int_{t-2L_x/c}^{t} h(t')\,dt'}_{\substack{\text{GW-induced} \\ \text{phase deviation}}} \tag{1.15}$$

$$\phi_y = \omega_0 \tau_y = \underbrace{\frac{2\omega_0 L_y}{c}}_{\substack{\text{static phase rotation due to} \\ \text{light travelling a length of } 2L_y}} + \underbrace{\frac{\omega_0}{2}\int_{t-2L_y/c}^{t} h(t')\,dt'}_{\substack{\text{GW-induced} \\ \text{phase deviation}}} \tag{1.16}$$

The phase difference between x and y arm is [3, 8],

$$\begin{aligned} \phi_x - \phi_y &= \frac{2\omega_0(L_x - L_y)}{c} + \Delta\phi_g \\ \Delta\phi_g &\equiv \omega_0 \int_{t-2L/c}^{t} h(t')\,dt' \quad [\text{for } L_x \approx L_y = L] \end{aligned} \tag{1.17}$$

Therefore, GW will change the interference condition and will manifest as a power fluctuation at the AS port. When GW has a long wavelength such that the induced phase shift does not vary as fast as the round-trip time of $2L/c$, it can be approximated as [3, 8],

$$\Delta\phi_g \approx \frac{2\omega_0 L}{c} h = \frac{4\pi}{\lambda}\Delta L \tag{1.18}$$

A monochromatic GW at an angular frequency of ω_g represented by, $h(t) = he^{i\omega_g t}$, when plugged into Equation 1.17 gives the frequency response of the Michelson interferometer to GW as [3, 8],

$$H_{MI}(\omega_g, L) \equiv \frac{\Delta\phi_g}{he^{i\omega_g t}} = \frac{2\omega_0}{\omega_g}\sin\left(\frac{\omega_g l}{c}\right)e^{-i\frac{\omega_g t}{c}} \tag{1.19}$$

At low frequencies, the above equation can be approximated as follows, which is consistent with Equation 1.18 [3, 8],

$$H_{MI}(\omega_g, L) \approx \frac{2\omega_0 L}{c} \tag{1.20}$$

When the frequency of GW becomes higher than the inverse of the round-trip time $c/2L$, the above approximation is invalid because the phase of the GW signal will start cancelling when the light is still travelling in the arms. This effect depends on the baseline length of the arms and determines the bandwidth of the Michelson interferometer or the cut-off in the frequency response curve.

The resulting electric field at the AS port is a function of the optical path difference for the laser in the two orthogonal arms, and can be represented as [8, 9],

$$E_{AS} = E_{in}(r^x_{ETM} t_{BS} r_{BS} e^{i2\phi_x} - r^y_{ETM} t_{BS} r_{BS} e^{i2\phi_y}) \tag{1.21}$$

where the r^x_{ETM}, r^y_{ETM} are the reflectivity of ETM in two arms, t_{BS}, r_{BS} are the transmission and reflection of the BS, and ϕ_x and ϕ_y are the phase accumulated by laser in travelling across the arm. For ETMs with identical reflectivity , $r^x_{ETM} = r^y_{ETM} = r$, the Equation 1.21 will simplify. The power at the AS port can then be represented using $P_{AS} = E^* \cdot E = 4|E_{in}|^2 (r\, t_{BS} r_{BS})^2 \sin^2\phi$. The phase sensitivity of the interferometer, as a result, can be represented using the differential as follows [8, 9],

$$\frac{dP}{d\phi} = 2|E_{in}|^2 \sin(\phi)\cos(\phi) \qquad \text{with, } r = 1,\ t_{BS} = r_{BS} = 1/\sqrt{2} \tag{1.22}$$

The measured power fluctuation due to shot noise can be represented by [8, 9],

$$\partial P_{shot} = \sqrt{\frac{2hc}{\lambda}} |E_{in}| \sin\phi \tag{1.23}$$

The equivalent phase noise can be obtained by dividing Equation 1.23 with Equation 1.22, and is expressed as [8, 9],

$$\frac{\partial\phi}{\sqrt{Hz}} = \sqrt{\frac{hc}{2\lambda}} \frac{1}{|E_{in}|} \frac{1}{\cos\phi} \tag{1.24}$$

Even though, in principle, the Michelson configuration can be used to detect gravitational waves, it cannot offer enough sensitivity for an actual detection. Therefore, some crucial modifications were implemented in the Michelson configuration. One of the most straightforward ways to increase sensitivity is by increasing the arm length of the detectors, following Equation 1.9. However, terrestrial gravitational wave detectors are constrained in the space they can take on a given land due to the cost (current ones are 3-4 km and planned future detectors are 10-40 km). The length of the two arms can be increased using the Fabry-Perot and the gain of the interferometer through some recycling configurations.

1.2.2 Fabry-Perot Configuration

An effective increase in arm length can be achieved by bouncing the laser beam multiple times in each arm using a cavity, as shown in Fig. 1.3. Such a configuration is called the Fabry-Perot Michelson configuration (FPMI). This configuration was proposed as a way of increasing the signal gain of the interferometer [10, 11]. Using different mirrors to bounce off light showed several impracticalities due to scattered light [12]. Therefore, the idea of multiple reflections on the same spot on a mirror was then used [13]. This can be done by using an additional input test mass (ITM), which is a partial transmitter. The ITM and ETM now form a Fabry-Perot resonator, where the laser travels a long distance before it exits through the ITM.

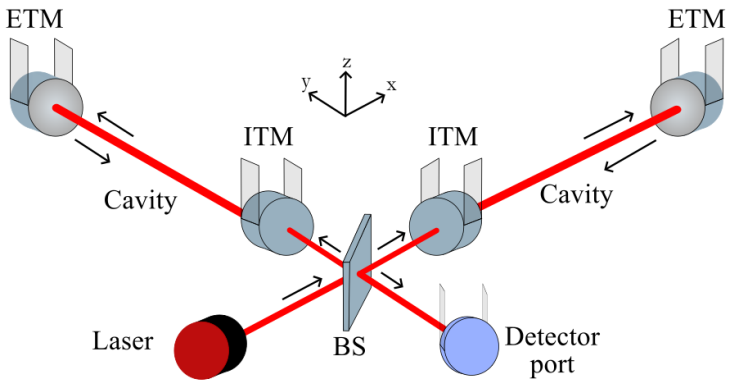

Figure 1.3: The Fabry-Perot Michelson interferometer configuration as a gravitational wave detector. The arms in this configuration offer a method to increase the effective distance travelled by the laser, thereby increasing the sensitivity.

One disadvantage in comparison to a long delay line is that the cavity must be operated near resonance to achieve a high power buildup and the corresponding phase shift gain. In contrast, a delay line provides this phase shift gain at its nominal operating point without requiring resonance. Maintaining the Fabry–Perot cavity near resonance, therefore, necessitates active feedback control of the cavity length [9].

1.2.3 Power recycling configuration

The power fluctuations observed at AS port are proportional to the power injected in the interferometer following Equation 1.24. So, increasing the input laser power will increase the sensitivity of the detector. In the Michelson configuration, all the light essentially returns to the laser, in the absence of the GW, which makes the Michelson or Fabry Perot configuration look like a highly reflecting mirror when it is operated. This laser power can be sent back to the interferometer, thereby increasing the laser power going into the Interferometer. The addition of a mirror called the Power recycling mirror (PRM) before the Fabry-Perot cavity will essentially form a resonating cavity for power enhancement, as shown in Fig. 1.4a. This configuration is usually referred to as a Power Recycled Fabry-Perot interferometer (PRFPMI) [14, 15, 13].

1.2.4 Signal recycling configuration

The signal recycling technique enables the recycling of the signal field induced by GWs which reach the AS port, and propagate it back to the interferometer [16]. This technique requires the use of a partial mirror, called a signal recycling mirror (SRM) at the output side of the

interferometer, as shown in Fig. 1.4b. The SRM couples with the differential motion of the two arm cavities, thereby increasing the effective finesse for the GW signals. Consequently, the storage time increases, which results in enhanced sensitivity at low frequencies. However, such a configuration leads to a narrower observational bandwidth.

The resonant sideband extraction scheme has the same optical configuration as signal recycling; however, it decreases the effective finesse [17] rather than increasing it. This property expands the observation bandwidth at the expense of the sensitivity at low frequencies. The signal recycling and resonant sideband configuration can be chosen by simply changing the round-trip phase inside the signal recycling cavity via microscopic length tuning.

1.2.5 Dual recycling configuration

The recycling schemes introduced above are independent of each other. The goal of power recycling is to increase the effective laser power, while the signal recycling or resonant sideband extraction goals are to modify the optical response. These detector configurations can be incorporated independently of each other, since in dark port condition, the power recycling affects the common mode of the interferometer, while the signal recycling affects the differential mode. The combination of power recycling with signal recycling or resonant sideband extraction is called a Dual Recycling Fabry Perot Michelson interferometer (DRFPMI), and the configuration is shown in Fig. 1.4c [8].

1.3 Terrestrial Laser Interferometers

1.3.1 Evolution from 1st Gen to 3rd Gen Detectors

The development of the laser interferometer was initiated in the early 1970's to detect GWs [18]. In the following years, several techniques were developed to improve the sensitivity of the detectors. The 1G detectors were room temperature, ground-based, 100-meter (TAMA in Japan [19], and GEO [20] in Europe) and km-scale (LIGO in the USA [21], VIRGO [22] in Europe) were established. They were operated in FPMI configuration. Although they were able to achieve their design sensitivity through rigorous commissioning and tuning, they did not detect GWs, and hence several upgrades were considered towards detection.

Then came the era of use of PRFPMI, which forms the 2nd generation Interferometers. In order to fully open GW astronomy, a worldwide network of detectors is required. The two LIGO detectors were upgraded for this configuration (towards Advanced LIGO) [23], and Advanced VIRGO (in Europe) [24], was also established. The 2G interferometer, LIGO, made

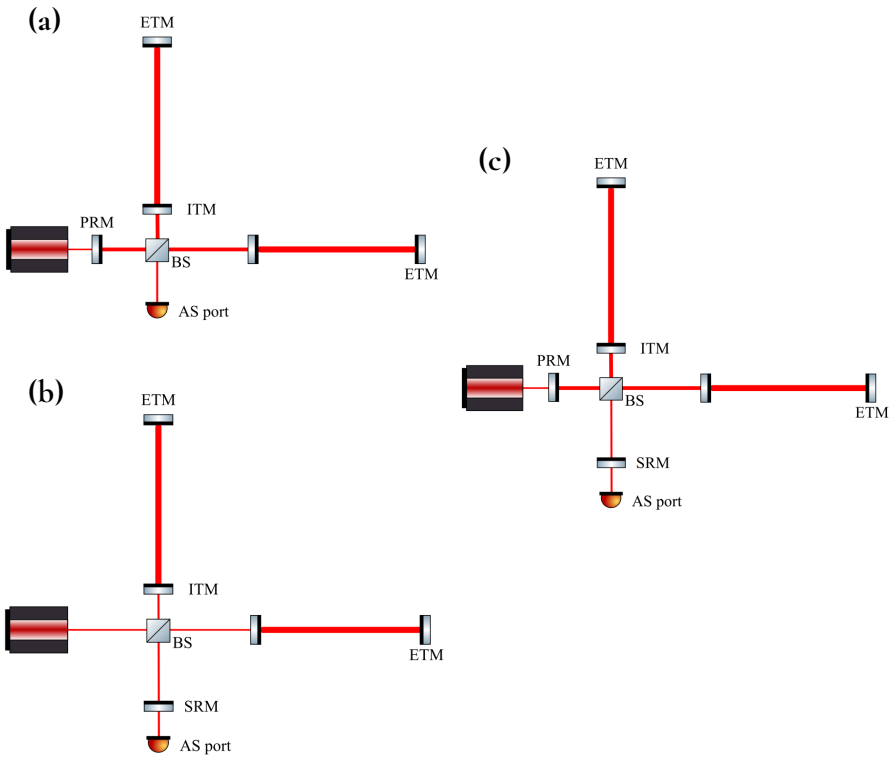

Figure 1.4: Different recycling configurations for a Fabry-Perot interferometer: (a) power recycling [14, 15, 13], (b) signal recycling (or resonant sideband extraction) [16, 17], (c) dual recycling [8].

the first detection of GW in 2015, from a binary black hole merger, and they were awarded the Nobel prize in physics for 2016. The observation of the first GW event GW150914 opened a new window in astronomy. The detected GW were produced in the final fraction of a second of the merger of the two black holes, which produced a single, more massive spinning black hole. The signal observed by LIGO could estimate the masses of the two black holes to be about 29 and 36 times the mass of the sun, and the merger happened 1.3 billion years ago. The two LIGO detectors recorded the event 7 ms apart, which helped to locate the source of GW to be in the Southern hemisphere, also establishing the use of the GW detector network for sky localisation [5].

The following years saw several detections by the gravitational wave network. Advanced LIGO (in DRFPMI configuration) and Advanced VIRGO [24] detected 94 merger events in the three observation runs between 2015 and 2020, including 90 binary black holes, 2 neutron star-black hole systems, and 2 binary neutron star mergers [25]. They also made a multi-messenger observation with other telescopes and detected the event GW170817, which was a binary neutron star merger with gamma bursts [26]. Several follow-up multi-messenger (optical, infrared) observations were done due to sky localisation enabled through

GW detector network. This opened a new window for new insights into the astrophysical processes and fundamental physics [27]. Amongst these insights are the origin of some gamma ray bursts, one formation site of the heaviest elements in the universe, a previously unknown population of heavier stellar-mass black holes, and the confirmation of the quasi -normal modes of the final black hole predicted by General Relativity [28].

While the 2G detectors made several remarkable detections, they do not yet enable the full potential of gravitational wave astronomy. This brings the GW community to advance towards 3G detectors, *i.e.,* more development and improvements to extend the range of GW detection and to reach into the past of the universe.

Before going to the 3G detector, there was motivation towards the development of a 2.5-generation interferometer, KAGRA, an underground detector in Japan [29]. Its configuration is PRFPMI and has some special features in comparison to other detectors, such as the mirror and suspensions are designed to be cooled to 20 K. As such, it uses crystalline materials for the test mass in contrast to LIGO or VIRGO (which operate at room temperature and use an isotropic test mass). The improvements through the use of underground and cryogenic system is discussed in 1.3.3. However, KAGRA has not yet detected GW and is currently under rigorous commissioning which is not a trivial task.

The future will see the development of 3G detectors: Einstein Telescope (in Europe) [28] and Cosmic Explorer (in the USA) [30] that are going to open a new window to observe new astrophysical sources. Part of the development of 3G detector involves increasing arm length (10 km for Einstein Telescope and 10-40 km for Cosmic Explorer), using megawatts of optical power, larger and heavier mirrors, amongst several others [28, 30].

The 3G GW detectors aim to observe several enticing phenomena. As shown in Fig. 1.5 and Fig. 1.6. The detection of mergers with redshifts of >10 will enable the analysis of how the black hole and neutron star populations evolved over the history of the universe. Future detectors will also provide improved source localisation for multi-messenger astronomy, which will allow observation along with other astronomical Telescopes in different wavelengths. This paves the path to reveal how matter behaves under the most extreme condition including the internal structure and equation of state of neutron stars, heavy element nucleosynthesis, and highly relativistic jets. Furthermore, the 3G detectors will enable the study of the nature of the strongest gravity and test theories on dark matter and dark energy. They also have the potential to reveal some unexpected discoveries from the old universe. [28, 30]. The entire journey from 1G to 3G detectors involved several noise improvements through developments of different techniques to mitigate noise, and therefore, it is crucial to understand some of the main noise sources in the detector.

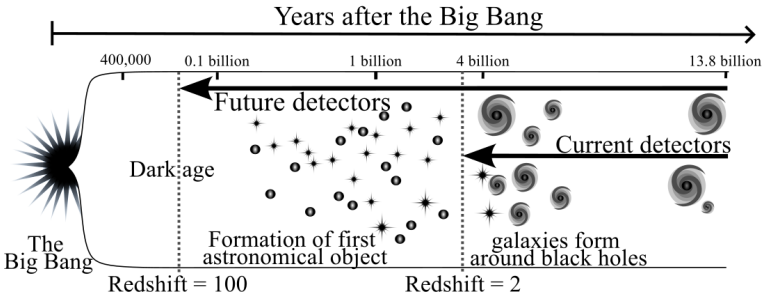

Figure 1.5: Prospects of observation through improvements of future detectors.

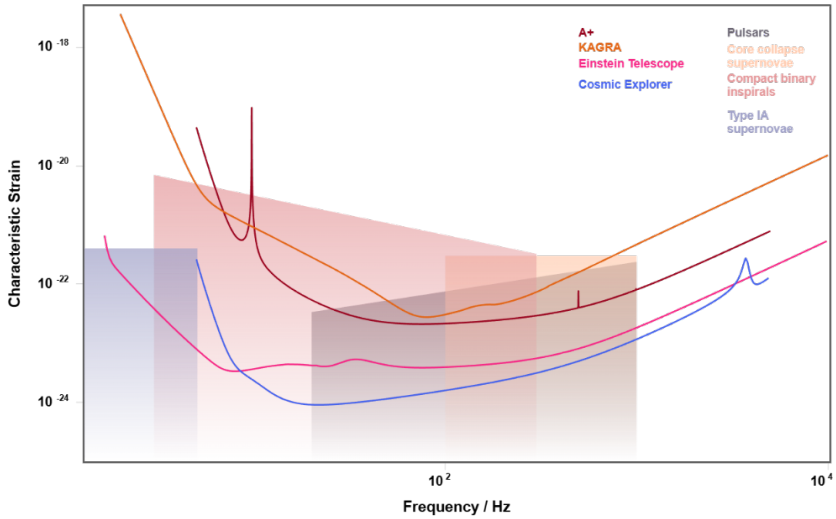

Figure 1.6: Sensitivity curve showing strain with respect to frequency of the future upgrade for LIGO (A+), and design sensitivity of KAGRA, Einstein Telescope and Cosmic Explorer respectively. The increased sensitivity will offer frequency detection of GW events as well as detection of GW from new sources such as supernovae [31].

1.3.2 Noise Sources

Various noise source relevant to understanding the need for research mentioned in this thesis is described below.

1.3.2.1 Seismic noise

Any presence of seismic noise introduces a change in the mirrors' position, which then manifests as a change in optical lengths. Even though the mirrors are suspended to reduce the effect of seismic noise through isolation, there still remains a non-negligible amount of vibration. Seismic noise, hence, introduces fluctuations in the length of optical cavities more than their resonance linewidth at low frequencies. This causes the optical cavities to be non-stationary at the operating point without any active control. There are several techniques

in use and development to reduce this noise further. One of many is the development of a longer version of the current Superattenuator seismic platform of VIRGO for 3G detectors [28], or the use of a multi-stage (inverted pendulums, geometric anti-spring filters, etc.), vibration isolation system in KAGRA [29].

1.3.2.2 Newtonian noise

Newtonian noise, also known as gravity-gradient noise, arises from fluctuations in the local gravitational field caused by time-varying mass-density perturbations in the detector environment. These perturbations are primarily due to seismic waves in the ground and, at lower frequencies, atmospheric density fluctuations. Unlike seismic noise, Newtonian noise does not couple through mechanical contact or suspension systems; instead, it acts directly on the test masses via gravity, producing apparent mirror displacements that are indistinguishable from a gravitational-wave signal. As a result, Newtonian noise sets a fundamental limit to the low-frequency sensitivity of ground-based gravitational-wave detectors, typically below $\sim$ 10–20 Hz. Mitigation strategies, therefore, focus on reducing environmental mass-density fluctuations through careful site selection, underground installation (for instance, KAGRA is placed underground), and active subtraction using environmental sensor arrays [32, 28].

1.3.2.3 Quantum noise

The quantum noise in an interferometer is classified into shot noise and radiation pressure noise. Shot noise is a consequence of vacuum fluctuation in the electromagnetic fields, which enters the interferometer from any open ports. It results in white noise and can therefore be improved by increasing the laser power, as it is inversely proportional to the square root of laser power. While the number of photons fluctuates due to shot noise, these photons impinging on the suspended mirrors introduce fluctuations in their momentum due to radiation pressure. This effect is directly proportional to the square root of laser power, and therefore, the issue due to radiation pressure increases with an increase in laser power [33, 34]. Techniques like the frequency-dependent squeezing are used in Advanced LIGO and Advanced VIRGO to address both the issue of quantum noise and make it broadband. [35]. Additionally, both noises can also be reduced by using heavier mirrors and increasing laser power.

1.3.2.4 Thermal noise

The mirrors and the suspension systems are operated at some fixed temperature, and therefore, they exhibit thermal fluctuations. The intrinsic mechanical noise is caused by thermal energy, which causes random motion within the material, and is also refereed as Brownian noise. The mirror, therefore, itself exhibits the thermally induced fluctuations. The suspension at finite temperature has some excited mechanical mode which result in the displacement of the mirror hanging from the suspension [36]. Both the thermal noise from mirrors (substrate and coating) and suspensions induces unwanted changes in the optical lengths of the arms. One of the methods to lower thermal noise is to reduce the temperature of the mirrors, which is utilised by KAGRA by cooling mirrors to 20 K.[29] and is also planned for the Einstein Telescope [28].

1.3.2.5 Sensing noise

There are several technical noises that can affect the performance of the detector, such as laser noise, oscillator noise (generator for the sidebands) in both amplitude and phase, readout electronics noise, etc. [9].

Any laser exhibits fluctuations in both amplitude and frequency (or phase). Since the signal at the AS port is read out as an intensity (photocurrent) on the PD, laser amplitude noise can couple directly through power fluctuations at the photodetector and appear as excess sensing noise. Laser frequency noise can also couple into the gravitational-wave readout because frequency fluctuations change the optical phase and can be converted into effective length fluctuations when the interferometer is not perfectly held at its operating point (e.g., due to imperfect control, asymmetries, or contrast defects). In practice, laser amplitude and frequency noise are reduced using stabilisation schemes such as active feedback control.

1.3.3 KAGRA

KAGRA is a 3 km gravitational-wave interferometer built in the Kamioka mine and operated with cryogenic sapphire test masses. Its two key design choices are (i) an *underground* facility to reduce seismic noise and seismic Newtonian (gravity-gradient) noise, and (ii) *cryogenic* operation to reduce mirror thermal noise, which limits room-temperature detectors around $\sim$ 100 Hz [29].

In the low-frequency band, the noise budget is typically dominated by seismic motion and gravity-gradient coupling. For KAGRA, measurements show that the seismic motion

inside the mine is lower than *outside* by a factor of $\gtrsim 100$ above 10 Hz (*i.e.*, about two orders of magnitude reduction in ground-motion amplitude) [29]. The same reference reports that KAGRA's total seismic Newtonian-noise level is approximately one order of magnitude smaller than LIGO above 10 Hz [29].

In the most sensitive mid-band (tens to a few hundred Hz), thermal noises (mirror/coating and suspension) become important. Cooling reduces thermal-noise contributions through their temperature dependence; for many dissipation-driven thermal noises, a useful rule of thumb for the *amplitude* spectral density is $\propto \sqrt{T}$, so cooling from 300 K to ∼22 K corresponds to a reduction by $\sqrt{300/22} \approx 3.7$, *i.e.*, about 0.6 orders of magnitude in amplitude. Akutsu *et al.* also show that the detailed thermal-noise behaviour is not purely monotonic in all components: mirror thermal noise increases rapidly between 22–50 K, while suspension thermal noise increases rapidly between 100-150 K due to thermoelastic mechanisms becoming significant above characteristic temperatures [29]. Achieving the design sensitivity of any detector is an extremely challenging task, and KAGRA is under active commissioning to improve its sensitivity. A representative sensitivity curve is shown in Fig. 1.7.

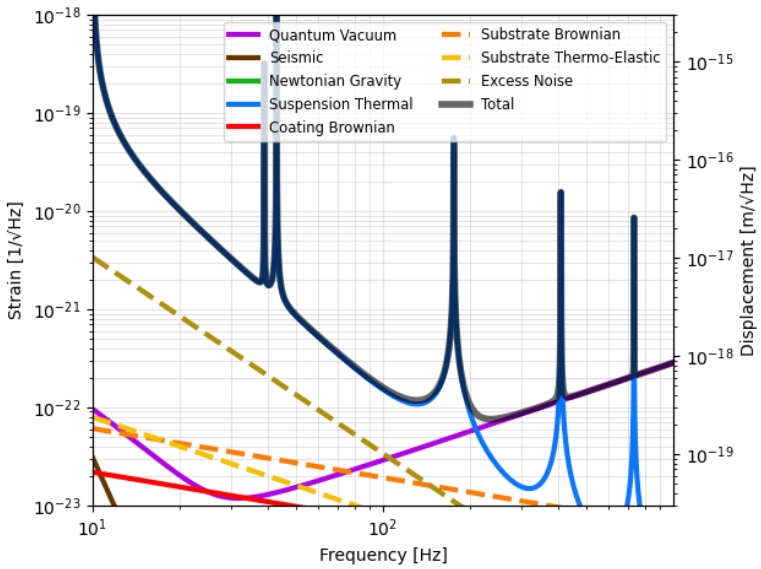

Figure 1.7: Representative KAGRA strain sensitivity curve (O4b configuration) [37].

1.4 Discussion

This chapter highlights the technique of detecting gravitational waves using interferometers. However, the noise present in the detector worsens the sensitivity to the GW events. The

exploration of new physics and sources can be done through improvement in the technology of the detector and mitigation of the noise sources. The upcoming chapter will show the issue of concern for the research mentioned in this thesis and lay the foundation for the work presented from Chapter 3 through Chapter 5.

2

The birefringence issue

Contents

2.1 Theoretical description

The story of the polarisation of light is essential for understanding its use in a measurement system. The most interesting story the author came across is that Vikings used a calcite crystal to navigate by observing the polarised sky patterns. The laser in the GW detector essentially forms a scale to measure properties of cosmic events. However, the current test masses in KAGRA exhibit non-uniform birefringence, which causes spatial differences in the polarisation of the laser circulating in the detector. This introduces several issue that

limits the performance of the detector. Hence, it is important to have a good understanding of the polarisation of light and polarisation elements. With this perspective in mind, the following section delves into the depths of polarisation.

2.1.1 Polarization of light

Light is a transverse wave and can be treated as a vector quantity, and its vector nature is called *polarisation*. A light field propagating in $\hat{z}$ direction can be illustrated as Fig. 2.1. The transverse components of light can be represented in the direction orthogonal to the propagation direction as,

$$\begin{aligned} E_x(z,t) &= A_x \cos(\tau + \phi_x) \quad &= A_x(\cos\tau\cos\phi_x - \sin\tau\sin\phi_x), \\ E_y(z,t) &= A_y \cos(\tau + \phi_y) \quad &= A_y(\cos\tau\cos\phi_y - \sin\tau\sin\phi_y) \end{aligned} \tag{2.1}$$

where, $\tau = \omega t - kz$ is the propagator. $E_{x,y} = A_{x,y}e^{-i\phi_{x,y}}$ are the complex amplitudes of the electrical fields in the $\hat{x}$- and $\hat{y}$-direction (circumflex indicates normalization) respectively. They are expressed in polar coordinates with polarisation-dependent amplitude $A_{x,y}$ and phase $\phi_{x,y}$.

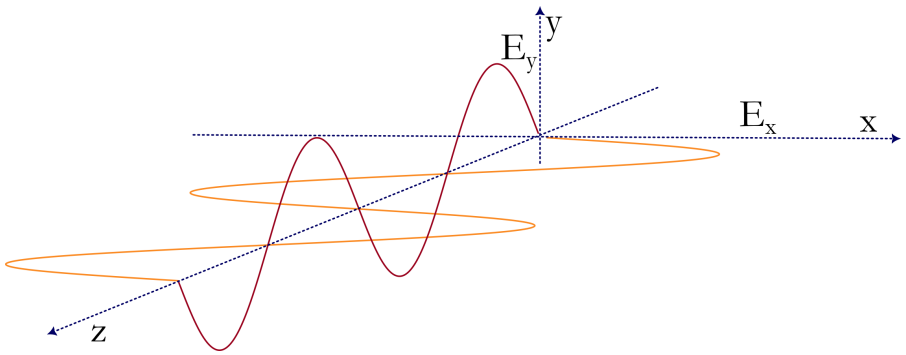

Figure 2.1: Illustration of light propagating in $\hat{z}$ directional as transverse wave.

As the light field propagates, E_x and E_y give rise to a resultant vector. The vector then describes a locus of points described by the optical field at any instant of time. The transverse wave shown in Fig. 2.1 when projected along an orthogonal plane will hence trace an ellipse represented as Fig. 2.2, where the lengths of the major and minor axes are $2a$ and $2b$ respectively.

The axes of the ellipse can be rotated by some angle ψ relative to the coordinate axes. The components for a rotated ellipse, E'_x and E'_y in $\hat{x}$ and $\hat{y}$ direction can be represented as,

$$\begin{aligned} E'_x &= E_x\cos\psi + E_y\sin\psi = a\cos(\tau + \phi') \\ E'_y &= -E_x\sin\psi + E_y\cos\psi = \pm b\sin(\tau + \phi') \end{aligned} \tag{2.2}$$

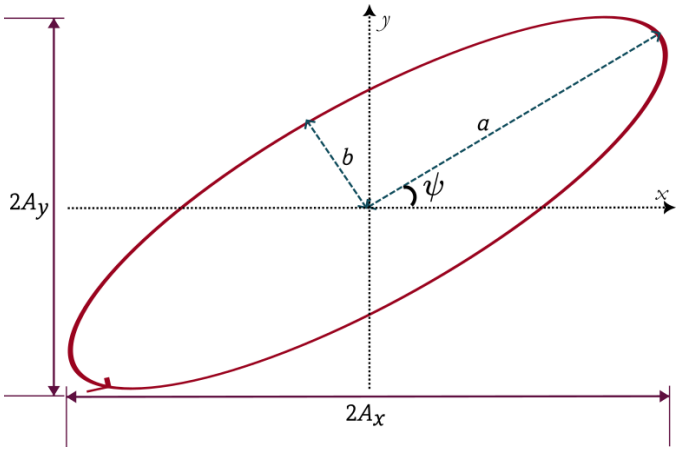

Figure 2.2: Polarization Ellipse

where ϕ' is an arbitrary phase, and the $\pm$ sign indicates that the two possible senses in which the endpoint of the field vector can describe the ellipse. The above two equations, when squared and added, are used to represent the polarisation using a standard equation of an ellipse, as follows,

$$\frac{E_x'^2}{a^2} + \frac{E_y'^2}{b^2} = 1 \tag{2.3}$$

The angle of ellipticity of the polarisation ellipse χ can be represented using the major and minor axes of the ellipse as

$$\tan\chi = \pm\frac{b}{a} = \tan(\sin^{-1}(\sin 2\alpha \sin\phi)); \qquad \frac{-\pi}{4} \leq \chi \leq \frac{\pi}{4} \tag{2.4}$$

where α is the ratio of the amplitudes taken as $\alpha = \tan\frac{A_y}{A_x}$. While the angle of orientation of the ellipse ψ can be expressed as

$$\tan 2\psi = \tan 2\alpha \cos\phi \tag{2.5}$$

The polarisation ellipse can be used to understand the electric field magnitude in different directions, for instance along the coordinate axes, $\hat{x}$ and $\hat{y}$. The polarisation of monochromatic light propagating along the $\hat{z}$-direction at the position $z = 0$ can be described in Cartesian coordinates using a vector *i.e.*, the Jones vector [38] following the decreasing phase convention [39], as:

$$E = \begin{pmatrix} E_x \\ E_y \end{pmatrix} = \begin{pmatrix} A_x e^{-i\phi_x} \\ A_y e^{-i\phi_y} \end{pmatrix} \tag{2.6}$$

Following Equation 2.3, the electric field can also be expressed as the normalised Jones vector in terms of azimuth and ellipticity (ψ and χ respectively, with $0 \leq \psi \leq \pi$ and $-\pi/4 \leq \chi \leq \pi/4$) [40] as :

$$E = \frac{1}{\sqrt{(1+\tan(\chi))^2}} \begin{pmatrix} \cos(\psi) + i\tan(\chi)\sin(\psi) \\ \sin(\psi) - i\tan(\chi)\cos(\psi) \end{pmatrix}. \tag{2.7}$$

A factor $\sqrt{2P/(c\epsilon_o \pi r_s^2)}$ with the beam power P, the beam radius r_s, the speed of light c, and the vacuum dielectric constant ϵ_0, has to be multiplied to E to obtain the Jones vector having the specifications such as common amplitude and phase of the system.

2.1.2 Polarization elements

In order to understand the change of polarisation of light upon interaction with any element, we need to understand the property, refractive index. Upon interaction, the light can undergo a change in phase or amplitude. This is described in the following sections.

2.1.2.1 Refractive Index

The phase of light changes upon traversing through any medium due to its refractive index. The speed of light essentially slows down by $1/n$ when interacting with a medium of refractive index n. A birefringent medium has a different refractive index along different axes. This results in light changing its speed differently along the different axes. This splits light into two rays travelling with different speeds c/n_e, c/n_o for extraordinary and ordinary refractive index, respectively. The axis in which light travels faster is called the fast axis, while the other is the slow axis. This implies that the axis with the larger refractive index is the slower axis. The refractive index can vary with the wavelength of light and also the temperature change brought about by the incident beam.

The refractive index of a crystal can be the same or different along different axes of symmetry. The refractive index of two waves as a function of the direction of their common wave normal can be obtained by using an ellipsoid known as the indicatrix [41], as shown in Fig. 2.3. If some crystal has three principal axes x_1, x_2, and x_3 of the dielectric constant (or the permittivity) tensor, the indicatrix can be expressed using

$$\begin{aligned} \frac{x_1^2}{n_1^2} + \frac{x_2^2}{n_2^2} + \frac{x_3^2}{n_3^2} &= 1 \\ B_1 x_1^2 + B_2 x_2^2 + B_3 x_3^2 &= 1 \end{aligned} \tag{2.8}$$

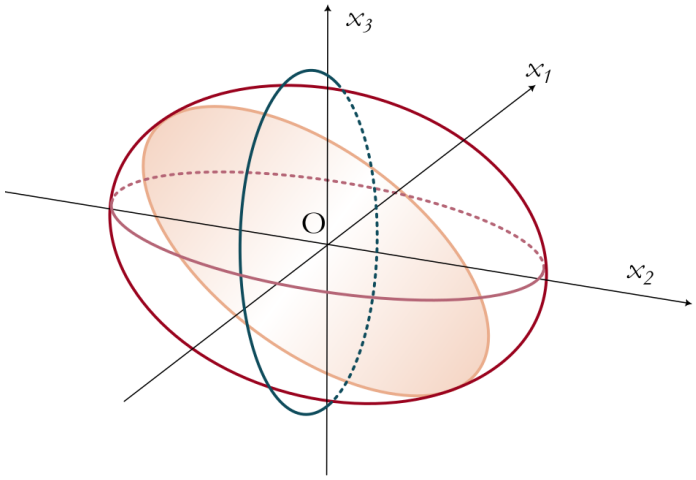

Figure 2.3: The indicatrix construction giving two refractive indices for the two plane-polarised waves associated with a given wave normal. The red surface is the refractive-index ellipsoid (indicatrix). The orange plane represents a section through the origin (typically the plane perpendicular to the chosen wave normal); its intersection with the indicatrix gives an index ellipse, whose principal semi-axes correspond to the two allowed refractive indices for orthogonal polarisations (fast and slow waves). The teal and pink curves illustrate additional section ellipses of the indicatrix (e.g., principal sections in coordinate planes), with dashed portions indicating the hidden parts of the curves on the far side of the 3-D surface.

where $n_1 = \sqrt{K_1}$, $n_2 = \sqrt{K_2}$ and $n_3 = \sqrt{K_3}$. K_1, K_2 and K_3 are the principal dielectric constants. B_1, B_2 and B_3 are the relative dielectric impermeability.

In an isotropic (cubic) crystal, the refractive index is the same in all directions, *i.e.*, $n_1 = n_2 = n_3$, and the indicatrix reduces to a sphere. In contrast, hexagonal, tetragonal, and trigonal crystals are uniaxial, with rotational symmetry about the principal crystallographic axis (taken here as x_3, *i.e.*, the c axis), so the indicatrix is an ellipsoid of revolution about this axis. In this case, the indicatrix can be written as [41]

$$\frac{x_1^2}{n_o^2} + \frac{x_2^2}{n_o^2} + \frac{x_3^2}{n_e^2} = 1 \tag{2.9}$$

where n_o and n_e denote the ordinary and extraordinary refractive indices. Uniaxial materials are the most common anisotropic crystals and are the main focus of the birefringent materials discussed in this thesis. A key geometric property is that the indicatrix section in any plane perpendicular to the optical (c) axis is a circle of radius n_o. This circular cross-section implies azimuthal symmetry in the transverse plane: for propagation along the c-axis, the crystal does not select a preferred transverse polarisation direction in the ideal case, which supports operation in a single, well-defined polarisation. For this reason, in KAGRA, the laser beam in Sapphire is aligned to propagate along the crystal c-axis; by contrast,

off-axis propagation generally yields an elliptical section with distinct eigenpolarisations and different refractive indices, increasing the risk of unwanted polarisation splitting/mixing.

The birefringence for a uniaxial crystal is $\Delta n = n_e - n_o$. The corresponding phase difference Γ of light with wavelength λ when passing through a material of thickness L is

$$\Gamma = \frac{2\pi}{\lambda}\Delta n L \tag{2.10}$$

A crystal can be negative or positive uniaxial, having negative or positive birefringence, respectively. For instance, Sapphire is a negative uniaxial crystal with $n_e < n_o$, where the extraordinary axis is the fast axis. While retardation forms one property of birefringence, which is related to the phase of light, there is another important property related to the birefringent materials that is diattenuation.

2.1.2.2 Diattenuation

Any polarisation element can also change the intensity transmittance as a function of incident polarisation state. This property is diattenuation. It is defined in terms of the maximum T_{max} and minimum T_{min} intensity transmittance over all polarization states, as

$$D = \frac{T_{max} - T_{min}}{T_{max} + T_{min}}, \qquad 0 \leq D \leq 1 \tag{2.11}$$

The extinction ratio, which is the ratio of maximum to minimum transmission, can be expressed using the diattenuation as

$$E = \frac{T_{max}}{T_{min}} = \frac{1 + D}{1 - D} \tag{2.12}$$

The value of diattenuation varies from 0 to 1, with 0 representing an element that transmits all polarisation states equally and 1 representing a polariser. An ideal polariser has an extinction ratio ∞. When an unpolarised light is incident on an element, the exiting degree of polarisation is the diattenuation of that polarisation element. The polarisation-dependent loss of any element can be calculated using the extinction ratio as $10 \log_{10} E$ [39]. Hence, knowing both retardation and diattenuation, we can know the effect of the polarisation element in any system. The properties of birefringence and diattenuation can be used to understand the effect of polarisation elements on light using Jones calculus.

2.1.2.3 2D Jones calculus

Polarisation elements are described in the Jones formalism using 2×2 complex Jones matrices [38], J. The polarised light E^{in} after interaction with an optical element, J is described using $E^{out} = J \cdot E^{in}$. This equation is also true for a cascade of N components in series by expressing $J = J_N \cdot J_{N-1} \cdot \quad ... \quad \cdot J_1$. The Jones matrix of a linear retarder with retardance, $\Gamma = |\phi_1 - \phi_2|$, where ϕ_1 and ϕ_2 are the phase change for two orthogonal states, can be written as

$$LR(\Gamma, 0) = \begin{pmatrix} e^{-i\phi_1} & 0 \\ 0 & e^{-i\phi_2} \end{pmatrix} \tag{2.13}$$

Any Jones matrix can be transformed to represent the orientation of the fast axis of the element by multiplying it by the Cartesian rotation matrix. The rotated Jones matrix is $J(\theta) = R(\theta) \cdot J \cdot R(-\theta)$ or rotated vector $E(\theta) = R(\theta) \cdot E$, where the rotation matrix is

$$R(\theta) = \begin{pmatrix} \cos\theta & -\sin\theta \\ \sin\theta & \cos\theta \end{pmatrix} \tag{2.14}$$

A retarder has two degrees of freedom, an absolute phase change and retardance. Therefore, when constructing the Jones matrix for a retarder, there is a choice of phase associated with a phase convention [39]. In the research mentioned in this thesis, we have taken the symmetric phase convention. The symmetric phase convention advances the phase of the fast eigenpolarization and retards the phase of the slow eigenpolarization symmetrically. According to this convention, the Jones matrix of a linear retarder with a horizontally polarised fast axis and with fast axis orientation at some angle θ will look like [39]

$$LR(\Gamma, 0) = \begin{pmatrix} e^{-i\Gamma/2} & 0 \\ 0 & e^{i\Gamma/2} \end{pmatrix} \tag{2.15}$$

$$\begin{aligned} LR(\Gamma, \theta) &= R(\theta) \begin{pmatrix} e^{-i\Gamma/2} & 0 \\ 0 & e^{i\Gamma/2} \end{pmatrix} R(-\theta) \\ &= \begin{pmatrix} e^{-i\Gamma/2}\cos^2\theta + e^{i\Gamma/2}\sin^2\theta & -i\sin(\Gamma/2)\sin(2\theta) \\ -i\sin(\Gamma/2)\sin(2\theta) & e^{i\Gamma/2}\cos^2\theta + e^{-i\Gamma/2}\sin^2\theta \end{pmatrix} \end{aligned} \tag{2.16}$$

The diattenuator Jones matrix can be written in terms of diattenuation D using a term d, which is related to diattenuation as $d = \tanh^{-1}(D/2)$, as

$$LD(D, 0) = \begin{pmatrix} \cosh d + \sinh d & 0 \\ 0 & \cosh d - \sinh d \end{pmatrix} \tag{2.17}$$

2.1.2.4 3D Jones calculus

When the light changes its propagation direction upon interaction with an optical element, the Jones matrix no longer solely represents the component's birefringence but also includes an additional phase owing to the coordinate transformation. In such a case, the Jones vector defined in Equation 2.7 and the associated Jones matrix are represented in local coordinates $\left(\hat{s}, \hat{p}, \hat{k}\right)$ associated with a particular transverse plane. Hence, we use polarisation ray tracing (PRT) calculus to get rid of geometrical transformations and obtain the Jones matrix in a global frame and the proper birefringence of the component as described below.

A 3D Jones vector can be expressed using the local coordinates $\left(\hat{s}, \hat{p}, \hat{k}\right)$. The $\hat{s}$ and $\hat{p}$ vectors are perpendicular and parallel to the plane of incidence, respectively, for a light propagating along $\hat{k}$. For an interface with surface normal $\hat{n}$, we can obtain the local coordinates $\hat{s}, \hat{p}$ for the incident and exiting light, from the $\hat{x}, \hat{y}, \hat{z}$-coordinates as :

$$\hat{s}_{in} = \hat{s}_{out} = \frac{\hat{k}_{in} \times \hat{n}}{|\hat{k}_{in} \times \hat{n}|}, \; \hat{p}_{in} = \hat{k}_{in} \times \hat{s}_{in}, \; \hat{p}_{out} = \hat{k}_{out} \times \hat{s}_{out}. \tag{2.18}$$

If the cross product $\hat{k}_{in} \times \hat{n}$, cannot be defined because $\hat{k}_{in}$ and $\hat{n}$ are in the same direction, then in such a case, $\hat{s}_{in}$ assumes the value of the original $\hat{s}$ vector.

It is more insightful to study the Jones vector and matrix in 3D format when encountering geometric transformations, *i.e.*, where the propagation direction of light changes. As such, we can incorporate the vector change of light using a three-element electric field vector $\tilde{E}$. The 3×3 polarisation ray tracing matrix P characterises the changes in $\tilde{E}$ that arise upon interaction with one or several optical elements [42].

$$\tilde{E}_{out} = P \cdot \tilde{E}_{in}, \text{ where } \tilde{E} = [E_x, E_y, E_z]^T. \tag{2.19}$$

It can be seen from Equation 2.19 that P and $\tilde{E}$ are a 3D extension of the Jones matrix and Jones vector, respectively. The P matrix for a ray intercept upon interaction with an optical element having local Jones Matrix J, is defined as Equation 2.20. J_L is simply the local J with padded zeros and one, to represent as 3×3 matrix.

$$P = O_{out} \cdot J_L \cdot O_{in}^{-1}, \text{ where } J_L = \begin{pmatrix} & J & & 0 \\ & & & 0 \\ 0 & 0 & & 1 \end{pmatrix}. \tag{2.20}$$

O_{in} and O_{out} are orthonormal matrices that convert the vectors in the local coordinate basis (associated with J_L) to global coordinates. These 3×3 matrices are defined at each

interface as $O = [\hat{s}, \hat{p}, \hat{k}]^T$. The matrix O_{in}^{-1} operates on the incident $\tilde{E}_{in}$ in the global coordinates and projects it onto the incident local coordinates. The matrix O_{out} rotates the local surface vectors back to global coordinates.

The parallel transport matrix Q, representing the change exclusively due to the change in coordinate systems [43], is:

$$Q = O_{out} \cdot M \cdot O_{in}^{-1}. \tag{2.21}$$

In the case of a refractive interface, $M = diag[1, 1, 1]$, and in the case of a reflective interface, $M = diag[1, -1, 1]$, to take into account the change in the direction of propagation.

For a cascade of elements, we have $P_{total} = P_N \cdot P_{N-1} \ldots P_1$ and $Q_{total} = Q_N \cdot Q_{N-1} \ldots Q_1$. We then remove the geometrical transformation to obtain the 3×3 Jones matrix for one component or a cascade using:

$$J_G = Q^{-1} \cdot P = Q_{total}^{-1} \cdot P_{total}. \tag{2.22}$$

If the light's propagation is in the $\hat{x}\hat{z}$ plane, the 2×2 global Jones matrix can be extracted from the top left elements of J_G while a different propagation plane requires another technique [42].

2.1.2.5 Stokes polarization parameters

Another way to visualise any polarisation is using the Stokes vector, which is a 4×1 vector. It is sometimes easier to visualise if all the polarisation can be generated or measured simply by looking at the 4 parameters of the Stokes vector. If all the 4 parameters can be generated or measured, the system can be refereed as complete. It was hence used in the case of PSA used in this thesis. The Stokes vector for any beam of light with intensity I_0, can be expressed using orientation angle ψ and ellipticity χ as [40],

$$S = I_0 \begin{pmatrix} 1 \\ \cos 2\chi \cos 2\psi \\ \cos 2\chi \sin 2\psi \\ \sin 2\chi \end{pmatrix} \tag{2.23}$$

Since the Stokes vector has 4 parameters, the relation between input S_{in} and output polarisation S_{out} is now done using a 4×4 matrix Mueller matrix, as $S_{out} = M \cdot S_{in}$. The Mueller matrix of the retarder with retardation Γ at some angle θ will be used in some instances in this thesis, and is hence described below, [39]

$$M(\Gamma,\theta)=\begin{pmatrix}1 & 0 & 0 & 0\\ 0 & \cos^2 2\theta+\cos\Gamma\sin^2 2\theta & (1-\cos\Gamma)\sin 2\theta\cos 2\theta & -\sin\Gamma\sin 2\theta\\ 0 & (1-\cos\Gamma)\sin 2\theta\cos 2\theta & \sin^2 2\theta+\cos\Gamma\cos^2 2\theta & \sin\Gamma\cos 2\theta\\ 0 & \sin\Gamma\sin 2\theta & -\sin\Gamma\cos 2\theta & \cos\Gamma\end{pmatrix} \tag{2.24}$$

The Mueller matrix has 16 unknowns, which requires at least 16 measurements for each unique evaluation of the birefringence of any element. It becomes computationally expensive, and therefore the representation of the Stokes vector and the Mueller matrix was reserved only for verifying the capability to measure all polarisation using PSAs in 2.4.2. It will be seen in the upcoming section that having the capability to measure all polarisations enables measurement of the Jones matrix using any arbitrary polarisation. As a result, all the birefringence information contained in the Jones matrix can be extracted.

With the framework of polarisation and birefringence in mind, the non-uniform birefringence issue in KAGRA can be discussed.

2.2 Test mass in KAGRA

2.2.1 Non-uniform birefringence of test mass

The substrate of the ITM and ETM is Sapphire crystal, with the c-axis aligned to the propagation direction of the main laser beam [29]. While the ETM is highly reflective and the beam does not propagate through the bulk, the same is not true for ITM. The beam of the interferometer enters through the ITM before circulating in the arms, as described using the FPMI configuration described in Chapter 1. As a result, the bulk properties of ITM such as absorption, birefringence and scattering are crucial to meet the requirements of the detector. One of the issues with the currently manufactured large Sapphire is non-uniform birefringence, *i.e.,* different values of retardation and the axis orientation of the crystal at different spatial points. This results in the laser beam entering the arms with varying spatial polarisation. The detector is optimised for one polarisation, and as such presence of additional polarisation causes loss. Moreover, the non-uniform birefringence of ITMs of two arms might not be the same, resulting in a mismatch between the two arms, and degrading the dark fringe condition at the AS port.

The presence of non-uniform birefringence in the current ITMs was not known before installation. The first measured non-uniform birefringence of a large substrate was that of a spare ITM (which was not installed because it did not meet the absorption requirements). The following pictures show the non-uniform birefringence characteristics of the spare that were produced using a linear polariscope-based characterisation setup (discussed later in 2.3.1) [44].

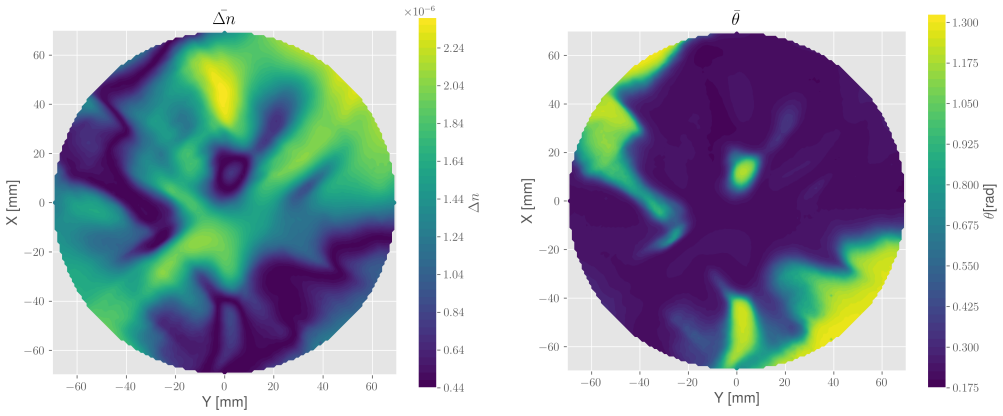

Figure 2.4: The non-uniform birefringence of a candidate test mass of KAGRA [44].

2.2.2 Consequences of non-uniform birefringence

The birefringence maps of the current installed ITMs were later reconstructed using wavefront measurements [45]. The birefringence and its inhomogeneity were found to be higher than expected [46, 47]. Due to the introduction of polarisation change, the power lost on reflection is estimated to be around 10% when arm cavities are not on resonance [29, 48].

The effect of non-uniform birefringence was quantified through several simulations in Somiya *et al.* [46]. This article showed that the total amount of spatial higher-order modes' power is 16 times larger at the AS port. It was found that the power-recycling gain was reduced (from 9.4 to 8.5), thereby increasing shot noise by 7% and 16% at low and high frequencies, respectively. The laser frequency noise was also found to be increased by an order of magnitude in the observation band. Amongst several issues, the major issue is the laser noise coupling in the detector. All these effects due to the non-uniform birefringence degrade the sensitivity of the KAGRA.

Michimura *et al.* [48] puts requirements on the phase difference between ordinary and extraordinary axes for future GW detectors as $10^{-8}\mathrm{rad}/\sqrt{\mathrm{Hz}}$ for substrate and $10^{-10}\mathrm{rad}/\sqrt{\mathrm{Hz}}$ for coating, by using static birefringence $\Delta n = 10^{-7}$ and $\Delta\phi_r = 1\mathrm{mrad}$ for substrate and coating respectively.

These studies show that it is important to know the birefringence of ITM, and prepare method to reduce the effect of non-uniform birefringence. The non-uniform birefringence issue of the installed ITM came to be known after it was already installed in KAGRA. It is therefore crucial to perform characterisation of ITMs and have all the knowledge of their properties beforehand. There have been some attempts in the GW community to characterise the ITMs. The previous techniques used are introduced briefly to get an idea of

birefringence measuring systems along with their pros and cons. The following subsections highlight the current methods to set the stage for the requirement of a new birefringence characterisation technique developed in Chapter 3.

2.3 Previous Birefringence characterisation techniques for test mass

There are several techniques to characterise the birefringence magnitude and axis orientation of the sample. However, this thesis will only describe the methods used in the GW community to characterise samples (of the size of an ITM for a detector). Although there exist certain setups that could be used to measure diattenuation, none of the setups in the community were measuring the diattenuation. Hence, it has not been introduced here.

2.3.1 Linear Polariscope

A linear polariscope characterises any sample by studying the effect of the unknown birefringence on a few rotated linearly polarised lights. Such a setup could have a retarder, like a HWP, to generate several rotated polarisations. The output signal is then observed at the transmission and reflection of a polarising beam splitter after the sample. This configuration was used in NAOJ along with a translation stage to produce the 2D birefringence maps shown in Fig. 2.4. A simplified representation of the previous setup used in NAOJ is shown below, [44],

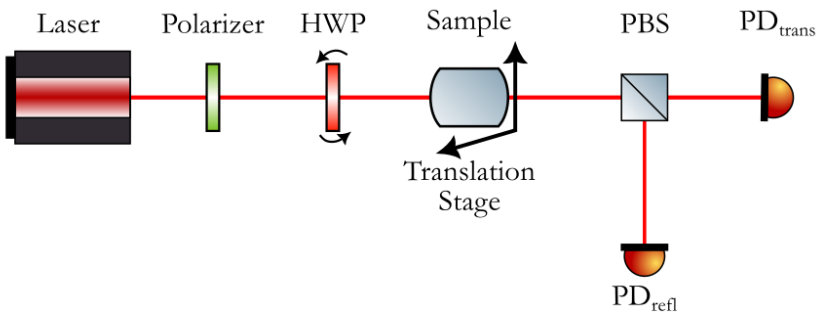

Figure 2.5: A simplified representation of a rotating polarisation-based linear polariscope. This setup relies on using a rotating HWP to generate rotated linear polarisation.

The sensitivity and accuracy of such a setup rely on the alignment of the polarising optics, accuracy of linear polarisation, calibration of PBS, and the two PDs. Additionally, this setup becomes quite difficult to characterise a reflecting material. This was one of the many motivations to upgrade the setup in NAOJ and produce birefringence maps for both

transmissive and reflective materials, with relaxed requirements on input and output optics. While this setup could estimate the magnitude of linear birefringence and axis orientation of the material, it failed to provide any information on the sign of birefringence, as well as the value of circular birefringence, linear, or circular diattenuation. It is difficult to get all the information through a single (regardless of averaging) measurement for characterisation, which is also a common issue in other techniques.

2.3.2 Photoelastic modulator

A photoelastic modulator (PEM) is a variable retarder that uses stress as actuation (using a piezo) and produces polarisation using the photoelastic effect. The PEM based birefringence characterisation method was originally developed by Wang *et al.* [49]. For the characterisation setup, the PEM is inserted between two polarisers with their relative angle at 45° relative to each other at first. The retardation of the PEM can be modulated at kHz speed to change the polarisation and hence the laser power intensity reaching the PD. The technique constructs the birefringence magnitude and axis orientation by combining two signals taken at the output polariser at 0° and another at 45°. This setup was used in UWA to produce 2D maps of the silicon test mass for the GinGin detector [50], whose simplified schematic is shown as

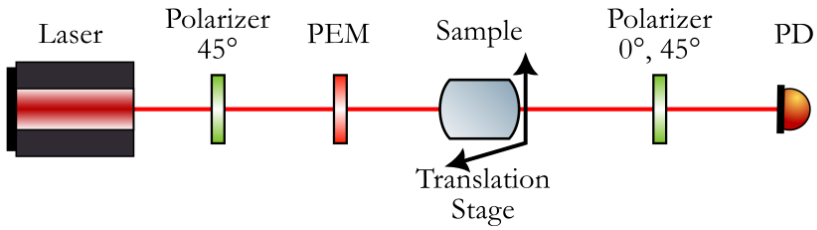

Figure 2.6: A simplified representation of a PEM-based characterisation setup.

The accuracy of this technique depends on the accuracy to which the setup is known, *i.e.*, wavelength, orientation of polariser, PEM retardation magnitude, linearity, and accuracy of lock-in amplifier and detectors etc.. However, if there is some discrepancy from a perfect condition, *i.e.*, deviation from the alignment or retardation requirement, the sensitivity and accuracy of the setup decrease [49]. Additionally, obtaining a precise map with this method takes a long time.

2.3.3 Transmitted wavefront error

Another method that was used to characterise the ITM (especially in the KAGRA community) is by studying the effect of birefringence on the wavefront. A simplified schematic of the measurement done using a Fizeau interferometer is shown below, [45]

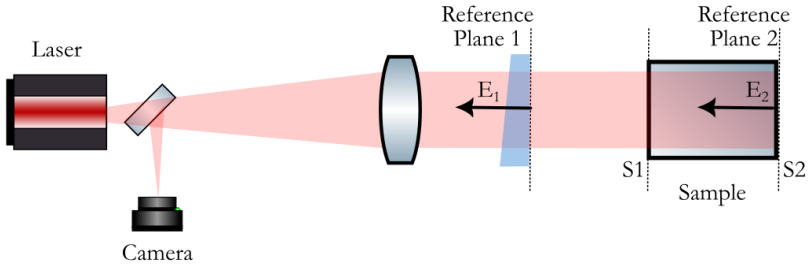

Figure 2.7: A simplified representation of a TWE-based characterisation setup based on a Fizeau interferometer. E_1 denotes the reference field, and E_2 denotes the field after a round trip through the sample with anti-reflective and highly-reflective coated surfaces S1 and S2, respectively.

The TWE is measured by interfering light that has made a round trip through the substrate with some unchanged reference field. The corresponding TWE can be measured by measuring variations in optical power reaching the camera. Using a camera allows for faster characterisation of a large surface area and mapping. While the measurement accuracy could be improved by rotating the input polarisation to make maps with different input polarisation orientations, the measurement reported in Wang *et al.* [45] was performed by rotating the sample. Consequently, imperfect alignment can affect the sensitivity of such a system. Additionally, the birefringence evaluated here again is only the magnitude of linear birefringence, along with axis orientation and no other information is derived.

In summary, there is a need for a setup that can measure birefringence maps more rapidly while remaining robust against imperfections in the measurement system. Additionally, a measurement setup that can measure linear and circular birefringence and diattenuation (with sign) at the same time, *i.e.*, complete birefringence of transmissive and reflective materials, will be favourable. As such, there is a need to move on from power-based measurement setups (discussed in 2.3) to polarisation-based measurement setups. The development of such a birefringence-characterisation setup is presented in Chapter 3. Before that, however, we first review several key concepts related to polarisation control.

2.4 Towards polarization-based characterization

2.4.1 Polarization state generator

A system that can generate a set of polarisations lying on the surface of the Poincaré sphere is a polarisation state generator. The actuation of such a system can vary from mechanical motion (such as rotation or stress) to electrical (such as voltage).

2.4.1.1 Mechanically Rotating retarder

A pair of rotating retarder usually a rotating QWP or a HWP, can control the polarisation of light. When a linear polarisation passes through such a system, its polarisation can vary as a function of the angle the fast axis of the retarders makes with the input polarisation. Such a setup can generate all possible polarisation states and is a typical candidate for polarisation actuation in optical setups. The expression of the polarisation generated can be expressed using their respective Jones matrix, as

$$\begin{aligned} J_{out} &= J_{HWP}(\theta') \cdot J_{QWP}(\theta) \cdot J_{in} \\ &= \begin{pmatrix} -i\cos 2\theta' & i\sin 2\theta' \\ -i\sin 2\theta' & i\cos 2\theta' \end{pmatrix} \cdot \frac{1}{\sqrt{2}} \begin{pmatrix} 1 - i\cos 2\theta & -2i\cos\theta\sin\theta \\ -2i\cos\theta\sin\theta & 1 + i\cos 2\theta \end{pmatrix} \cdot \begin{pmatrix} 1 \\ 0 \end{pmatrix} \\ &= \begin{pmatrix} \sin 2\theta'\sin 2\theta - \cos 2\theta'\cos 2\theta - i\cos 2\theta \\ \cos 2\theta'\sin 2\theta - \sin 2\theta'\cos 2\theta - i\sin 2\theta \end{pmatrix} \end{aligned} \tag{2.25}$$

It can be seen that QWP rotation mainly acts on ellipticity and HWP rotation on the orientation of polarisation. The orientation of the two retarders, when changed in the range of 0-360 °, will produce all polarisations where the orientation can range from $[-\pi/2, \pi/2]$ and ellipticity can range from $[-\pi/4, \pi/4]$. However, since it is required to mechanically move the retarder, whose speed has practical limitations (up to a few 100 Hz), it can take a long time to generate all polarisation. Another mechanism to generate polarisation can be through the use of a variable retarder, which has much less requirement for mechanical motion.

2.4.1.2 Variable retarder

A variable retarder is usually a component that can vary its retardance response by actuation in the form of voltage, stress or temperature. An example of a voltage-controlled retarder is Liquid crystal (LC) and Pockels cells, which are the main focus in Chapter 3 and Chapter 4 respectively, and hence voltage-controlled retarders are introduced here. Another form of temperature-controlled variable retarder is at focus in Chapter 5, but its workings are not described in this section, and is contained in the corresponding chapter.

For a variable retarder, the permittivity and dielectric constant, and therefore the refractive index, are functions of the applied electric field and the applied stress on the element. The biased electric field can be applied using electrodes across the element, and a stress can be applied in terms of mechanical stress or temperature-induced stress. This biasing field E_0 and a stress σ can alter the refractive index of the element following the relation [41],

$$n = n^0 + aE_0 + a'\sigma + bE_0^2 + b'\sigma^2 + b''\sigma \ldots \tag{2.26}$$

Any presence of an electric field or stress can cause a change in the refractive index, and thereby the shape, size, and orientation of the indicatrix. The change due to some applied electric field E_k and stress σ_{kl} is then manifested in the coefficients B_{ij}.

$$\Delta B_{ij} = z_{ijk}E_k + \pi_{ijkl}\sigma_{kl} \tag{2.27}$$

where z_{ijk} is a third rank tensor with coefficients for electro-optical effect, and π_{ijkl} is a fourth rank tensor whose coefficients give the photoelastic effect [41].

2.4.1.2.1 Liquid crystal

Liquid crystals (LC) are anisotropic molecules and have properties between solid and liquid. The highly anisotropic nature of the molecules affects the preferred orientation of the nearby molecules, thereby exhibiting crystal properties. The molecules are elongated or rod-like and exhibit a large permanent dipole moment. The molecules locally remain aligned with each other to reduce their potential energy. However, some mechanical or electrical forces can cause a change in their orientation. The application of an electric field, hence, can rotate the LC molecules, providing a means for tunable birefringence. The molecules can orient parallel or perpendicular to the electric field for positive or negative dielectric anisotropy, respectively. [39]

LC cells are devices with layers of LC packaged between electrodes to modulate the distribution of molecules and thereby the phase of the transmitted light. The initial research focused on using LC to control polarisation due to its lower cost and low voltage requirements. It is quite cumbersome to develop high-voltage required for other actuators like PEM or Pockels cell, as will be seen in Chapter 4. The polarisation states changing due to interaction with the LC can be visualised using its Jones matrix, T,

$$T\left(\theta, \epsilon\left(V\right)\right) = \begin{pmatrix} \cos\theta & -\sin\theta \\ \sin\theta & \cos\theta \end{pmatrix} \begin{pmatrix} e^{\frac{i\epsilon(V)}{2}} & 0 \\ 0 & e^{\frac{-i\epsilon(V)}{2}} \end{pmatrix} \begin{pmatrix} \cos\theta & \sin\theta \\ -\sin\theta & \cos\theta \end{pmatrix} \tag{2.28}$$

where θ and $\epsilon(V)$ are the fast axis orientation and voltage dependent retardation of LC. The effect of a pair of LCs (oriented at 45° relative to each other) on linearly polarised light can be visualised again using the Jones matrix formalism, as

$$J_{out} = T\left(0, \epsilon(V_2)\right) \cdot T\left(45, \epsilon(V_1)\right) \cdot \begin{pmatrix} 1 \\ 0 \end{pmatrix} = \begin{pmatrix} \cos\frac{\epsilon(V_1)}{2} \cdot e^{+i\frac{\epsilon(V_2)}{2}} \\ i\sin\frac{\epsilon(V_1)}{2} \cdot e^{-i\frac{\epsilon(V_2)}{2}} \end{pmatrix} \tag{2.29}$$

The liquid crystal LCC1111T-C [51] used in this thesis was purchased from Thorlabs. They offer up to 2π retardation for the 1064 nm laser. The primary task at hand was to first characterise the liquid crystals using a cross-polariser configuration, as shown in Fig. 2.8, and to understand their working. In a cross-polariser configuration, the two polarisers have their axes perpendicular to each other, such that either only the x or the y component of polarisation can exist after this configuration. Upon sending a polarised light along the $\hat{x}$ axis through the first polariser, no light exits the last polariser.

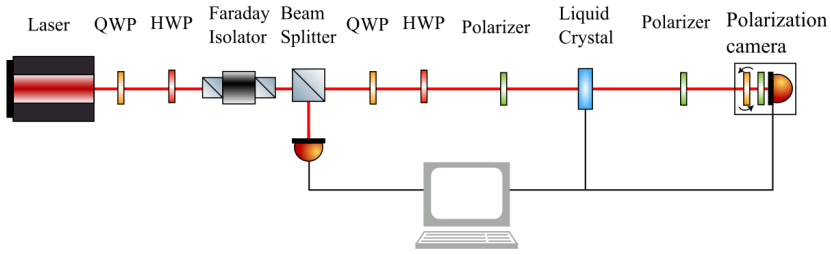

Figure 2.8: The cross polariser configuration used for characterisation of the retardation of a variable retarder

When the LC at an angle θ is placed between the two polarisers, the exiting light can be monitored, as it contains only the y component of polarisation from Equation 2.29. Upon changing the voltage of the LC, its birefringence will change, manifesting as a power change after the exiting polariser, thereby providing the retardation vs. voltage characteristics. The vector exiting the output polariser, J_{out} can be represented using Jones calculus as follows,

$$J_{tra} = \underbrace{\begin{pmatrix} 0 & 0 \\ 0 & 1 \end{pmatrix}}_{\text{Polariser}} \cdot T\left(\theta, \epsilon\left(V\right)\right) \cdot \begin{pmatrix} 1 \\ 0 \end{pmatrix} = \begin{pmatrix} 0 \\ 2\cos\left(\theta\right)\sin\left(\theta\right)\cos\left(\frac{\epsilon\left(V\right)}{2}\right) \end{pmatrix} \cdot \tag{2.30}$$

The normalised transmitted power $P(\theta)$ is then computed from the power in one polarisation of the above Jones vector, as

$$P\left(\theta\right) = \left(2\cos\left(\theta\right)\sin\left(\theta\right)\cos\left(\frac{\epsilon\left(V\right)}{2}\right)\right)^2 = \cos^2\left(\frac{\epsilon\left(V\right)}{2}\right)\sin\left(2\left(\theta\right)\right)^2 \tag{2.31}$$

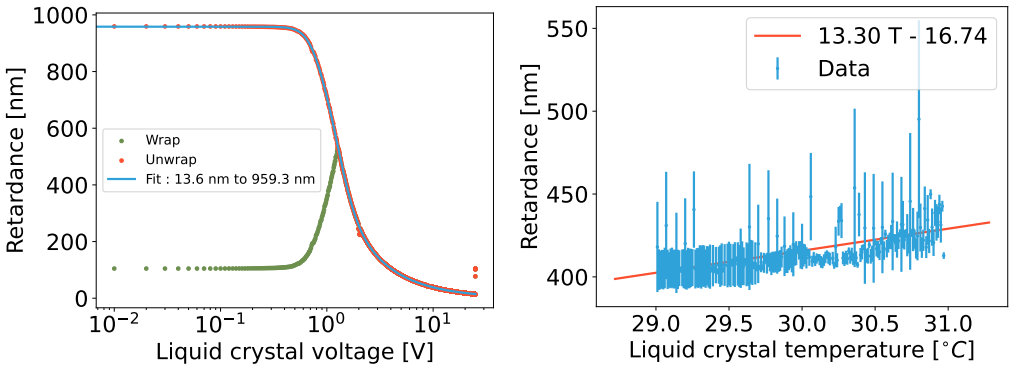

Figure 2.9: (a) The retardation characterisation curve of liquid crystal as the voltage is changed across the electrodes of LC at constant temperature is shown. The retardation (in nm) for wavelength λ, can be computed from the transmitted power P, as $R^{nm} = 2\arcsin\sqrt{P}\frac{\lambda}{2\pi}$, It can be seen from the figure that the LC is generating more than half-wave retardation, hence it is required to unwrap the reconstructed retardation. The LC used in this experiment is uncompensated, and as a result, at high voltage, it induces a small positive retardation. As we expect the maximal retardation to be at minimum voltage, the unwrapping is done by flipping all retardation over the maximum unwrapped retardation at low voltages. As a result, when the voltage is changed from 0-25 V, the retardation changes from 959.3 nm to 13.6 nm. (b) The wrapped retardation characteristics of the liquid crystal are shown as the temperature is changed at a constant voltage of 0 V. The rate of change is 13.3 nm/°C. Large error bars at temperatures larger than 30.5°C are due to not fully optimised PID control required for temperature stabilisation. The temperature was later fixed at (30±0.1)°C using a PID implemented to ensure that each LC temperature is stabilised over long periods of time. As a result, the temperature-induced fluctuations were reduced to 1.3 nm.

Using the same technique, a corresponding change in birefringence can be observed for a temperature change. The retardation characterisation plot with respect to change in voltage and temperature is shown in Fig. 2.9.

It is also crucial to characterise the LC axis orientation, as a pair of them with a relative angle of 45° is required later on. This characterisation is also done in a cross-polariser setting using Equation 2.30. The maximal and minimum power are observed when the LC's fast axis is at θ is at 45° and 0° relative to the input polarisation orientation, respectively. In Fig. 2.10, the left plot is a measurement of the transmitted power with varying angle of LC, and the right plot is the fit representing measurements at all voltages.

If the two-variable retarder can each achieve a range of 2π retardation change independently, then a pair of them (at 45° relative to each other) will generate all the polarisation states. The two LCs can hence form a Polarisation State Generator (PSG) by actuating their respective voltage. The LCs were characterised on a tabletop to examine the number of polarisation states that can be generated, which is as shown in Fig. 2.11. The voltages applied to each LC are scanned from 0-25 V with 10 mV steps. The light transmitted by

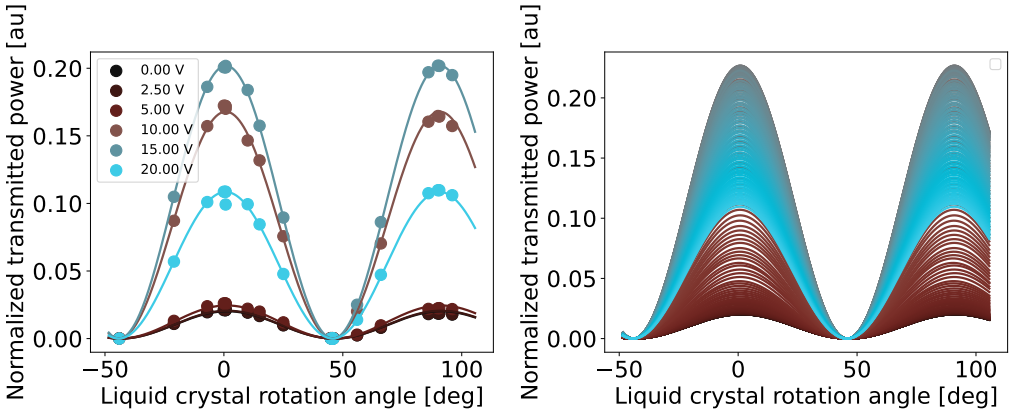

Figure 2.10: The axis orientation characterisation curve of liquid crystal (a) Measurement of power as the LC axis is changed at different voltage (mentioned in legend). (b) The axis orientation extrapolated to produce orientation for all LC voltages.

the pair of LCs is then acquired by the polarisation camera. It can be seen in Fig. 2.11 (a) and (b) that LC1 (LC2) mainly acts on the azimuth (ellipticity) angle. Furthermore, about 6.3 million polarisation states are generated at 40 Hz, which cover most of the polarisation states' parameter space as shown Fig. 2.11 (c).

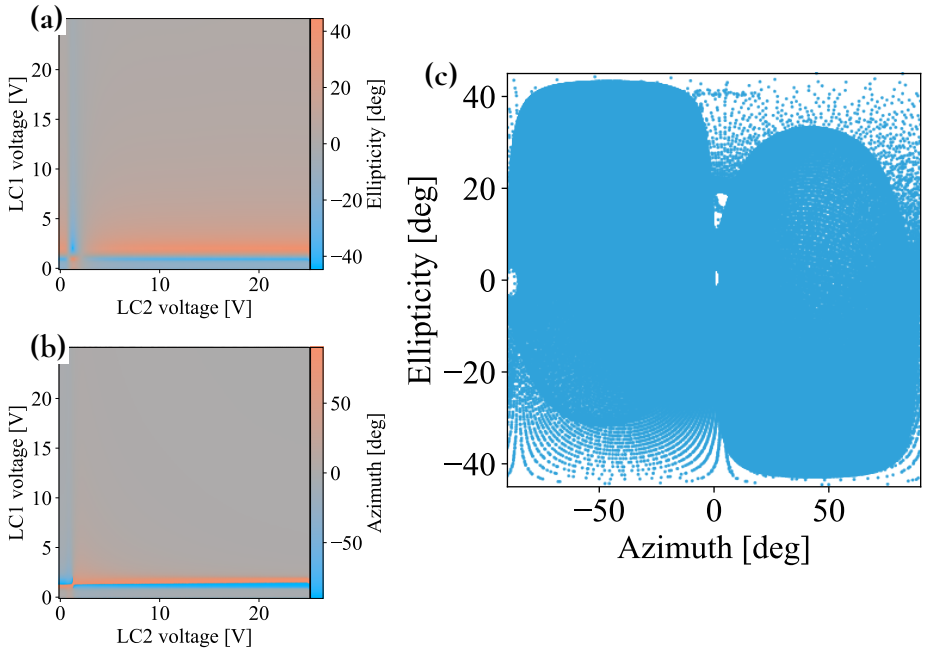

Figure 2.11: The polarisation generated using a pair of liquid crystals by varying the applied voltage. (a) The variation in ellipticity of polarisation obtained at different combinations of voltages provided to the two LCs. (b) The variation in orientation of polarisation obtained at different combinations of voltages provided to the two LCs. (c) Ellipticity as a function of orientation representing the several unique polarisations that were generated when changing the voltage of both LCs.

2.4.2 Polarization state analyser

Any system that can describe the orientation and ellipticity of the polarisation state incident on it is a Polarisation State Analyser (PSA). While there are several different kinds of polarisation state analysers, this manuscript only focuses on a complete PSA. It can measure all orientations and ellipticity of light ranging from $[-\pi/2, \pi/2]$ and $[-\pi/4, \pi/4]$ respectively or in other words, all 4 parameters of Stokes vector in Equation 2.23, thereby identifying all the polarisation states.

The polarisation of light can be constructed through a series of power measurements using a photodetector at the output of the PSA for its varying configurations. For any PSA, the different configurations can vary from mechanical rotation to changing voltage, depending on the type of retarder, but the essence is to take measurements at different retardances of the PSA. As long as the retardance of the actuator is known, the polarisation state characteristics can be reconstructed. An analyser vector of any PSA can be formed by multiplying a linearly polarised light by the Mueller matrix of the components inside the polarisation state analyser. This analyser vector can give information on the four components of the Stokes vector of the incident polarisation state.

Polarisation measurements using a polarimeter are better in comparison to the use of a PBS with two detectors at its output. Using two detectors can introduce some issues due to their relatively imperfect alignment, beam incident on different regions, mismatch between the gain of their circuit, imperfect PBS transmission and reflection ratio, etc.. In a polarimeter, the issues from the mismatch between two detectors are not of concern, as all measurements are performed using a single detector.

2.4.2.1 Rotating retarder and fixed polariser

This is the most commonly used polarimeter. Such a commercially available polarisation camera (1 pixel) from Thorlabs [52] was used for the development of the birefringence characterisation system in Chapter 3. The system can be visualised as

The polarimeter can measure all four components of a Stokes vector and hence forms a complete Stokes polarimeter. A series of measurements is acquired using the photodetector, after rotating the retarder to a series of angles θ_q. The signal will be observed with a modulation at the photodetector, and the light power can be expressed using the following Fourier series [39].

$$P = \frac{a_0}{2} + \frac{1}{2}\sum_{n=1}^{\infty}\left(a_{2n}cos(2n\theta) + b_{2n}sin(2n\theta)\right) \tag{2.32}$$

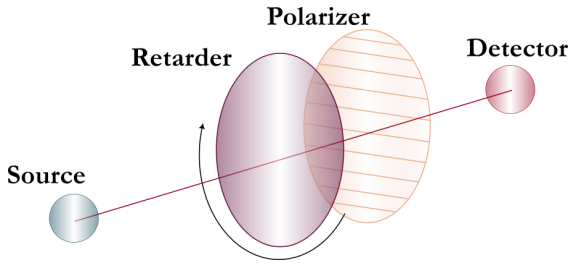

Figure 2.12: Rotating Retarder and Fixed Analyser

where θ is the azimuthal angle of the retarder. In order to get to the analyser vector of this system, we first need to understand the effect of the polariser. If there is a rotating LP in front of a detector, the analyser vector is a function of the transmission axis of the LP, and is represented as,

$$A_{LP}(\theta) = \frac{1}{2}\left(1, \cos 2\theta \sin 2\theta, 0\right)^T \tag{2.33}$$

Therefore, the analyser vector of the system with a rotating retarder in front of a horizontal LP as Fig. 2.12 can now be expressed as [39],

$$\begin{aligned} A(\theta) &= A_{LP}(0) \cdot LR(\Gamma, \theta) \\ &= \frac{1}{2} \cdot \begin{pmatrix} 1 \\ \cos^2 2\theta + \cos\Gamma sin^2 2\theta \\ (1-\cos\Gamma)\cos 2\theta \sin 2\theta \\ -\sin\Gamma \sin 2\theta \end{pmatrix} \quad \text{Using Equation 2.33 and Equation 2.24} \end{aligned} \tag{2.34}$$

Therefore, in case of the use of a QWP (for the case of Thorlabs camera), the analyser vector Equation 2.34 can be expressed as, [39]

$$A_{QWP}(\theta) = \frac{1}{2} \cdot \begin{pmatrix} 1 \\ \cos^2 2\theta + \cos\frac{\pi}{2} \sin^2 2\theta \\ (1-\cos\frac{\pi}{2})\cos 2\theta \sin 2\theta \\ -\sin\frac{\pi}{2} \sin 2\theta \end{pmatrix} = \frac{1}{2} \cdot \begin{pmatrix} 1 \\ \frac{1+\cos 4\theta}{2} \\ \frac{\sin 4\theta}{2} \\ -\sin 2\theta \end{pmatrix} \tag{2.35}$$

From Equation 2.34 we can see that if a HWP ($\Gamma = \pi/2$) were instead used, the last element of the analyser vector would be zero. As such, a rotating HWP-based PSA would be an incomplete polarimeter. In the case of the rotating QWP, a series of intensity measurements taken over 360° rotation of the retarder will help reconstruct the polarisation. The intensity $P(\theta)$ can be expressed as a Fourier series, where the Stokes parameters will be related to the Fourier coefficients and can be expressed as [39],

$$\begin{aligned} P(\theta) &= A_{QWP}(\theta) \cdot S \\ &= \frac{1}{2}S_0 + \frac{1}{4}S_1 + \frac{\cos 4\theta}{4}S_1 + \frac{\sin 4\theta}{4}S_2 + \frac{-\sin 2\theta}{2}S_3 \\ &= a_0 + b_2 \sin 2\theta + a_4 \cos 4\theta + b_4 \sin 4\theta \end{aligned} \tag{2.36}$$

where the coefficients a and b are related to cos and sin, respectively, and their subscript corresponds to the harmonics in which the signal is observed. Other frequency components should be zero or riddled with noise. Using the signal observed in the respective fundamental and harmonics, during the intensity measurements, the value of the Stokes vector can then be expressed using the Equation 2.36 as [39],

$$S_0 = 2(a_0 - a_4), S_1 = 4a_4, S_2 = 4b_4, S_3 = -2b_2 \tag{2.37}$$

While the rotating retarder-based polarimeter is the commonly used one, it has some demerits. The mechanical rotation of the retarder can cause scattering of light and introduce loss, which can affect some crucial measurements. Owing to the mechanical rotation, the speed of such polarimeters is usually limited to a few 100 Hz. As a result, measurements in the higher frequency range are not possible. Owing to such limitations, several research efforts were devoted to making a high-speed polarisation readout with good sensitivity. This brings us to the next type of polarimeter.

2.4.2.2 Two variable retarder and fixed polariser

Another example of a complete Stokes polarimeter is one comprising two variable retarders and an analyser. The polarimeter has two variable retarders with the fast axis of the second retarder at 45° from the first retarder's transmission axis. The polariser fast axis is 45° relative to the second retarder. Such a polarimeter is capable of measuring all polarisation, and the configuration is as follows [39],

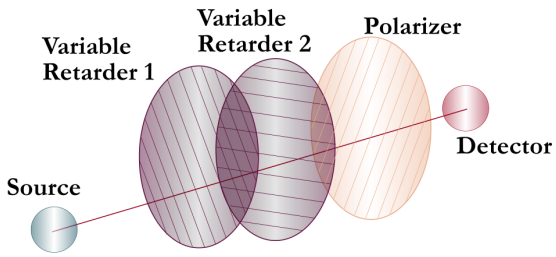

Figure 2.13: Pair of Variable Retarder and Fixed Analyser

Using the analyser vector of polariser from Equation 2.33 and placing it at an angle of $\pi/4$ and using Equation 2.24 for the two retarders at angles $\pi/4$ and 0 respectively, the analyser vector expression for this system can be expressed as follows,

$$\begin{aligned} A(\delta_1, \delta_2) &= A_{LP}(-\pi/4) \cdot LR(\delta_2, 0) \cdot LR(\delta_1, \pi/4) \\ &= \frac{1}{2} \begin{pmatrix} 1 \\ 0 \\ -1 \\ 0 \end{pmatrix}^{\top} \begin{pmatrix} 1 & 0 & 0 & 0 \\ 0 & 1 & 0 & 0 \\ 0 & 0 & \cos\delta_2 & \sin\delta_2 \\ 0 & 0 & -\sin\delta_2 & \cos\delta_2 \end{pmatrix} \begin{pmatrix} 1 & 0 & 0 & 0 \\ 0 & \cos\delta_1 & 0 & -\sin\delta_1 \\ 0 & 0 & 1 & 0 \\ 0 & \sin\delta_1 & 0 & \cos\delta_1 \end{pmatrix} \\ &= \frac{1}{2} \begin{pmatrix} 1 \\ -\sin\delta_1 \sin\delta_2 \\ -\cos\delta_2 \\ -\cos\delta_1 \cos\delta_2 \end{pmatrix} \end{aligned} \tag{2.38}$$

A series of measurements can be taken when modulating the variable retarder's voltage V at some frequency ω. Since the retardation modulation produced is $\delta = \pi \frac{V}{V_\pi} = \pi \frac{V_m \sin \omega t}{V_\pi}$, the corresponding intensity measurements can be used to evaluate the Stokes vector.

$$\begin{aligned} P(\delta_1, \delta_2) &= A(\delta_1, \delta_2).S \\ &= \frac{1}{2} S_0 + \frac{-\sin\delta_1 \sin\delta_2}{2} S_1 + \frac{-\cos\delta_2}{2} S_2 + \frac{-\cos\delta_1 \cos\delta_2}{2} S_3 \end{aligned} \tag{2.39}$$

The Stokes vector can then be constructed using different methods depending on the modulation mechanism of the variable retarder. This has been elaborately described in Chapter 4.

2.5 Discussion

This chapter highlighted the topic of birefringence and the issues due to its non-uniformity in the detector. It highlights the theoretical and experimental framework required to improve the current birefringence characterisation methods. It lays the foundation of the need for better birefringence characterisation setups, and also techniques to control polarisation for this purpose.

The previous setups could only provide information on absolute linear birefringence. No information on circular birefringence was available, and it will require the use of an independent setup for such measurement. None of the previously existing birefringence characterisation setups could estimate the sign of birefringence, *i.e.,* positive or negative. Moreover, they are cumbersome to incorporate the measurement of reflecting materials.

Additionally, in order to measure different properties such as retardation or diattenuation, one would need to use independent setups. As such, none of the setups could measure different forms of retardation and diattenuation of both transmissive and reflecting materials in one go. Therefore, there was a motivation to develop a birefringence characterisation setup which could measure all the properties of any element, thereby providing complete birefringence characterisation. A setup being able to provide complete birefringence will give linear birefringence of x with respect to y axis, of $+45°$ with respect to $-45°$ axis, circular birefringence, effective birefringence and the axis orientation of birefringence. The same form of information should be available for diattenuation. The upcoming Chapter 3 will show the development of a new birefringence characterisation setup, which is robust against issues present in previous setups.

3

Complete birefringence characterization

Contents

The work described in this chapter focuses on getting all the birefringence information of any material. While the traditional techniques in the GW community focused on simply evaluating the magnitude of linear retardation, we were interested in knowing much more about the linear and circular birefringence (diattenuation) and their sign. This work was

developed and summarised in

'Complete birefringence and Jones matrix characterization using arbitrary polarization' [53].

The following sections are excerpts from the paper with a detailed description of the elements measured. Additionally, the system was adapted to produce birefringence maps and also for the analysis of stress birefringence on certain materials. At the end, a setup that can measure the birefringence of both transmissive and reflective materials with as much ease as switching the sample was developed. The sections below delve into arbitrary polarisation-based characterisation through measurement of the Jones matrix and evaluation of all the birefringence components.

3.1 Polarisation elements from Decomposition of the Jones matrix

Jones matrices can be distinguished into homogeneous, inhomogeneous, and degenerate matrices depending on their eigenvectors, using an inhomogeneity parameter, η. The eigenvectors E_q and E_r, associated with the complex eigenvalues μ_q and μ_r, represent the polarisation states that are unchanged through interaction with the polarisation element (or eigenpolarizations) such that $J \cdot E_q = \mu_q \cdot E_q$ and $J \cdot E_r = \mu_r \cdot E_r$. The inhomogeneity parameter η can be computed as the inner product of the normalized eigenpolarizations [54] as :

$$\eta = |\hat{E}_q \cdot \hat{E}_r|, \quad 0 \leq \eta \leq 1. \tag{3.1}$$

A Jones matrix can have $\eta = 0$, $\eta = 1$, or $0 < \eta < 1$, representing orthogonal, parallel, and non-orthogonal eigenpolarizations, also referred to as homogeneous, degenerate, and inhomogeneous Jones matrix respectively. They can also be understood using optical components, for instance, $\eta = 0$ corresponds to a pure retarder and $\eta = 1$ corresponds to a pure polariser. Depending on the inhomogeneity of the Jones matrix, Pauli or Polar decomposition techniques are used to compute birefringence.

3.1.1 Pauli decomposition

Together with the identity matrix, the Pauli matrices that are expressed as in the Equation 3.2, form an orthonormal basis for any 2×2 complex matrix [55] and can be related to common phase or amplitude, x/y linear, $+/-45°$ linear and left/right circular birefringence respectively.

$$\sigma_0 = \begin{pmatrix} 1 & 0 \\ 0 & 1 \end{pmatrix}, \quad \sigma_1 = \begin{pmatrix} 1 & 0 \\ 0 & -1 \end{pmatrix}, \quad \sigma_2 = \begin{pmatrix} 0 & 1 \\ 1 & 0 \end{pmatrix}, \quad \sigma_3 = \begin{pmatrix} 0 & -i \\ i & 0 \end{pmatrix}. \tag{3.2}$$

These matrices can be used to decompose a Jones matrix as

$$J = \sum_{k=0}^{3} c_k.\sigma_k = \begin{pmatrix} c_0 + c_1 & c_2 - ic_3 \\ c_2 + ic_3 & c_0 - c_1 \end{pmatrix}, \tag{3.3}$$

where each c_k is complex and represents the birefringence associated with each Pauli matrix.

Owing to the commutative properties of homogeneous Jones matrices, Equation 3.3 can be expanded to express the logarithm or exponential form of these matrices as in Equation 3.4. In such a case, the real parts of the Pauli coefficients relate to diattenuation, while the imaginary part relates to retardation [39]. The retardation and diattenuation properties appear in an order-independent form *i.e.,* one can be calculated before the other.

$$J = e^{b_0\sigma_0 + b_1\sigma_1 + b_2\sigma_2 + b_3\sigma_3}, \quad \ln J = b_0\sigma_0 + b_1\sigma_1 + b_2\sigma_2 + b_3\sigma_3. \tag{3.4}$$

The Pauli basis also reveals properties of a cascaded polarization element, e.g., a multilayer dielectric coating or a cavity. The polarization coupling can be understood in detail from the multiplicative and the anti-commutative properties of the Pauli-matrices, *i.e.,* $\sigma_\alpha \cdot \sigma_\beta = -i\sigma_\gamma$ and $\sigma_\alpha \cdot \sigma_\beta = -\sigma_\beta \cdot \sigma_\alpha$, respectively (where, α, β, γ are the order of coefficients 1,2,3 respectively) [39]. This gives us a detailed insight into the generation of new polarisation properties that may be absent in the individual polarisation elements. For instance a sequence of two diattenuator at 0° and 45° can produce circular retardation, *i.e.,* $\sigma_1 \cdot \sigma_2 = -i\sigma_3$.

3.1.2 Polar decomposition

The polar decomposition theorem states that any $n \times n$ complex matrix can be expressed as the product of a nonnegative definite Hermitian matrix and a unitary matrix [56]. Therefore, any Jones matrix can be expressed using a retarder (unitary) Jones matrix J_R and a diattenuator (non-negative definite Hermitian) Jones matrix J_D, as $J = J_R \cdot J_D$ [54]. With the use of polar decomposition, the diattenuation matrix J_D can be determined using $J_D = \sqrt{J^\dagger \cdot J}$ which holds for non-singular with non-zero determinant matrices J_D and J. We can then obtain the retarder matrix, as $J_R = J \cdot J_D^{-1}$.

From this decomposition, the Jones matrix can be expressed as a product of homogeneous matrices with diattenuation and retardation contributions separated. This allows us to compute the complete retardation and diattenuation from their logarithm.

3.2 Birefringence from different types of Jones matrix

Depending on the inhomogeneity of the Jones matrix, different decompositions can be applied to extract the birefringence information.

3.2.1 Homogeneous Jones matrices

A homogeneous Jones matrix can yield retardation and diattenuation using the Equation 3.4 representation.

$$\ln J = (\ln(\rho_0) - i\phi_0)\sigma_0 + \frac{d_H - i\delta_H}{2}\sigma_1 + \frac{d_{45} - i\delta_{45}}{2}\sigma_2 + \frac{d_L - i\delta_L}{2}\sigma_3. \tag{3.5}$$

The minus signs on the retardance components are from the decreasing phase sign convention [39]. The real (imaginary) parts of the Pauli coefficients are used to derive d_H (δ_H) the x/y linear, d_{45} (δ_{45}) the $+/-45°$ linear, and d_L (δ_L) the left/right circular diattenuation (retardation) respectively.

The effective diattenuation D_{eff} and effective retardation δ_{eff} can be extracted using :

$$D_{eff} = \tanh\left(\sqrt{d_H^2 + d_{45}^2 + d_L^2}\right), \quad \delta_{eff} = \sqrt{\delta_H^2 + \delta_{45}^2 + \delta_L^2}. \tag{3.6}$$

The diattenuation coefficients are normalised to be within -1 to 1 using a scaling factor [39]. This results in $D_H = \frac{D_{eff}}{\tanh^{-1}(D_{eff})} d_H$, $D_{45} = \frac{D_{eff}}{\tanh^{-1}(D_{eff})} d_{45}$, $D_L = \frac{D_{eff}}{\tanh^{-1}(D_{eff})} d_L$, as the diattenuation components.

Finally, the retardation and diattenuation axis orientation (the eigenpolarization with the larger eigenvalue) can be determined independently. Since σ_0 and σ_3 are invariant under rotation, the axis orientation can be determined using the σ_1 and σ_2 coefficients as :

$$\theta = 0.5 \cdot \tan^{-1}(x_{45}/x_H), \tag{3.7}$$

where x is either the retardation or diattenuation coefficient.

3.2.2 Inhomogeneous Jones matrices

The birefringence computation of homogeneous Jones matrices holds as their 0 inhomogeneity factor ensures the commutation of the unitary (retarder) and hermitian (diattenuator) parts [39, 54]. However, it fails for the inhomogeneous Jones matrix, since the eigenpolarizations of J are not orthogonal. In such a case, first, polar decomposition is used to extract the homogeneous diattenuator J_D and then the homogeneous retarder J_R matrix. The birefringence can then be evaluated from their exponential representation using:

$$J_D = \rho_o\, e^{-i\phi_o}\left(\sigma_o + \sum_{k=1}^{3} d_k\sigma_k\right) = \rho_o\, e^{-i\phi_o}\, exp\left(\frac{D_H\sigma_1 + D_{45}\sigma_2 + D_L\sigma_3}{2D_{eff}\ /\ \tanh^{-1}(D_{eff})}\right),$$
$$J_R = \rho_o\, e^{-i\phi_o}\, \exp\left(-i\sum_{k=1}^{3} d_k\sigma_k\right) = \rho_o\, e^{-i\phi_o} exp\left(\frac{-i\delta_H\sigma_1 - i\delta_{45}\sigma_2 - i\delta_L\sigma_3}{2}\right). \tag{3.8}$$

The diattenuation coefficients d_k are real and are expressed using Equation 3.8 which satisfy $d_{tot} = d_1^2 + d_2^2 + d_3^2 \leq 1$. The coefficients are normalized to obtain the diattenuation as, $D_{eff} = 2\frac{\sqrt{d_{tot}}}{1+d_{tot}}$, $D_H = \frac{D_{eff} \cdot d_1}{\sqrt{d_{tot}}}$, $D_{45} = \frac{D_{eff} \cdot d_2}{\sqrt{d_{tot}}}$, $D_L = \frac{D_{eff} \cdot d_3}{\sqrt{d_{tot}}}$. The diattenuation axis orientation can be computed from Equation 3.7.

The retardance $\delta_H = 2\delta_1$, $\delta_{45} = 2\delta_2$, and $\delta_L = 2\delta_3$ are linear x/y, linear $+/-45°$, and left/right circular retardance, respectively, and are calculated from Equation 3.8. The retardation axis and the effective retardation are calculated using Equation 3.7 and Equation 3.6.

3.2.3 Degenerate Jones matrices

A degenerate J has only one linearly independent eigenpolarization. Hence, matrix logarithms and polar decomposition can't be used. But, it is still possible to extract effective diattenuation and retardation using the eigenvalue μ_q and degeneracy parameter $\eta' = |J_{xy}| + |J_{yx}|$ [54] as :

$$D_{eff} = \frac{\eta' \sqrt{4|\mu_q|^2 + \eta'^2}}{2|\mu_q|^2 + \eta'^2}, \quad \delta_{eff} = 2\cos^{-1} \frac{|\mu_q|}{\sqrt{|\mu_q|^2 + \eta'^2/4}}. \tag{3.9}$$

3.2.4 Physically realisable Jones matrix

The previous sections have introduced how to extract birefringence from the Jones matrix of polarisation elements. In practice, such measurements can be affected by noise or uncertainties that could lead to an ill-determined Jones matrix. In order to discard such matrices, the physical realizability of the Jones matrix was first tested.

In this manuscript, the focus is on the study of passive polarisation elements. Since the polarisation-independent optical gain for such an element cannot exceed unity [57], all the measured J should obey the inequality :

$$0 \leq \det\left(J^\dagger \cdot J\right) \leq 1. \tag{3.10}$$

Furthermore, the transmittance of any given input polarisation state for a passive optical system also can not exceed unity. The matrix $[J^\dagger \cdot J]$ has two real non-negative eigenvalues T_{max}, T_{min}, representing the maximum and minimum transmittance for any input polarisation state, respectively. The required condition is that $T_{max} \leq 1$; which can be consequently expressed as a limit to the inhomogeneity parameter η_{max} for a physically realisable Jones matrix [58]:

$$0 \leq \eta \leq \eta_{max} \leq 1, \quad \text{with} \quad \eta_{max} = \frac{\mathcal{AB}}{\sqrt{\mathcal{A}^2\mathcal{B}^2 + \mathcal{F}^2}}, \tag{3.11}$$

where $\mathcal{A} = \sqrt{1 - |\mu_q|^2}$, $\mathcal{B} = \sqrt{1 - |\mu_r|^2}$, and $\mathcal{F} = |\mu_q - \mu_r|$ are eigenvalues-dependent quantities.

A physically realisable Jones matrix of any passive polarisation element should satisfy Equation 3.10 and Equation 3.11. The matrix should be scaled to follow the condition of physical realizability [39].

3.3 Birefringence measurement

3.3.1 Analysis Workflow

Having described Jones matrix formalism and its inhomogeneity-dependent decompositions, we present the workflow for measuring the Jones matrix of any passive polarisation element and extracting its birefringence.

By generating a pair of input Jones vectors from arbitrary polarisation inputs and then measuring the corresponding output Jones vectors, the 4 complex degrees of freedom (DoF) of the Jones matrix are evaluated, using Equation 3.12 for a ray propagating along $\hat{z}$.

$$\begin{pmatrix} E_x^{in1} & E_y^{in1} \\ E_x^{in2} & E_y^{in2} \end{pmatrix} \begin{pmatrix} J_{xx} & J_{yx} \\ J_{xy} & J_{yy} \end{pmatrix} = \begin{pmatrix} E_x^{out1} & E_y^{out2} \\ E_x^{out1} & E_y^{out2} \end{pmatrix}. \tag{3.12}$$

The global Jones matrix is evaluated if the incident ray propagating along $\hat{z}$ is not aligned along $\hat{z}$ after interaction with the polarisation element. The physical realizability of the Jones matrix (satisfying Equation 3.10 and Equation 3.11) is then verified.

Subsequently, depending on the inhomogeneity of the Jones matrix, we use the equations of homogeneous (Equation 3.5), inhomogeneous (Equation 3.8), or degenerate (Equation 3.9) J to obtain the birefringence of any polarisation element. We use an error of 10^{-4} for inhomogeneity near 0 or 1 to define it as homogeneous or degenerate. Using the workflow in Fig. 3.1, we obtain complete birefringence ($\delta_H, \delta_{45}, \delta_L, \delta, \theta_R, D_H, D_{45}, D_L, D, \theta_D, \delta_{eff}, D_{eff}$), or effective birefringence (δ_{eff}, D_{eff}).

3.3.2 Experimental setup

The analysis presented in Fig. 3.1 works for any arbitrary pair of input polarisation states. To demonstrate this, we used a polarisation State Generator (PSG): a pair of temperature-stabilised, voltage-controlled liquid crystal cells (Thorlabs, LCC-1111-TC) with their fast-axis oriented at 45° relative to each other [59]. The fast-axis orientation of each liquid crystal cell was aligned by placing each of them between cross-polarisers and measuring the transmitted

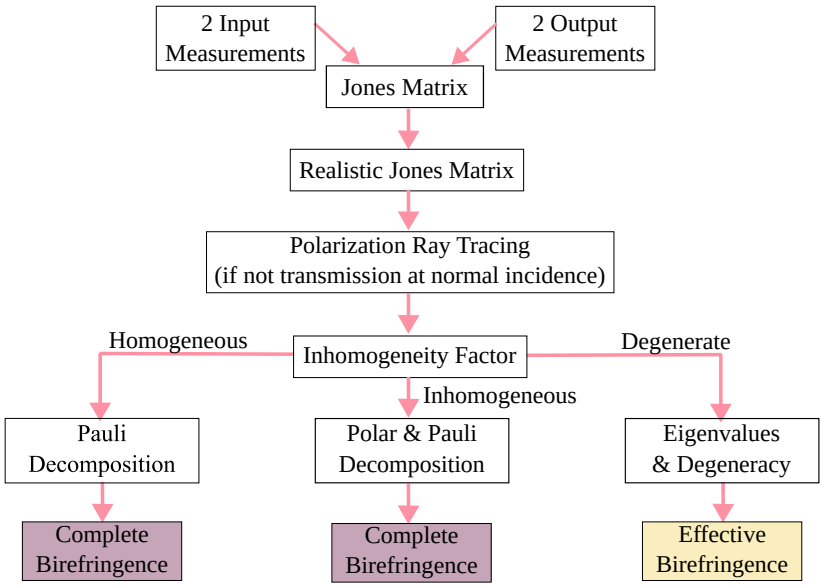

Figure 3.1: The Workflow used to retrieve birefringence from Jones vectors for any passive material. Polarisation Ray Tracing is required to recover the global Jones matrix in case of reflective or non-normal incidence measurements.

power as a function of the liquid crystal rotation angle. The PSG was able to generate any arbitrary polarisation states. By varying the voltage applied to each liquid crystal from 0 to 3.5 V with 0.1 V increments, 1296 arbitrary polarisation states (corresponding to 839160 unique polarisation pairs) were generated, as shown in Fig. 3.2.

The generated polarisation states were then measured by a PSA (Thorlabs, PAX-1000-IR2), as shown in Fig. 3.2. The PSA was able to measure the azimuth, ellipticity, and power of the polarisation state. It was located in the transmission of the sample or the reflection of BS_3 when reflective samples were measured. Since the sample and the PSA were kept at the same distance from the beam waist, corresponding to a beam size of 0.688 mm and 0.422 mm, respectively, for all measurements, the laser beam size was omitted. The PSA provided all required information to compute the Jones vector associated with the measured polarisation state using Chapter 2 Equation 2.7. In addition to the laser power measured by the PSA, a power meter in reflection of BS_1 was used to eliminate laser power fluctuations. Furthermore, since the input and output Jones vectors were not measured simultaneously, a power meter in reflection of BS_2 is used to monitor and take into account possible fluctuations of the PSG transmittance.

For each voltage applied to the PSG, an average of 100 measurements was performed. The uncertainty recorded during measurements is 0.05°, 0.08° and 0.001 on azimuth, ellipticity, normalized power respectively. These uncertainties are propagated throughout

the analysis using the GTC python library [60] and were used to define the bin widths of histograms presented in the section 3.4. The histogram distribution of the Jones matrices and birefringence from all the combinations of polarisation pairs was fitted with a Gaussian curve to estimate the statistical mean value and statistical standard deviation.

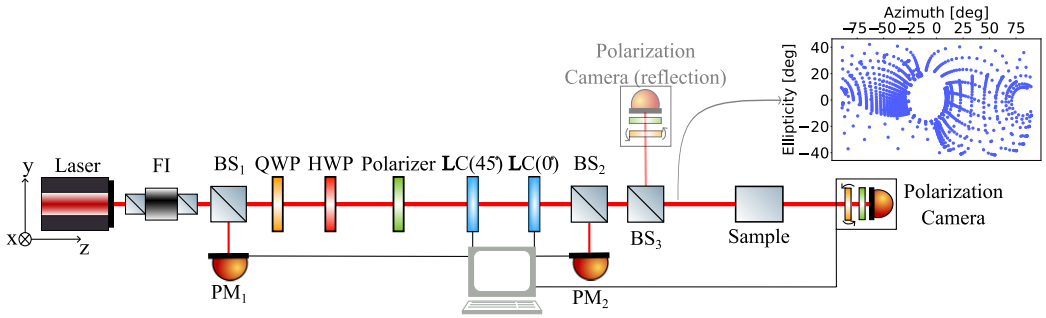

Figure 3.2: Jones matrix Polarimeter using PSG and PSA for transmissive and reflective samples. FI : Faraday Isolator, BS : Beam-Splitter, QWP : Quarter-Wave Plate, HWP : Half-Wave Plate, LC : Liquid Crystal, PM : Power-Meter. The azimuth vs. ellipticity inset shows the generated polarisation states after BS_2 and BS_3 corresponding to the input polarisation states.

3.3.3 Uncertainty

It is crucial to understand the uncertainty of the setup developed. For this purpose, the birefringence of air ('no sample') was measured. The analysis was used to evaluate the Jones matrix and birefringence of air between the PSG and PSA. The two required sets of measurements corresponding to measurements without and with the sample were separated by 1 h. The measured Jones matrix is shown in Fig. 3.3, where the top (bottom) row shows the real (imaginary) parts of the 4 Jones matrix elements. The measured Jones matrix of this non-polarising medium is an identity matrix within $7 \cdot 10^{-4}$, and is obtained from the Gaussian fit of the distributions in Fig. 3.3, as:

$$J_{air} = \begin{pmatrix} 1 \pm 3.6 \cdot 10^{-4} + i\,(-1.2 \pm 3.2) \cdot 10^{-4} & (0.6 \pm 4.0) \cdot 10^{-4} + i\,(2.0 \pm 4.3) \cdot 10^{-4} \\ (-0.2 \pm 4.6) \cdot 10^{-4} + i\,(2.5 \pm 4.2) \cdot 10^{-4} & 1 \pm 3.5 \cdot 10^{-4} + i\,(3.6 \pm 7.0) \cdot 10^{-4} \end{pmatrix}. \tag{3.13}$$

The uncertainties on the azimuth, ellipticity, and power measured by the PSA can be propagated to the elements of J_{air}. As the Jones matrices are computed from 839160 polarisation pairs, we estimate the median of the uncertainties of each element of J_{air} as :

$$\Delta J_{air} = \begin{pmatrix} 4 \cdot 10^{-4} + i2 \cdot 10^{-4} & 3 \cdot 10^{-4} + i3 \cdot 10^{-4} \\ 2 \cdot 10^{-4} + i2 \cdot 10^{-4} & 4 \cdot 10^{-4} + i2 \cdot 10^{-4} \end{pmatrix}. \tag{3.14}$$

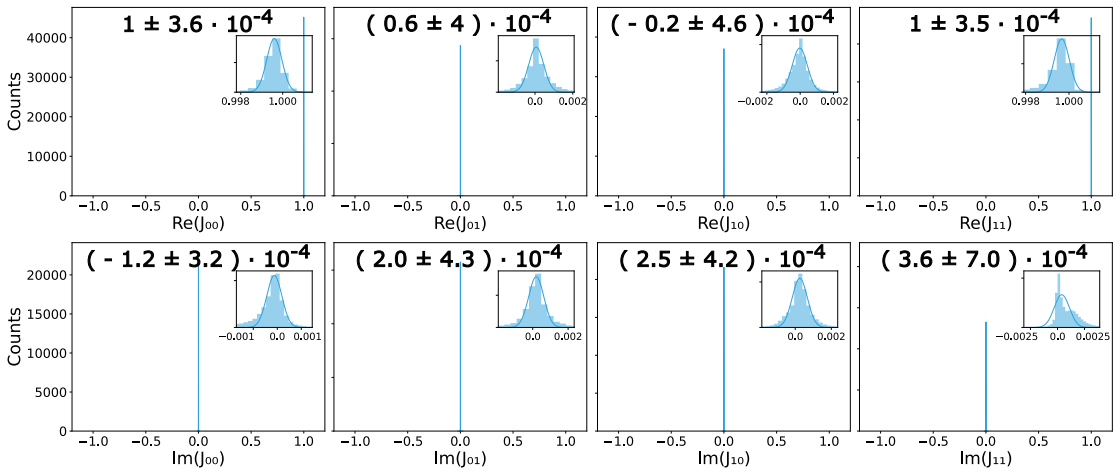

Figure 3.3: Jones matrix of air. The top (bottom) row shows the real (imaginary) parts of $(J_{00}, J_{01}, J_{10}, J_{11})$ from left to right.

It can be seen that the uncertainties of J_{air} in Equation 3.13 arising from the statistical uncertainty of the measurements are of a similar order of magnitude as the uncertainties from the PSA propagated to J_{air} in Equation 3.14. It indicates that the measurement of the Jones matrix is limited by the resolution of the PSA, and improving this resolution would lead to direct improvement in the estimation of the Jones matrix.

The complete birefringence was computed from this Jones matrix measurement as in Fig. 3.4. The complete birefringence parameters are presented in Table 3.1 and did not affect the evaluation of the following materials. Additionally, since air is not a birefringent material, the retardation and diattenuation axis is not well defined. The complete birefringence parameters are presented in Table 3.1. This measurement allows us to investigate the effects of Jones vector uncertainties from the PSA to the birefringence resolution. The median of the uncertainties from the 839160 polarization pairs were computed as $\Delta\rho_0 = 0.009°, \Delta\delta_x = 0.018°, \Delta\delta_{45} = 0.030°, \Delta\delta_L = 0.028°, \Delta\delta_{eff} = 0.024°, \Delta D_x = 0.0002, \Delta D_{45} = 0.0006, \Delta D_L = 0.0005, \Delta D_{eff} = 0.0005$. These values, which correspond to the bin size of the associated data in Fig. 3.4, are at least one order of magnitude smaller than the statistical uncertainty of the measured birefringence. It means that the current resolution of the birefringence measurement is not limited by uncertainties of the PSA but rather by fluctuations throughout the measurement, likely arising from the PSG. This measurement corresponds to the setup's resolution and noise over 1 h that separated the two sets of measurements. If there is a need for improved resolution, this noise could be removed by multiplying the measured J by J_{air}^{-1}.

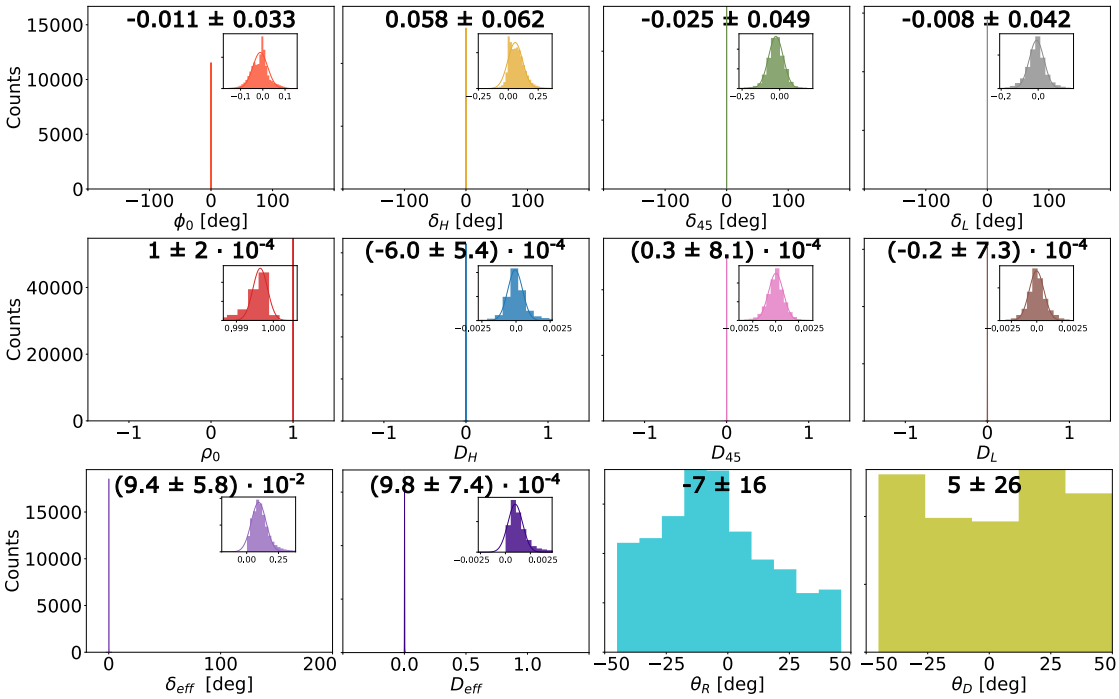

Figure 3.4: Birefringence of Air. The common phase (amplitude), x/y,+/-45°, left/right retardation (diattenuation) are ordered left to right in the 1st (2nd) row. The 3rd row shows the effective retardation, effective diattenuation, and their axis orientation, respectively.

3.4 Results from different Samples

The analysis presented in the article was implemented to measure the properties of a retarder, a diattenuator, a beam-splitter, and a dielectric-coated mirror. The results are explained in the following subsections and are summarised in Table 3.1 and Table 3.2.

3.4.1 Half-Wave Plate

A perfect half-wave plate (HWP) is described by a pure retarder matrix. We measured the J and birefringence of HWP (WPH10M-1064, Thorlabs) installed inside a rotator mount with its fast-axis oriented at $\approx 10°$. The expected Jones matrix forHWP in the symmetric phase convention is,

$$J = e^{-i\pi/2} \begin{pmatrix} \cos 2\theta & \sin 2\theta \\ \sin 2\theta & -\cos 2\theta \end{pmatrix}. \tag{3.15}$$

The measured Jones matrix at a given θ is :

$$J_{HWP} = \begin{pmatrix} (0.944 \pm 0.003) + i\,(0.000 \pm 0.001) & (0.320 \pm 0.003) + i\,(0.001 \pm 0.003) \\ (0.322 \pm 0.002) + i\,(-0.002 \pm 0.002) & (-0.939 \pm 0.003) + i\,(0.001 \pm 0.001) \end{pmatrix}. \tag{3.16}$$

The measured Jones matrix has the real value of primary diagonal elements similar in magnitude and opposite in sign. The real value of secondary diagonal elements matches both in value and sign, as expected. The common phase of $\phi_0 = (-90 \pm 0.12)^\circ \approx -\pi/2$ can be observed from Table 3.1.

We measure an effective retardation of $\delta_{eff} = (180.0 \pm 0.3)^\circ = (\lambda/2 \pm \lambda/1200)$ in agreement with the manufacturer specifications of $(\lambda/2 \pm \lambda/300)$. Furthermore, the measured retardation axis orientation $\theta_R = (9.43 \pm 0.08)^\circ$ is consistent with the installation value within error. It also agrees with the direct evaluation of $\theta = 0.5 \cdot \tan^{-1}(J_{01}/J_{00}) = (9.36 \pm 0.09)^\circ$ using Equation 3.15. This measurement is further confirmed with HWP rotation by $\approx -38^\circ$ and measuring $\theta_R = (-28.5 \pm 0.04)^\circ$.

The diattenuation is extremely low with an effective diattenuation of $D_{eff} = (8.2 \pm 3.9) \cdot 10^{-3}$ and meets expectations from a pure retarder.

3.4.2 Linear polariser

A perfect Linear Polariser (LP) is described by a pure diattenuator Jones matrix. We measured the Jones matrix and birefringence of a LP (GTPC-10-33SN, Opto-Sigma). The Jones matrix of a perfect LP rotated by θ is expressed as,

$$J = \begin{pmatrix} \cos^2\theta & \sin\theta\cos\theta \\ \sin\theta\cos\theta & \sin^2\theta \end{pmatrix}. \tag{3.17}$$

The measured Jones matrix is,

$$J_{LP} = \begin{pmatrix} (0.696 \pm 0.035) + i\,(0.001 \pm 0.071) & (-0.422 \pm 0.017) + i\,(-0.02 \pm 0.12) \\ (-0.419 \pm 0.021) + i\,(0.001 \pm 0.043) & (0.254 \pm 0.010) + i\,(0.011 \pm 0.072) \end{pmatrix}. \tag{3.18}$$

The secondary diagonal elements' real value matches in sign and magnitude. The primary diagonal elements sum up to 0.95 ± 0.04, which is close to the expectation $\cos^2\theta + \sin^2\theta = 1$ from Equation 3.17.

The computed birefringence of the rotated LP is shown in Table 3.1. We measured an effective diattenuation $D_{eff} = 1 \pm 2.5 \cdot 10^{-8}$. The extinction ratio specified by the manufacturer is $ER > 2 \times 10^5$ corresponding to a diattenuation $D = (ER - 1)/(ER + 1) \geq 0.99999$, which is in agreement with our measurement.

The diattenuation axis orientation can be evaluated directly as $\theta = 0.5 \cdot \sin^{-1}(2 \cdot J_{01}) = (-28.8 \pm 1.8)^\circ$, using data from Equation 3.18, which agrees with $\theta_D = (-31.2 \pm 1.3)^\circ$ in Table 3.1.

The large uncertainty on the LP's retardation arises because the LP is a pure degenerate diattenuator matrix. This leads to most of the measured Jones matrix being degenerate or inhomogeneous. Since polar decomposition for the inhomogeneous matrix is order dependent, the degenerate diattenuator matrix of the polariser is computed before the retardation matrix. The non-invertibility of the diattenuator matrix affects the computation of the retardation matrix. On the contrary, this is not the case for the diattenuation of a pure retarder, since the diattenuator matrix is simply an identity matrix.

3.4.3 Beam Splitter

One of the motivations during the development of this setup was also to be capable of performing birefringence measurement of reflective materials. As such, we had to characterise a beam splitter that will be used to separate the reflected ray from any material. J_{BS} was measured by installing BS_3 backwards, corresponding to the reflective surface seen by the light reflected from the sample in Fig. 3.2. The input Jones vectors were measured between BS_2 and BS_3 while the output Jones vectors were measured in reflection of BS_3 as :

$$J_{BS} = \begin{pmatrix} (0.605 \pm 0.030) + i(0.002 \pm 0.027) & (0.014 \pm 0.053) + i(0.016 \pm 0.093) \\ (0.007 \pm 0.015) + i(-0.002 \pm 0.021) & (-0.563 \pm 0.041) + i(-0.13 \pm 0.13) \end{pmatrix}, \tag{3.19}$$

Note that J_{BS} is the local Jones matrix of BS_3, hence the negative sign on J_{11}. It is possible to recover the global Jones matrix by applying PRT calculus to Equation 3.19 using the incident and exiting laser propagation direction and the BS_3 surface normal, $\hat{k}_{in} = [0, 0, 1]$, $\hat{k}_{out} = [-1, 0, 0]$ and $\hat{n} = [1/\sqrt{(2)}, 0, 1/\sqrt{(2)}]$ respectively. The P and Q matrices were computed using Equation 2.20 and Equation 2.21. Equation 2.22 was then used to get the following Jones matrix :

$$J^G_{BS} = \begin{pmatrix} (0.563 \pm 0.041) + i(0.13 \pm 0.13) & (0.007 \pm 0.015) + i(-0.002 \pm 0.021) \\ (-0.014 \pm 0.053) + i(-0.016 \pm 0.093) & (0.605 \pm 0.030) + i(0.002 \pm 0.027) \end{pmatrix}, \tag{3.20}$$

The effectiveness of PRT calculus in reconstructing the global Jones matrix, even at a large angle of incidence (45° for BS_3), is visible in Equation 3.20 which now takes a form close to the expected one: $\sqrt{T_{BS}} \cdot \sigma_0$, with $T_{BS} \approx 0.36$ the polarization-independent reflectivity of BS_3. The common amplitude of $\rho_0 = 0.6 \pm 0.003$, in Table 3.2 show the nature of BS is close to 50/50 transmission and reflection. The beam splitter should, in an ideal case, not

change the polarisation properties of the laser, and this can be seen through the measured retardation and diattenuation. The retardation components are not well defined as shown in Table 3.2, and is because the BS is not a retarder, and is an amorphous material. This can be seen through the evaluated axis orientation of both retardation and diattenuation as $\theta_R = [-0.7 \pm 15]^\circ$ and $\theta_D = -[0.7 \pm 23.5]^\circ$ respectively, representing an absence of a well-defined axis. However, the effective retardation $\delta_{eff} = [22.6 \pm 4]^\circ$ and x/y linear diattenuation of $D_H = -0.04 \pm 0.08$ suggests there is some induced retardation and polarisation-dependent reflection. It was important to have the BS characterised as it will be used in the characterisation of a reflecting material.

3.4.4 Dielectric Mirror

We measured the Jones matrix and birefringence in reflection at the normal incidence of a dielectric mirror (BB1EO3, Thorlabs). The PSA was placed in the reflection of BS_3 as shown in Fig. 3.2 to extract the reflected beam from the mirror. Hence, the measured Jones matrix J_{total} included contributions from BS_3 and the measured mirror. The mirror's Jones matrix J_{mir} was recovered using $J_{mir} = J_{BS}^{-1} \cdot J_{total}$ where J_{BS} is the Jones matrix of BS_3 reflection from Equation 3.19.

To extract J_{mir}, the BS matrix was divided by its common amplitude of $\rho_0 = (0.6 \pm 2.8) \cdot 10^{-3}$ to avoid bias in the physical realizability condition of the mirror. Since the birefringence computed from the mirror J_{mir} showed a common amplitude of $\rho_0 = (0.706 \pm 0.004)$, we used it to normalise the matrix. The Jones matrix of a perfect dielectric mirror should be the identity matrix. The measured Jones matrix of this mirror is :

$$J_{mir} = \begin{pmatrix} (0.991 \pm 0.008) + i(0.005 \pm 0.008) & (0.020 \pm 0.033) + i(0.001 \pm 0.012) \\ (0.022 \pm 0.011) + i(0.001 \pm 0.003) & (-0.989 \pm 0.006) + i(0.01 \pm 0.005) \end{pmatrix}. \tag{3.21}$$

When we removed the common amplitude from the measured J_{mir}, we verified the physical realizability condition again, which helped to improve the measurement's resolution by more than a factor of 10 for the Jones matrix and birefringence. In the case that the diattenuator matrix extracted from the Jones matrix is not physically realisable, the removal of common amplitude might result in a non-physically realisable matrix. In that case, we may rescale the Jones matrix using a scaling factor of $(\sqrt{T_{max}}/\mu_q)$, where μ_q is the eigenvalue of the diattenuator matrix (extracted from the Jones matrix) and T_{max} the maximum expected intensity transmission for any given polarization state [39]. Both these scalings can be applied

to any optical element as long as T_{max} is known. In this study, we only scaled the Jones matrix for the case of BS and mirror using common amplitude, as the half transmission of the BS led to non-physically realisable matrices of the mirror before scaling.

The birefringence of the dielectric mirror is shown in Table 3.2. Due to the geometric transformation, it can be seen that the linear x/y and effective retardation are $\approx \pi$ and the common phase is $\approx -\pi/2$ in local frame. Both these phases can be removed to recover the proper birefringence through the transformation of J_{mir} in the local frame to J^G_{mir} in the global frame.

PRT calculus was implemented on the local Jones matrix shown in Equation 3.21 using $\hat{k}_{in} = [0, 0, 1]$, $\hat{k}_{out} = [-1, 0, 0]$ and $\hat{n} = [0, 0, 1]$. Equation 2.22 was then used to get the global J^G_{mir} of the mirror as:

$$J^G_{mir} = \begin{pmatrix} (0.989 \pm 0.006) + i(-0.010 \pm 0.005) & (0.022 \pm 0.011) + i(0.001 \pm 0.003) \\ (-0.02 \pm 0.033) + i(-0.001 \pm 0.011) & (0.991 \pm 0.008) + i(0.005 \pm 0.008) \end{pmatrix}, \tag{3.22}$$

We can see that the negative sign in the J_{11} term has been removed. Also, since the local J_{mir} is represented in local $\hat{s}, \hat{p}$ coordinates, upon changing to global coordinates, we can see them representing $\hat{y}$ and $\hat{x}$ respectively, explaining the row interchange in the 2×2 matrix. This corresponds to the removal of the geometrically induced phases as well. The proper birefringence is then shown as Mirror (global) in Table 3.2.

The linear retardation magnitude of another BB1EO3 mirror from the same vendor was previously measured to be (23 ± 1) mrad in LaBollita *et al.* [61]. The previous birefringence measurement is performed using two orthogonal beams and examining the relative phase difference after interaction with the mirror. This corresponds to the x/y linear retardation in our study. The evaluated x/y linear and effective linear retardation is $\delta_H = (24 \pm 13)$ mrad and $\sqrt{\delta_H^2 + \delta_{45}^2} = (1.38 \pm 0.72)^\circ = (24 \pm 13)$ mrad, respectively. The retardation presented in this article is in good agreement with the measurement from the previous method, within the error.

The evaluated x/y linear and effective linear diattenuation is $\sqrt{D_H^2 + D_{45}^2} = (0.8 \pm 2) \cdot 10^{-2}$ and $D_H = (-4 \pm 7) \cdot 10^{-3}$, respectively. The x/y linear diattenuation from the manufacturer at 6° angle of incidence is given as $1.7 \cdot 10^{-4}$. The values of diattenuation are in agreement with our measured values within the uncertainty of our measurements.

The retardation and diattenuation axis orientations have a large uncertainty, which arises from the fact that this mirror does not possess a well-defined axis.

The measured circular retardation $\delta_L = (2.6 \pm 2.6)^\circ$ is compatible with 0 within uncertainty. While the 0 circular retardation is expected, an offset from 0, however, could indicate either that this dielectric mirror was not optimised for circular diattenuation or that this circular diattenuation is a result of polarisation coupling between the different dielectric layers. For instance D_H and D_{45} could couple to produce $-\delta_L$. Improvement in the measurement resolution is needed to investigate this possibility further.

The birefringence of all the elements discussed in this section is summarised in Table 3.1 and Table 3.2 below.

Component	Air	HWP	LP
ϕ_0 [deg]	-0.011 ± 0.033	-90 ± 0.12	$0.2 \pm 36^\dagger$
δ_H [deg]	0.058 ± 0.062	170 ± 0.15	$-15 \pm 44^\dagger$
δ_{45} [deg]	-0.025 ± 0.049	-58.2 ± 0.4	$30 \pm 46^\dagger$
δ_L [deg]	-0.008 ± 0.042	0.02 ± 0.66	$-3.6 \pm 12^\dagger$
ρ_0	$1 \pm 2.0 \cdot 10^{-4}$	0.994 ± 0.003	0.477 ± 0.007
D_H	$(-6.0 \pm 5.4)\,10^{-4}$	$(4.4 \pm 4.9)\,10^{-3}$	0.469 ± 0.06
D_{45}	$(0.3 \pm 8.1)\,10^{-4}$	$(-1.0 \pm 4.1)\,10^{-3}$	-0.88 ± 0.03
D_L	$(-0.2 \pm 7.3)\,10^{-4}$	$(1.4 \pm 4.5)\,10^{-3}$	0.04 ± 0.34
δ_{eff}	$(9.4 \pm 5.8)\,10^{-2}$	180.0 ± 0.3 [180 ± 1.2]	$93 \pm 38^\dagger$
D_{eff}	$(9.8 \pm 7.4)\,10^{-4}$	$(8.2 \pm 3.9)\,10^{-3}$	$1 \pm 2.5 \cdot 10^{-8}$ [> 0.99999]
θ_R [deg]	$-7 \pm 16^\dagger$	9.43 ± 0.08	$-26 \pm 12^\dagger$
θ_D [deg]	$5 \pm 26^\dagger$	$-0.3 \pm 15^\dagger$	-31.2 ± 1.3

Table 3.1: Complete birefringence for all transmissive components. The † sign indicates that the value is coming from the median and standard deviation of the distribution, while otherwise coming from a Gaussian fit. The values in the bracket correspond to manufacturer data or are measured by other experiments.

Component	BS (global)	Mirror (local)	Mirror (global)
ϕ_0 [deg]	-6.6 ± 7.6	-90.0 ± 0.3	0.1 ± 0.24
δ_H [deg]	-17.8 ± 10.3	178 ± 0.72	1.38 ± 0.72 [1.32 ± 0.06[61]]
δ_{45} [deg]	0.84 ± 11.3	3.82 ± 4.2	-0.02 ± 0.7
δ_L [deg]	-2.05 ± 9.08	-0.1 ± 1.1	-2.6 ± 2.6
ρ_0	0.6 ± 0.003	0.991 ± 0.007	0.991 ± 0.007
D_H	-0.04 ± 0.08	0.004 ± 0.008	-0.004 ± 0.007 [0.00017]
D_{45}	0.001 ± 0.08	-0.007 ± 0.023	0.007 ± 0.023
D_L	-0.04 ± 0.15	-0.002 ± 0.015	-0.002 ± 0.015
δ_{eff}	22.6 ± 4	179.0 ± 0.76	3.3 ± 1.8
D_{eff}	0.15 ± 0.18	0.026 ± 0.013	0.026 ± 0.013
θ_R [deg]	$-0.7 \pm 15^{\dagger}$	0.6 ± 0.6	$-6 \pm 20^{\dagger}$
θ_D [deg]	$-0.7 \pm 23.5^{\dagger}$	$-20 \pm 28^{\dagger}$	$-20 \pm 28^{\dagger}$

Table 3.2: Complete birefringence for all reflective components. The † sign indicates that the value is coming from the median and standard deviation of the distribution, while otherwise coming from a Gaussian fit. The values in the bracket correspond to manufacturer data or are measured by other experiments.

3.4.5 Sapphire

In order to produce birefringence maps *i.e.*, measurement across the entire spatial regime of the sample, the technique of polarisation-based measurement was adapted to be used inside the clean room available in NAOJ, which houses a translation stage. This was previously used for the characterisation of the KAGRA size ITM. Additionally, the optical setup here measures absorption using the Photo-thermal Common-path Interferometer [62], and as such uses high power laser. Since the optics bench is primarily used for absorption, and most of the optics shares a path with a high-power laser, it was not optimal to install LC. As such, the methods were implemented with a rotating HWP to generate the arbitrary polarisation required to make maps. The rotating HWP generates at least 9 arbitrary polarisation states, which are then used to produce the corresponding Jones matrix and the birefringence of the optics under investigation. Several samples from different manufacturers were characterised to better understand the properties of the samples. Two such maps are shown in Fig. 3.5 and Fig. 3.6, corresponding to a small Sapphire and a larger one, which were recently manufactured. While greater uniformity is observed in smaller samples, larger samples may still exhibit unpredictable non-uniformity in birefringence.

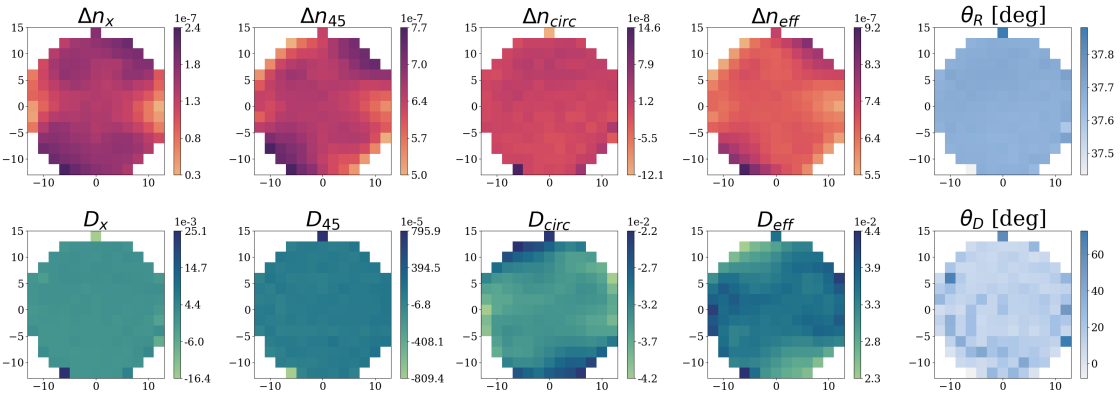

Figure 3.5: A small sample (30 mm in diameter and 20 mm in thickness) provided by Aztec in South Korea.

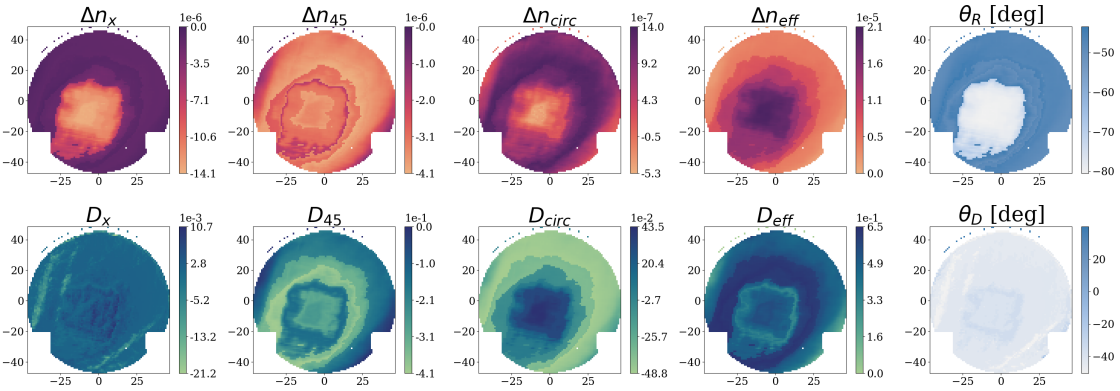

Figure 3.6: A large Sapphire sample (of 100 mm in diameter and 21 mm in thickness) provided by the colleagues of iLM and LMA laboratories from Lyon in France.

3.4.6 Hydrogel

Another material that was characterised using the LC setup was hydrogel. In this section of research, biologists from UEC collaborated to study the characteristics of the hydrogel when exposed to stress. The aim was to produce the hydrogels with different doping of certain molecules and produce positive, zero, or negative stress optic coefficient, C, of the hydrogels.

The setup involved the uniaxial stretching of the hydrogel, along the y axis, using a force gauge and measurement of the birefringence at one spatial point. After each stretch, the stress σ was noted as the force and the change in thickness and width of the hydrogel. The birefringence at each stretched position was measured by injecting 25 arbitrary polarisation states for several hydrogels, one of which is shown in Fig. 3.7 and Fig. 3.8. The number of polarisation states used was reduced to speed up the measurement time, as otherwise the hydrogel dried up, thereby changing its dimensions and the stress. It was seen in several hydrogels that with an increase in stress, the error in birefringence increased. This could indicate that there was some fluctuations of the material itself at higher stress.

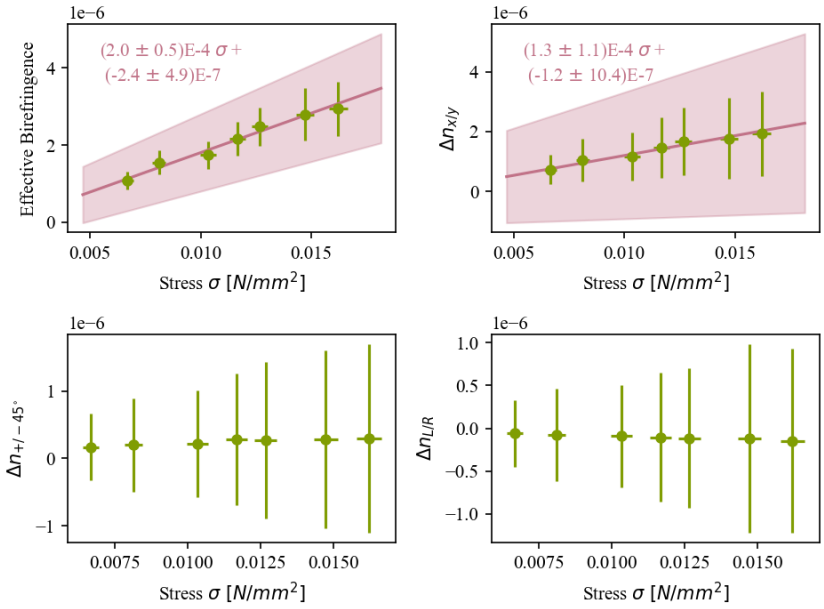

Figure 3.7: Plots showing the effect of stress (shown on x axis) on the retardation (on y axis) of the hydrogel. The green points are measurements, and the red line is a fit to evaluate the stress-optic coefficient, following $\delta = C \cdot \sigma + \delta_0$. The first row shows effective and linear x/y retardation. It can be seen that there is a significant change in the retardation in the direction of stress. The second row shows the linear $+/-45°$ and circular retardation. Since stress is not applied in their direction, no change in retardation is observed within the error bar.

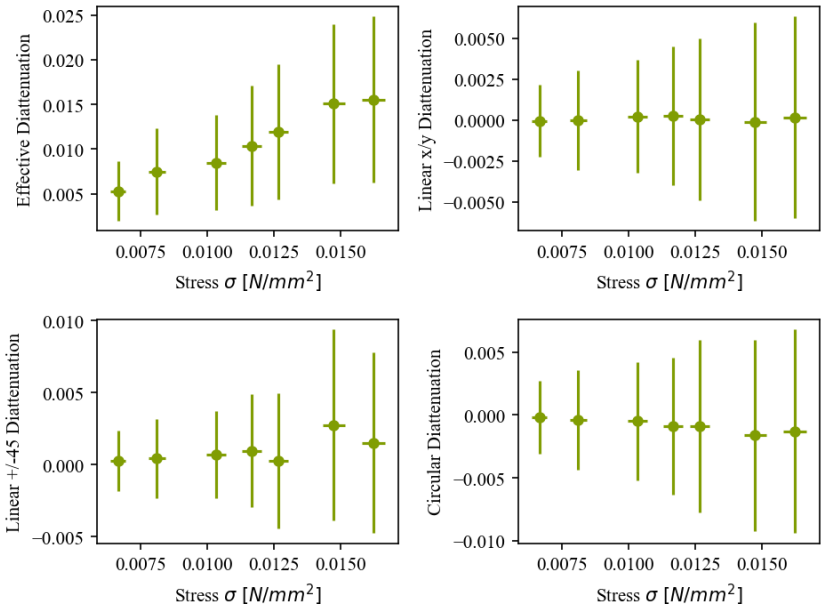

Figure 3.8: Plots showing the effect of stress (shown on x axis) on the diattenuation (shown on y axis) of the hydrogel, where green points are measurements. The first row shows effective and linear x/y diattenuation, while the second row shows the linear $+/-45°$ and circular diattenuation. Some change in effective diattenuation can be seen, although within the error bar.

3.5 Discussion

The quality and reliability of the technique were demonstrated by measuring several components and achieving birefringence measurements in agreement with their expected values. The current sensitivity on Jones matrix elements, retardation, and diattenuation is about $7 \cdot 10^{-4}$, 0.06°, and $8 \cdot 10^{-4}$, respectively. Note that these statistical uncertainties arise from the fit of the measurement distributions of air.

The drift of the liquid crystal (PSG) and the sensitivity of the polarisation camera (PSA) are the current suspected elements that limit the sensitivity of the birefringence and Jones matrix, respectively. There are several ways to improve this resolution. First, the drifts could be taken into account by multiplying all measured Jones matrix with the inverse of the air Jones matrix measured over an extended period of time. Another possible improvement could be to replace liquid crystals with electro-optical modulator crystals [63]. Since they can generate polarisation states at far higher speeds (typically up to a few tens of MHz), they could drastically improve the statistical uncertainty while simultaneously avoiding long-term drifts of the apparatus. Additionally, the sensitivity of the PSA can be addressed by using an optimised Stokes polarimeter-based polarisation camera [64] and not relying on a mechanically rotating retarder. This would lead to improved measurement speed and, therefore, higher statistics and faster measurements. Another benefit of replacing the PSA would be to avoid the decreased resolution at polarisation azimuth orthogonal to the analyser and increase the laser power at the photodetector, possibly increasing the signal-to-noise ratio of the measurement. The development of an improved polarisation actuator is discussed in Chapter 4, which involves the development of MHz speed polarisation control.

Finally, the scaling of the Jones matrix by the common amplitude ρ_0 and expected transmission/reflection of the sample led to improved resolution for the dielectric mirror measurement by one order of magnitude, resulting from a better constrained physical realizability condition. A systematic implementation of this scaling would improve the resolution of both the Jones matrix and the birefringence. The resolution could be further enhanced by improving the resolution in power measurements before and after the sample.

Being able to resolve both linear and circular birefringence makes this analysis attractive to any experiment relying on polarised light. Furthermore, this extended information could be useful to better understand the mechanisms underlying the apparition of birefringence in various materials. The Pauli basis can help better understand the birefringence couplings between retardation and diattenuation or between different birefringence axes, and hence

lead to an improved understanding of the origin of birefringence. This could assist in bringing more stringent requirements on polarisation components for high-precision optical elements and possibly help manufacturers design and fabricate lower birefringence optical elements. As mentioned in the computed results of the dielectric mirror, polarisation coupling may produce circular birefringence. This will especially bring careful restrictions on cascaded systems when using crystalline materials with non-uniform axis orientation.

The advantages of the work can be implemented using a 2D PSA which could allow to directly probe non-uniform birefringence of samples or studying its effects on optical cavities. Finally, having access to complete birefringence with their sign paves the way to develop an efficient birefringence compensation system with minimised actuation.

4

Development of high speed polarization actuation

Contents

This chapter puts forth the development of an MHz speed actuator required for addressing the issues in birefringence characterisation in Chapter 3. The following section discusses the development of a modulation mechanism for the Pockels cell and the modulation achieved in this pursuit.

4.1 Pockels Cells

4.1.1 Polarization modulation

As explained in Chapter 2, voltage controlled retarder uses the principle of linear electrooptic effect to provide a means of tuning the retardation of the laser passing through such an element. The linear electro-optic effect is called the Pockels effect, where the retardation change is proportional to the electric field strength. Only materials exhibiting linear electrooptic effect are classified as electrooptic crystals or Pockels cells. This effect only exists in crystals that do not have inversion symmetry, for instance, in Lithium Niobate ($LiNbO_3$) crystal [41].

For the research work mentioned in this manuscript, a non-resonant Pockels cell with a crystal of $LiNbO_3$ doped with magnesium oxide was purchased from Thorlabs. The presence of doping makes the crystal more tolerant to higher optical intensities and renders it immune to a higher level of photorefractive damage, making it favourable for the desired use. The presence of doping does not change the electrooptic tensor or the refractive index of the crystal much ($0.1 - 0.3\%$). The Thorlabs crystal [65] exists in orientation as shown in Fig. 4.1 and houses two crystals of dimensions $3 \times 3 \times 20\ mm^3$ each. The two crystals are placed opposite each other to cancel out any effect of static and thermal-induced birefringence. While ideally a perfect cancellation is expected, even small deviations in the thickness of the two crystals will exhibit some static birefringence.

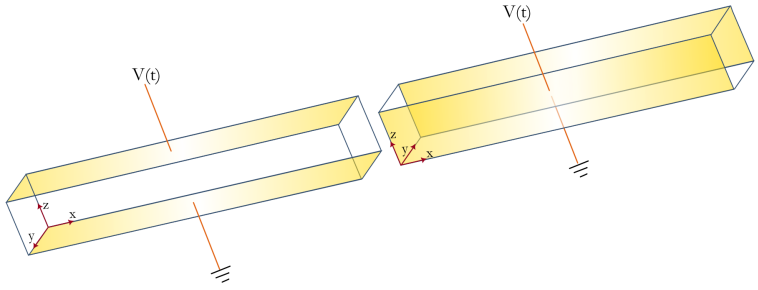

Figure 4.1: The orientation of the Pockels cells used. One Pockels cell houses a pair of oppositely oriented crystals. The electrodes(yellow in colour) are mounted to provide the required electric field. For a perfect alignment and an identical pair of crystals, the static birefringence in such an arrangement should be zero [65]. The [x,y,z] are representations of the crystal's individual frame of reference.

In order to produce the desired retardation, it is first important to understand the electrooptic effect within $LiNbO_3$ and the voltage required to achieve the desired retardation

control. Hence, the following sections delve into this aspect. The $LiNbO_3$ crystal falls under the $3m$ symmetry class. Following this convention, the electrooptic tensor can be written as [66],

$$r_{ij} = \begin{pmatrix} 0 & -r_{22} & r_{13} \\ 0 & r_{22} & r_{13} \\ 0 & 0 & r_{33} \\ 0 & r_{51} & 0 \\ r_{51} & 0 & 0 \\ -r_{22} & 0 & 0 \end{pmatrix} \tag{4.1}$$

The linear change due to the electric field can be expressed using the electric field E and the electrooptic tensor r_{ij} as, [66]

$$\Delta\left(\frac{1}{n^2}\right)_i = \sum_{j=1}^{3} r_{ij} E_j \tag{4.2}$$

The expansion of the above for $LiNbO_3$ can be written as

$$\begin{pmatrix} \Delta\left(\frac{1}{n^2}\right)_1 \\ \Delta\left(\frac{1}{n^2}\right)_2 \\ \Delta\left(\frac{1}{n^2}\right)_3 \\ \Delta\left(\frac{1}{n^2}\right)_4 \\ \Delta\left(\frac{1}{n^2}\right)_5 \\ \Delta\left(\frac{1}{n^2}\right)_6 \end{pmatrix} = \begin{pmatrix} -r_{22}E_y + r_{13}E_z \\ r_{22}E_y + r_{13}E_z \\ r_{33}E_z \\ r_{51}E_y \\ r_{51}E_x \\ -r_{22}E_x \end{pmatrix} \tag{4.3}$$

In the presence of the electric field, the refractive index ellipsoid of the $LiNbO_3$ crystal can be written as,

$$\begin{aligned} &\left(\frac{1}{n^2}\right)_1 x^2 + \left(\frac{1}{n^2}\right)_2 y^2 + \left(\frac{1}{n^2}\right)_3 z^2 + 2\left(\frac{1}{n^2}\right)_4 yz + 2\left(\frac{1}{n^2}\right)_5 xz + 2\left(\frac{1}{n^2}\right)_6 xy = 1 \\ &\implies \left(\frac{1}{n^2}\right)_1 x^2 + \left(-r_{22}E_y + r_{13}E_z\right)x^2 + \left(\frac{1}{n^2}\right)_2 y^2 \\ &\quad + \left(r_{22}E_y + r_{13}E_z\right)y^2 + \left(\frac{1}{n^2}\right)_3 z^2 + r_{33}E_z\, z^2 \\ &\quad + 2r_{51}E_y yz + 2\, r_{51}E_x\, xz - 2\, r_{22}E_x\, xy = 1 \\ &\implies \left(\frac{1}{n_o^2}\right)x^2 + \left(\frac{1}{n_o^2}\right)y^2 + \left(\frac{1}{n_e^2}\right)z^2 \qquad (n_x = n_y = n_o; n_z = n_e) \\ &\quad + \left(-r_{22}E_y + r_{13}E_z\right)x^2 + \left(r_{22}E_y + r_{13}E_z\right)y^2 + r_{33}E_z\, z^2 \\ &\quad + 2\, r_{51}E_y\, yz + 2\, r_{51}E_x\, xz - 2\, r_{22}E_x\, xy = 1 \end{aligned} \tag{4.4}$$

As can be seen in the above equation, upon application of the electric field not parallel to z, the refractive index ellipsoid expression exhibits several 'mixed' terms like xy, which

shows that the major axes of the ellipsoid are no longer aligned parallel to x, y and z axes. In such a case, it is crucial to find the direction and magnitudes of the new axes to determine the effect of the propagating field. However, for the investigation mentioned in this thesis, the direction of the applied field is chosen parallel to the crystal's z axis, *i.e.*, $E_x = E_y = 0$ and $E_z = E$. As such, the mixed terms disappear, which indicates that the principal axes of the new indices ellipsoid remain unchanged for $LiNbO_3$. This can be better visualised with the following refractive index ellipsoid expression [66].

$$\begin{aligned} &\frac{x^2+y^2}{n_o^2} + \frac{z^2}{n_e^2} + \Big(r_{13}x^2 + r_{13}y^2 + r_{33}z^2\Big)E = 1 \\ &\Big(\frac{1}{n_o^2} + r_{13}E\Big)x^2 + \Big(\frac{1}{n_o^2} + r_{13}E\Big)y^2 + \Big(\frac{1}{n_e^2} + r_{33}E\Big)z^2 = 1 \end{aligned} \tag{4.5}$$

The lengths of the new semi axes of the ellipsoid are

$$\begin{aligned} n_x &= n_o - \frac{1}{2}n_o^3 r_{13}E \\ n_y &= n_o - \frac{1}{2}n_o^3 r_{13}E \\ n_z &= n_3 - \frac{1}{2}n_e^3 r_{33}E \end{aligned} \tag{4.6}$$

The alignment of the crystal used is shown in Fig. 4.1. Under the influence of an electric field along the z or c axis of $LiNbO_3$, and for a light propagating along its x axis, the birefringence seen by the light is [66],

$$n_z - n_y = \underbrace{(n_e - n_o)}_{\text{static birefringence}} - \underbrace{\frac{1}{2}\Big(n_e^3 r_{33} - n_o^3 r_{13}\Big)E}_{\text{electro-optic birefringence}} \tag{4.7}$$

Usually, the electrooptic crystals are designed to have almost 0 static birefringence. However, there might be some residual birefringence. For the case where there is no static birefringence, the retardation under the influence of the electric field can be evaluated using the Equation 4.8, *i.e.*, as a function of the thickness l and electrode spacing d, and can be expressed as

$$\Gamma = \frac{2\pi}{\lambda}(n_z - n_y)l = \frac{2\pi}{\lambda}\frac{1}{2}\Big(n_e^3 r_{33} - n_o^3 r_{13}\Big)El = \pi\frac{\Big(n_e^3 r_{33} - n_o^3 r_{13}\Big)}{\lambda}V\frac{l}{d} = \pi\frac{V}{V_\pi} \tag{4.8}$$

where the voltage applied to the crystal is $V = Ed$ (since the crystal is a capacitive load). V_π is the characteristic voltage at which the crystal produces π retardation. For the $LiNbO_3$ crystal the V_π voltage can be written as,

$$V_\pi = \frac{\lambda}{\left(n_e^3 r_{33} - n_o^3 r_{13}\right)} \frac{d}{l} \tag{4.9}$$

where, $\lambda = 2\pi c/\omega$ is the free space wavelength. For $LiNbO_3$ with l =40 mm and d =3 mm the value of V_π can given as follows using its electrooptic coefficient $r_{13} = 9$ pm/V, $r_{33} = 25$ pm/V [67], $n_o = 2.2321$, $n_e = 2.1555$ [68] at 1.064μm as $V_\pi = 530\ V$. The manufacturer suggests a fitting formula based on their crystal characterisation as, [65],

$$V_\pi = 0.361\lambda[nm] - 23.844 \tag{4.10}$$

which suggests $V_\pi = 360.3\ V$ at 1064 nm [65]. The Pockels cell received from Thorlabs was characterised by the manufacturer at 1.31 μm and was found to have V_π of 508 V, with 12 pF capacitance. This resultant V_π at 1.31 μm is off from the fitting formula (Equation 4.10) V_π by 59 V. Therefore, a speculative voltage requirement for use at 1.06 μm was in the range of 360-420 V.

At the voltage of V_π the Pockels cell, a linearly polarised light oriented at 45° relative to the z axis of the crystal (since the crystal is housed at 45°, a S polarisation is injected), will transform as follows at the output plane $x = d$ of the crystal as follows [66],

$$\frac{1}{\sqrt{2}}\begin{pmatrix}1\\1\end{pmatrix} \longrightarrow \frac{1}{\sqrt{2}}\begin{pmatrix}e^{i\Gamma/2}\\e^{-i\Gamma/2}\end{pmatrix} \tag{4.11}$$

4.1.2 Electrooptic Amplitude Modulation

To characterise the Pockels cells, we require data on retardation as a function of the voltage applied to the crystal. Since the Pockels cell is a capacitive load, it cannot be driven with the commercially available DC voltage supply to obtain the π retardation. As such, a modulation voltage is applied using a resonant circuit at some particular frequency to maximise voltage at the cost of the bandwidth. The resonance frequency will lie in >kHz regime due to practical reasons, such as the size of the inductor or the quality factor of the circuit. However, no commercially available polarisation camera (such as from 2.4.2.1) can observe such fast modulation. So, the Pockels cells under the application of an electric field are characterised by observing the transmission change of the laser passing through in a cross-polariser configuration.

The configuration of such a characterisation method can be represented as Fig. 4.2, and the Pockels cell in this state is refereed as an electrooptic amplitude modulator. The electrooptic

crystal under investigation can be placed between two crossed polarisers. The electrooptic crystal should receive the input polarisation at a relative angle of 45° to its z axis to obtain maximum transmission. However, since the purchased Thorlabs crystal (EO-AM-NR-C2) is placed in a housing with a mounting angle of 45°, the input polarisation is chosen to be linear along the X axis in the lab frame or the z axis in the crystal frame, *i.e.,* p polarisation.

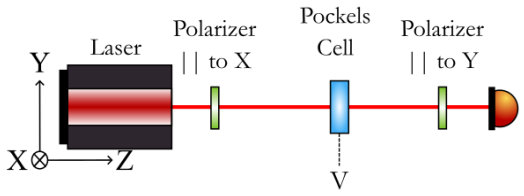

Figure 4.2: A cross-polariser configuration used to characterise the Pockels cell. A laser polarised along X axis enters through the input polariser, and the intensity at the output is observed after the exiting polariser. The lab frame is shown using [XYZ].

If a light of amplitude A polarised along the X axis of the lab frame is sent to the Pockels cell, then it has equal in-phase components along x and y of the crystal axes. The incident intensity before entering the crystal can be given by,

$$I_i \propto E \cdot E^* = |E_x(0)|^2 + |E_y(0)|^2 = 2A^2 \tag{4.12}$$

When the light exits after travelling across the length of the crystal, l, the x and y components acquire a relative phase difference of Γ, which can be represented as,

$$\begin{aligned} E_x(l) &= Ae^{-i\Gamma} \\ E_y(l) &= A \end{aligned} \tag{4.13}$$

The total complex field exiting the output polariser can be given as the sum of the Y components (from both E_x and E_y) in the lab frame, which is expressed as,

$$(E_Y)_o = \frac{A}{\sqrt{2}}(e^{-i\Gamma} - 1) \tag{4.14}$$

and corresponds to an output intensity measuring,

$$\begin{aligned} I_o &\propto [(E_Y)_o(E_Y^*)_o] \\ &= \frac{A^2}{2}[(e^{-i\Gamma} - 1)(e^{i\Gamma} - 1)] = 2A^2 \sin^2 \frac{\Gamma}{2} \end{aligned} \tag{4.15}$$

The ratio of output and input intensity can then be represented as the following ratio,

$$\frac{I_o}{I_i} = \sin^2 \frac{\Gamma}{2} = \sin^2 \left[\frac{\pi}{2}\frac{V}{V_\pi}\right] \tag{4.16}$$

Now, since the input laser power can experience some fluctuation, during the characterisation, instead of calculating the ratio of intensity using the input laser, the sum of intensity from the photodiodes(PD) at the transmission and reflection of a PBS was instead used. This makes the measurement immune to laser power fluctuations during the characterisation. To properly take the PBS into account, and the corresponding PD gain and alignment, the polarisation-dependent characterisation of the two photodiodes could be done during future characterisation.

Since the Pockels cell is being characterised using the transmission change or peak-to-peak value of transmission, which can only be positive, it is important to bias the crystal response at 50% transmission, *i.e.,* in a balanced configuration. This process of amplitude modulation is better visualised using Fig. 4.3.

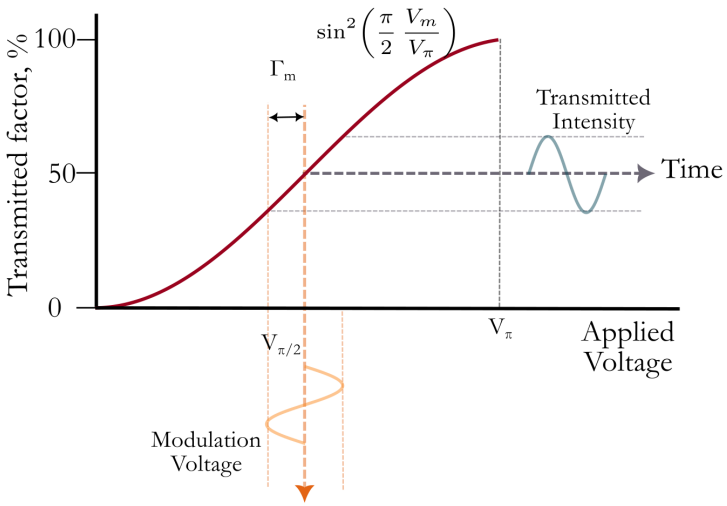

Figure 4.3: The plot representing transmission factor of an electrooptic modulator as a function of applied voltage in cross-polariser configuration. The modulator is biased at 50% intensity transmission. Any applied sinusoidal TransmissionFactor modulates the transmitted intensity about the bias point.

The modulator is biased with a fixed retardation of $\Gamma = \pi/2$ to the 50% transmission point. The bias can be applied using two methods. One is by applying a voltage equivalent to $V_{\pi/2}$. For a crystal, this voltage can be very large; for instance, the crystal at hand would require a DC bias of $420/2 = 210V$. On the other hand, such a bias can also be achieved, using a naturally birefringent crystal, for instance, a QWP can introduce a phase difference of $\pi/2$ between the x and y components, as shown in the Fig. 4.4 configuration.

Taking into account the retardation bias of $\pi/2$, on applying a modulation voltage of $V_m \sin \omega_m t$ the retardation equation can be represented as, [69]

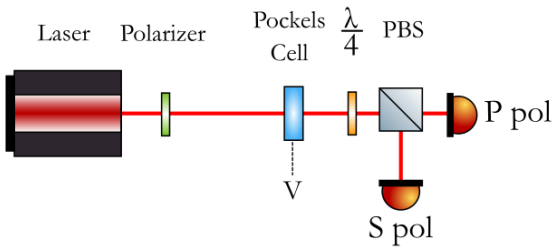

Figure 4.4: The characterisation setup of Pockels cells by biasing it to a 50% transmission point or $\Gamma = \pi/2$ using a QWP. The Pockels cells were placed between a polariser and a polarising beam splitter, instead of two polarisers. As such, we can characterise the Pockels cell independent of input laser power fluctuations.

$$\Gamma = \frac{\pi}{2} + \Gamma_m \sin \omega_m t, \quad \text{where } \Gamma_m = \pi V_m / V_\pi \tag{4.17}$$

Taking this into account, the ratio of output intensity for the case of biasing at 50% transmission can look as, [69]

$$\begin{aligned} \frac{I_o}{I_i} &= \sin^2 \left(\frac{\pi}{4} + \frac{\Gamma_m}{2} \sin \omega_m t \right) \quad \text{using Equation 4.16} \\ &= \frac{1}{2} \left(1 + \sin \left(\Gamma_m \sin \omega_m t \right) \right), \end{aligned} \tag{4.18}$$

After characterisation of each Pockels cell independently, they can be used as polarisation actuators to generate and read polarisation, as shown using mathematical analysis in the upcoming subsections.

4.1.3 Non-moving rotating half-wave plate

The aim of using these ultra-fast actuators is for birefringence characterisation as discussed in Chapter 3. The pair of Pockels cells with different voltages applied across their electrodes, and oriented at 45° relative to each other as Fig. 4.5, can, in principle, generate any polarisation as shown in Fig. 4.5b.

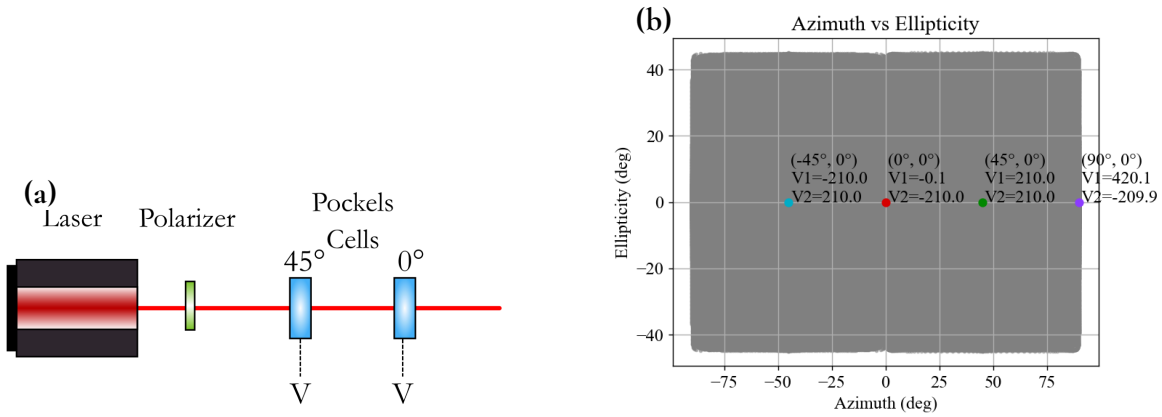

Figure 4.5: The setup showing a pair of Pockels cells which can generate several polarisations. (b) Simulation showing all the polarisation states that will be generated with the available Pockels cell upon modulating with the designed driver. Markings of voltage at which some linear polarisation (of our interest) is shown.

Since the voltage modulation is a sinusoidal function, if data during characterisation is collected at each point of the sinusoidal curve, there would be too large a dataset to deal with. For this purpose, the data collection is reduced to a certain select points where the pair of Pockels cells collectively acts as a rotating HWP. The use of such a method of rotating polarisation offers several advantages over the mechanically rotating retarders.

A 360° mechanically rotating Half-Wave Plate (HWP) will produce the polarisation states shown in Fig. 4.6a. However, a mechanically rotating HWP can have several disadvantages for a highly precise metrological setup, by introducing noise such as scattering noise, misalignment of HWP (it could be possible that the HWP has a differing angle in pitch or yaw at different angles of rotation), etc.. As such, a non-mechanically moving HWP offers an ideal workaround to such issues. Upon selecting the voltages along the modulation curve which give such a rotation of polarisation orientation, an effect on polarisation rotation similar to rotating a HWP can be seen. The pair of Pockels cells can change the polarisation orientation, as shown in Fig. 4.6b, forming an optimal PSG required for birefringence characterisation with improved sensitivity.

4.1.4 Stokes Polarimeter

Another component required for improved birefringence characterisation is an improved PSA, as discussed in Chapter 3. As shown in section 2.4.2.2, a complete Stokes polarimeter can be made using a pair of variable retarders. The pair of Pockels cells can be placed in such a configuration to read all polarisation states.

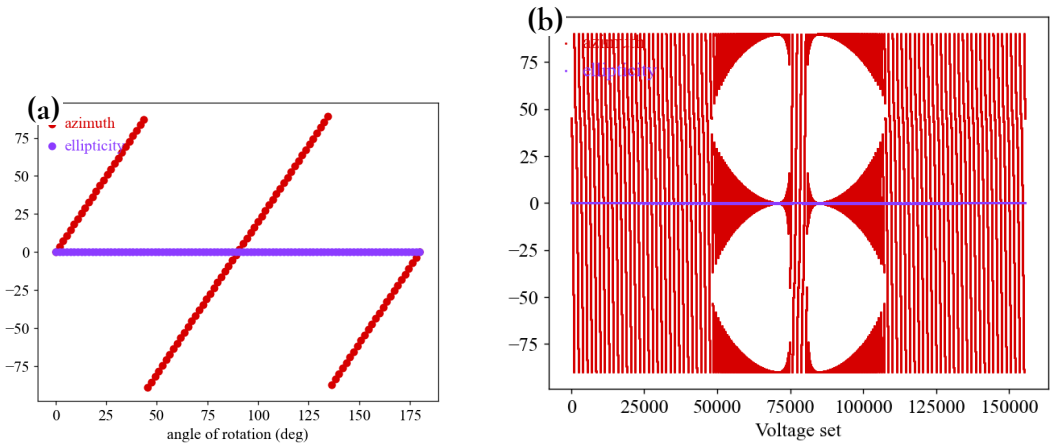

Figure 4.6: (a) A mechanically rotatingHWP. As the half-wave plate rotates, the input linear polarisation is rotated by an angle ranging from -90 to 90 deg (represented in red), while the ellipticity of the polarisation remains at $(0 \pm 0.1)°$, as seen from mathematical analysis using Jones calculus. (b) Polarisation rotation control using a pair of Pockels cells is available at several voltage combinations of the sinusoidal modulation obtained from simulation. The x axis of the plot shows a unique voltage combination applied to the pair of Pockels cells, following the resolution of the waveform generator used to provide the signal for modulation.

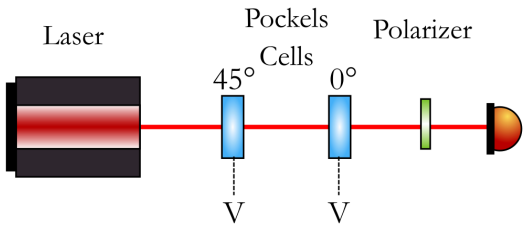

Figure 4.7: Pockels cell-based polarisation analyser capable of high-speed polarisation readout.

Several power measurements can be performed by varying the retardation (or voltage) of the variable retarder, thereby enabling reconstruction of the incident polarisation state. Expanding upon Equation 2.39 from Chapter 2, the power measurement can be expressed as,

$$
\begin{aligned}
&P(\delta_1,\delta_2) = A(\delta_1,\delta_2).S \\
&= \frac{1}{2}S_0 + \frac{-\sin\delta_1\sin\delta_2}{2}S_1 + \frac{-\cos\delta_2}{2}S_2 + \frac{-\cos\delta_1\cos\delta_2}{2}S_3 \\
&= \frac{1}{2}S_0 - \cos\left[\frac{\pi}{V_\pi}V_2\sin\omega_2 t\right]\frac{S_2}{2} \qquad \left[\delta_x = \frac{\pi}{V_\pi}V_x\sin\omega_x t\right] \\
&- \sin\left[\frac{\pi}{V_\pi}V_1\sin\omega_1 t\right]\sin\left[\frac{\pi}{V_\pi}V_2\sin\omega_2 t\right]\frac{S_1}{2} \\
&- \cos\left[\frac{\pi}{V_\pi}V_1\sin\omega_1 t\right]\cos\left[\frac{\pi}{V_\pi}V_2\sin\omega_2 t\right]\frac{S_3}{2} \\
&= \frac{1}{2}S_0 - \cos\left[B\sin\omega_2 t\right]\frac{S_2}{2} \qquad \left[A = \frac{\pi}{V_\pi}V_1; B = \frac{\pi}{V_\pi}V_2\right] \\
&- \sin\left[A\sin\omega_1 t\right]\sin\left[B\sin\omega_2 t\right]\frac{S_1}{2} - \cos\left[A\sin\omega_1 t\right]\cos\left[B\sin\omega_2 t\right]\frac{S_3}{2}
\end{aligned} \tag{4.19}
$$

$$
\begin{aligned}
&= \frac{1}{2}S_0 - \left[J_0(B) + 2\sum_{n=1}^{\infty}J_{2n}(B)\cos\left(2n\omega_2 t\right)\right]\frac{S_2}{2} \qquad \text{[Jacobi-Anger]} \\
&- \left[2\sum_{n=1}^{\infty}J_{2n-1}(A)\sin\left[(2n-1)\omega_1 t\right]\right]\left[2\sum_{n=1}^{\infty}J_{2n-1}(B)\sin\left[(2n-1)\omega_2 t\right]\right]\frac{S_1}{2} \\
&- \left[J_0(A) + 2\sum_{n=1}^{\infty}J_{2n}(A)\cos\left(2n\omega_1 t\right)\right]\left[J_0(B) + 2\sum_{n=1}^{\infty}J_{2n}(B)\cos\left(2n\omega_2 t\right)\right]\frac{S_3}{2}
\end{aligned} \tag{4.20}
$$

We keep signal upto 2nd harmonics

$$
\begin{aligned}
&= \frac{S_0}{2} - J_0(B)\frac{S_2}{2} - 2J_2(B)\cos\left(2\omega_2 t\right)\frac{S_2}{2} - J_0(A)J_0(B)\frac{S_3}{2} \\
&- 4J_1(A)J_1(B)\sin\left(\omega_1 t\right)\sin\left(\omega_2 t\right)\frac{S_1}{2} - 2J_0(A)J_2(B)\cos\left(2\omega_2 t\right)\frac{S_3}{2} \\
&- 2J_0(B)J_2(A)\cos\left(2\omega_1 t\right)\frac{S_3}{2} - 4J_2(A)J_2(B)\cos\left(2\omega_1 t\right)\cos\left(2\omega_2 t\right)\frac{S_3}{2}
\end{aligned} \tag{4.21}
$$

$$
\begin{aligned}
P(\delta_1,\delta_2) = \frac{S_0}{2} &- J_0(B)\frac{S_2}{2} - J_2(B)\cos\left(2\omega_2 t\right)S_2 - J_0(A)J_0(B)\frac{S_3}{2} \\
&- J_1(A)J_1(B)\left[\cos\left(\omega_1-\omega_2\right)t - \cos\left(\omega_1+\omega_2\right)t\right]S_1 - J_0(A)J_2(B)\cos\left(2\omega_2 t\right)S_3 \\
&- J_0(B)J_2(A)\cos\left(2\omega_1 t\right)S_3 - J_2(A)J_2(B)\left[\cos 2(\omega_1-\omega_2)t + \cos 2(\omega_1+\omega_2)t\right]S_3
\end{aligned} \tag{4.22}
$$

The above expression shows that there will be several frequencies (such as $2\omega_1$, $2\omega_2$, $\omega_1-\omega_2$, $2(\omega_1-\omega_2)$, $\omega_1+\omega_2$, $2(\omega_1+\omega_2)$) that can give us the Stokes parameter. It will depend on the bandwidth of detector/PD used for the power measurement. This can be very useful in case the readout, such as a camera, cannot operate at MHz speed. In such a case, values can

be accessible in beat frequency ($\omega_1 - \omega_2$). Therefore, a slight difference of 30 Hz between the modulation of two Pockels cells can be easily observed by a camera (of speed 60 Hz). As such, the signal in the beat frequency and the power measurements can be represented as,

$$\begin{aligned} P(\delta_1, \delta_2) = \frac{S_0}{2} - J_0(B)\frac{S_2}{2} - J_0(A)J_0(B)\frac{S_3}{2} \\ - J_1(A)J_1(B)\left[\cos\left(\omega_1 - \omega_2\right)t\right]S_1 - J_2(A)J_2(B)\left[\cos 2(\omega_1 - \omega_2)t\right]S_3 \\ = a_0 + a_1\cos\left(\omega_1 - \omega_2\right)t + a_2\cos 2(\omega_1 - \omega_2)t \end{aligned} \tag{4.23}$$

Using the developed polarisation readout, the Stokes parameters can then be constructed using the following relations,

$$\begin{aligned} S_0 &= 2a_0; && \text{when A=B=0 } \textit{i.e.}\text{, modulation is off} \\ S_1 &= \frac{-a_1}{J_1(A)J_1(B)}; \\ S_2 &= \frac{S_0 - J_0(A)J_0(B)S_3 - 2a_0}{J_0(B)}; \\ S_3 &= \frac{-a_2}{J_2(A)J_2(B)}; \end{aligned} \tag{4.24}$$

With the mathematical analysis of the high-speed PSG and PSA in place, it is time to delve into the development of the driver required to provide the modulation voltage to the Pockels cell.

4.2 Development of driver for Pockels cell

The Pockels cell is a capacitive load (14 pF for the purchased Thorlabs one). However, since it is not a standard 50 Ω load, a conventional voltage source cannot be used to drive it. Additionally, a large voltage of >400 V is required, and no voltage source as far as it is known is commercially available for such a task. Hence, an off-the-shelf generator could not be used.

Usually, crystals are also sold as a resonant model, for instance, a resonant Pockels cell. The resonant modulators cannot be operated at long wavelengths to generate large phase shifts since the internal tank circuit can only handle up to 35 Vpp. The Thorlabs resonant Pockels cell requires modulation with 25 V amplitude at a wavelength of around 1 μm to generate π retardation. As such, the resonant Pockels cell was not suitable for use because of its limitation on the maximum RF input power and the retardation it can generate.

Additionally, they cannot be operated for a long time due to heat-induced degradation of the components. This makes us choose the non-resonant modulator.

As such, it was necessary to figure out the problem of supplying the required (>400 V) voltage to the crystal to generate a large range of retardation. However, since the high voltage requirement of >400 V can be achieved using a resonant circuit, the focus was on the development of the resonant circuit as shown in the following sections.

4.2.1 Resonant circuit

The resonant circuit utilises the concept of having minimum reactive impedance at one frequency, which helps the circuit draw a large current and supplies the components with the necessary voltage. Since the Pockels cell crystal is a capacitive load, at the resonant frequency of the circuit, the voltage over the crystal is passively amplified, while reducing the required driving voltage. A series resonant circuit has an inductor L and a crystal with capacitance C, which forms the tank circuit. Additionally, it might have some resistive losses indicated by R, as shown in Fig. 4.8.

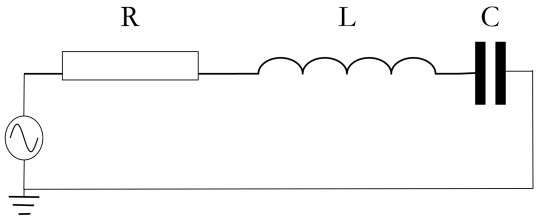

Figure 4.8: A series resonant circuit.

The total impedance of the circuit at a frequency ω is given as,

$$Z = R + i\omega L + \frac{1}{i\omega C} = R + i\omega L\left(1 - \frac{1}{\omega^2 LC}\right) \tag{4.25}$$

The resonant frequency f_0 of the circuit is when the imaginary part of the above equation goes to zero, *i.e.*, the overall impedance of the reactive components is zero. The resonant frequency is therefore given by,

$$\omega_0 = 2\pi f_0 = \frac{1}{\sqrt{LC}} \tag{4.26}$$

Following Ohm's law, it can be seen that at the resonant frequency, because the impedance is reduced, the voltage over the capacitor is amplified compared to the input voltage. This is called the quality factor of the tank circuit, Q, and is written as,

$$Q = \frac{V_c}{V_{in}} = \frac{1}{R}\sqrt{\frac{L}{C}} = \frac{\omega_0 L}{R} \tag{4.27}$$

In a series LC circuit, the overall quality factor Q, is related to the Q_L quality factor of the inductor and Q_C quality factor of the Pockels cell, as

$$\frac{1}{Q} = \frac{1}{Q_L} + \frac{1}{Q_C} \tag{4.28}$$

It can be easily visualised using the above equation that the quality factor of the tank circuit can be increased by increasing the quality factor of the inductor (such as by reducing wiring resistance). Since the Pockels cell is a purchased entity, its quality factor cannot be changed, and hence, the focus is on other components. Several different categories of resonant circuits were tested in this attempt. They are briefly described below. Using the following sections, a better understanding of the choice of components and the resonant frequency will be obtained.

4.2.2 Low Voltage and low current

An initial phase of development of the driver circuit involved the use of an off-the-shelf lead inductor [70] for the tank circuit with an inverting amplifier at its input. The lead inductors used are small in size, owing to which they become quickly saturated at high current or voltage, and they do not have a high quality factor. Additionally, their self-resonant frequency is as low as 2 MHz, which indicate dominant effect from parasitics will be present. While a resonant peak could be observed in the transfer function, it was a rather broadband one due to the use of Opamp.

The tank circuit was impedance matched to the source (50 Ω) using the inverting amplifier configuration by using a 50 Ω resistor as the input impedance of the Opamp. The tested Op27 [71] and Op37 [72] did not render high current to the tank, thereby hindering the attainment of the required voltage at the Pockels cell. Additionally, the output voltage at the Opamp is generally low, thereby limiting the input to the tank circuit to around 9 V. While high-output-voltage Opamp (PA83 [73]) could be used, they are very expensive. Since a total of 4 driver circuits is required, this was considered a costly option. Additionally, the high-voltage Opamp does not offer high output current, and so, at the end, not much amplification can be anticipated at the Pockels cell. The resonant frequency was in the range of 100 kHz when testing the Op27-based circuit, and in the range of 1-5 MHz when testing the Op37-based circuit. The use of different values of inductors available from Coilcraft [70] corresponds to the resonant frequency of the tank being in the range of 100 kHz - 1 MHz. While the inductors' self-resonant frequency increased with the decrease in inductance, not much gain in voltage was observed.

Additionally, it was seen that the gain of the circuit at the resonant frequency decreased with the increment of input voltage provided from the source. This further decreases the voltage at the Pockels cell. It could be seen that since the tank circuit did not have a high quality factor, and the use of an Opamp did not provide a high voltage at the input of the tank circuit, this style of driver circuit didn't work for the Pockels cell. A retardation of only ≈ 20-40% of $\pi/2$ across the Pockels cell was obtained using these steps.

In this phase, Moku-GO was being used for readout of the signal from the photodiode, which has a bandwidth of 30 MHz. It was anticipated to include the 4^{th} harmonic during modulation for possible information on polarisation; as a result, the resonant frequency was chosen within 7 MHz. However, the Moku-GO was replaced, as will be seen in the following subsections 4.2.4, and there was an option to shift the resonant frequency to a higher range in MHz.

4.2.3 Low voltage and high current

Since in the previous attempts it seemed as if the output current of the Opamps restricts the passive voltage amplification at the resonant circuit, a buffer at the output of the inverting amplifier was used. The buffer BUF634 [74] offers an output current of 0.25 A. The addition of a buffer to Op37 didn't provide a significant increase in gain. It seemed as if the current limit was not enough. Hence, another higher current Opamp was tested.

The use of Opamp EL2099CT [75], which has an output current limit of 0.44 A, was explored. Having such a large current margin at hand, it was upto the tank circuit to make the passive amplification. However, the required voltage at the Pockels cell was not observed. A retardation of only ≈ 40-55 % of $\pi/2$ across the Pockels cell was obtained using these steps. The tests at the end provided conclusive evidence that the inductor's quality factor needs to be improved.

4.2.4 High voltage and high current

A typical lead inductor is wire wound around a core. The material of the core and its size determine the quality factor of the inductor. While toroidal cores can be used, they are very lossy (>10 Ω in theory [76]) in the upper kHz and MHz range. Additionally, both the lead-type and toroidal core-based inductors are susceptible to magnetic saturation. This was also the reason why the option of impedance matching using a transformer was eliminated.

The best option was an air core inductor [77]. The use of air as a core will remove issues from saturation and also allow for a very high quality factor. However, a resonant peak in

the upper kHz or lower MHz range will require a large inductance, implying a large inductor. It was rather unfeasible to design a large air core inductor. During tests with large air core inductors (of dia. 10 cm), it was found that they are mechanically unstable, very difficult to design by hand, have a much lower self-resonant frequency and exhibit several parasitics. This made the resonant frequency choice to be more than 15 MHz, and the signal acquisition was now being done using Moku-Lab (bandwidth 200 MHz). As such, a smaller inductor with a smaller inductance of around 4 μH was designed.

The options of the Opamp for impedance matching were also eliminated. Rather, a ladder of capacitor network was taken into consideration to lower the introduction of parasitics and improve the quality of resonant peak *i.e.,* removing the wideband width due to the Opamp. Additionally, chip-based transformers (TT25-1-X65+ [78] and T-626-X65+ [79]) were tested for impedance matching. However, they showed incompatibility for high current, and as such, their use was not further pursued.

An overall improvement in the voltage amplification at the Pockels cell was observed with the use of an air core inductor. The details of the components are discussed in the next section.

4.3 Suitable driver: High Q resonant circuit

In order to drive the Pockels cells at a large RF power, *i.e.,* large current and large voltage, it is crucial to address issues of loss, such as resistance and parasitic capacitance in the circuit. A lowered loss through improved inductor and impedance matching from 4.2.4 will increase the quality factor of the circuit as indicated by Equation 4.27. This section focuses on developments involved in the final circuit for the Pockels cell. The task at hand was to maximise the quality factor of each component used, and additionally reduce any increased resistance or parasitic capacitance from wiring, PCB. The details of each components is discussed in subsequent sections.

4.3.1 High Q inductor

In order to increase the quality factor of the inductor, it is important to understand its loss mechanism. The dominant loss for an inductor is the resistance of its wiring, which prohibits it from drawing a large current, thereby dropping the overall Q of the tank circuit. For frequencies in the MHz range and above, the resistance of the wire increases dramatically due to skin effect [80]. When the current experiences skin effect, it starts flowing only in the outer surfaces of the conductor *i.e.,* within the outer skin, thereby making the conductor

narrower, and thus increasing the resistance from its DC value. At one skin depth, the current density reaches $1/e$ of its surface value (e is Euler's number). A good approximation for the skin depth in copper can be provided by Equation 4.29, which suggests 20 μm of skin depth at 10 MHz. The formula for skin depth of a copper wire of resistivity ρ, relative permeability μ_r and operating in free space of permeability μ_0 carrying current at frequency f, is [81].

$$\text{Skin depth} = \sqrt{\frac{\rho}{\pi f \mu_r \mu_0}} = \frac{6.61}{\sqrt{f[Hz]}}[cm] \tag{4.29}$$

The use of less-susceptible plating material can help reduce the skin effect. Hence, the wire chosen for the helical inductor is a solid copper core with silver plating and was 10 AWG (2.5 mm) with a >1.5 μm thick silver plating, SPCW2R5 from Welco Plus [82]. The solid copper core gives it enough mechanical strength to retain the helical shape, while the silver helps reduce the AC resistance increase associated with skin effect. The skin depth of silver is less than that of copper; this is offset by the higher electrical and thermal conductivity. The silver, when exposed to air for long periods, will form silver oxide on the outside of the wire, which also has much lower resistivity in comparison to copper oxide. So, an inductor made by such a wire will provide a good enough response even in the long term of decades.

An ideal inductor has even spacing of its turns and follows the relation of diameter/length ≈ 1. In order to make inductors by hand with good spacing and a symmetric shape, a mould was 3D printed. The mould had grooves in place to shape the wire while being able to turn the mould. Additionally, the mould was made like a jigsaw puzzle, and the wire could be kept on it till after soldering. Once the inductor was soldered, the centre cylinder could be removed, thereby removing the inductor from the mould without any resistance. After several iterations in the design process, the finalised mould and the designed inductor are shown below,

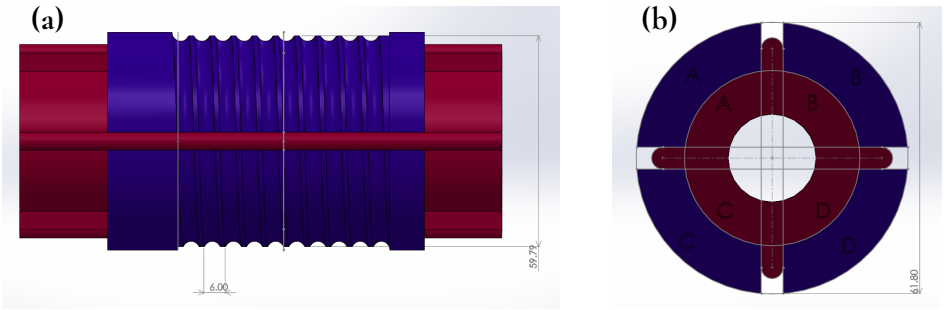

Figure 4.9: Design of 3D printed mould made to make the inductor. (a) front view (b) side view

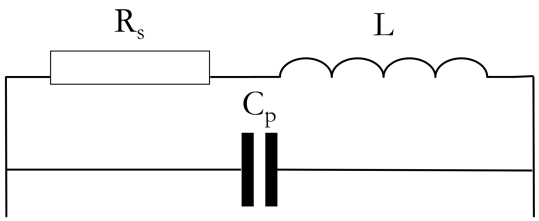

Figure 4.11: Lumped equivalent circuit model of the inductor. L is the frequency-independent inductance, R_s and C_p are the series AC resistance and parallel stray capacitance of the coil at design frequency.

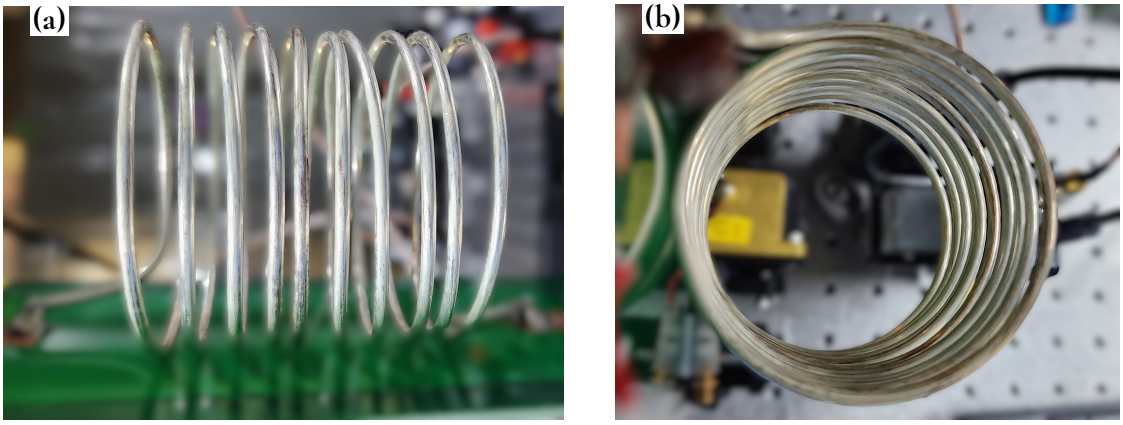

Figure 4.10: The inductor after being made using the 3D printed mould and soldered on the PCB (a) front view (b) side view

The inductance of the inductor is based on the choice of resonant frequency, as $L = 1/\left(4\pi^2 f_0^2 C\right)$. To achieve a certain inductance, the dimensions of the helical inductor were based on the tool by the reference [83] recommended by Schiworski [77], which also evaluates the lumped equivalent circuit of the inductor. The theoretical design of the inductor yields a lumped equivalent circuit model as Fig. 4.11.

The diameter to length ratio of the helical inductor is unity, with the turns spaced at least a wire diameter apart [83]. At the design frequency of 16 MHz, the chosen diameter and length of the coil are 60 mm, containing 10 turns with a winding pitch of 6 mm. Thereby, making $L = 4.04\mu H$, $R_s = 0.32\Omega$ and $C_p = 0.3pF$. The estimated self-resonant frequency of this inductor was 53.6 MHz. The effective unloaded quality factor of the coil was predicted to be 1271 at its design frequency of 15 MHz. Ideally, a very large inductor (in diameter and length) will give a high Q_L. It was discovered while making the inductors that the inductor diameter cannot be larger than roughly 25-30 times that of the wire diameter. An inductor too large in size became unstable in its shape and was acting like a spring, making it infeasible to be stable

without the need for external supports. Additionally, it was seen that a large inductor might have increased parasitic capacitance at the design frequency and also a lower self-resonant frequency, in comparison to a smaller inductor with the same value of inductance.

4.3.2 Stray capacitance of Pockels cells

The connection from the inductor to the crystal is crucial. Using a cable which is not meant to be used with high voltage or high frequency will reduce the quality factor of the tank circuit. The commonly used litz wire has its voltage rating at around 300 V, making it not optimal for use in this case. Additionally, it cannot tolerate high temperatures for prolonged periods of time, making it unsuitable for long-term operation. Hence, a 22 AWG stranded silver-coated copper wire with FEP insulation was used. The wire is rated for 20 kV and operating range of $-65°C$ to $200°C$.

The transmission line between the inductor and the Pockels cell, *i.e.,* the connection, also adds some stray capacitance. That is to say that the length of cable and trace will increase the capacitance of the Pockels cell. As such, the connection was made by keeping the minimum distance between the leg of the inductor and the trace. Additionally, the stray capacitance will make the Pockels cell impedance change from Z_C to Z'_C due to the transmission line as [84],

$$Z'_C = R_0 \cdot \frac{Z_C \cos(\beta l) + \mathrm{i} R_0 \sin(\beta l)}{R_0 \cos(\beta l) + \mathrm{i} Z_C \sin(\beta l)} \tag{4.30}$$

where l is the length of the cable with $R_0 = 50\,\Omega$ carrying current and $\beta = 2\pi f/C$. The available Pockels cells had a capacitance of 12-14 pF [65]. So the use of a 0.6 m cable will change the capacitance to 52 pF. This will not only cause a change in resonant frequency but will also lead to a reduction in the quality factor (if the cable used is not optimal) or gain of the circuit. This stray capacitance should be minimised by keeping the transmission line used as small as possible, and otherwise should be taken into account when calculating the resonant frequency.

4.3.3 PCB Design

A high-performance circuit design, which might look good in simulation can give mediocre performance due to a sloppy board layout. Usually, PCB designing comes as a last step in such development, and a poorly designed one will lead to introducing additional parasitic capacitance to the tank circuit. Consequently, despite having a high quality factor components, the circuit might fail to deliver the expected current or voltage to the tank circuit. It might also

fail to efficiently transfer the current between the inductor and the Pockels cell with reduced parasitics. As a result, there are several factors to keep in mind when designing the PCB.

Copper foil is the conducting layer used in the PCB that forms the trace, pads, and or planes responsible for carrying electrical signals and power. In high voltage or current applications, the voltage or current can (for our purpose) range from 300-700 V and 1-2 A, respectively. Around resonance, the current will be quite low, and it will be in this phase that the PCB will be used most. However, since there might be some requirement to tune frequency or impedance, and in the absence of such tuning, there could be some high voltage and high current at the same time, due to which the PCB should be designed with this safety factor in mind [85, 81].

Considering the use of the PCB to carry high current from the source to Pockels cells, a good amount of copper layer thickness of 2 oz/ft^2 (70 μ m) was chosen, to have good thermal stability. Additionally, the minimum space between traces was selected as 0.2 mm. This should be carefully optimised by keeping two factors in mind: the stability of the PCB and the manufacturer's capability. Additionally, the minimum trace width for a 2 A current should be 0.75 mm [86]. While thicker copper is beneficial for high voltage, it makes it difficult to etch too fine traces. Care must be taken to consider the specs from the corresponding manufacturers' limitations.

Ideally, a layer of PCB should be dedicated to serve as a ground plane alone. A ground plane acts as a reference for common voltage, and it provides shielding and reduced stray inductance (but might increase parasitic capacitance). The ground plane reduced trace inductance through the cancellation of the magnetic field between the conductor and the ground plane. Additionally, the ground plane also aids in heat dissipation. As such, an unbroken ground plane was chosen at the bottom layer of the PCB, as well as on the top layer in the section outside the region of the circuit, for best performance, and both were connected by vias. Since the presence of vias can introduce parasitics (both inductance and capacitance), adding a ground plane on the top layer removes such an issue [81]. All the components were soldered only on the top of the PCB.

4.4 Characterisation of Pockels cells

To estimate the performance of the driver, the overall performance of the resonance circuit was measured. Several characterisations were done, as will be seen in the following subsections, and all of them were performed iteratively to observe maximum modulation of the Pockels cell.

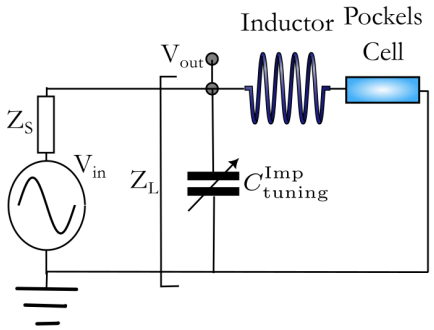

Figure 4.12: A representation of the impedance of the tank circuit and source. The tuning capacitor is to match the impedance of the tank to the source.

4.4.1 Impedance matching

For any circuit to maximise the power transfer, the circuit should be matched in impedance with the source. For the research mentioned, impedance matching is required to use all the power provided by the source and to ensure efficient energy transfer. An impedance-matched circuit also reduces reflections between the tank circuit and the source. An impedance-unmatched circuit can be visualised using a voltage divider circuit Fig. 4.12.

The efficiency η, which is given by the ratio of power dissipated by the load to the total power dissipated by the entire circuit, is related to the impedance of the tank circuit Z_L and the output impedance Z_S of the source as,

$$\eta = \frac{P_{load}}{P_{total}} = \frac{Z_L/Z_S}{Z_L/Z_S + 1} \tag{4.31}$$

The condition for maximum transfer is when $Z_L = Z_S$, giving $\eta = 0.5$. [87]. The impedance tuning of the tank circuit is done using capacitors in parallel to the tank circuit, indicated as $C^{\text{Imp}}_{\text{tuning}}$. The resonant frequency in the presence of an impedance matching capacitor network will become,

$$\omega_0 = \sqrt{\frac{1}{L}\left(\frac{1}{C^{imp}} + \frac{1}{C}\right)} \tag{4.32}$$

The impedance matching was done by using several fixed capacitors and one tunable capacitor. The fixed capacitors chosen were mica capacitors, with several of them connected in parallel to meet the expected impedance. While the exact specs of the capacitors were unknown, as they were picked off the shelf of the electronics lab, mica capacitors are known to have Q >1000 at 1 MHz and rated for $\approx$ 500 DC voltage. Additionally, they are known

to have low resistive and inductive losses, offering stability and being optimal for use at high frequencies [88, 89]. While a large part of impedance tuning was done with multiple capacitors of 5-471 pF, some small tuning was done using a tunable capacitor in parallel.

In order to evaluate the impedance, the tank circuit can be treated as a one-port device, *i.e.*, it has one unique input. As such, the scattering parameter of a one-port device can be written by relating the input voltage V^+, and reflected voltage V^- as,

$$\left[V^-\right] = \left[S_{11}\right] \cdot \left[V^+\right] \tag{4.33}$$

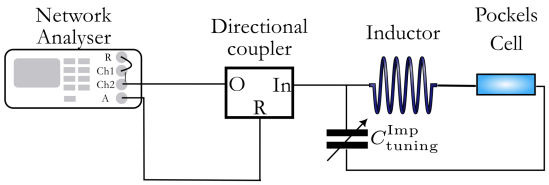

Figure 4.13: Setup to measure the S11 parameter of the tank circuit using a vector network analyser and a directional coupler. The tuning capacitor is then tuned to make the impedance of the circuit around 50Ω.

The impedance of the circuit was hence evaluated by measuring S_{11} using an available VNA (R3754B from Advantest [90]), as shown in Fig. 4.13. In order to measure the reflection, a directional coupler was used. The purpose of a directional coupler is to separate the reflected signal when power is going from the input to the output port. Therefore, the tank circuit was connected to the In port of the directional coupler, and the source was connected to the Output port of the coupler. The reflection was obtained from the reflection port, and a transfer function was obtained for the Reflection/Input. This is the S_{11} parameter of the circuit, which was used to get the impedance as Equation 4.34.

$$Z_L = Z_S \cdot \frac{1 + S_{11}}{1 - S_{11}} \tag{4.34}$$

The capacitors were added in parallel iteratively to bring the impedance closer to 50 Ω. Correspondingly, the S_{11} parameter can be fit using the algorithm NLQFIT6 [91, 92] to obtain the loaded and unloaded quality factor of the circuit. In order to see the improvements from using high Q components, the loaded quality factor should be much smaller than the unloaded quality factor. More improvements in tank circuit components manifest as an increased value of the unloaded quality factor.

The quality factor obtained from the fit can be used to estimate the loss of the circuit as $R = \omega L/Q$, and this can be further used to calculate the capacitance, C_{imp} required to match impedance to a source with real impedance R_s [full derivation in Appendix A].

$$C^{imp} = \frac{C}{2RR_s}\left(\sqrt{R(R_s - R)\left(R(R_s - R) + \frac{4L}{C}\right)} - R(R_s - R)\right) \tag{4.35}$$

Using the configuration shown in Fig. 4.13, the S11 parameters for the tank circuit on custom PCB were measured, and are shown in Fig. 4.14. The unloaded and loaded quality factors obtained are 91 and 37, respectively. The impedance at the resonant frequency of 15.914 MHz is measured to be 50.04+0.09j. As can be seen by the plots in Fig. 4.14, this measurement also gives the measurement on resonant frequency, which will be discussed in detail in the next subsection.

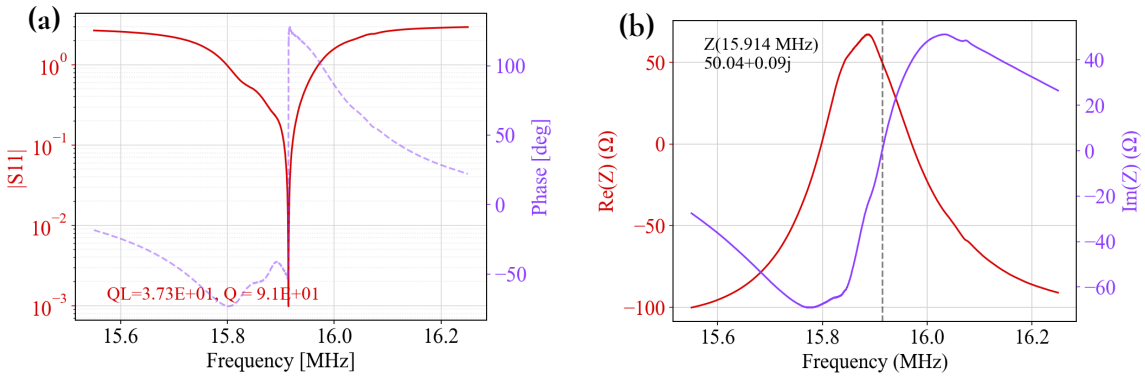

Figure 4.14: The plots show characteristics of the finalised version of the circuit *i.e.,* inductor installed on custom PCB with tuning capacitors. The plots show (a) measured S11 parameter with a minimum absolute value of $9.8 \cdot 10^{-4}$ and (b) the evaluated impedance with best matching of 50.04+0.09j observed at 15.914 MHz, respectively. The plots were made without calibrating the VNA with any standards (open, short, load).

4.4.2 Resonant frequency tuning

The resonant frequency of the circuit should be where the imaginary part of impedance becomes zero, or is minimum (pertaining to just losses), as seen in Fig. 4.14. The resonant frequency of the circuit can be tuned by using a tuning capacitor in parallel to the Pockels cell, as shown in Fig. 4.15. In order not to destroy the quality factor of the tank circuit, a high-quality factor tuning capacitor (AT40HV, from Knowles Voltronics [93]) was used. The tuning capacitor is rated for a voltage of 1 kV and has a quality factor of 2000 at 100 MHz. It offers a tuning range of 1.5-40 pF, which corresponds to a tuning bandwidth of 10 MHz.

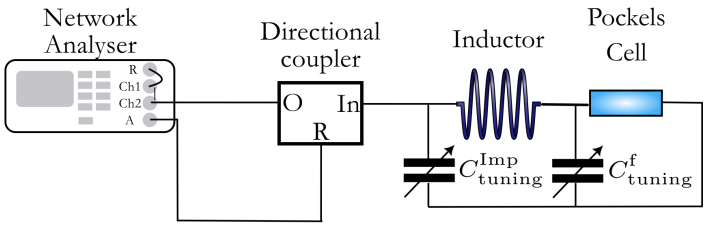

Figure 4.15: Representation of setup to measure the resonant frequency using a network analyser.

Tuning the impedance will sometimes change the resonant frequency, as can be seen using Equation 4.32. It was hence crucial to tune both capacitors to obtain the desired resonant frequency. While the resonant frequency can be evaluated by measuring the transfer function of the Pockels cell, it is not recommended. The probes available in the market have quite a large capacitance value, commonly twice as large as the capacitance of the Pockels cell itself. As such, using any probes across the Pockels cell will disrupt the true resonant frequency, and the capacitance of the probe will dominate the measured frequency.

A workaround is to measure the output of the photodiode in transmission of the Pockels cell as the setup in Fig. 4.16. The resonant frequency was measured optically as well, apart from using the network analyser as mentioned in the previous section. This was to ensure that the circuit's characteristics were preserved while being transferred from the electronics shop to the optical lab (which did not have a network analyser or freedom to tune capacitance by adding new capacitors due to the infeasibility of soldering in a clean room). The photodiode will show maximum signal at the resonant frequency. Additionally, the directional coupler was used to monitor reflection. The impedance could only be evaluated by using a split signal from the waveform generator, and S11 was evaluated without calibration. As such, the S11 parameter was not a true representation of the actual S11 due to differing cable length. However, there was not much difference between the minimum S11 value observed and the resonant frequency, and as such was a reliable way to get the resonant frequency. The resonant frequency can still be ensured to be near the previous estimation by observing the maximum photodiode signal and minimum reflection of the circuit, as shown in Fig. 4.17, which estimates the resonant frequency to be 15.916 MHz. The overall performance of the circuit was also investigated using simulations to understand the losses and the measured quality factor of the circuit, shown in Fig. 4.18.

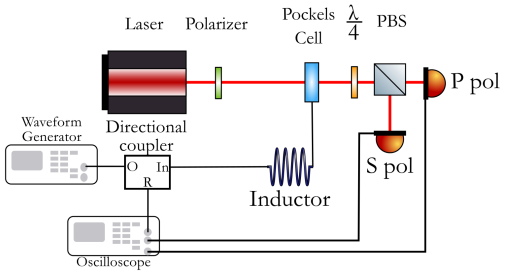

Figure 4.16: The optical setup to measure the response of the Pockels cell during modulation using photodiodes.

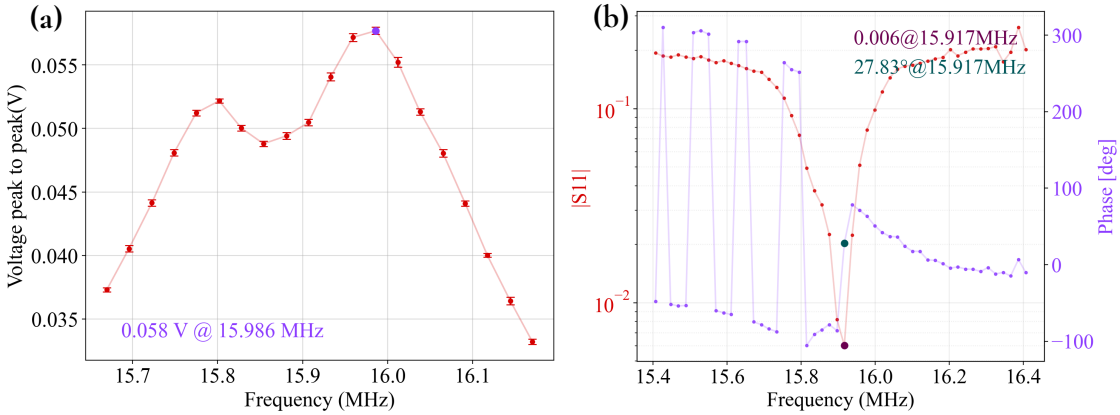

Figure 4.17: The plots show optical, and S11 characterisation with the inductor installed on a custom PCB, without enclosure. The plots show (a) Response of the photodiode at reflection of PBS with voltage modulation provided to the Pockels cell at different frequencies. Although two peaks are seen in the PD signal, there is not much difference in the voltage amplification observed. (b) The measured reflection of the circuit was observed by using the directional coupler signal and a split signal from the waveform source.

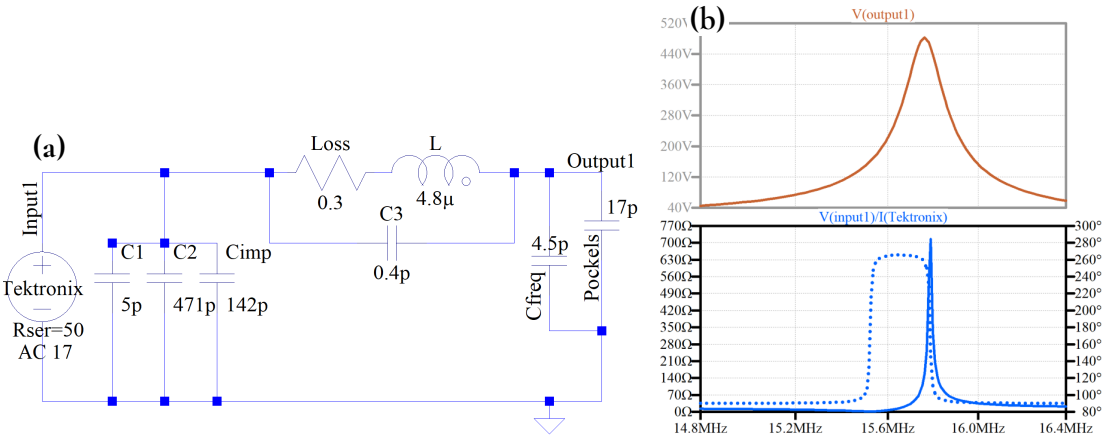

Figure 4.18: (a) Simulation of the tank circuit taking into account the parasitics and losses of the designed components. (b) The estimated voltage and impedance response of the circuit. Such a simulation helped in understanding which losses were dominant and had to be reduced, and for further optimisation towards achieving high voltage. However, it was difficult to incorporate the effect of parasitics and to replicate the exact measured impedance.

4.4.3 Measurement of modulation depth

This optical characteristic to evaluate retardation or the modulation depth was done using setups in Fig. 4.15. Firstly, the transmission response of the Pockels cell was observed by changing the peak-to-peak voltage applied using the waveform generator, indicated using Equation 4.18 in Fig. 4.19a below. Then the transmission characteristics were used to evaluate the generated retardation and the modulation depth, as indicated in Fig. 4.19b and Fig. 4.20 respectively.

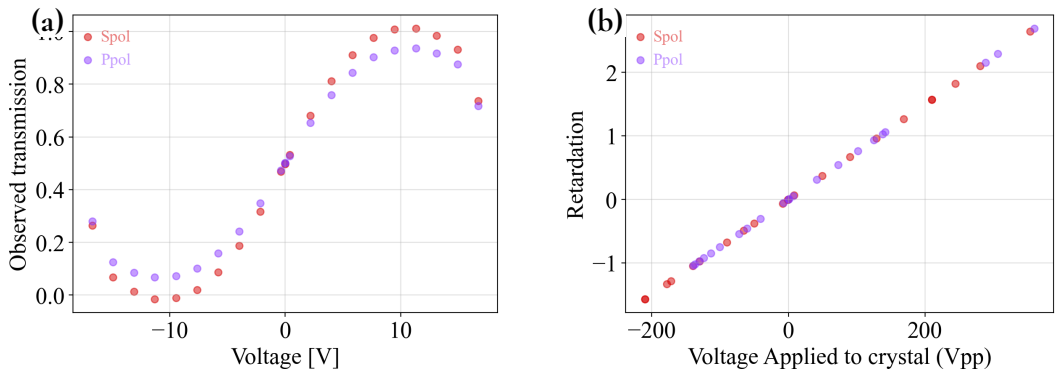

Figure 4.19: The plots show (a) the transmission characteristics were observed at both photodiodes. The signals are shifted by π in their response at the two photodiodes. However, since the transmission is a $\sin^2$ curve, the two responses appear coincidently. (b) The retardation modulation ranging from [-1.5, 2.65] rad and [-1.04, 2.69] rad is observed by PD at Spol and Ppol, respectively. The axisymmetric in retardation seen is due to the ratio in transmission being below 1 or above 1, around the maxima and minima, and should be a matter for future investigations to improve the characterisation.
The plots shown here are measurements of the inductor on a prototype board (which has high parasitic capacitance) without enclosure, as the finalised custom PCB was not tested in time for this thesis. As a result, the impact of PCB is not yet quantified in terms of retardation enhancement.

As can be seen through the characteristics plot, the tank circuit was able to drive the Pockels cell to achieve a large retardation range and modulation depth. The Q of the tank circuit can then be estimated using the observed optical response. The retardation change of $\Gamma = 2.7$ rad is obtained and hence the quality factor can be estimated as,

$$Q = \frac{\Gamma V_\pi}{\pi V_0} = \frac{2.7 * 420}{\pi * 17} \approx 21 \tag{4.36}$$

The final characterisation of retardation, modulation depth and quality factor will be performed in the future using the inductor with the custom PCB (which was also impedance matched), inside an appropriate enclosure. As such, further improvements in the characteristics are anticipated.

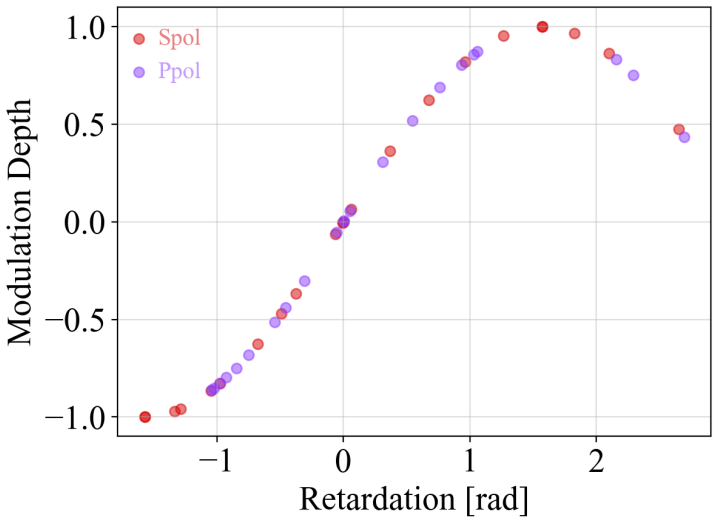

Figure 4.20: The plots here show that the modulation depth of range [-1, 1] is achieved using the Pockels cell during modulation, where maximum modulation occurs when the retardation is $\pi/2$. The measurements here are with the inductor on a prototype board, as the finalised version was not tested in time for this thesis. As a result, the impact of PCB is not yet quantified in terms of retardation enhancement.

In reality, all the above characterisations of the Pockels cell and the development of the circuit were done through several iterations, with back-and-forth between the development of the circuit and the characterisation. The optimisation of the circuit was done to get a large range of retardation modulation from the individual Pockels cells, and also the maximum modulation depth.

4.5 Discussion

The chapter showcases the development of high speed polarization actuator. The research involved the development of a driver circuit for the Pockels cell and its characterisation.

The Pockels cell can be used in lieu of the liquid crystal as PSG and polarisation camera as PSA for birefringence characterisation (shown in Chapter 3). Even though the speed of LC can go upto kHz, the speed of the polarisation camera is limited to Hz due to mechanical rotation. A pair of Pockels cells can generate several arbitrary polarisations required for birefringence characterisation at MHz speed. As such, the previously used polarisation readout based on rotating QWP, can be replaced using a pair of Pockels cells, enabling a much faster response at the readout. Additionally, the pair of LCs can be replaced with the pair of Pockels cells, offering the use of higher laser power (4 W/mm^2) and stability over long periods of time. This will increase the statistics during measurement, and also offer more sensitivity, as

readout from PD in the MHz range and higher laser power helps get rid of several noises. The overall upgraded setup will look as shown in Fig. 4.21 and the birefringence characterisation speed will improve from 60 Hz in Chapter 3 to >10 MHz following the developments in this chapter. The use of a camera instead of PD will offer faster 2D mapping as well.

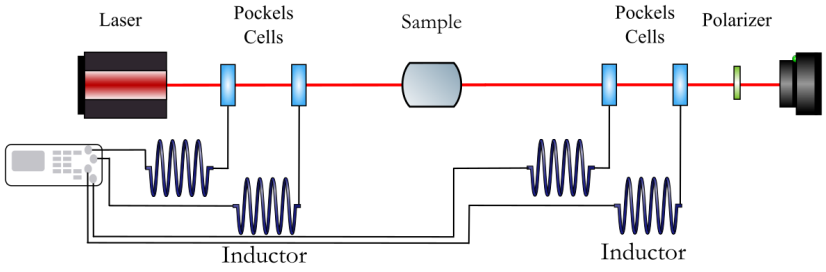

Figure 4.21: The experimental setup for use of PSG and PSA to measure birefringence and birefringence noise

One of the future improvements towards finalised characterisation of Pockels cells would be optical characterisation with a custom PCB inside an enclosure, as well as taking some calibration to take into account the effect of PBS used. Additionally, a total of 4 driver circuits for the Pockels cells would have to be finalised for the configuration mentioned in Fig. 4.21.

There are several intended uses of the developed Pockels cell-based birefringence setup. One of them is to address the issues of low sensitivity for coating's birefringence pointed out in Chapter 3, and use the setup to measure dielectric materials and crystalline materials like AlGaAs. AlGaAs is a candidate material for mirror coatings for future improvements in the detector, as it exhibits low thermal noise [94]. However, due to its crystalline nature, it might exhibit some non-uniform birefringence. It will be interesting to make an investigation into its birefringent nature. Additionally, the upgraded setup will be capable of measuring birefringence fluctuations, which is one of the rising interests in the GW community [48] and will be a promising study to understand its effect in the GW detector.

On the other hand, being able to resolve polarisation at the speed of MHz can give a window to access polarisation information in the detector, such as KAGRA. For instance, the Pockels cell-based PSA can be used inside the detector to observe polarisation and its fluctuation in the sideband of the detector. Moreover, in some later phases, a reference field can be injected with respect to which the birefringence and its fluctuations can also be evaluated in the GW detector.

While Chapter 3 and Chapter 4 summarised efforts on birefringence characterisation, the issue of birefringence will remain. This brings me to the Chapter 5 which elaborates efforts on removing the issues of non-uniform birefringence.

5

Design of compensation plates for GW detector

Contents

In the previous chapter, the focus was on birefringence characterisation. However, the reality is that non-uniform birefringence is a problem that's going to stay for a while unless a breakthrough in the growth process of materials happens. Even though small Sapphire samples are being manufactured with increased uniformity in birefringence, the issue in

big samples remains. The issue will become more prominent for bigger samples of 200 kg intended for use in future detectors like the Einstein Telescope. As of now, no test mass larger in size than 11 cm radius and 15 cm thickness, *i.e.*, KAGRA size, has been characterised. This casts the future into profound uncertainty and raises serious questions about the continued use of crystalline materials. The best way to tackle birefringence is not only by its characterisation but also by developing techniques for compensation. The uniform birefringence compensation method exists, for instance, in the case of lasers [95]; however, non-uniform compensation has not yet been demonstrated and is unexplored. The research mentioned in the following sections sets the stage for a birefringence compensation system applicable for use in a GW detector. A proof-of-principle demonstration was performed showing birefringence compensation at one point, as mentioned in 5.1.1, and resulted in an article *'Birefringence compensation method of test-mass substrates for gravitational wave detectors with arbitrary polarization states'* [59]. Further investigations were done to identify the best possible candidate for the non-uniform birefringence compensation plate compatible for use in the detector.

5.1 Birefringence compensation using polarisation actuators

GW detectors require the use of the laser in one linear polarisation. A compensator that can cancel out the effect of the substrate birefringence and retrieve the linear polarisation can act as a birefringence compensation system. As a result, any polarisation state generator that can encompass a wide range of polarisation will be able to compensate for the birefringence of any sample. For the proof-of-principle demonstration, birefringence compensation was performed for a single spatial point.

5.1.1 1D compensation using a pair of variable retarders

A pair of variable retarder for instance LC, introduced in Chapter 2, offers a large range of polarisation actuation via voltage control. Having a variable retarder at hand, one could generate the polarisation required to correct polarisation changes of the laser passing through ITM. For instance, the linear polarised light can, upon passing through a pair of LCs generate the polarisation such that a linear polarisation is recovered after interaction with ITM. Hence, they can offer a way for birefringence compensation. While birefringence compensation is also possible using some custom wave plate, with non-uniform birefringence opposite to the ITM, they will not be able to offer any actuation for feedback. The non-uniform

birefringence maps of ITMs are obtained in table top experiment, with conditions not the same as those of the interferometer, such as laser power, temperature, and suspension. This could result in some different birefringence characteristics of ITM when used in the detector. Additionally, the laser beam could move on the ITM, thereby changing the birefringence it experiences. Therefore, having a method of active actuation with feedback can also help to correct for any additional offset required during birefringence compensation.

The purpose of this demonstration was to show birefringence compensation at one point of the test mass candidate, shown in Chapter 2, Fig. 2.4, for which the LC setup explained in Chapter 3 was used as,

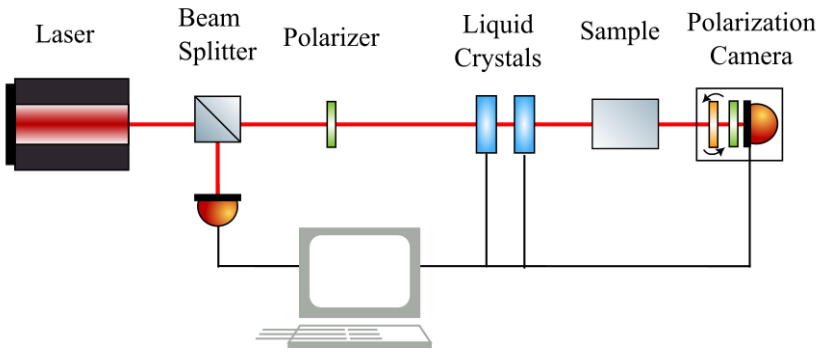

Figure 5.1: The setup for 1D birefringence compensation of a sample (test mass candidate) using a pair of liquid crystals.

A linear polarisation was injected before the pair of LCs. The candidate test mass was inserted between the PSG (pair of LCs) and the PSA (polarisation camera). In the absence of compensation or optimal voltages of the LCs, a non-linear polarisation reaches the polarisation camera due to the birefringence of the test mass around $[X, Y] : [-40, 0]$ cm. The voltages of both LC were scanned from 0-25 V to look for a pair of voltages that resulted in a linear polarisation reaching the PSA. The following plots show that for a particular voltage, the value of rotation and birefringence were minimised.

For these figures, the LC_1 voltage is kept constant at 13.59 V while LC_2 voltage is varying between 1.96 and 2.06 V. These values were chosen so that both residual Δn and θ reach their minimum absolute value for identical voltages applied to the pair of LCs. The data in blue represents measurements with associated error bars from the polarisation camera uncertainty, whereas the red line depicts a linear fit of the data, and the red area represents the 1σ fitting error. The fit gives a residual Δn of $(-2 \pm 8.7) \cdot 10^{-10}$ and residual θ of $(0.2 \pm 1.5) \cdot 10^{-3}$ rad. This shows that the injected polarisation was recovered.

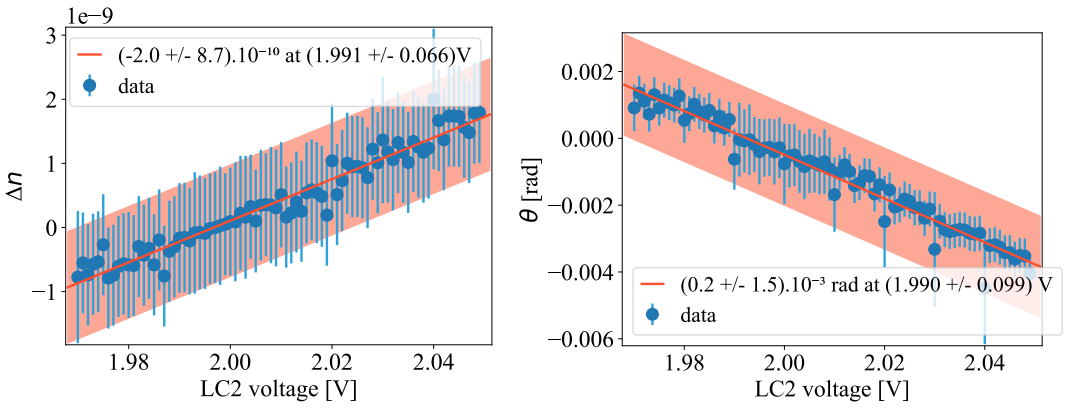

Figure 5.2: The plots showing reduction in the effect of birefringence on linear polarisation, at a fixed voltage of for LC_1 at 13.59 V, while LC_2 voltage varies between 1.97-2.05 V. The voltage of the second LC are scanned to find minima in both Δn and θ simultaneously. The blue dots are measurements, and the orange line is a fit across the measured data. The value of minimum birefringence is shown in the legend. (a) The plot shows residual Δn and the minimum value of $(-2 \pm 8.7) \cdot 10^{-10}$ is observed at 1.991 ± 0.066 V of LC_2. (b) The plot shows residual θ and the minimum value of $(0.2 \pm 1.5) \cdot 10^{-3}$ rad is observed at 1.991 ± 0.066 V of LC_2.

It can be seen from the residual values that the uncertainty is dominated by the polarisation camera error. On the other hand, the LC actuation is limited by its voltage driver resolution (1 mV). From the fitted slope, it is possible to extract the actuation of the pair of LCs on both Δn and θ to be $(3.25 \pm 0.09) \cdot 10^{-8}$ /V and $(-6.55 \pm 0.15) \cdot 10^{-2}$ rad/V. It means that the smallest achievable birefringence actuation is $\Delta n_{min} = (3.25 \pm 0.09) \cdot 10^{-11}$ and $\theta_{min} = (-6.55 \pm 0.15) \cdot 10^{-5}$ rad.

Although in this manuscript the characterisation is shown beforehand, birefringence compensation was the first experiment to be done during the research. In the process of testing the compensation of other materials, we observed that the polarisation produced by the LC is not stable for a few days, and we needed to characterise it every time. In this process, we thought it would be best to have simultaneous (or on-spot) birefringence characterisation for faster actuation. In this way, we will not have to scan around the entire LC voltage range to look for a potential minimisation point.

5.1.2 Improvements required for non-uniform compensation

A compensation system suitable for use in a detector should meet certain requirements. The essence of the system should be to reduce issues due to non-uniform birefringence and not increase trouble.

First of all, the system should be capable of handling the high intensity of the main laser. Electrooptic materials usually has some damage threshold after which they can start lasing.

Other variable retarders like PEM cannot tolerate too high laser power either. Additionally, PEM is difficult to manufacture for a 2D polarisation control, as it would require several stress inducers, arranged in a closed space.

Secondly, the compensation system should not cause too much loss from scattering or absorption. Transparent LCs are known to be very lossy, sometimes going as high as 98% [59]. However, optical components used in GW detectors, especially in front of ITM, are required to meet the stringent loss requirements. The loss requirement for KAGRA ITM itself is 50 ppm/cm, so the compensation plate loss should be carefully considered. On the other hand, electrooptic requires an array of electrodes for 2D control. The presence of such a configuration for a reflecting style array of electrooptics may not be an issue. However, the electrodes can cause trouble for a transparent style electro-optics array. The use of a reflecting style electrooptics might be too cumbersome to be incorporated as a compensation system before the ITM. The electrodes can cause scattering or wavefront distortion. It is also difficult to manufacture an array of electrooptics large enough to actuate the large-sized laser beam as in a detector.

From these few points in mind, it is evident that it is not feasible to share the optical path of either the actuators or the compensation plate with the main laser beam at the same time. This gives rise to the requirement of a variable retarder, which is not lossy, and whose actuators can be placed far from the material itself. Such a variable retarder can be a temperature-controlled one. Instead of using voltage or stress directly induced on some material, a temperature change can be used for actuation. The temperature change can be provided by projecting a CO_2 laser on a suitable material, which has high absorption for the CO_2 laser. As a result of this absorption, the material will go temperature change, and offer a mechanism for polarisation control.

5.2 Design of compensation plate for GW Detector

The preliminary phase of the design involved looking for the best material to serve as a candidate for the compression plate. While the main idea in mind was to look for a uniaxial crystal, several other parameters needed to be correctly estimated to understand the range of retardation that can be achieved using a given laser intensity. For this purpose, a detailed Finite Element Modelling (FEM) was done to estimate the behaviour of the material exposed to a certain CO_2 laser intensity.

5.2.1 Temperature-controlled variable retarder

Temperature change of a material can cause several changes in the material, for instance, physical deformation or refractive index change. The physical change depends on several properties of the material, such as thermal conductivity, absorption coefficient, and elastic constants, which can then induce changes in the incident polarisation state. A PSG that can produce a change in polarisation state by some induced temperature change can be regarded as a thermally actuated PSG. An easy way to change the temperature of a material is with the use of an appropriate wavelength that can be absorbed efficiently by the material. For our case of application, a CO_2 laser of wavelength around 10 μm is a convenient candidate for heating the material. Previously, CO_2 laser has also been used in GW detectors for thermal compensation [96], and so they are an optimal wavelength candidate for use. The material can be heated, and the main laser beam will experience birefringence in the configuration as shown in Fig. 5.3.

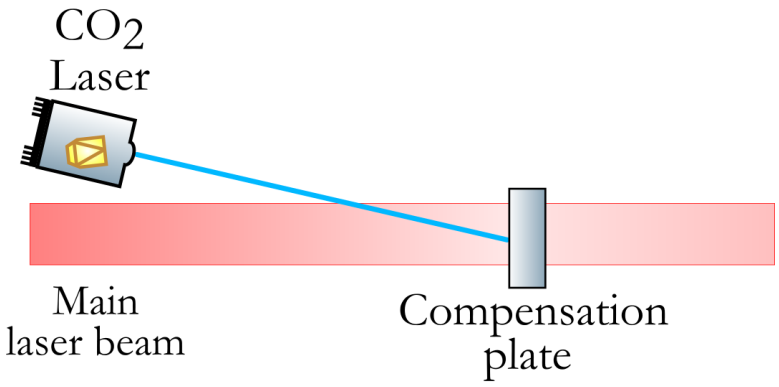

Figure 5.3: Illustration of heating a material using a CO_2 laser to make the temperature change and induce phase change for the main laser. While during the experiment, the CO_2 laser will be incident at some angle ($\neq 90°$), for the simulation of optimal material, the CO_2 laser was chosen to be incident at normal incidence.

The first task was to identify a material that can act as an efficient variable retarder with an accessible CO_2 laser power. The required ΔT for several materials was predicted using FEM in COMSOL. The analysis was then used to estimate the laser power required to generate a range of $0 - 2\pi$ retardation without too high a requirement of CO_2 power. The following sections describe the temperature-induced retardation properties.

5.2.1.1 Thermorefractive effect

Upon a change in temperature of any material, the refractive index of the material can deviate from that at room temperature. The variation of refractive index with temperature at constant pressure is called the thermo-optic coefficient, γ [97]. It can be expressed as $\frac{dn}{dT} = \gamma$.

The corresponding change in optical path length can then be obtained by integrating the response across the propagation axis or thickness,

$$\Delta OPL_{TR} = \gamma \int_L \Delta T \, dL \tag{5.1}$$

The thermo-refractive retardation response can be written as a response for only the change in refractive index,

$$\Gamma_{TR} = \frac{2\pi}{\lambda} \cdot [\gamma_e - \gamma_o] \cdot \Delta T \cdot L = \frac{2\pi}{\lambda} \cdot \frac{d\Delta n}{dT} \cdot \Delta T \cdot L \tag{5.2}$$

5.2.1.2 Thermoelastic effect

The temperature change also causes a change in the material's thickness, *i.e.,* thermal expansion. The thermo-elastic response accounts for the change in phase due to thermal expansion. This change can be depicted as the bulging of the first and back faces inwards or outwards, depending on the expansion coefficients.

The displacement field vector, w in $\hat{z}$ direction, can be used to obtain the total change in the thickness of the material, as the sum of the motion or displacement w_f of its front face and w_b of its back face. Consequently, the thermoelastic retardation response can be written as,

$$\Gamma_{TE} = \frac{2\pi}{\lambda} \cdot \Delta n \Delta L = \frac{2\pi}{\lambda} \cdot \Delta n |w_f - w_b| \tag{5.3}$$

5.2.1.3 Photoelastic Effect

The change of refractive index caused by stress is called the photoelastic response. The absorption of a temperature-inducing laser causes a change in the physical properties and consequently adds some stress on the crystal. The presence of some stress or strain leads to a corresponding change in the shape, size, and orientation of the indicatrix [41].

The change in the relative dielectric impermeability under an applied stress σ_{kl} or strain ϵ_{rs}, and can be expressed using the π_{ijkl}, the piezooptic coefficients, or p_{ijrs}, the elastooptic coefficients. [41]

$$\Delta B_{ij} = \pi_{ijkl} \sigma_k l = p_{ijrs} \epsilon_{rs} \tag{5.4}$$

The piezo-optical coefficients and elasto-optical coefficients are related to each other using the elasticity matrix c_{klrs}, the relation $p_{ijrs} = \pi_{ijkl} c_{klrs}$. Since the number of independent coefficients is reduced due to symmetry, it is possible to represent B_{ij} with only one suffix, as [41],

$$\begin{pmatrix} B_{11} & B_{12} & B_{13} \\ B_{21} & B_{22} & B_{23} \\ B_{31} & B_{32} & B_{33} \end{pmatrix} \longrightarrow \begin{pmatrix} B_1 & B_6 & B_5 \\ B_6 & B_2 & B_4 \\ B_5 & B_4 & B_3 \end{pmatrix} \tag{5.5}$$

Correspondingly, the coefficient π_{ijkl} can be represented as π_{ij}. The matrix equation can then be written in simplified form as [41],

$$\begin{aligned} \Delta B_i &= \pi_{ij}\sigma_j \\ \begin{pmatrix} \Delta B_1 \\ \Delta B_2 \\ \Delta B_3 \\ \Delta B_4 \\ \Delta B_5 \\ \Delta B_6 \end{pmatrix} &= \begin{pmatrix} \pi_{11} & \pi_{12} & \pi_{13} & \pi_{14} & \pi_{15} & \pi_{16} \\ \pi_{21} & \pi_{22} & \pi_{23} & \pi_{24} & \pi_{25} & \pi_{26} \\ \pi_{31} & \pi_{32} & \pi_{33} & \pi_{34} & \pi_{35} & \pi_{36} \\ \pi_{41} & \pi_{42} & \pi_{43} & \pi_{44} & \pi_{45} & \pi_{46} \\ \pi_{51} & \pi_{52} & \pi_{53} & \pi_{54} & \pi_{55} & \pi_{56} \\ \pi_{61} & \pi_{62} & \pi_{63} & \pi_{64} & \pi_{65} & \pi_{66} \end{pmatrix} \begin{pmatrix} \sigma_{11} \\ \sigma_{22} \\ \sigma_{33} \\ \sigma_{23} \\ \sigma_{13} \\ \sigma_{12} \end{pmatrix} \end{aligned} \tag{5.6}$$

Then we can get the new coefficients as [41],

$$B'_i = B_i + \Delta B_i = 1/n_i^2 \tag{5.7}$$

While the dielectric impermeability tensor B_{ij} is a symmetric tensor, we can obtain the change it introduces to the axis of the material by transforming the stress tensor to its principal axes, as [41],

$$\begin{pmatrix} B'_1 & B'_6 & B'_5 \\ B'_6 & B'_2 & B'_4 \\ B'_5 & B'_4 & B'_3 \end{pmatrix} \longrightarrow \begin{pmatrix} B''_1 & 0 & 0 \\ 0 & B''_2 & 0 \\ 0 & 0 & B''_3 \end{pmatrix} \tag{5.8}$$

In the case when the B tensor is not aligned along its principal axes, we will have to estimate the fast axis orientation change. In this case, we can estimate the B components along its principal axis orientation. This can be done by rotating the tensor about the axis x_3 through an angle θ measured from axis x_1 towards x_2. Following the convention of transforming to principal axes using the Mohr circle, we get (for $B_1 > B_2$), [41]

$$\begin{aligned} \frac{1}{n''^2_1} = B''_1 &= \frac{1}{2}\left((B'_1 + B'_2) + \sqrt{(B'_2 - B'_1)^2 + 4B'^2_6}\right) \\ \frac{1}{n''^2_2} = B''_2 &= \frac{1}{2}\left((B'_1 + B'_2) - \sqrt{(B'_2 - B'_1)^2 + 4B'^2_6}\right) \\ \tan 2\theta &= \frac{2 \cdot B'_6}{B'_1 - B'_2} \end{aligned} \tag{5.9}$$

It can be seen from the above equation that if the tensor is aligned along the principal axes, then $B'_6 = 0$ and this will make $B''_1 = B'_1$ and $B''_2 = B'_2$. For such a case, it can be seen that $\theta = 0$, which indicates the principal axis orientation case. The birefringence

for light travelling along x_3 *i.e.*, a axis (for our purpose) is then calculated as, $\Delta n_\epsilon = \Delta n_1'' - \Delta n_2''$. During the FEM analysis $B_6'^2 \approx 10^{-11}$. Hence, it was assumed that all tensors were aligned along their principal axes.

5.2.1.4 Total temperature dependent response

The deviation from the room temperature optical path length change will cause the light to undergo a retardation change, which can be expressed as the sum of thermo-refractive, thermo-elastic, and photoelastic responses. For simplification, the birefringence due to change in temperature ΔT and strain ϵ, can be written in terms of thermorefractive, thermoelastic, and photoelastic response as,

$$\begin{aligned}\Gamma' &= \Gamma + (k\,\Delta n\,L)' \\ &= \underbrace{\Gamma}_{\text{static}} + \underbrace{k\,\frac{d\Delta n}{dT}\,\Delta T\,L}_{\text{thermorefractive bire.}} + \underbrace{k\,\Delta n\,\frac{dL}{dT}\,\Delta T}_{\text{thermoelastic bire.}} + \underbrace{k\,\Delta n_\epsilon\,L}_{\text{photoelastic bire.}}\end{aligned} \tag{5.10}$$

where L is the thickness of the material, and k is the wave vector. The relative phase change in the main laser due to the heating now becomes

$$\begin{aligned}\Delta\Gamma' &= \Gamma_{TR} + \Gamma_{TE} + \Gamma_{PE} \\ &= \frac{2\pi}{\lambda} \cdot [(\gamma_e - \gamma_o) \cdot \Delta T \cdot L + \Delta n \cdot \Delta L + \Delta n_\epsilon L]\end{aligned} \tag{5.11}$$

To only have contribution from the temperature-induced birefringence, we can estimate the thickness that will make the room temperature birefringence an integer multiple, i of 2π. As such, it can be regarded as a 0 phase change.

$$L = \frac{i \cdot \lambda}{\Delta n} \tag{5.12}$$

The thermo-refractive and thermo-elastic birefringence responses produced are multiples of the laser intensity used for the initial simulation (0.1 W/mm^2). We can approximate the birefringence for any laser power using a simple unitary method. If an intensity of 0.1 W/mm^2 laser produces a Γ_{TR} and Γ_{TE} (neglecting photoelastic response), then a multiple i of 0.1 W/mm^2 laser will produce the following birefringence

$$\Gamma = i \cdot 0.1 \cdot \Gamma_{TR} + i \cdot 0.1 \cdot \Gamma_{TE} \tag{5.13}$$

The thermorefractive and thermoelastic birefringence have a sign, plus or minus, depending on their coefficients. The sum should therefore be calculated with the respective sign in consideration.

5.2.2 Candidate material

Before doing the simulation, we looked for materials that have a substantial difference in extraordinary and ordinary coefficients for thermal expansion and thermo-optic. This will create a good enough change in phase upon a change of temperature. We also take into consideration the absorption coefficient of the materials for the CO_2 laser, as these changes will be driven by the absorption. Too low a value will not cause enough temperature change, whereas too high an absorption coefficient will cause temperature change in an extremely small thickness of the material, and will not produce enough phase change, due to less optical path length. Keeping this in mind, a few materials were first shortlisted, and their characteristics are listed below.

5.2.2.1 Material Properties

There were mainly two classes of uniaxial crystals, trigonal and tetragonal, studied. The trigonal crystal namely: αBBO, $CaCO_3$ (Calcite), Al_2O_3 (Sapphire), αSiO_2 (Quartz) and tetragonal crystals namely: YVO_4, TiO_2 (Rutile), and MgF_2, were explored. This wide range of crystals with properties summarised in the following tables, was analysed using FEM.

Material		αBBO	$CaCO_3$	Al_2O_3	αSiO_2
Crystal		Hexagonal [98]	Trigonal [99]	Trigonal[100]	Trigonal [101]
Density [g/cm^3]		3.85 [98]	2.7 [99]	3.98 [100]	2.65 [101]
Elasticity [GPa]	C_{11}	118.8	137	452	86.8
	C_{12}	54.9	45.6	150	7
	C_{13}	27.2 [102]	45.1 [103]	107 [104]	11.8 [105]
	C_{14}	−4.9	−20.8	20	−18
	C_{33}	41.8	79.7	454	105.4
	C_{44}	6.42	34.2	132	58.2
ElastoOptic [TPa^{-1}]	π_{11}	1.58	−0.784	−0.117	1.091
	π_{12}	2.08	0.705	1.563	2.963
	π_{13}	−4.3	2.716	0.344	2.108
	π_{14}	−14.22 [106]	−1.636 [107]	0.035 [108]	−1.094 [109]
	π_{31}	1.5	1.145	2.265	3.058
	π_{33}	−7.24	0.400	−0.977	0.264
	π_{41}	2.85	−1.230	0.616	−1.040
	π_{44}	−24.58	−2.949	−3.353	−2.001

Table 5.1: Mechanical Properties of trigonal material in untransformed configuration.

Material		YVO_4	TiO_2	MgF_2
Crystal		Tetragonal [110]	Tetragonal [111]	Tetragonal [112]
Density [g/cm^3]		4.22 [110]	2.7 [111]	3.177 [112]
Elasticity [GPa]	C_{11}	250.96	267.3	452
	C_{12}	46.3	174.1	150
	C_{13}	83.59 [113]	146.4 [114]	107 [115]
	C_{33}	323.03	483.9	20
	C_{44}	16.88	123.8	454
	C_{66}	49.88	190.4	132
Elastooptic [TPa^{-1}]	π_{11}	0.735	−0.367	3.069
	π_{12}	0.476	1.049	0.938
	π_{13}	−0.091	−0.496	−4.447
	π_{31}	21.646 [113]	−0.206 [116]	1.829 [117]
	π_{33}	−11.098	0.007	−4.061
	π_{44}	1.955	−0.01	1.367
	π_{66}	−1.564	−0.326	0.468

Table 5.2: Mechanical Properties of Tetragonal crystal in untransformed configuration.

Material		αBBO	$CaCO_3$	Al_2O_3	αSiO_2
Heat Capacity [J/g/K]		0.49 [98]	0.852 [99]	0.761 [118]	0.742 [119, 120]
Thermal Conductivity κ [w/m/K]	$\perp_C$	1.25 [121]	3.2 [122]	7 [118]	23.1 [122]
	$\parallel_C$	1.65	3.65	10.4	25.2
Thermal Optic γ [10^{-6} /K]	$\perp_C$	-8 [123]	1.514 [97]	-13.6 [97]	12.29 [97]
	$\parallel_C$	-2	12.217	-15.5	14.7
Thermal expansion α [10^6 /K]	$\perp_C$	0.9 [124]	-5.8 [97]	8.98 [97]	7.15 [97]
	$\parallel_C$	36.3	25.6	6.87	6.65

Table 5.3: Temperature Dependent Properties of Trigonal Crystals

Material		YVO_4	TiO_2	MgF_2
Heat Capacity [J/g/K]		0.556 [125]	0.71128 [111]	1.003 [112]
Thermal Conductivity κ [w/m/K]	$\perp_C$	9 [126]	7 [127, 128]	33.6 [129]
	$\parallel_C$	12	10.4	21
Thermal Optic γ [10^{-6} /K]	$\perp_C$	13.8 [130]	-13.6 [97]	0.88 [97]
	$\parallel_C$	8	-15.5	0.32
Thermal Expansion α [10^6 /K]	$\perp_C$	2 [130]	-5.8 [97]	9.4 [97]
	$\parallel_C$	8.5	25.6	13.7

Table 5.4: Temperature Dependent Properties of Tetragonal crystal

Material		αBBO	$CaCO_3$	Al_2O_3	αSiO_2
Sellmeier [λ in μm] $n^2 = A_0 + \sum_i \frac{A_i}{\lambda^2 - B_i} - D\lambda^2 + \sum_i \frac{E}{\lambda^{2i}}$	A_0^o	2.7471	2.69705	1	2.3573
	A_1^o	0.01878	0.0192064	$1.4313493\lambda^2$	0.01170
	B_1^o	0.01822	0.01820	0.0726631^2	0
	A_2^o	-	-	$0.65064713\lambda^2$	-
	B_2^o	-	-	0.1193242^2	-
	A_3^o	-	-	$5.3414021\lambda^2$	-
	B_3^o	-	-	18.0258251^2	-
	D^o	0.01354	0.0151624	-	-
	E_1^o	-	-	-	-
	E_2^o	-	-	-	1.34141E−4
	E_3^o	-	-	-	4.4537E−7
	E_4^o	-	-	-	5.92361E−8
	A_0^e	2.3174 [131]	2.18438 [132]	1 [133]	2.3849 [101]
	A_1^e	0.01224	0.0087309	$1.5039759\lambda^2$	0.01259
	B_1^e	0.01667	0.01018	0.0740288^2	0
	A_2^e	-	-	$0.55069141\lambda^2$	-
	B_2^e	-	-	0.1216529^2	-
	A_3^e	-	-	$6.5927379\lambda^2$	-
	B_3^e	-	-	20.072248^2	-
	D^e	0.01516	0.0024411	-	-
	E_1^e	-	-	-	0.01079
	E_2^e	-	-	-	1.6518E−4
	E_3^e	-	-	-	1.9474E−6
	E_4^e	-	-	-	9.3648E−8
Absorption coefficient 10 μm β [$/cm$]		87 [134]	67.7 [135]	8000 [136]	628.3 [137]
Absorption coefficient 1 μm β [$/cm$]			<0.01 [135]	2513† [138] $11 \cdot 10^{-6}$ [139]	

Table 5.5: Wavelength-dependent Properties of a trigonal crystal.
†: The old value is shown to understand the improvement in absorption of Sapphire achieved through several years of research.

Material		YVO_4	TiO_2	MgF_2
Sellmeier [λ in μm] $n^2 = A_0 + \sum_i \frac{A_i}{\lambda^2 - B_i} - D\lambda^2 + \sum_i \frac{E}{\lambda^{2i}}$	A_0^o	3.77834	5.913	1
	A_1^o	0.069736	$2.441E15$	$0.48755108\lambda^2$
	B_1^o	0.04724	$0.803E15$	0.04338408^2
	A_2^o	-	-	$0.39875031\lambda^2$
	B_2^o	-	-	0.09461442^2
	A_3^o	-	-	$2.3120353\lambda^2$
	B_3^o	-	-	23.793604^2
	D^0	0.0108133 [140]	- [141]	- [142]
	A_0^e	4.59905	7.197	1
	A_1^e	0.110534	$3.322E15$	$0.41344023\lambda^2$
	B_1^e	0.04813	$0.843E15$	0.03684262^2
	A_2^e	-	-	$0.50497499\lambda^2$
	B_2^e	-	-	0.09076162^2
	A_3^e	-	-	$2.4904862\lambda^2$
	B_3^e	-	-	23.771995^2
	D^e	0.0122676	-	-
Absorption coefficient 10 μm β [$/cm$]		4.605†	1884.6 [143]	15.1 [144]
Absorption coefficient 1 μm β [$/cm$]			<0.0001 [143]	4.3E-16 [145]

Table 5.6: Wavelength-dependent Properties of Tetragonal crystal. † This value was inferred from 20 dB transmission attenuation since no direct absorption data was available at 10 μm.

5.2.2.2 Optical axis and Crystal orientation

The crystalline materials used in this thesis typically have three axes. Since all of them are uniaxial, the properties of the two axes *a* and *b* are the same. In the case of Sapphire, the optic axis in the GW detector is aligned with the *c* axis. This makes the material non-birefringent for the incoming laser. For the case of birefringence correction actuators, it is desirable to have the optic axis aligned along the *a* or *b* axis. Throughout this manuscript, the laser is propagating along the *a* axis of the thermal actuator. This is shown in a simplified representation using Fig. 5.4.

However, there are certain transformations required to properly perform the FEM in this orientation. There is an important difference between the stress tensor and all other second-rank tensors. Tensors that measure crystal properties, such as permittivity and

magnetic susceptibility, represented by quadrics, have definite orientation within a crystal. Such tensors are called *matter tensor* as they must conform to a crystal symmetry. On the other hand, the stress (strain) tensor can have any orientation within the crystal. They can exist in both isotropic bodies and anisotropic bodies. The stress tensor does not represent a crystal property but is akin to a force impressed on the crystal [41]. Such tensors are called *field tensors*. It is therefore necessary to keep in mind the respective rules to perform the transformation on the different categories of matter or field tensors.

5.2.2.2.1 Elasticity matrix transformation

Elasticity is a centrosymmetric property. Due to symmetry, the representation simplifies to two suffixes; however, the values c_{ij} inside the elasticity matrix are not the components, and so they do not transform like components of a second rank tensor. In order to transform them to other axes, it is necessary to use the tensor notation. The same transformation method is for the photoelastic matrix; however, owing to different symmetry rules, the value of the transformed matrix for each class of crystals is different.

To transform the elasticity matrix, the stress and strain components are written with a single suffix using numbers from 1 to 6.

Tensor notation	11	22	33	23, 32	31, 13	12, 21
Matrix notation	1	2	3	4	5	6

The elasticity matrix defined is in the orientation $[a, b, c] = [x, y, z]$. For our case, we want it to be in the orientation of $[c, b, a]$ or [100]. For this, we have to transform our elasticity tensor following some symmetry arguments.

The desired transformation is to have a crystal orientation as shown in Fig. 5.4. This would require a change as,

$$1 \to -3, \;\; 2 \to 2, \;\; 3 \to 1 \tag{5.14}$$

Hence, in the four-suffix notation, the pairs of suffixes transform as follows:

$$11 \to 33, \; 22 \to 22, \; 33 \to 11, \; 23 \to 21, \; 31 \to -13, \; 12 \to -32 \tag{5.15}$$

In the two-suffix notation, the transformation will look as:

$$1 \to 3, \; 2 \to 2, \; 3 \to 1, \; 4 \to 6, \; 5 \to -5, \; 6 \to -4 \tag{5.16}$$

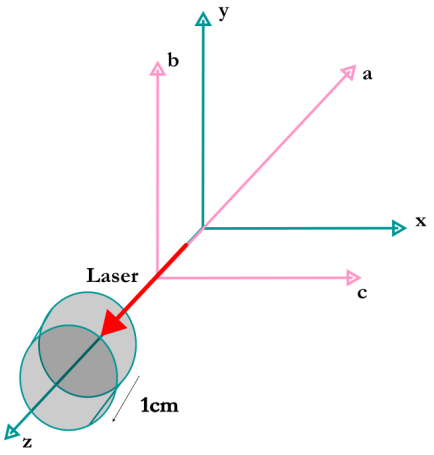

Figure 5.4: Crystal Orientation, where a axis of crystal is along $-z$ and laser is propagating along z axis.

The Equation 5.16 is then used to change the matrix. Following the above transformation, the matrix will change as Equation 5.17

$$\begin{bmatrix} C_{11} & C_{12} & C_{13} & C_{14} & C_{15} & C_{16} \\ & C_{22} & C_{23} & C_{24} & C_{25} & C_{26} \\ & & C_{33} & C_{34} & C_{35} & C_{36} \\ & & & C_{44} & C_{45} & C_{46} \\ & & & & C_{55} & C_{56} \\ & & & & & C_{66} \end{bmatrix} \longrightarrow \begin{bmatrix} C_{33} & C_{32} & C_{31} & C_{36} & -C_{35} & -C_{34} \\ & C_{22} & C_{21} & C_{26} & -C_{25} & -C_{24} \\ & & C_{11} & C_{16} & -C_{15} & -C_{14} \\ & & & C_{66} & -C_{65} & -C_{64} \\ & & & & C_{55} & C_{54} \\ & & & & & C_{44} \end{bmatrix} \tag{5.17}$$

Each matrix class follows different rules of symmetry. For the tetragonal matrix, the symmetry rules bring the 21 degrees of freedom to 6. Hence the coefficients following symmetry are, $C_{11} = C_{22}$, $C_{13} = C_{23}$, $C_{44} = C_{55}$ and $C_{16} = -C_{26}$. This makes the representation as

$$\begin{bmatrix} C_{11} & C_{12} & C_{13} & 0 & 0 & C_{16} \\ & C_{11} & C_{13} & 0 & 0 & -C_{16} \\ & & C_{33} & 0 & 0 & 0 \\ & & & C_{44} & 0 & 0 \\ & & & & C_{44} & 0 \\ & & & & & C_{66} \end{bmatrix} \tag{5.18}$$

For trigonal matrix, the symmetry rules bring the 21 degrees of freedom to 6. Hence the coefficients following symmetry are, $C_{11} = C_{22}$, $C_{13} = C_{23}$, $C_{14} = -C_{24}$, $C_{15} = -C_{25}$, $C_{46} = C_{25}$,$C_{44} = C_{55}$, $C_{56} = C_{14}$and $C_{66} = 2(C_{11} - C_{13})$. This makes the representation as

$$\begin{bmatrix} C_{11} & C_{12} & C_{13} & C_{14} & C_{15} & 0 \\ & C_{11} & C_{13} & -C14 & -C_{15} & 0 \\ & & C_{33} & 0 & 0 & 0 \\ & & & C_{44} & 0 & C_{25} \\ & & & & C_{44} & C_{14} \\ & & & & & C_{66} \end{bmatrix} \tag{5.19}$$

5.2.2.2.2 Photoelastic matrix Transformation

The elastic tensor follows several rules of symmetry, which reduce its degrees of freedom, depending on the crystal class. However, the photoelastic tensor is generally not symmetric. Both piezo-optic π and photoelastic tensor p have 36 independent components. In the general representation, the units of piezooptic constant and photoelastic constant are TPa^{-1} and unitless, respectively [107]. They are defined in the orientation $[a, b, c = x, y, z]$. For our case, we want it to be in the orientation of $[c, b, a]$ or [100].

The desired transformation is for configuration in Fig. 5.4 and is similar to the elasticity matrix transformation. However, the piezooptic matrix does not obey the same symmetry arguments as the elasticity matrix and hence several coefficient needs to be redefined. The Equation 5.16 is then used to change the matrix. Following the above transformation, the matrix will change as Equation 5.20

$$\begin{bmatrix} \pi_{11} & \pi_{12} & \pi_{13} & \pi_{14} & \pi_{15} & \pi_{16} \\ \pi_{21} & \pi_{22} & \pi_{23} & \pi_{24} & \pi_{25} & \pi_{26} \\ \pi_{31} & \pi_{32} & \pi_{33} & \pi_{34} & \pi_{35} & \pi_{36} \\ \pi_{41} & \pi_{42} & \pi_{43} & \pi_{44} & \pi_{45} & \pi_{46} \\ \pi_{51} & \pi_{52} & \pi_{53} & \pi_{54} & \pi_{55} & \pi_{56} \\ \pi_{61} & \pi_{62} & \pi_{63} & \pi_{64} & \pi_{65} & \pi_{66} \end{bmatrix} \longrightarrow \begin{bmatrix} \pi_{33} & \pi_{32} & \pi_{31} & \pi_{36} & -\pi_{35} & -\pi_{34} \\ \pi_{23} & \pi_{22} & \pi_{21} & \pi_{26} & -\pi_{25} & -\pi_{24} \\ \pi_{13} & \pi_{12} & \pi_{11} & \pi_{16} & -\pi_{15} & -\pi_{14} \\ \pi_{63} & \pi_{62} & \pi_{61} & \pi_{66} & -\pi_{65} & -\pi_{64} \\ -\pi_{53} & -\pi_{52} & -\pi_{51} & -\pi_{56} & \pi_{55} & -\pi_{54} \\ -\pi_{43} & -\pi_{42} & -\pi_{41} & -\pi_{46} & \pi_{45} & \pi_{44} \end{bmatrix} \tag{5.20}$$

The piezooptic matrix and photoelastic matrix follow the same rules of symmetry (with exceptions for a few coefficients). Each matrix class follows different rules of symmetry. For a tetragonal symmetry, the 36 degrees of freedom are reduced to 7. For tetragonal matrix symmetry $\pi_{11} = \pi_{22}$, $\pi_{12} = \pi_{21}$, $\pi_{13} = \pi_{23}$, $\pi_{31} = \pi_{32}$, $\pi_{44} = \pi_{55}$. This makes the representation as [41],

$$\begin{bmatrix} \pi_{11} & \pi_{12} & \pi_{13} & 0 & 0 & 0 \\ \pi_{12} & \pi_{11} & \pi_{13} & 0 & 0 & 0 \\ \pi_{31} & \pi_{31} & \pi_{33} & 0 & 0 & 0 \\ 0 & 0 & 0 & \pi_{44} & 0 & 0 \\ 0 & 0 & 0 & 0 & \pi_{44} & 0 \\ 0 & 0 & 0 & 0 & 0 & \pi_{66} \end{bmatrix} \tag{5.21}$$

For a trigonal matrix, the 36 degrees of freedom reduce to 8. For trigonal matrix symmetry $\pi_{11} = \pi_{22}, \pi_{12} = \pi_{21}, \pi_{13} = \pi_{23}, \pi_{14} = -\pi_{24} = \pi_{65}, \pi_{31} = \pi_{32}, \pi_{41} = -\pi_{42}, \pi_{44} = \pi_{55}$, $\pi_{56} = 2\pi_{41}$and $\pi_{66} = (\pi_{11} - \pi_{12})$. The only difference with an elastooptic matrix is that the coefficients are $p_{56} = p_{41}$and $p_{66} = 0.5(p_{11} - p_{12})$. This makes the representation as [41],

$$\begin{bmatrix} \pi_{11} & \pi_{12} & \pi_{13} & \pi_{14} & 0 & 0 \\ \pi_{12} & \pi_{11} & \pi_{13} & -\pi_{14} & 0 & 0 \\ \pi_{31} & \pi_{31} & \pi_{33} & 0 & 0 & 0 \\ \pi_{41} & -\pi_{41} & 0 & \pi_{44} & 0 & 0 \\ 0 & 0 & 0 & 0 & \pi_{44} & 2\pi_{41} \\ 0 & 0 & 0 & 0 & \pi_{14} & \pi_{66} \end{bmatrix} \tag{5.22}$$

With all the properties of crystals in place, the method of FEM can be understood using the following section.

5.3 Finite Element Modelling of materials

To find the best material candidate for the compensation plate, we need to check the range of retardation change a given material can produce with a given amount of heat. In order to estimate the value of ΔT, ΔL, and ϵ for any material upon which the CO_2 laser is incident, we need to solve the partial differential equation involving the finite element analysis. This was achieved by using three modules in COMSOL. One to simulate the laser incident on the compensation plate, one to simulate the heat distribution of the plate due to the absorption of the laser, and one to simulate the change in physical dimensions of the plate. The three modules hence used were 'Radiative beam in absorbing media', 'Heat transfer in solids', and 'Solid Mechanics'. Additionally, multiphysics coupling was used between the 'radiative beam in absorbing media' and 'heat transfer in solids', resulting in 'absorption'. Also, another multiphysics coupling was used between the 'heat transfer' and 'Solid mechanics', resulting in 'thermal expansion'. The corresponding details of the analysis are described in the following sections.

5.3.1 Radiative beam in absorbing media

This physics module is found under the 'Heat Transfer < Radiation' branch. The equation in this module is used to model the attenuation of an incident light when passing through a material due to absorption. The feature node of 'Incident Intensity' was used to simulate the laser beam. This module works under the assumption that the beam is collimated throughout the material. Additionally, each beam is assumed to propagate in the same

direction. Light experiences no refractions, reflection, or scattering within the material itself. No significant emission of material in the wavelength range of the incident light, for laser beams whose wavelength is in general much shorter than that of the radiation emitted by the medium [146, 147, 148].

The face at position z=0 was selected as the face for the incident intensity. The rest of the boundary was selected at the transparent surface. The intensity at any given point can be expressed as [146, 147, 148],

$$I_i = P_o \cdot f(o, e) \tag{5.23}$$

where P_o is the deposited beam power on the incident surface. The beam orientation is given by the normalised vector e, which was selected to be along the z-axis propagating into the material. The Gaussian beam expression $f(o, e)$ can then be expressed as [146, 147, 148],

$$f(O, e) = \frac{2}{\pi r^2} \exp\left(-\frac{2d}{r^2}\right) \quad , \quad d = \frac{||e \times (x - o)||}{||e||} \tag{5.24}$$

The radiative intensity I_i [W/m^2] of the i^{th} beam through the material decreases due to absorption as the beam propagates through the medium. This can be expressed using the Beer-Lambert Law as [146, 147, 148],

$$\frac{e_i}{||e_i||} \cdot \Delta I_i = -\beta I_i \tag{5.25}$$

where e_i is the orientation of the i^{th} beam and β is the absorption coefficient of the medium for a particular wavelength (given in Table 5.5 and Table 5.6). The radiative heat source Q_r corresponding to the energy deposited by the radiative beam is the one used in the multiphysics coupling 'Heat Transfer with Radiative Beam in Absorbing Media', and is given as [146, 147, 148],

$$Q = \sum_i \beta I_i \tag{5.26}$$

5.3.2 Heat Transfer in Solids

This physics module solves for changes in the temperature of a material in a time-dependent study. For a material of density ρ with given thermal conductivity κ, Heat capacity at constant pressure C_p, and thermal expansion α, (given in Table 5.3 and Table 5.4) the interface solves the following equation [149],

$$\rho C_p \frac{\partial T}{\partial t} + \rho C_p u \cdot \nabla T + \nabla \cdot (-\kappa \nabla T) = Q + Q_{ted} \tag{5.27}$$

where the term $Q_{ted} = -\alpha T : \frac{dS}{dT}$ is the thermoelastic damping accounting for any thermoelastic effect in the solid, S is the second Piola-Kirchhoff stress tensor, and u is the velocity vector of translation motion. When we use the multiphysics coupling 'Thermal Expansion', the thermoelastic damping is taken as a heat source. Q is any other additional heat source, for instance, as Equation 5.26 [149].

The boundary condition of 'Surface to ambient radiation' was defined on all surfaces for radiative cooling of the material. This takes the ambient temperature of the surroundings and the surface emissivity, ϵ_r, of the material as inputs. All the materials were given a surface emissivity of 1 for this case [149].

$$-n \cdot (-q) = \epsilon_r \sigma (T_{amb}^4 - T^4) \tag{5.28}$$

Here, the ambient temperature was defined as room temperature $T_{amb} = 298.15K$. This boundary condition implies that the object radiates as a grey body (if the $\epsilon_r < 1$, a black body if $\epsilon_r = 1$). However, the grey body assumption would imply that this material is opaque. This discrepancy is resolved by noting that the material absorptivity is highly wavelength-dependent. At the wavelength of the incident laser, we consider the penetration depth to be large. However, when the part heats up, it will radiate primarily in the long infrared regime. At long infrared wavelengths, we can assume that the penetration depth is very small, and thus the assumption that the material bulk is opaque for emitted radiation is valid [149].

5.3.3 Solid Mechanics

This module, found under the 'Structural Mechanics' branch, was used to solve equations of motion to estimate displacement and stress for the material due to thermal changes. The material was simulated as a linear elastic anisotropic material, with a 'Thermal expansion' boundary feature. The anisotropic feature takes into account that the material under study has different properties in different directions. The elasticity matrix, following the convention described in Equation 5.19, was used to define the material. The thermal expansion node adds an internal thermal strain caused by the temperature change of the material. The study was computed with 'include geometric nonlinearity', which defaults the behaviour of this module to use a large strain formulation in all domains. The thermal strain for a material with secant coefficients of thermal expansion α_{ij} (given in Table 5.3

and Table 5.4) after reaching a new temperature T from ambient temperature T_{amb} is given by [150, 151],

$$\epsilon_{ij} = \alpha_{ij}(T - T_{amb}) \tag{5.29}$$

It is important to note that since the thermal expansion of a crystal must possess the symmetry of the crystal, it cannot destroy the symmetry elements corresponding to that particular class. Hence, the class of the crystal does not depend on the temperature. [41].

A fixed constraint boundary condition, *i.e.*, displacement vector to be zero, was defined on the outer rim of the plate, to make it identical to a mounted optics. In order to have minimal effect from stress due to mounting of the compensation plate, an optimal design of the mount should be investigated. The 'Solid Mechanics' interface is coupled with 'Heat transfer in solids' using multiphysics 'Thermal expansion' to then use the estimated temperature for strain calculations [150, 151].

The displacement vector of each surface, calculated by FEM, is used to estimate the change in thickness of the material. COMSOL uses the standard relation between strain and displacement to estimate the displacement u, v, and w along different directions x, y, and z, respectively, using the corresponding strain. For the three direction we can consider x, y, and z, represented as 1, 2, and 3 respectively. The following relation shows that the strain tensor is defined as the symmetric part of the displacement gradient, which evaluates how rapidly the displacement changes through the material. [152]

$$\epsilon_{ij} = \frac{1}{2}\left(\frac{\partial u_i}{\partial x_i} + \frac{\partial u_j}{\partial x_j}\right) \tag{5.30}$$

The corresponding change in thickness can then be calculated as the absolute difference between the displacement vector along the $\hat{z}$ axis of the front and back face as $|w_f - w_b|$.

5.4 Results from Finite Element Modelling

5.4.1 Convergence study

The mesh of any FEM study can help obtain the best estimation of the properties under study. It is therefore crucial to estimate the number of mesh elements needed for a good estimation of the properties under investigation. For a single beam incident on the plate, most changes, especially sharp features such as a Gaussian peak, were expected to occur in the region of the incident beam. Hence, the body was divided into two regions, one with coarser elements

and one with finer elements. The geometry was extruded from two concentric circles in 2D to make a cylinder with such partitions, without any complex divisions required. The radius of the inner circle matches the radius of the laser beam incident on the plate, while the radius of the entire plate (the outer circle) was chosen to be 11 cm. The 2D geometry was extruded for a thickness of 1 cm. The mesh of the material looked as shown below

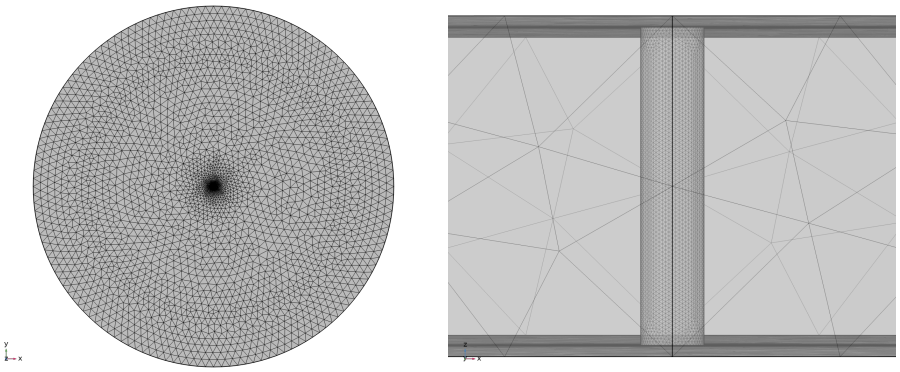

Figure 5.5: Mesh used for FEM. The left picture shows the front view, while the right picture shows a zoomed-in slice looking from the side of the central part.

The mesh of the 1 cm plate had to meet two conditions to be finalised. The estimation of temperature should converge *i.e.*, the temperature should not change much with a change in the number of elements. Additionally, the intensity estimation along the depth of the material should match the theoretical estimation of intensity along the depth of the material.

5.4.1.1 Varying mesh as beam spot size

As the mesh in the centre was refined, it introduced more and more elements, and hence increased the computation time. In an ideal world, if we continue to refine the mesh, we can achieve a highly convergent plot. However, we are limited by the available computational capabilities, and hence the maximum refinement that could be done was 1/8 mm.

The values that were observed were the maximum value and the value at the centre of the plate for both temperatures and intensity. Since the laser is incident at the centre of the plate, for a good mesh, the maximum value and the value at the centre should be in close proximity to each other. The trend for temperature and intensity was observed at $z = 0$ along the X and Y axes. The plot in Fig. 5.6 shows how the refinement of the central region brought a nice convergence to the estimated temperature and intensity.

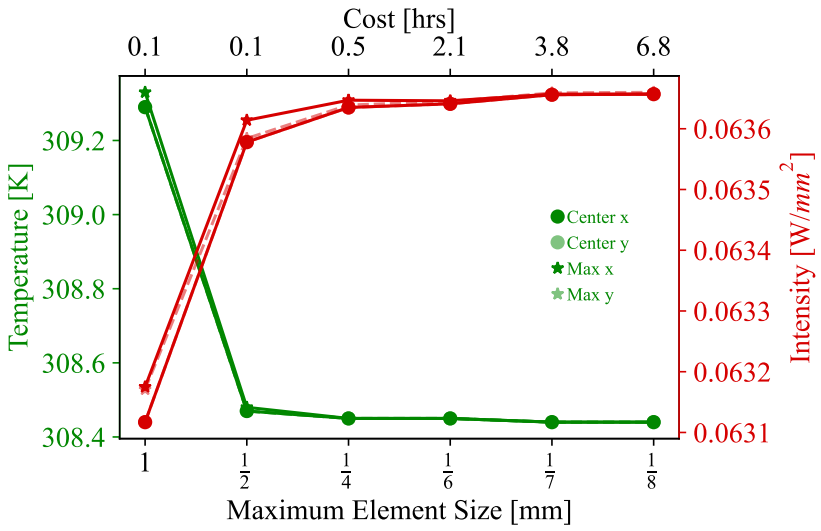

Figure 5.6: Comparison of temperature and intensity response from FEM for Calcite crystal, as the number of mesh elements is increased by decreasing the minimum element size from 1 mm to 1/8 mm. The 'center' value indicates the response at the center of the plate (X=Y=0) along the radial arc on the X axis (Y=Z=0) and Y axis (X=Z=0). The 'max' value indicates the value at the peak of the temperature distribution curve. For optimal mesh, the center value should coincide with the max value, as the Gaussian CO_2 beam is incident at the center.

5.4.1.2 Varying mesh along thickness

For highly absorbing materials like TiO_2 and Sapphire, most of the laser is absorbed in the few initial thicknesses of materials. An absence of enough mesh elements in the initial thickness will lead to poor estimation of temperature or displacement. Owing to this, a separate style of meshing was adopted for the two materials, where the mesh was refined only in the few initial mm of thickness from the front face.

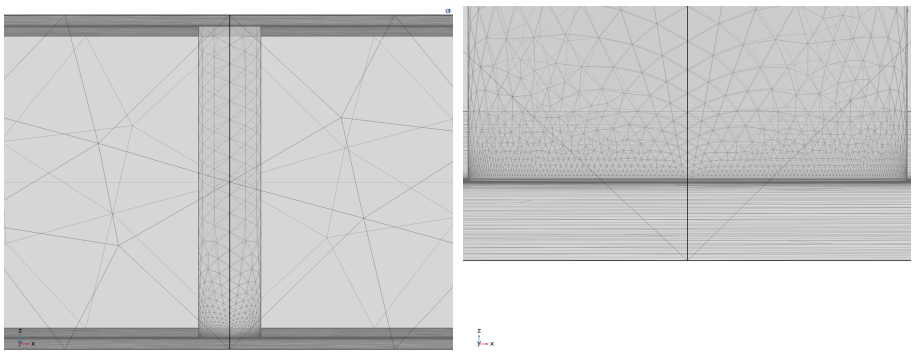

Figure 5.7: Mesh used for FEM for highly absorbing materials. The left picture shows the side view across the entire thickness, while the right picture shows a zoomed-in slice along the thickness.

The condition was to achieve a match between the theoretical and FEM estimation of the exponential decay of intensity within the computational capabilities. The plot shown

below shows that for a maximum and minimum element size of 1/50 mm and 1/100 mm, respectively, within a thickness of 10^{-3} cm, as shown in the mesh in Fig. 5.7. The estimated intensity from FEM follows the intensity estimation from the theoretical formula Equation 5.25. The refinement was done till we stopped seeing the intensity go below zero at some points and followed the theoretical curve.

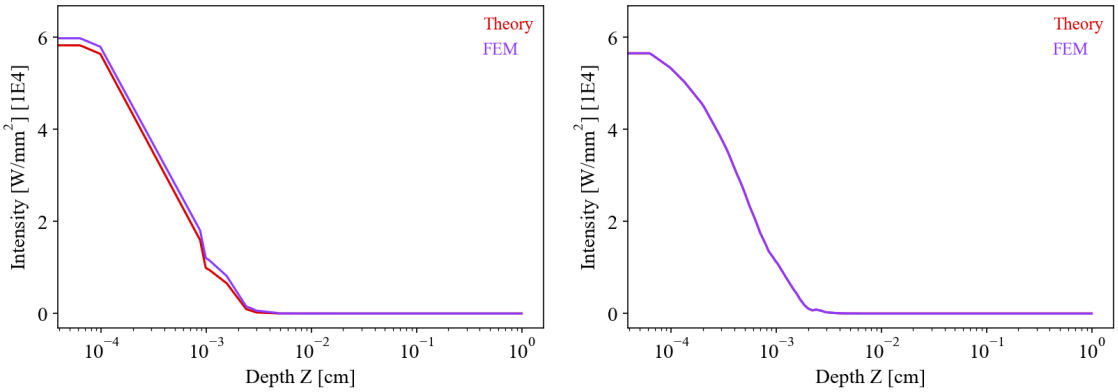

Figure 5.8: Comparison of intensity estimation across the thickness of the material for highly absorbing materials. The plot shown here is for TiO_2. The left plot shows data with no refinement, while the right plot shows data with extra fine refinement. The plots for the data with refinement show overlapping of red and purple curves. It can be seen that with a good mesh, the theoretical estimation and FEM estimation are in proximity of each other.

5.4.2 Response of different materials

A time-dependent study was performed in COMSOL with a time optimised to reach steady state for the plate. The time chosen was 1 hour, which minimised any large changes in the materials. The comparison of the birefringence Γ of materials due to different mechanisms (thermorefractive, thermoelastic and photoelastic) is summarised in Table 5.7. Subsequently, the plots of their thermorefractive, thermoelastic, photoelastic, and total birefringence are shown from Fig. 5.9 to Fig. 5.13 below. While the Table 5.7 presents only the most essential data, the comparison plots can help better understand the birefringence response at a given CO_2 laser intensity of 0.1 W/mm^2.

Material	YVO_4	$CaCO_3$	TiO_2	αSiO_2	αBBO	MgF_2	Al_2O_3
Γ_{TR}[rad]	-0.291	1.343	-0.112	-0.068	1.594	-0.014	0.093
Γ_{TE}[rad]	0.06	-0.042	0.219	0.011	-0.163	0.005	-0.003
Γ_{PE}[rad]	0.021	-0.438	0.39	-0.096	-0.453	-0.015	0.212
Γ_{TR+TE}[rad]	-0.231	1.301	0.107	-0.057	1.431	-0.009	0.09
$\Gamma_{TR+TE+PE}$[rad]	-0.210	0.863	0.496	-0.144	0.977	-0.024	0.302
$FWHM_{TR}$[mm]	19.7	11.71	18.2	19.2	9.2	35.1	41.9
$FWHM_{TE}$[mm]	46.2	13.8	20.7	18.2	8.9	85.5	56.03
$FWHM_{PE}$[mm]	–†	35.9	71.7	135.7	23.4	35.3	61.5
$FWHM_{TR+TE}$[mm]	15.8	11.6	23.6	19.4	9.2	27.3	41.6
$FWHM_{TR+TE+PE}$[mm]	–†	8.2	55.5	87.6	7.1	31.5	53
$P_{2\pi}$[W/mm^2]	2.8	0.5	5.9	11	0.4	69.8	7
$\Gamma_{0.01W}$[rad]	-0.023	0.13	0.01	-0.006	0.143	-0.001	0.009

Table 5.7: Results from Thermal Analysis of various materials. †: Due to a large stress response from the holder, there was a lack of Gaussianity similar to the incident Gaussian beam, and hence it was difficult to describe the FWHM of the birefringence distribution.

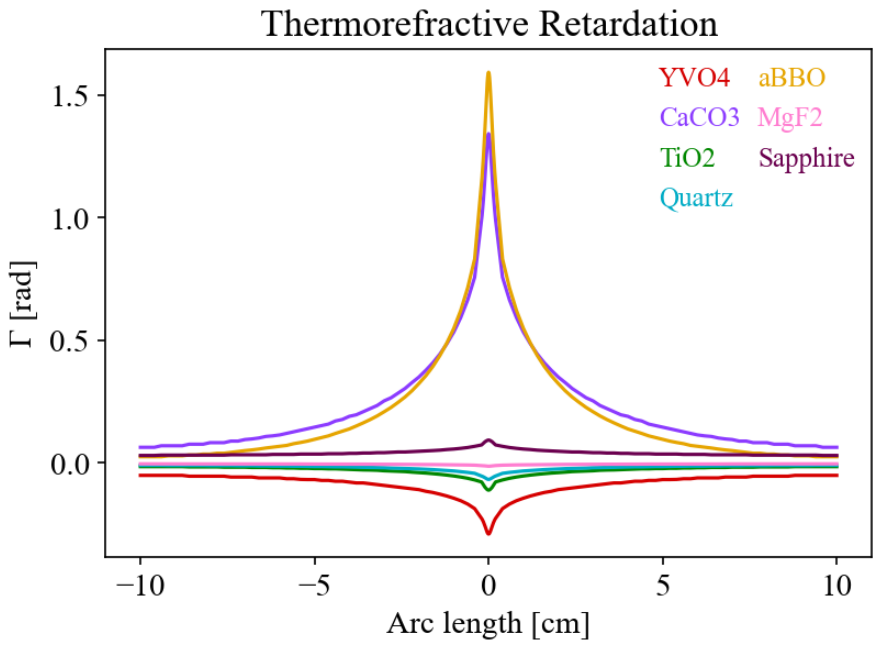

Figure 5.9: Comparison of thermorefractive response of crystals. It can be seen that the largest response is observed by αBBO.

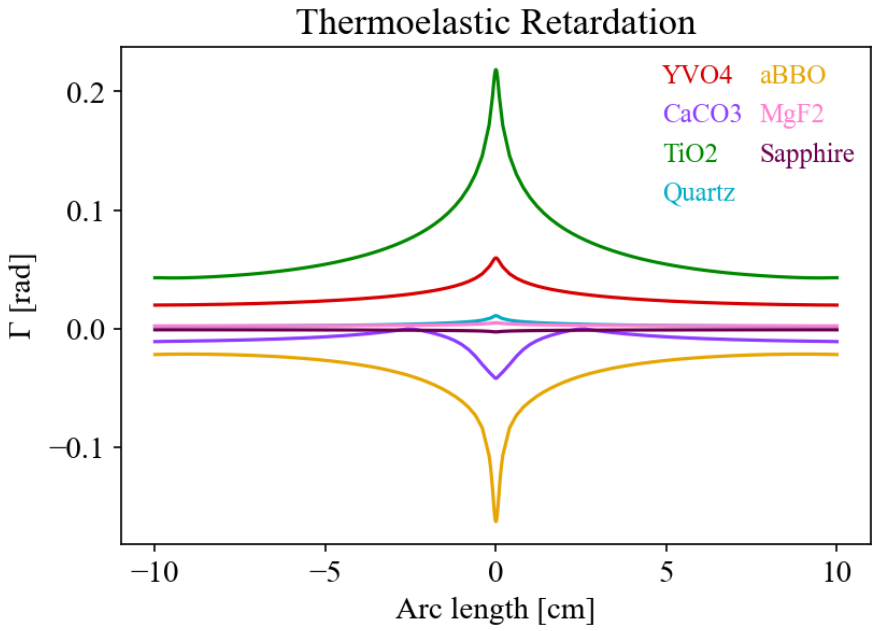

Figure 5.10: Comparison of thermoelastic response of crystals. It can be seen that the best response is observed by TiO_2. This is largely due to the large absorption of the CO_2 laser within a few mm of the thickness of the material, which causes a large thermal expansion.

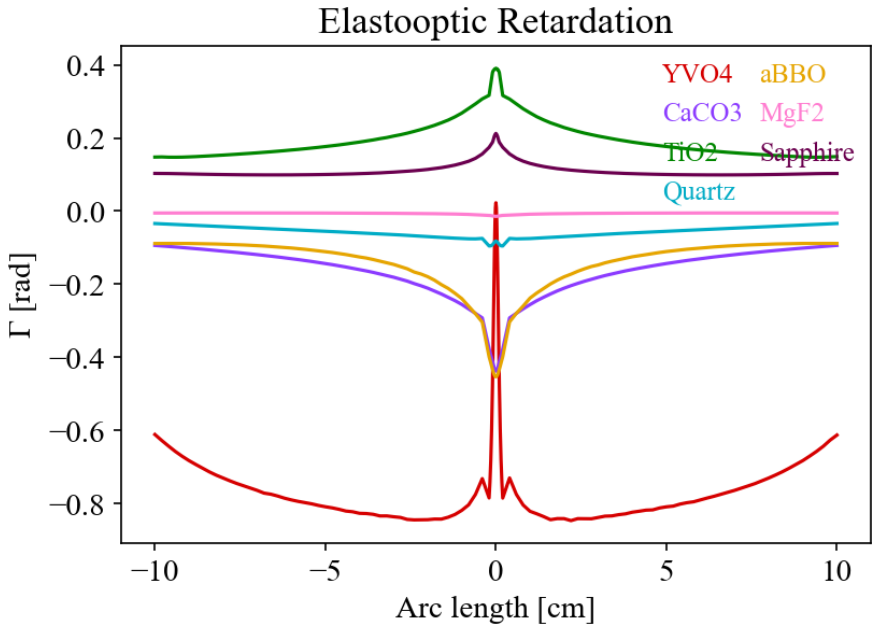

Figure 5.11: Comparison of photoelastic response of crystals. It can be seen that the best response is observed by αBBO and Calcite. While this response can be taken into account to understand its effect on actuation, it should be kept in mind that the suspension was not optimised to reduce the stress caused by the mounting of the plate. Hence, this response should be considered carefully. Additionally, the elastooptic coefficient of YVO_4 is 2 orders of magnitude larger along the x axis than in other crystals, which explains why the effect of the mount is especially prominent in the response of YVO_4.

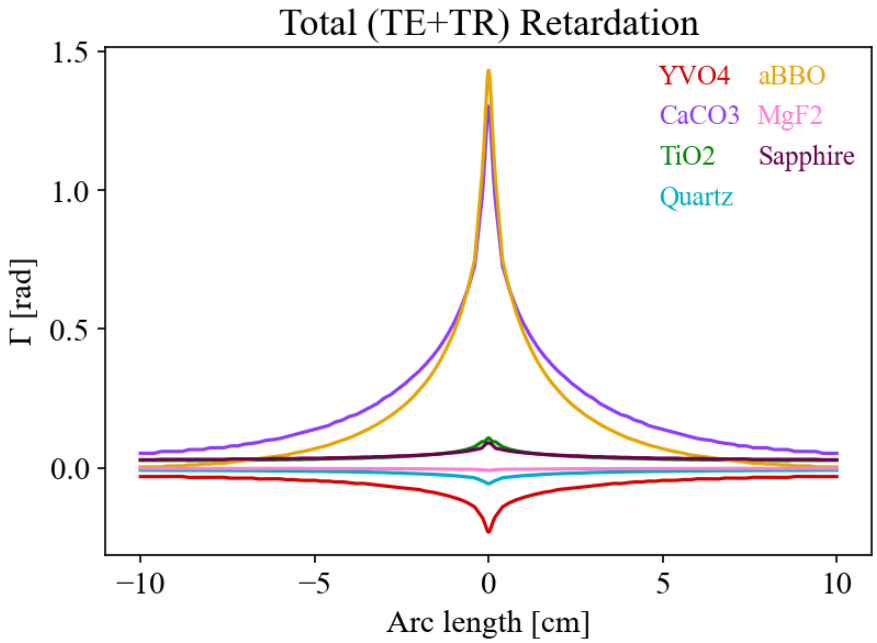

Figure 5.12: Comparison of the sum of thermoelastic and thermorefractive response of crystals. Although the thermorefractive and thermoelastic response of Calcite and αBBO are opposite in sign, they still show the largest response in the generated birefringence amongst all crystals.

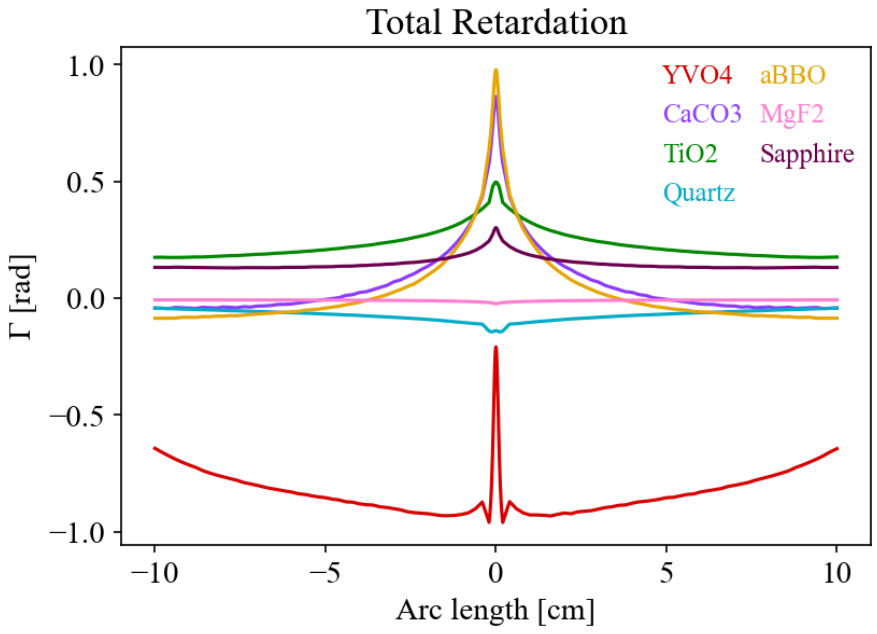

Figure 5.13: Comparison of the sum of thermoelastic, thermorefractive, and photoelastic response of crystals. Although the photoelastic and thermoelastic response of Calcite and αBBO are opposite in sign from thermorefractive, they still show the largest response in the generated birefringence amongst all crystals.

5.4.3 Optimal choice of material

As shown in the Table 5.7, the largest birefringence response was achieved using αBBO and Calcite. Upon contact with manufacturers, we came to know that it is difficult to get a large enough (1 cm thick and at least 2-inch diameter) Calcite. However, αBBO is somewhat available, and hence was later added to the analysis. Since the properties of αBBO lie close to those of Calcite, it was selected as an optimal candidate. The following plots show the in-depth analysis of temperature distribution and the birefringence of the αBBO crystal.

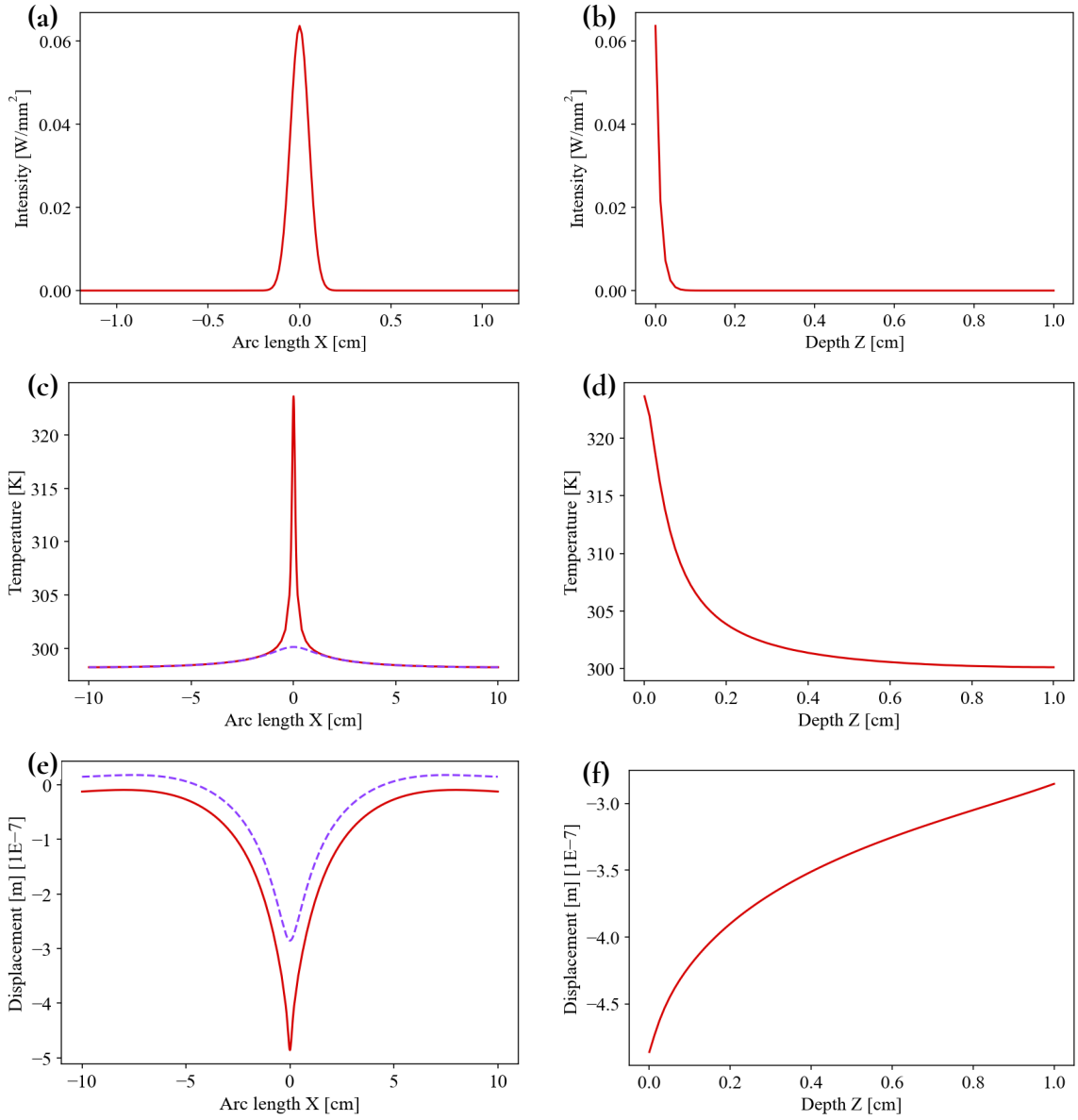

Figure 5.14: The changes in αBBO with 0.1 W of 10 μ m incident laser. The plots on the left (a,c,e) show the effect on the front and back face of the material along the radial arc (on the X axis, $Y = Z = 0$), after heating, using red and purple curves, respectively. The plots on the right (b,d,f) side show data along the thickness of the material. The first plots (a,b) show the intensity of the incident Gaussian beam of CO_2 at the centre of the plate. Following the heating due to the beam, the temperature shifts from room temperature (c,d) and displacement (e,f) occurs as shown.

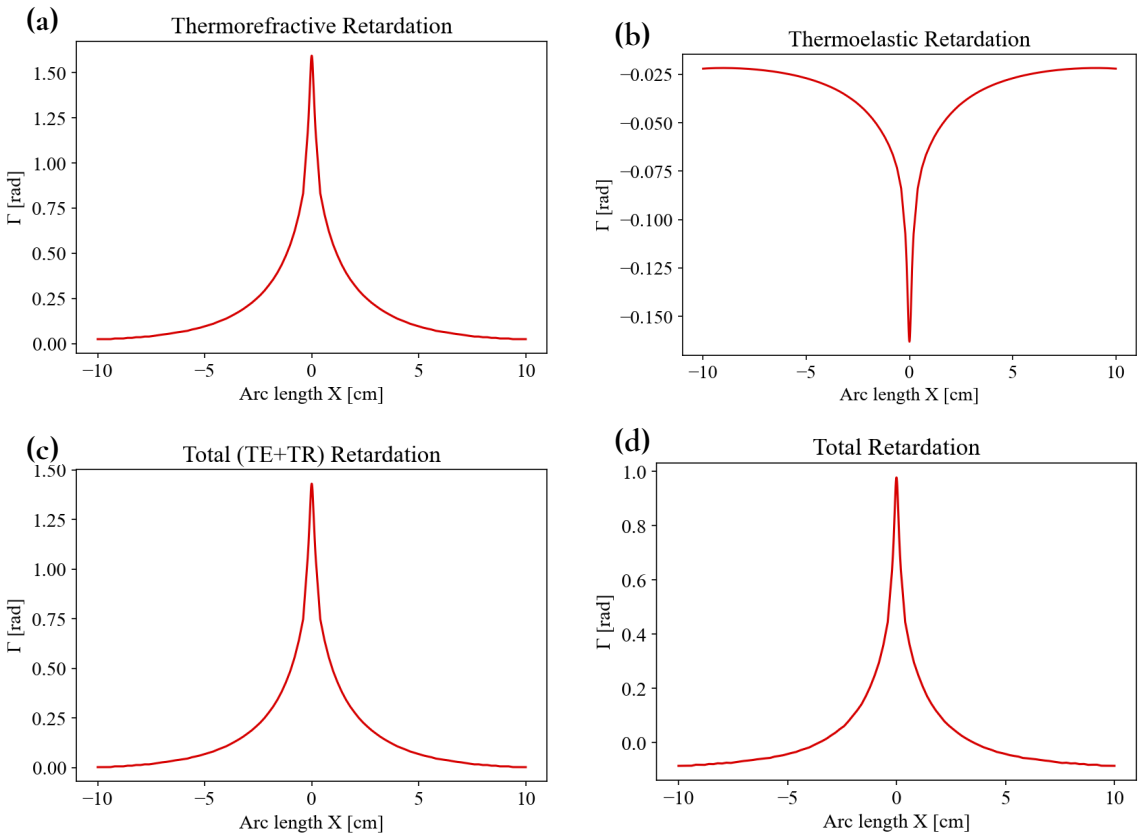

Figure 5.15: The birefringence response at the X axis (Y=Z=0) after the interaction with the αBBO plate of thickness 1 cm of when a 0.1 W of 10 μ m laser is incident.

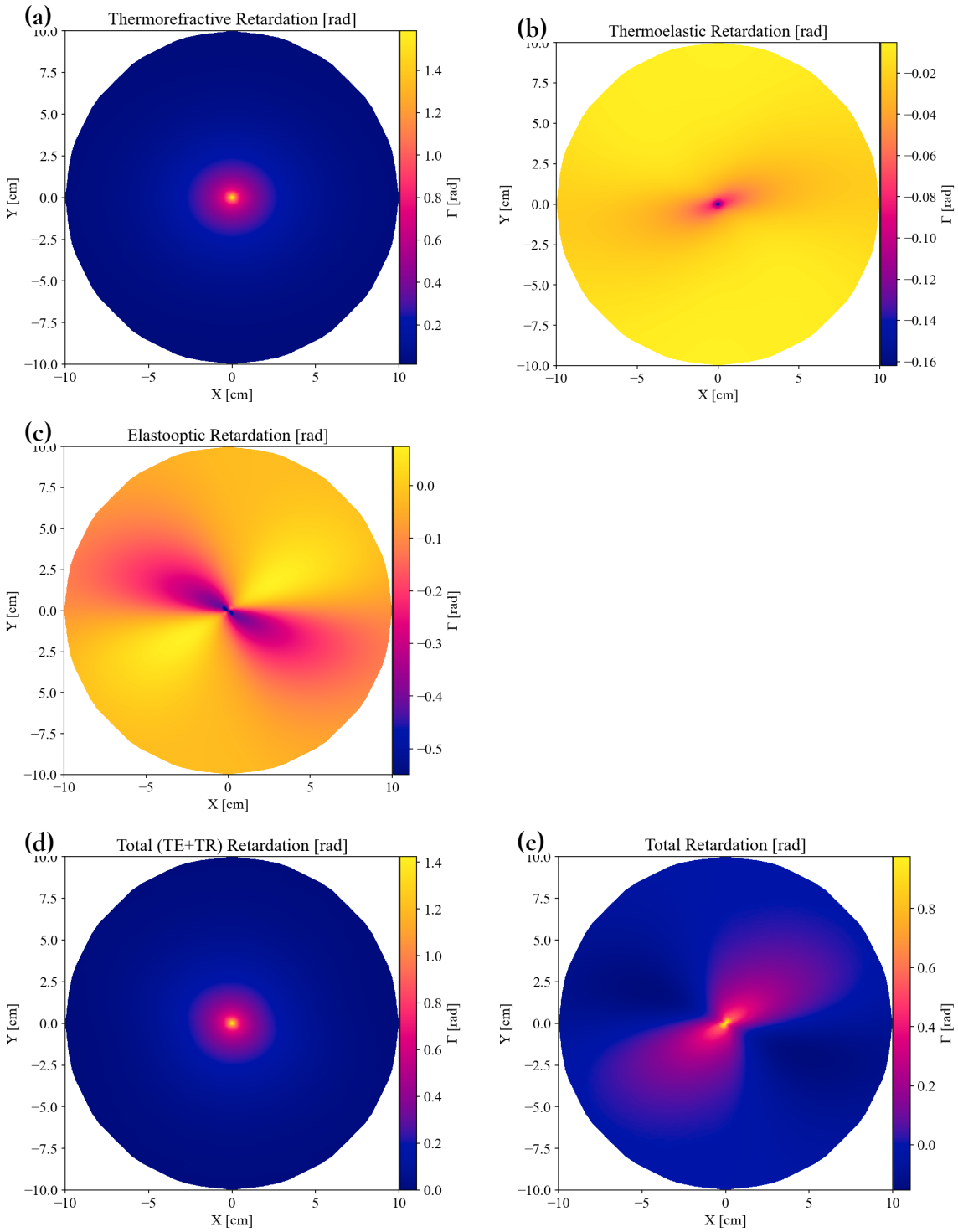

Figure 5.16: Birefringence maps obtained of αBBO with 0.1 W of 10 μ m incident laser.

5.5 Towards non-uniform compensation

With a promising actuator in mind, it is time to discuss the optical setup with the goal of non-uniform birefringence compensation. The motivation is to develop an optical setup compatible for installation in the detector.

5.5.1 Generation and compensation of non-uniform birefringence

Following the principle shown in 2.4.1 that a pair of variable retarders can generate any desired polarisation, a pair of compensation plates can be used to generate any polarisation. However, in contrast to the voltage-controlled LC, the plates are actuated with temperature. The temperature can be varied by varying the laser intensity incident on the plate using a patterned mask. A large CO_2 beam when passes through the patterned mask will get spatially divided into several beams reaching the plates with varying intensity. This is shown in Fig. 5.17.

To achieve a stable response in the birefringence generated by the power of the CO_2 laser, the power must be stabilised using an acousto-optic modulator. The voltage applied to the acousto-optic modulator will change its transparency, thereby changing the exiting laser power. A feedback loop can be in place for active control of the CO_2 laser power.

The compensation of non-uniform birefringence can be done by inserting the non-uniform birefringent material between the polarisation generator and polarisation readout (using the Pockels cell-based PSA from Chapter 4. The residual birefringence and any birefringence noise can be measured using the birefringence camera. This demonstration will bring us closer to a setup eligible for installation in a GW detector.

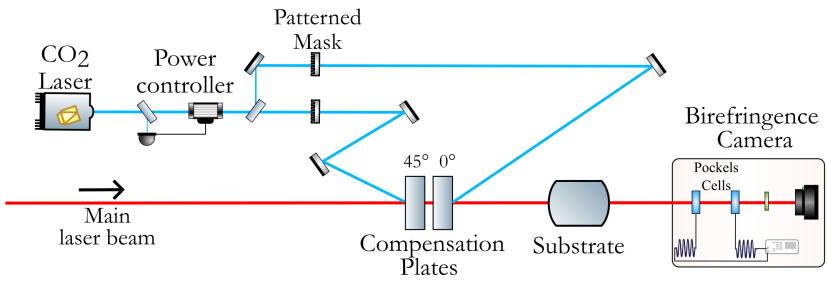

Figure 5.17: The setup to demonstrate the compensation of non-uniform birefringence of a substrate.

5.5.2 Implementation in GW detector

In order to compensate for non-uniform birefringence in the detector, KAGRA, a possible configuration can be the installation of compensation plates before the ITMs, as shown in Fig. 5.18. The birefringence camera can be installed at a pick off from the reflection of the arms, which will enable real-time monitoring of residual birefringence in the detector. The path to realisation will involve several investigations into the effect of bulk loss of compensation plates, birefringence noise, and beam jitter noise, spatial resolution of birefringence compensation, amongst several others.

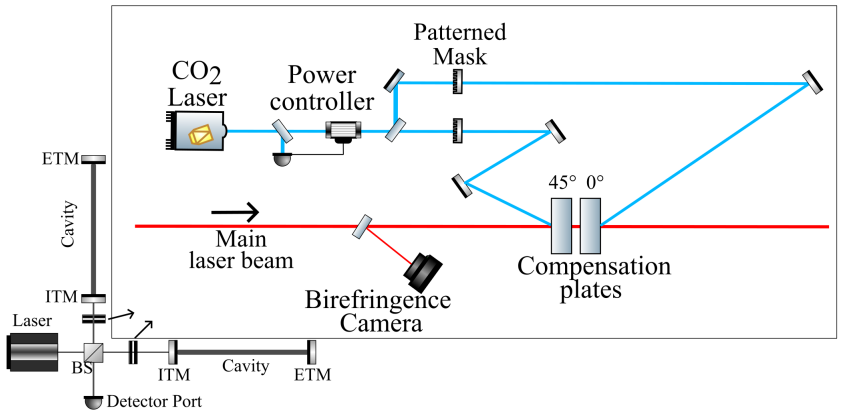

Figure 5.18: A possible configuration for birefringence compensation of ITM in GW detector.

Another possible implementation could be to install compensation plates to compensate for non-uniform birefringence in the control beams in the interferometer. For instance, installing at the detector input or output can compensate for residual detector birefringence. Additionally, such installations could have more relaxed requirements on power, loss, and space, hence offering a convenient solution to non-uniform compensation.

5.6 Discussion

This section highlighted the development of a technique for birefringence compensation. The demonstration of uniform birefringence compensation saw a reduction in birefringence by a factor 10^5. It paved a promising path towards the use of such a technique to tackle the issue of birefringence. Since voltage-controlled electro-optics are incompatible for use in GW detector environment, it gave rise to the need for a new actuator. With this in mind, a variety of materials were investigated to act as a temperature-controlled polarisation actuator. Such an actuator is compatible with the environment of GW detectors, such as high laser power, and can meet the loss requirements.

Detailed analysis of the different candidate materials showed the range of polarisation each of them can generate. Materials like αBBO and Calcite rose to the top as promising materials, mostly because of their large thermooptic coefficients. The materials could provide retardance actuation up to 1 rad with 0.1 W/mm^2 CO_2 laser, making the generation of any required non-uniform polarisation control feasible with the commercially available CO_2 laser. Such an analysis also paves the way for any other possible materials, which were left uncovered this time, but might meet the requirements. While the future experiments will involve demonstration of non-uniform polarisation control and compensation, careful analysis of the effect of such a system in a detector is required, and will form the future interests of such a study.

Conclusion

This thesis presents building blocks toward the realisation of non-uniform birefringence compensation in a GW detector. The work focused on improved characterisation techniques to extract more complete information about birefringence, and on developing a compensation approach compatible with in-detector operation. Chapter 1 and Chapter 2 introduce the GW detector context and the relevant birefringence background, while Chapter 3–Chapter 5 present the main results.

Chapter 3 demonstrates a birefringence characterisation method using arbitrary input polarisations, relaxing the requirement for strictly linear polarisation and accurate alignment of polarisation optics. The approach was validated using 839,160 polarisation-state pairs to reconstruct birefringence, yielding consistent results across independent reconstructions. Measurements were demonstrated on a range of samples—from everyday optics to sapphire and biological samples—highlighting the versatility of the technique. However, LC-based polarisation generation and QWP-based polarisation analysis were found to be too slow and insufficiently sensitive for characterising dielectric materials. This motivated the development of a faster actuator for characterisation.

Chapter 4 presents the development and characterisation of a Pockels-cell system. The Pockels cell achieves maximum modulation depth and more than $3\pi/2$ retardation modulation at 15 MHz. These characteristics enable several promising implementations of the Pockels cell as both a PSG and a PSA. In particular, the MHz-rate PSA addresses sensitivity limitations in measurements of dielectric and crystalline materials by providing improved statistics, use of higher laser power and enabling a custom high-speed PSA. A further advantage is the potential to measure polarisation and its fluctuations in GW detectors. Overall, the developed system supports multiple future implementations towards birefringence characterisation with improved sensitivity.

Chapter 5 shifts the focus from birefringence characterisation to compensation. The first phase demonstrates uniform birefringence compensation using an LC-based PSG, reducing birefringence by a factor of 10^5. This result motivates the need for a new polarisation actuator that meets requirements for use in a GW detector, including compatibility with

high laser power and low optical loss. Toward a detector-installable compensation system, voltage-actuated polarisation control can be replaced by thermal actuation. Several candidate materials were investigated using thermal simulations, and promising options such as αBBO and Calcite were identified. A configuration for compensating non-uniform birefringence using installed compensation plates is also presented.

To summarise the development, Chapter 3 paves the way to get new birefringence information through characterisation of samples. The developments in Chapter 4 lays groundwork for the characterisation of birefringence and its fluctuation with improved sensitivity, and also a way to observe birefringence in the detector using the high-speed polarisation actuation. Chapter 5 showcases the work towards reducing birefringence in the detector through the use of polarisation actuators. It is important to characterise the birefringence to compensate for it, and hence this thesis puts forward mechanisms to address both characterisation and compensation. Together, the results from Chapter 3 to Chapter 5 establish a practical path toward implementing non-uniform birefringence compensation in GW detector, KAGRA.

Appendices

A

Details on impedance matching network

Contents

A.1 Derivation of impedance matching capacitor

A.1.1 Circuit model

The model of interest is a one-port circuit consisting of a lossy series branch R–L–C in parallel with a shunt capacitor C_1. Here, L is the inductance of the designed inductor and C is the total effective capacitance of the Pockels cell at the EOM node (i.e., if a tuning capacitor is already added, then C denotes the resulting effective capacitance seen in series with the inductor). The series-branch impedance is

$$Z(\omega) = R + j\omega L + \frac{1}{j\omega C} = R + j\left(\omega L - \frac{1}{\omega C}\right), \tag{A.1}$$

The series reactance is defined as

$$X(\omega) \equiv \omega L - \frac{1}{\omega C}, \qquad \Rightarrow \qquad Z(\omega) = R + jX(\omega), \tag{A.2}$$

and the shunt-capacitor admittance is

$$Y_{C_1}(\omega) = j\omega C_1. \tag{A.3}$$

A.1.1.1 Input admittance

Since the shunt capacitor is in parallel with the tank circuit, it is convenient to express the matching condition in admittance form. The input admittance is

$$Y_{\text{in}}(\omega) = \frac{1}{Z_{\text{in}}(\omega)} = Y_{C_1}(\omega) + \frac{1}{Z(\omega)} = j\omega C_1 + \frac{1}{R + jX}. \tag{A.4}$$

Using

$$\frac{1}{R + jX} = \frac{R - jX}{R^2 + X^2}, \tag{A.5}$$

we obtain

$$Y_{\text{in}}(\omega) = \underbrace{\frac{R}{R^2 + X^2}}_{G(\omega)} + j \underbrace{\left(\omega C_1 - \frac{X}{R^2 + X^2}\right)}_{B(\omega)}, \tag{A.6}$$

where $G(\omega) = \Re\{Y_{\text{in}}(\omega)\}$ is the conductance and $B(\omega) = \Im\{Y_{\text{in}}(\omega)\}$ is the susceptance.

A.1.1.2 Matching conditions at the resonant frequency ω_0

We seek a frequency ω_0 such that the input impedance is purely real and equals a target resistance R_s:

$$Z_{\text{in}}(\omega_0) = R_s \in \mathbb{R}. \tag{A.7}$$

Since $Z_{\text{in}}(\omega) = 1/Y_{\text{in}}(\omega)$, this is equivalent to imposing both

$$B(\omega_0) = 0, \qquad \text{and} \qquad G(\omega_0) = \frac{1}{R_s}. \tag{A.8}$$

A.1.1.2.1 Zero susceptance. Setting $B(\omega_0) = 0$ gives

$$\omega_0 C_1 - \frac{X(\omega_0)}{R^2 + X(\omega_0)^2} = 0 \qquad \Rightarrow \qquad C_1 = \frac{X(\omega_0)}{\omega_0 \left(R^2 + X(\omega_0)^2\right)}. \tag{A.9}$$

A.1.1.2.2 Conductance match. Setting $G(\omega_0) = 1/R_s$ gives

$$\frac{R}{R^2 + X(\omega_0)^2} = \frac{1}{R_s} \qquad \Rightarrow \qquad R^2 + X(\omega_0)^2 = RR_s \qquad \Rightarrow \qquad X(\omega_0)^2 = R(R_s - R). \tag{A.10}$$

In most cases of a tank circuit the loss is low such that $R_s > R$, ensuring a real solution. The positive root is therefore chosen (which yields $C_1 > 0$):

$$X(\omega_0) = X \equiv \sqrt{R(R_s - R)}. \tag{A.11}$$

Using $R^2 + X^2 = RR_s$ together with (A.9) yields

$$C_1 = \frac{X}{\omega_0 \, R \, R_s}. \tag{A.12}$$

A.1.1.2.3 Solving for ω_0. By definition,

$$X(\omega_0) = \omega_0 L - \frac{1}{\omega_0 C} = X. \tag{A.13}$$

Multiplying both sides by ω_0 gives

$$L\omega_0^2 - X\omega_0 - \frac{1}{C} = 0, \tag{A.14}$$

which is a quadratic equation in ω_0. The positive root is

$$\omega_0 = \frac{X + \sqrt{X^2 + \frac{4L}{C}}}{2L}. \tag{A.15}$$

A.1.1.3 Expression for C_1

Substituting (A.15) into (A.12) gives

$$C_1 = \frac{X}{RR_s} \cdot \frac{2L}{X + \sqrt{X^2 + \frac{4L}{C}}}. \tag{A.16}$$

Using the identity

$$\frac{1}{X + \sqrt{X^2 + a}} = \frac{\sqrt{X^2 + a} - X}{a}, \qquad a > 0, \tag{A.17}$$

with $a = \frac{4L}{C}$, we obtain

$$C_1 = \frac{X}{RR_s} \cdot \frac{C}{2} \left(\sqrt{X^2 + \frac{4L}{C}} - X \right). \tag{A.18}$$

Equivalently,

$$C_1 = \frac{C}{2RR_s} \left(X\sqrt{X^2 + \frac{4L}{C}} - X^2 \right). \tag{A.19}$$

Finally substituting $X^2 = R(R_s - R)$ from (A.10) yields the closed-form expression

$$\boxed{C_1 = \frac{C}{2RR_s} \left(\sqrt{R(R_s - R)\left(R(R_s - R) + \frac{4L}{C} \right)} - R(R_s - R) \right)} \tag{A.20}$$

B

Details on other compensation plate materials

Contents

B.1 Detailed birefringence analysis of crystals

The following sections enclose the details of thermorefractive, thermoelastic, and elastooptic retardation of each crystal. It was not possible to put the maps of each category for all crystals in the main Chapter 5 to have good readability for the readers. However, the individual maps are shown here to have a more intuitive understanding of their thermal response.

B.1.1 YVO4

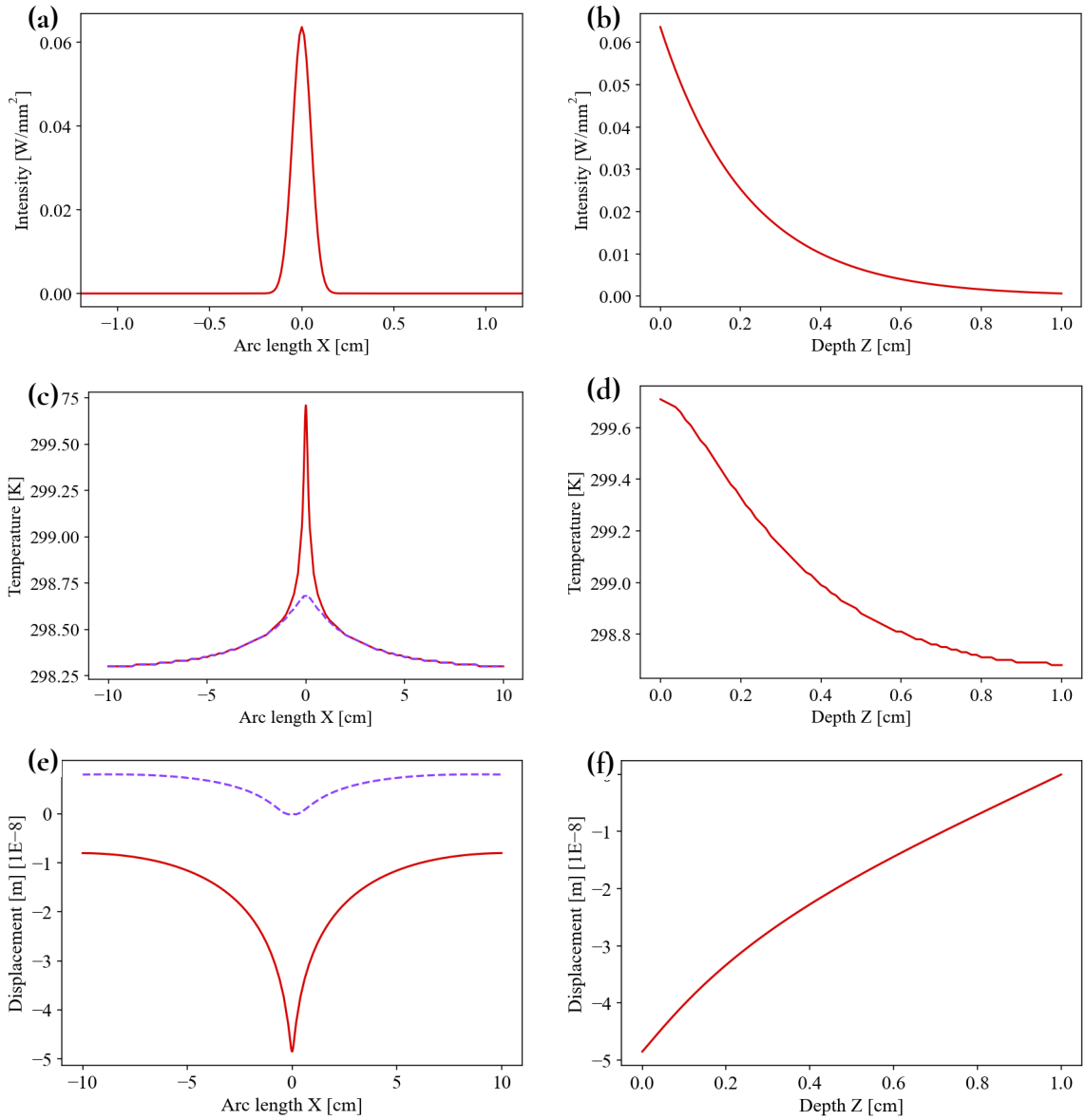

Figure B.1: The changes in YVO4 with 0.1 W of $10\mu m$ incident laser. The plots (a,c,e) on the left side show data for the front face of the material using the red curve, and the purple dashed curve shows data on the back face. The plots on the right (b,d,f) side show data along the thickness of the material. The first plot, showing Intensity along the radial arc (on the X axis, $Y = Z = 0$), shows the Gaussian beam incident on the centre of the plate. Following the heating due to the Gaussian beam, a change in temperature and displacement of the material are shown on the second and third rows, respectively.

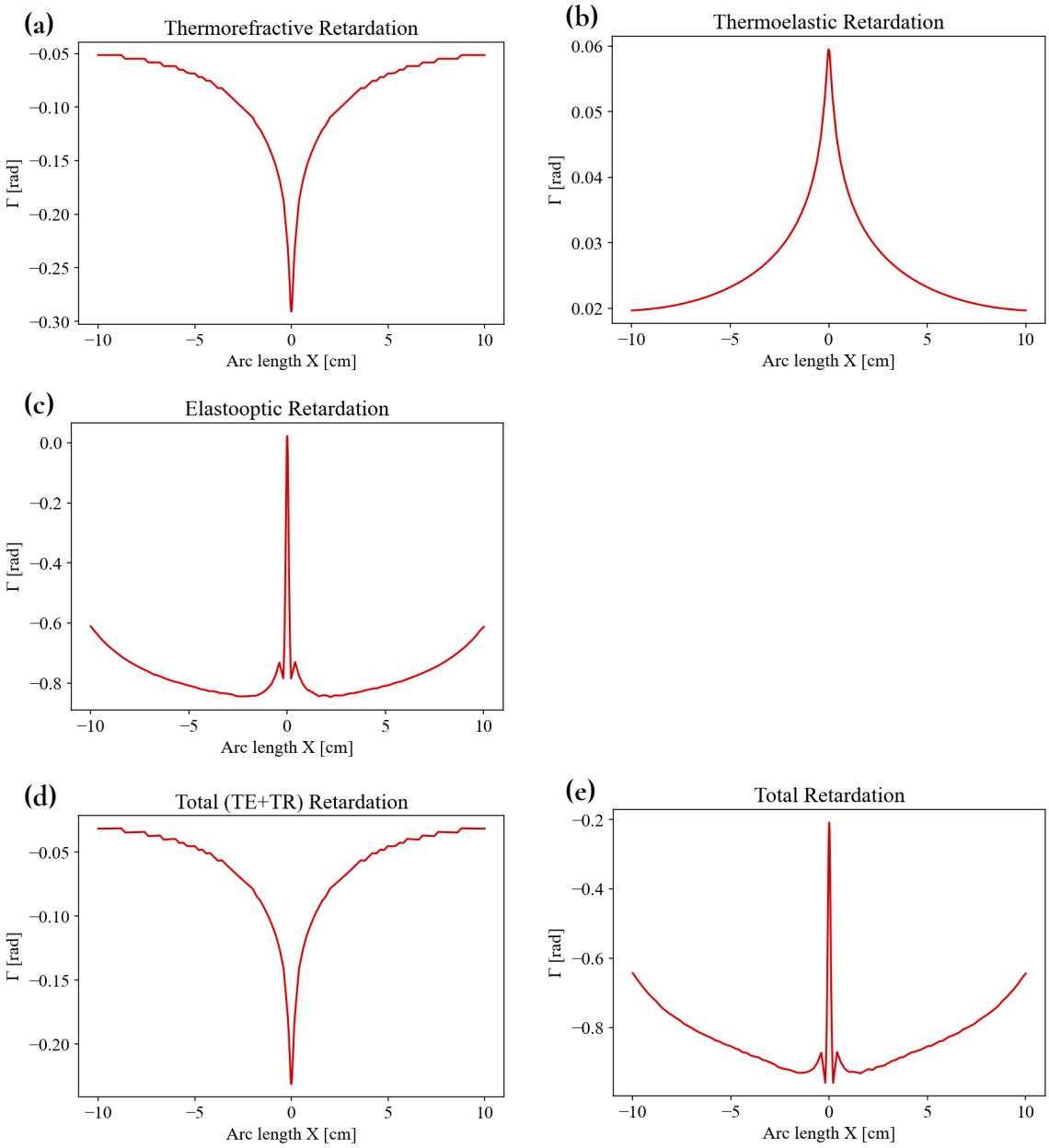

Figure B.2: The birefringence response at the central arc of YVO4 with 0.1 W of $10\mu m$ incident laser.

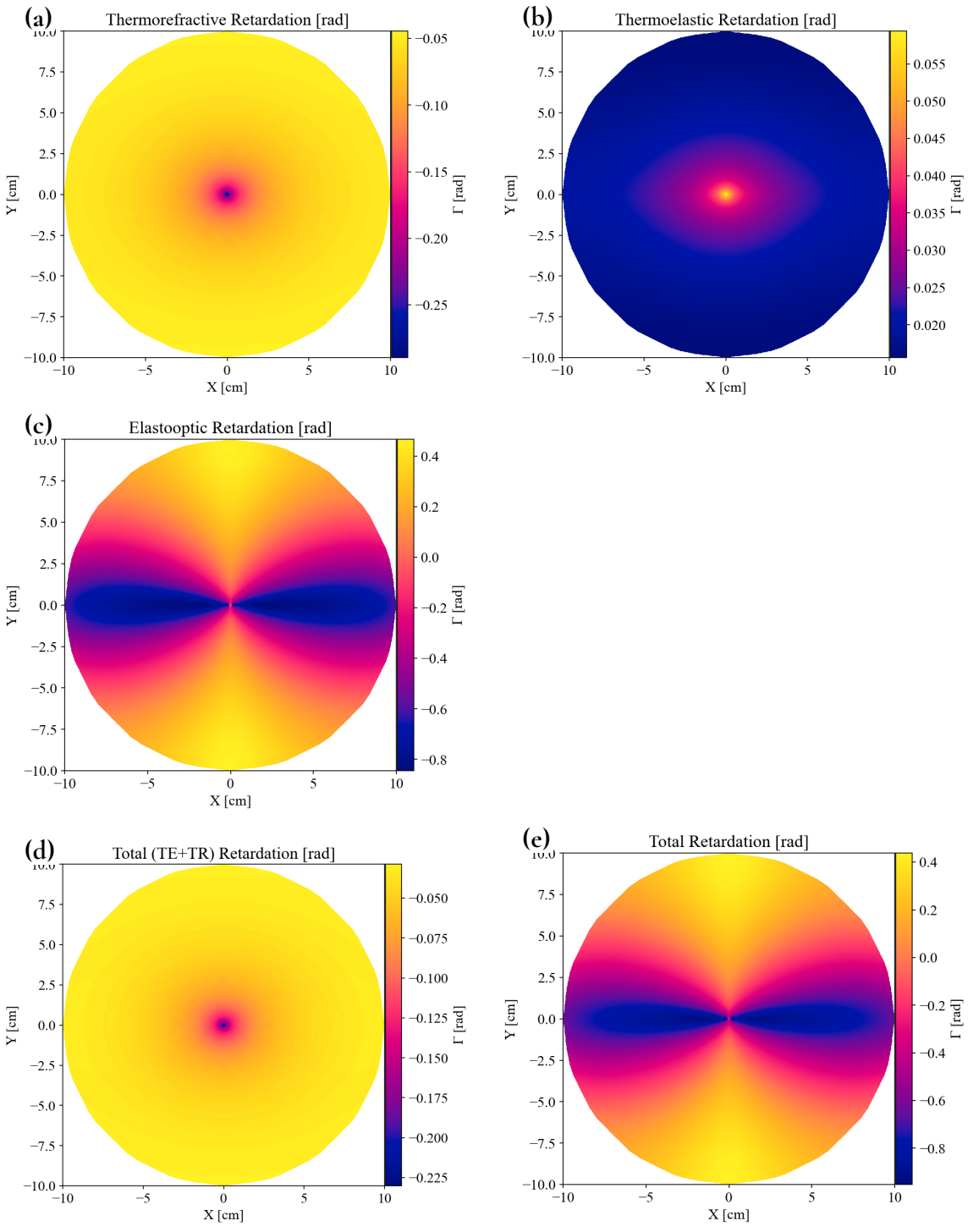

Figure B.3: Birefringence maps obtained of YVO4 with 0.1 W of $10\mu m$ incident laser.

B.1.2 CaCO3

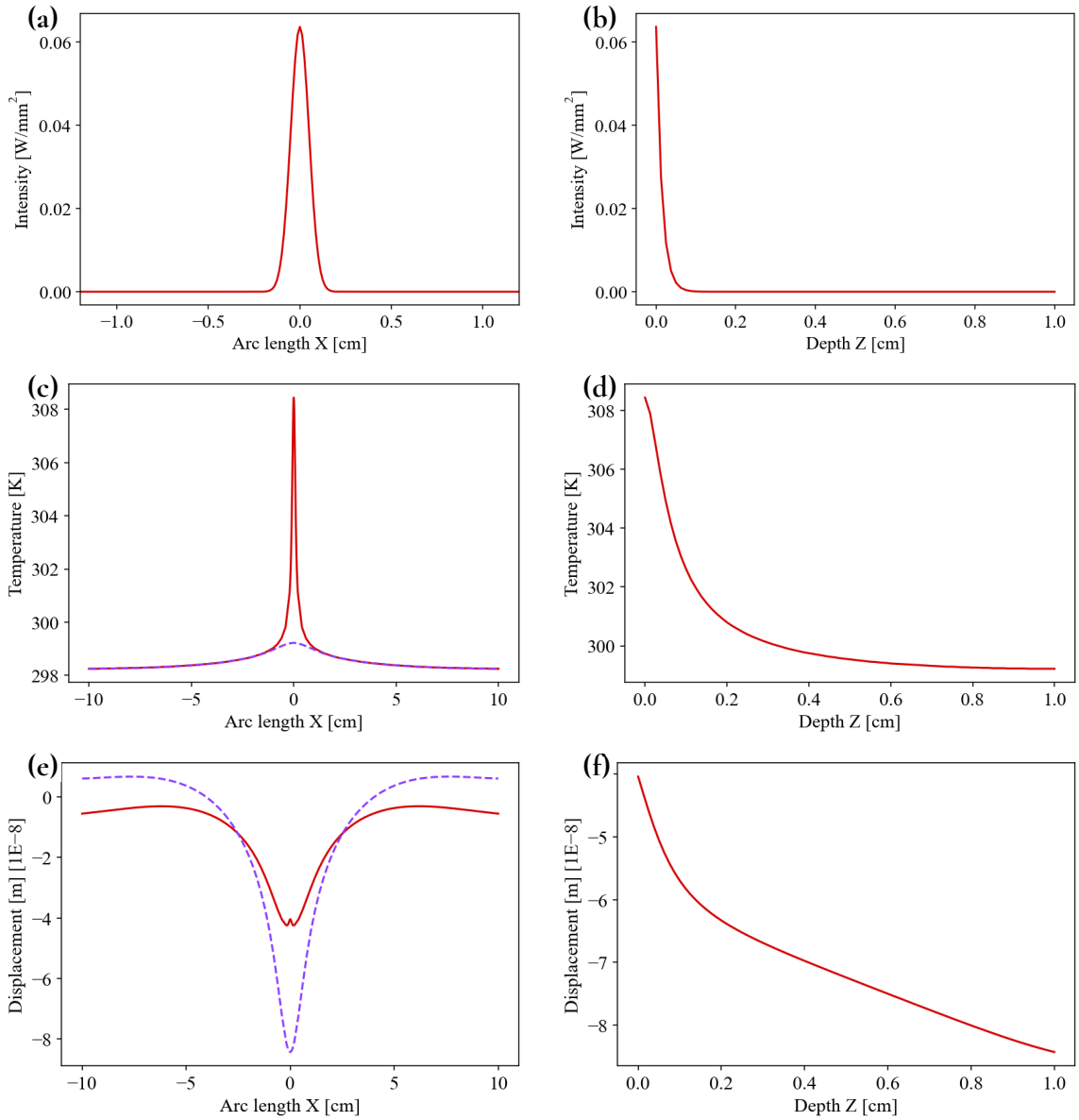

Figure B.4: The changes in CaCO3 with 0.1 W of $10\mu m$ incident laser. The plots (a,c,e) on the left side show data for the front face of the material using the red curve, and the purple dashed curve shows data on the back face. The plots on the right (b,d,f) side show data along the thickness of the material. The first plot, showing Intensity along the radial arc (on the X axis, $Y = Z = 0$), shows the Gaussian beam incident on the centre of the plate. Following the heating due to the Gaussian beam, a change in temperature and displacement of the material are shown on the second and third rows, respectively.

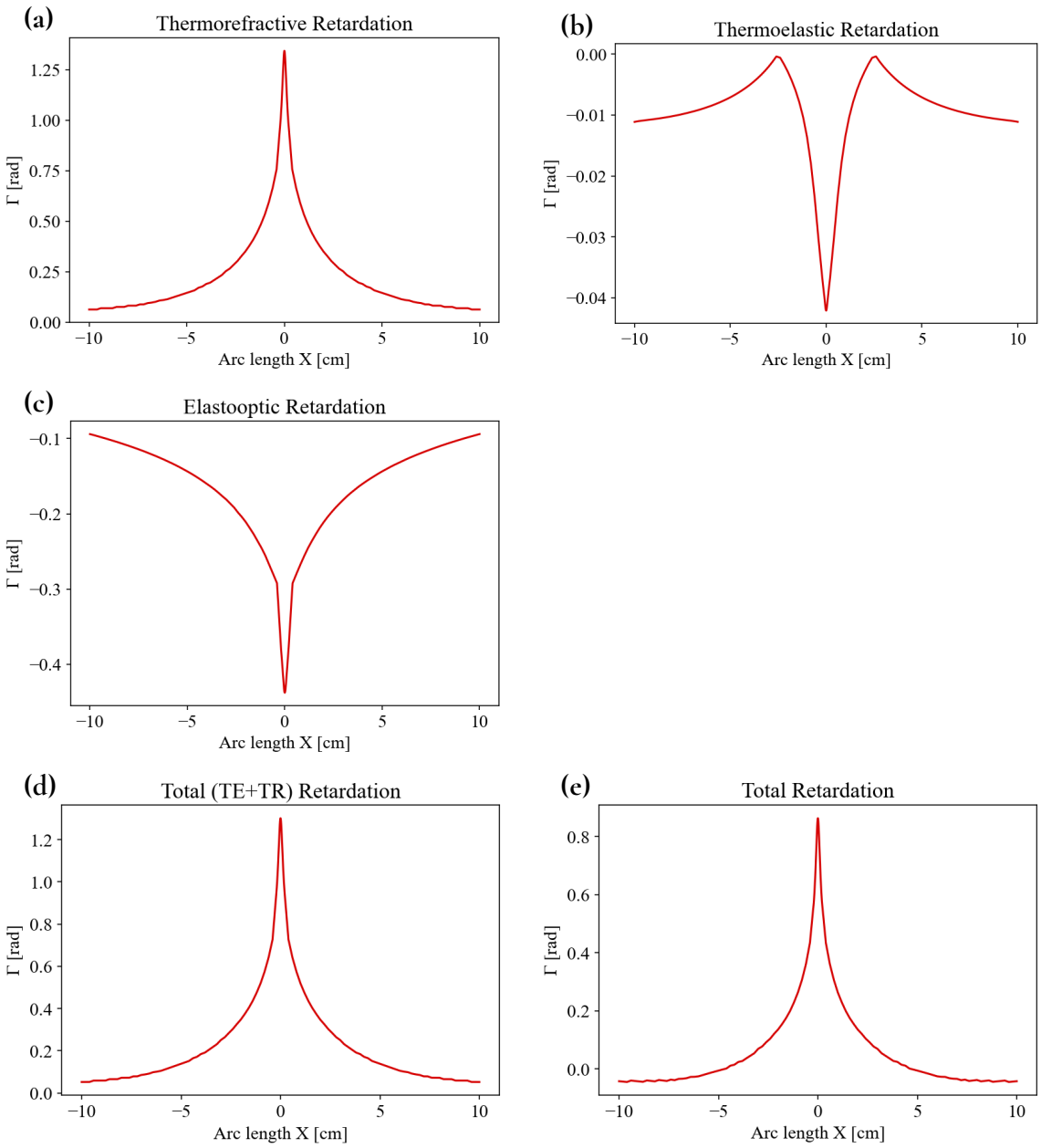

Figure B.5: The birefringence response at the central arc of CaCO3 with 0.1 W of 10μm incident laser.

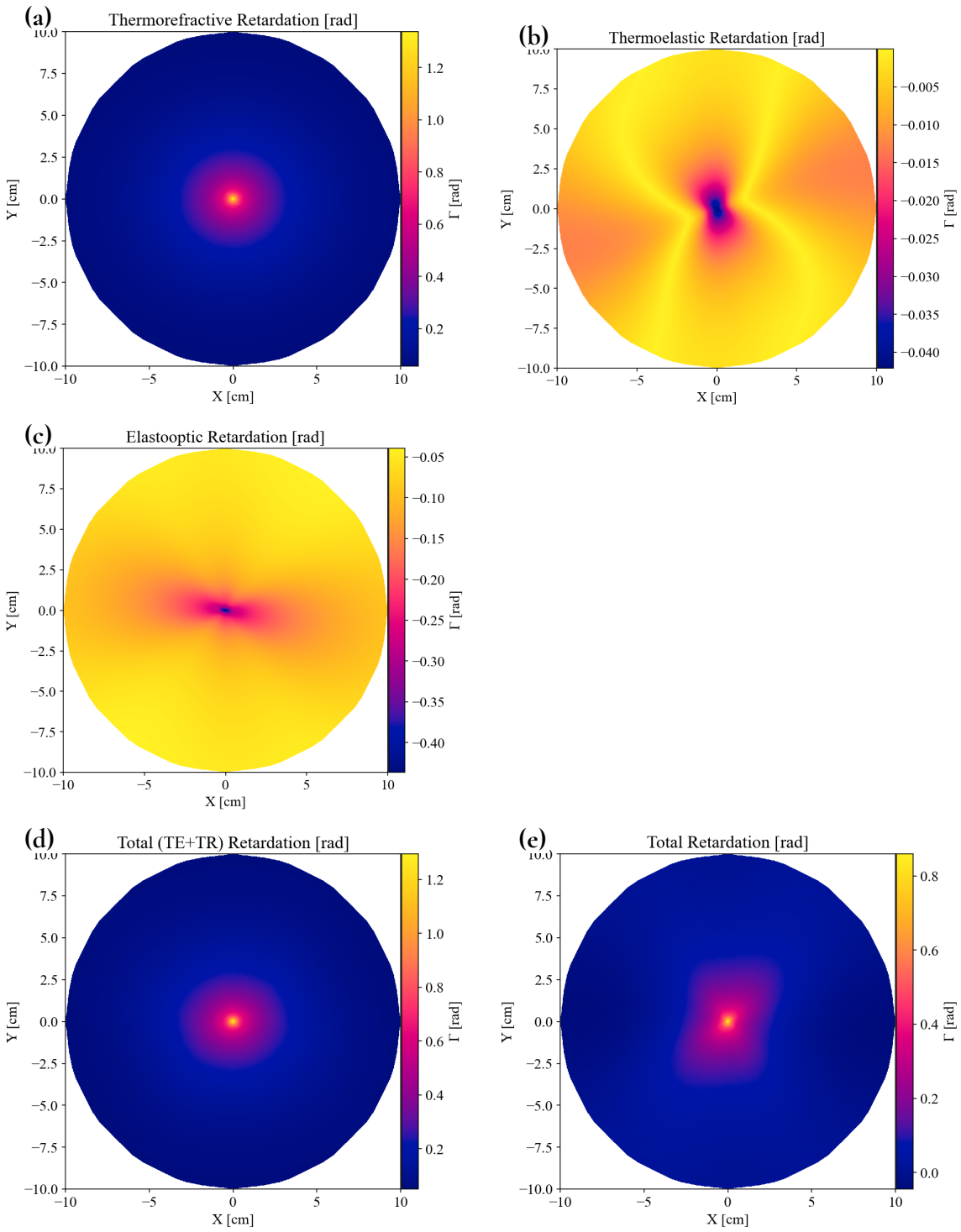

Figure B.6: Birefringence maps obtained of CaCO3 with 0.1 W of 10μm incident laser.

B.1.3 TiO2

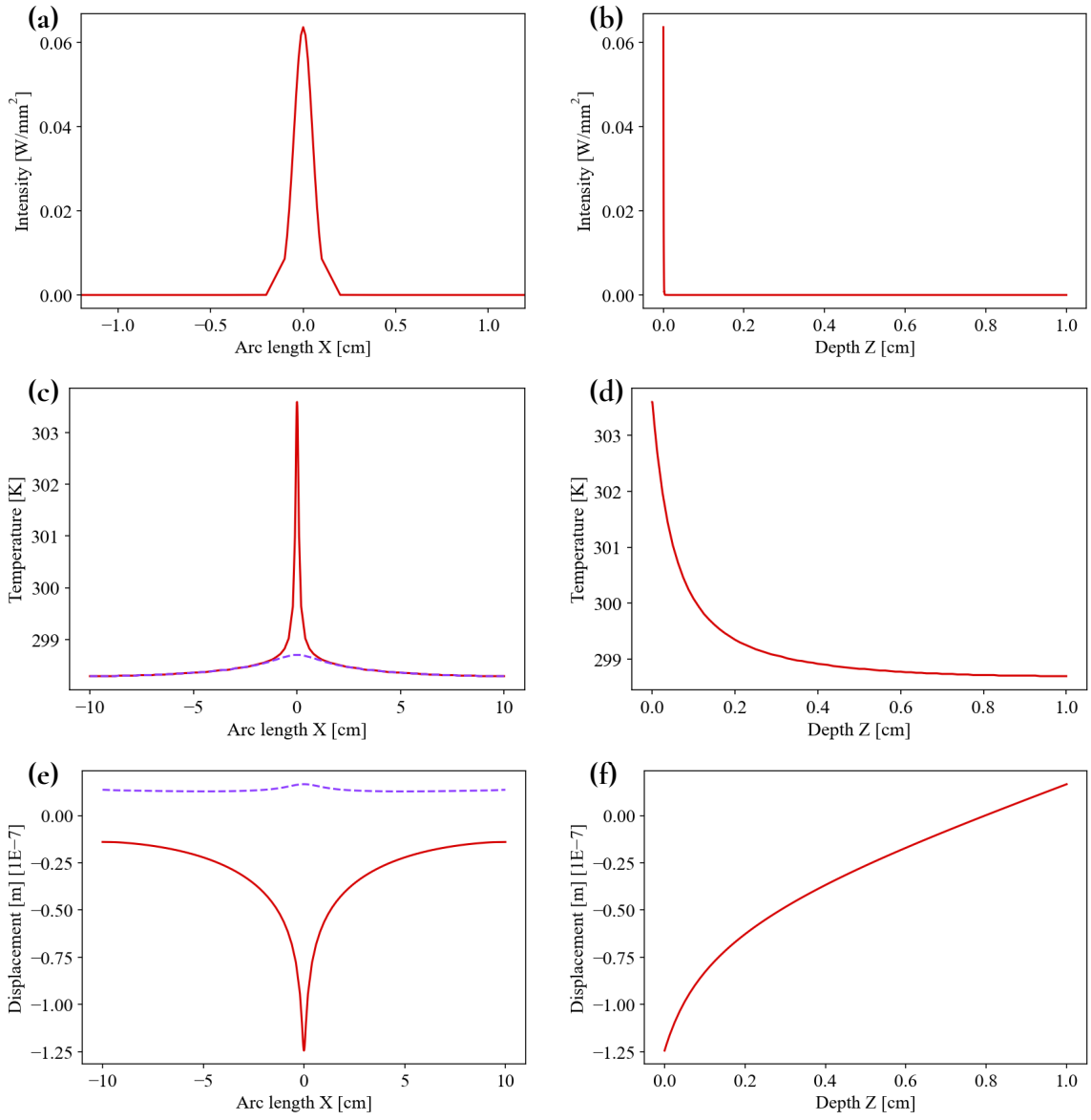

Figure B.7: The changes in TiO2 with 0.1 W of $10\mu m$ incident laser. The plots (a,c,e) on the left side show data for the front face of the material using the red curve, and the purple dashed curve shows data on the back face. The plots on the right (b,d,f) side show data along the thickness of the material. The first plot, showing Intensity along the radial arc (on the X axis, $Y = Z = 0$), shows the Gaussian beam incident on the centre of the plate. Following the heating due to the Gaussian beam, a change in temperature and displacement of the material are shown on the second and third rows, respectively.

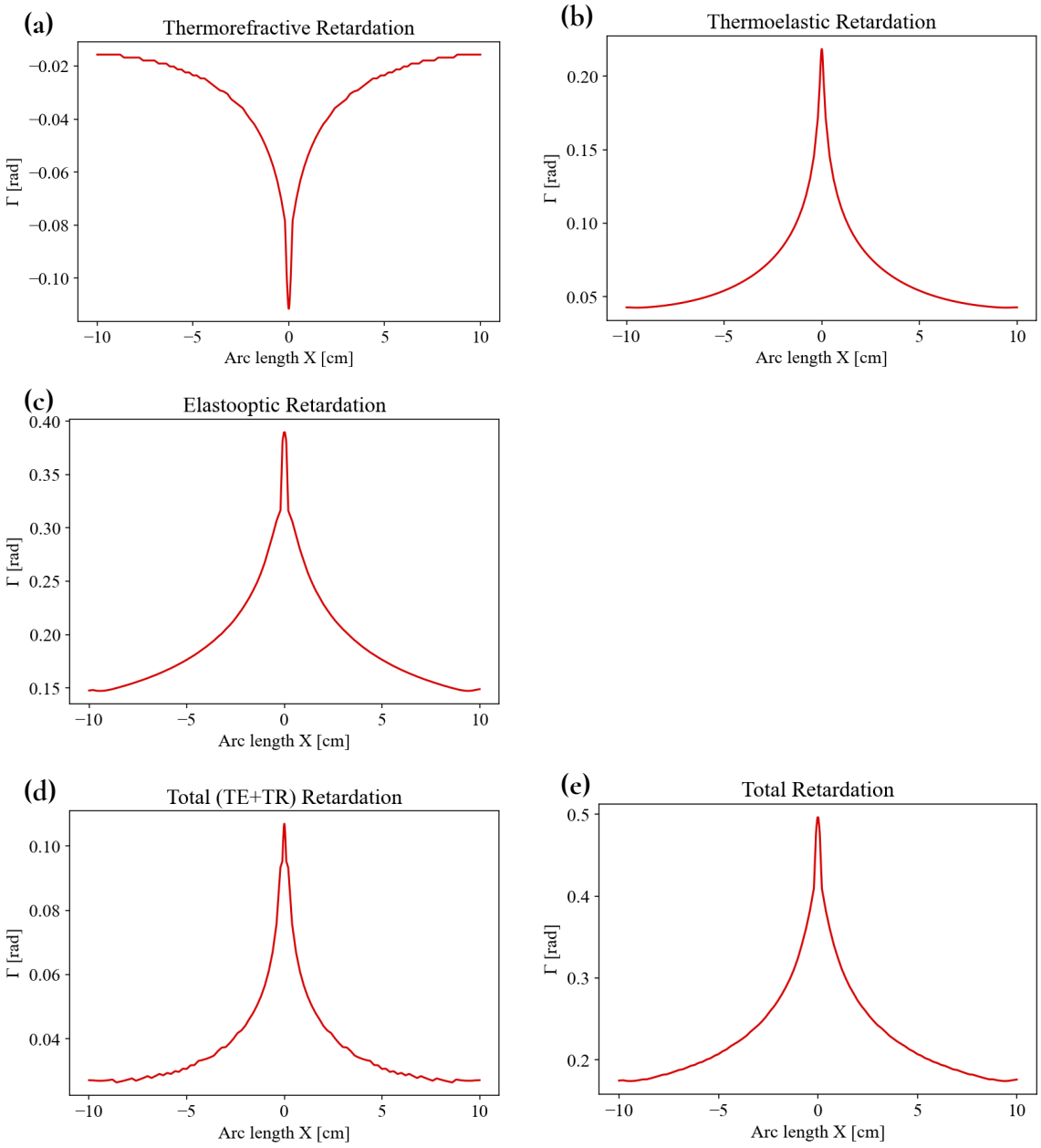

Figure B.8: The birefringence response at the central arc of TiO2 with 0.1 W of $10\mu m$ incident laser.

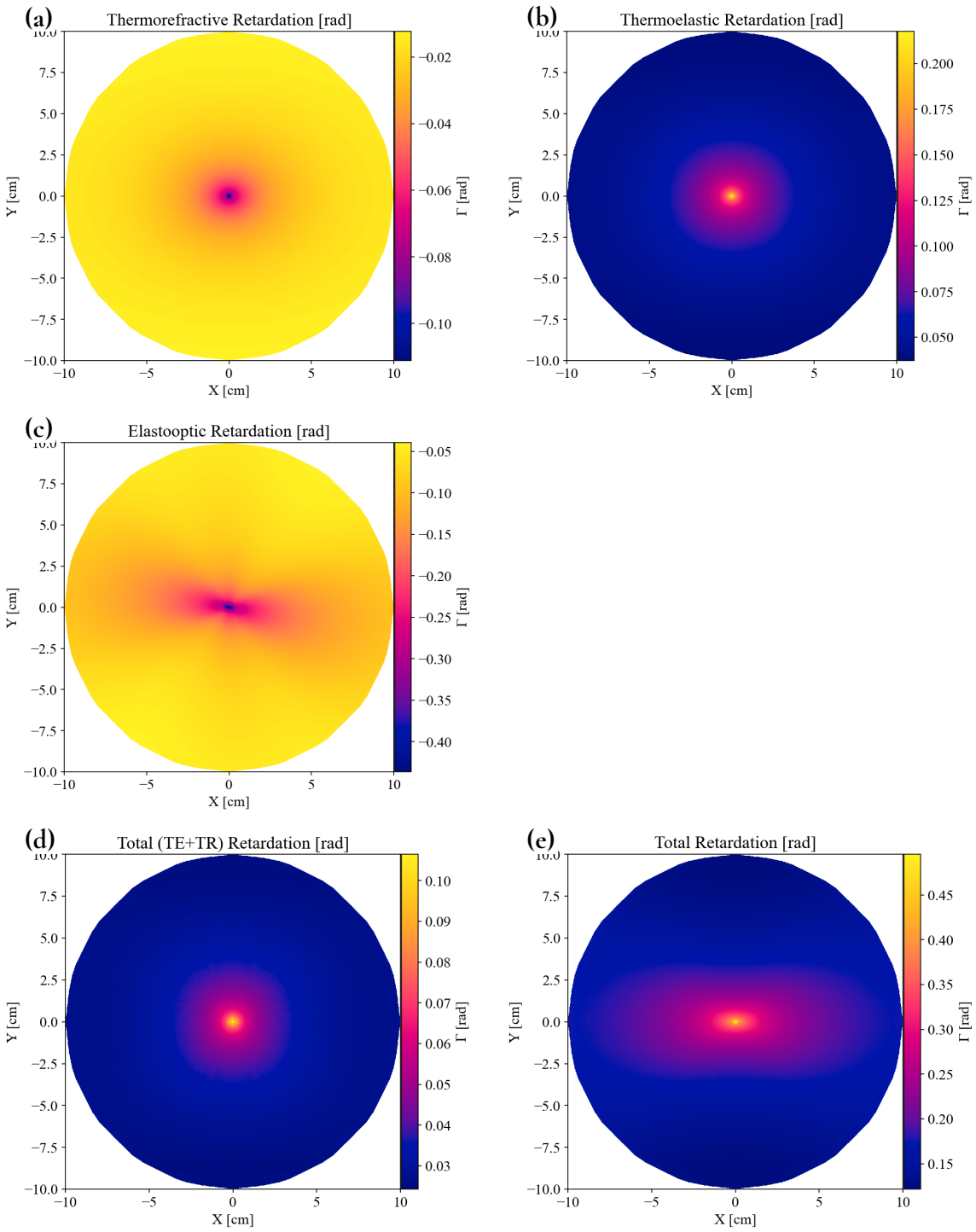

Figure B.9: Birefringence maps obtained of TiO2 with 0.1 W of 10μm incident laser.

B.1.4 Quartz

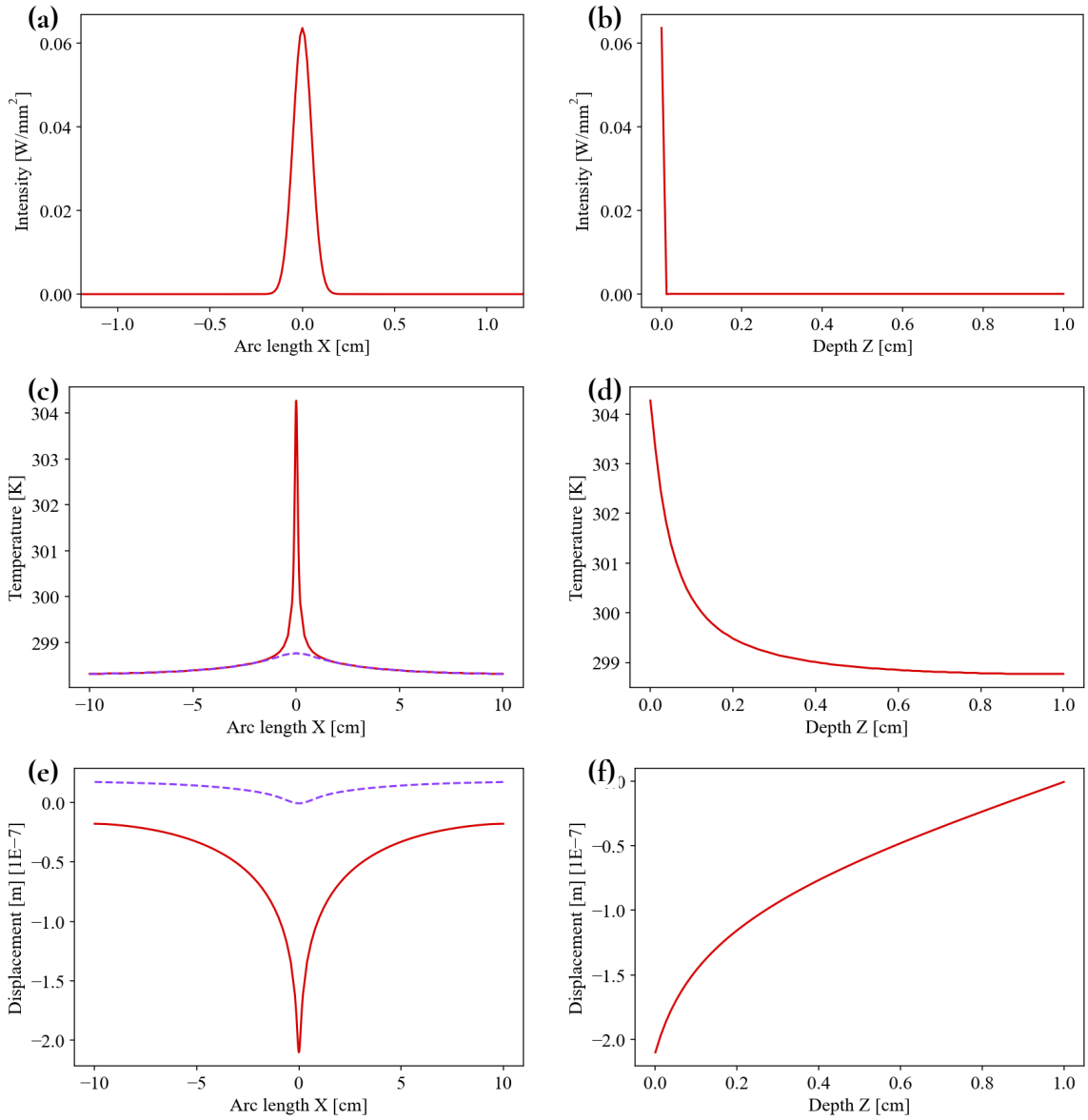

Figure B.10: The changes in Quartz with 0.1 W of $10\mu m$ incident laser. The plots (a,c,e) on the left side show data for the front face of the material using the red curve, and the purple dashed curve shows data on the back face. The plots on the right (b,d,f) side show data along the thickness of the material. The first plot, showing Intensity along the radial arc (on the X axis, $Y = Z = 0$), shows the Gaussian beam incident on the centre of the plate. Following the heating due to the Gaussian beam, a change in temperature and displacement of the material are shown on the second and third rows, respectively.

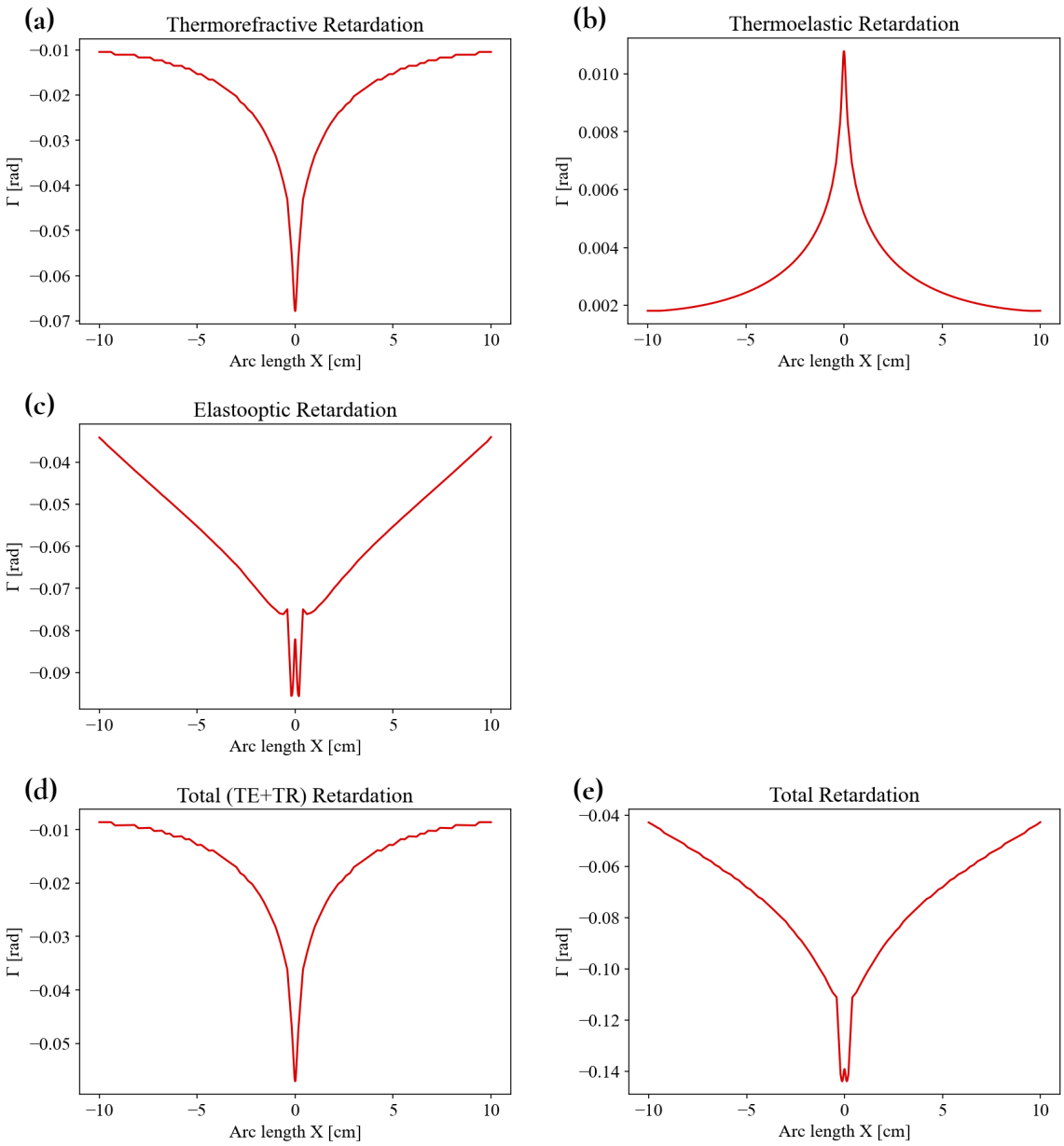

Figure B.11: The birefringence response at the central arc of Quartz with 0.1 W of 10μm incident laser.

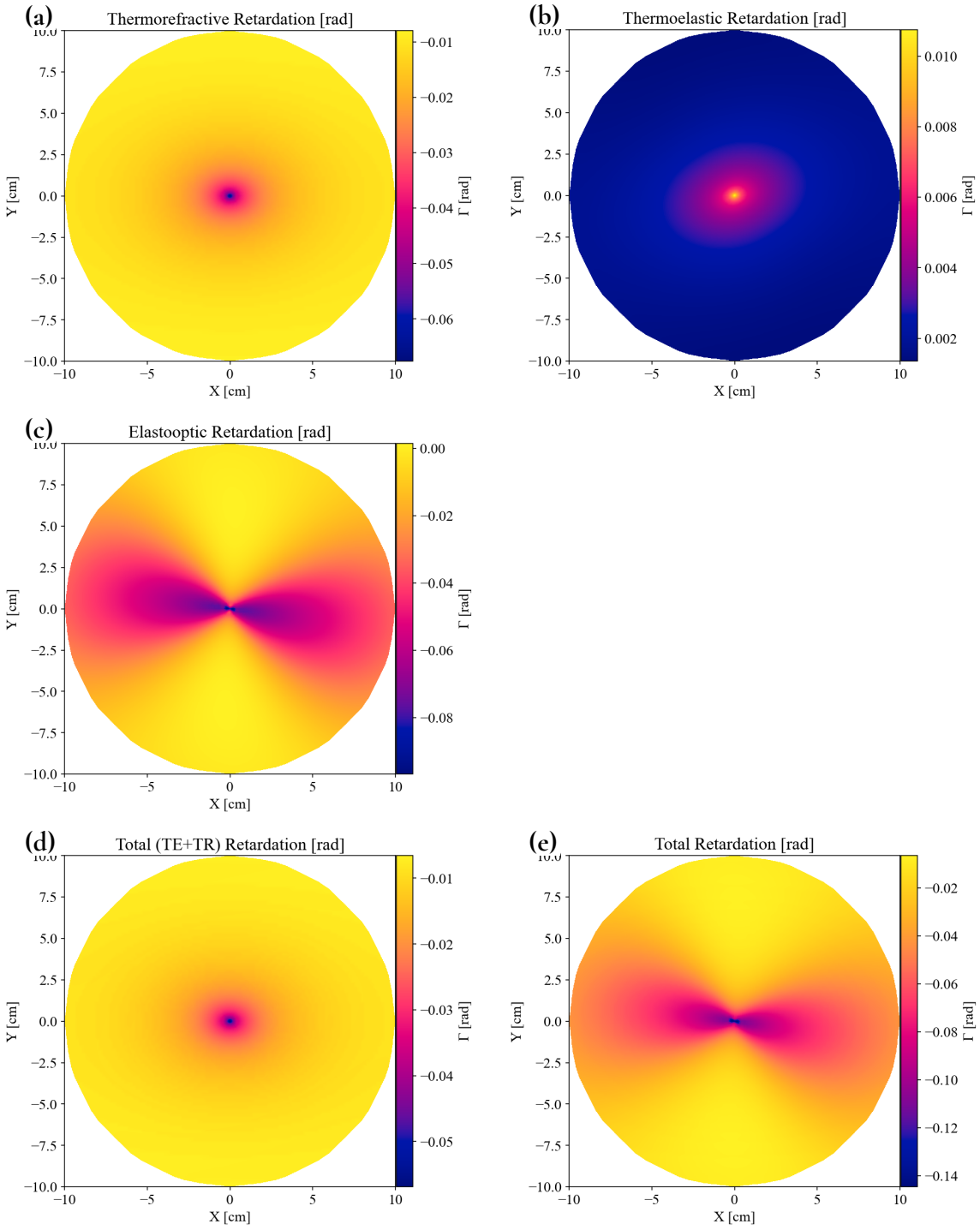

Figure B.12: Birefringence maps obtained of Quartz with 0.1 W of 10μm incident laser.

B.1.5 MgF2

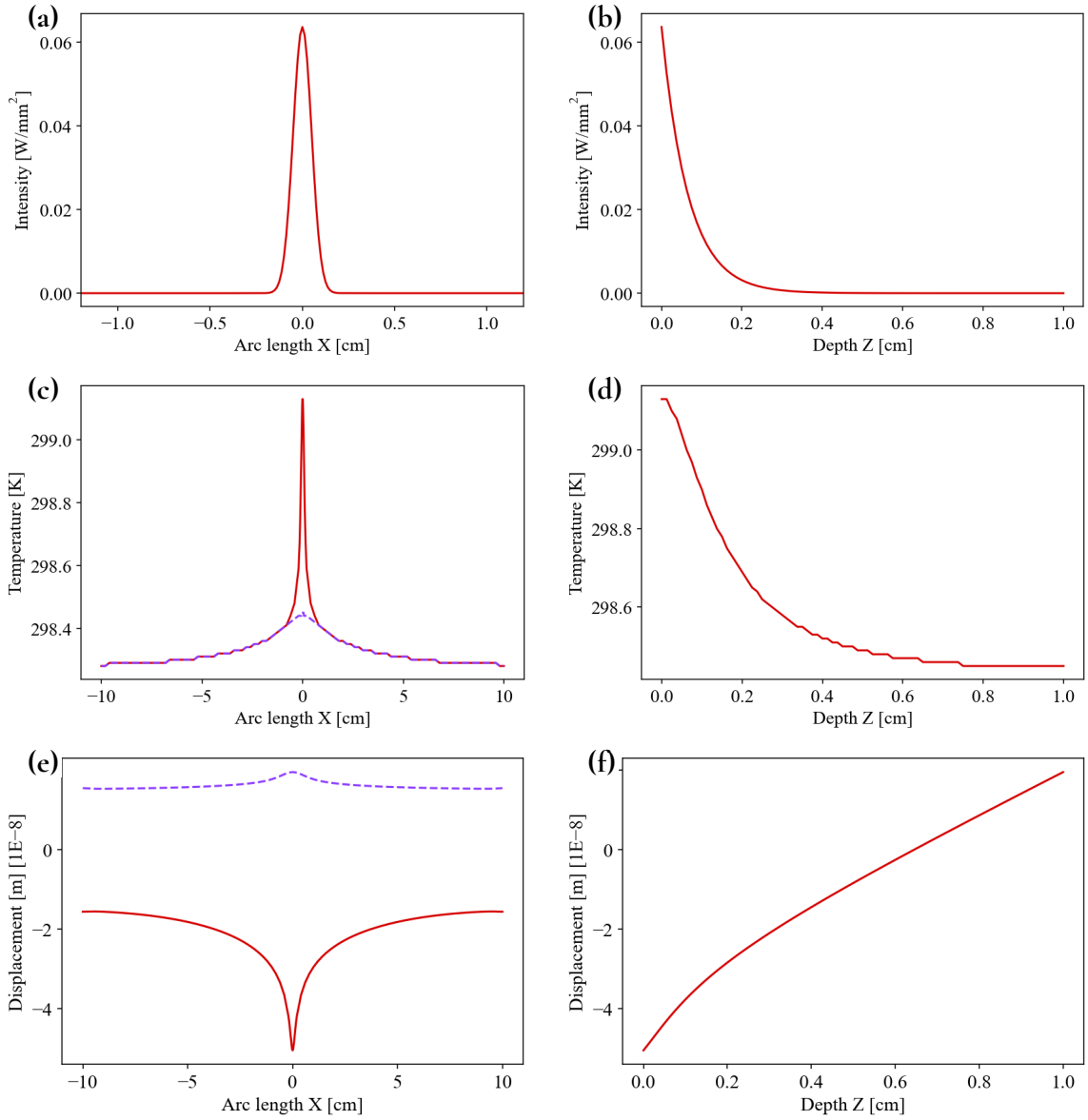

Figure B.13: The changes in MgF2 with 0.1 W of 10μm incident laser. The plots (a,c,e) on the left side show data for the front face of the material using the red curve, and the purple dashed curve shows data on the back face. The plots on the right (b,d,f) side show data along the thickness of the material. The first plot, showing Intensity along the radial arc (on the X axis, $Y = Z = 0$), shows the Gaussian beam incident on the centre of the plate. Following the heating due to the Gaussian beam, a change in temperature and displacement of the material are shown on the second and third rows, respectively.

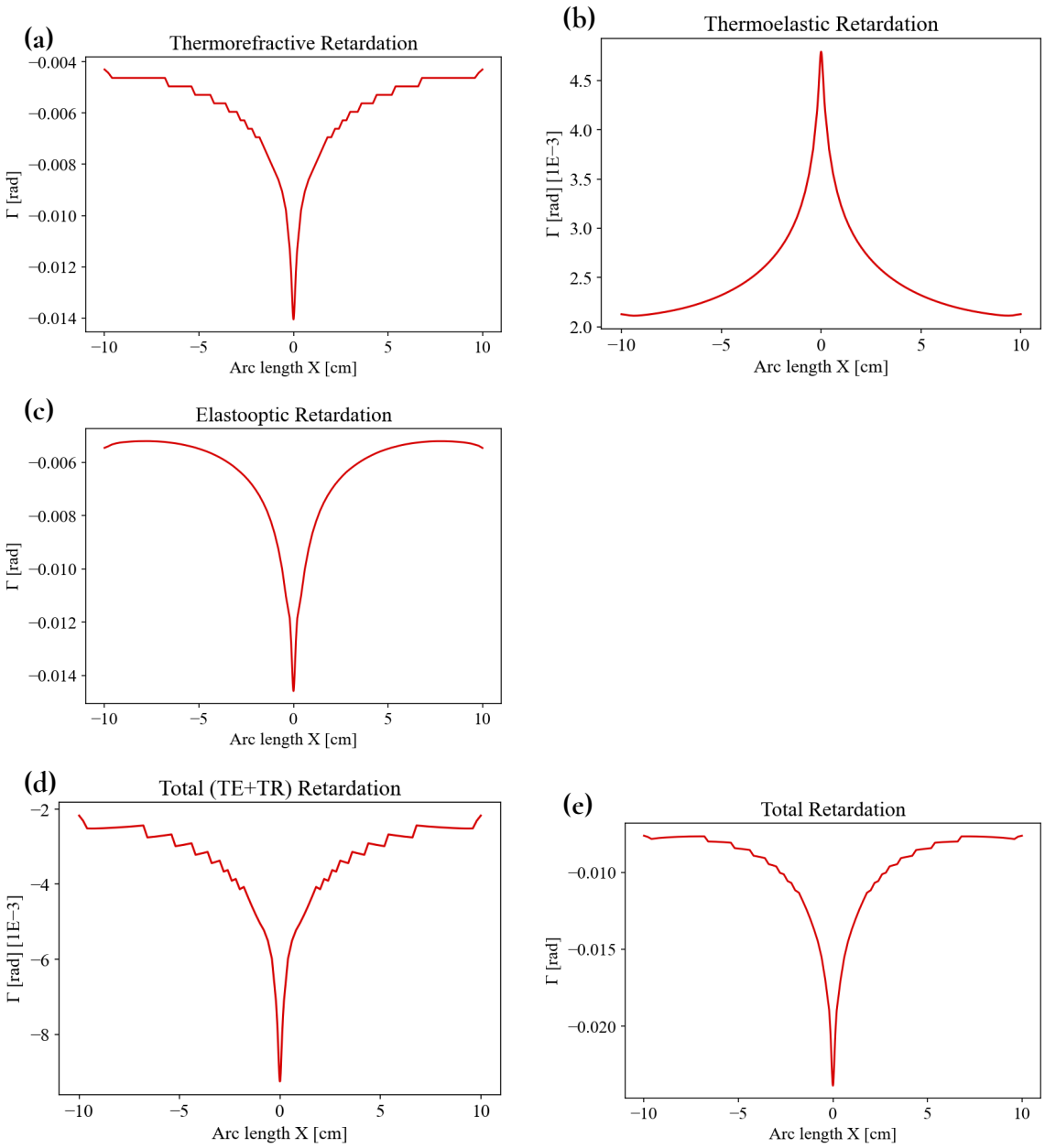

Figure B.14: The birefringence response at the central arc of MgF2 with 0.1 W of 10μm incident laser.

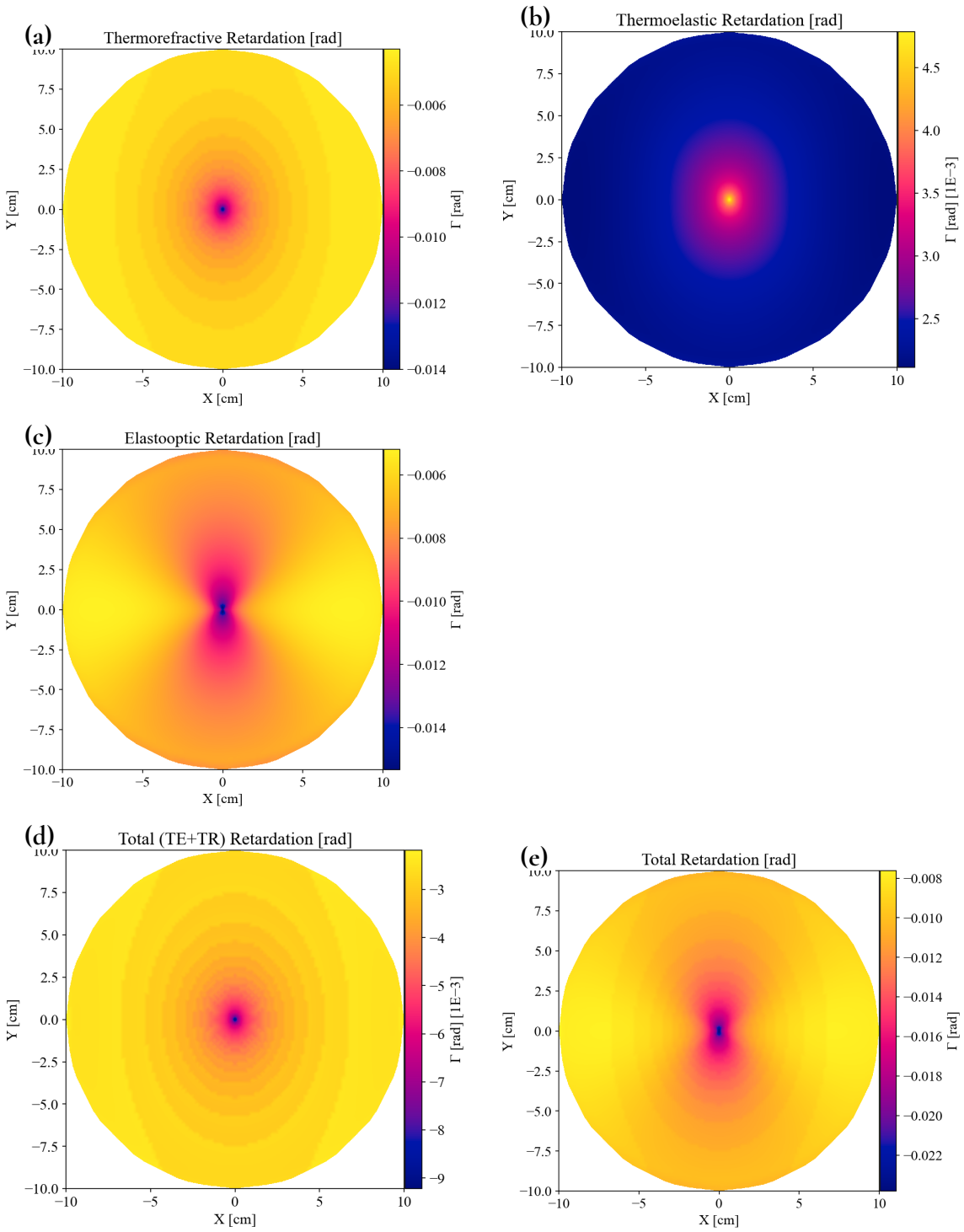

Figure B.15: Birefringence maps obtained of MgF2 with 0.1 W of 10μm incident laser.

B.1.6 Sapphire

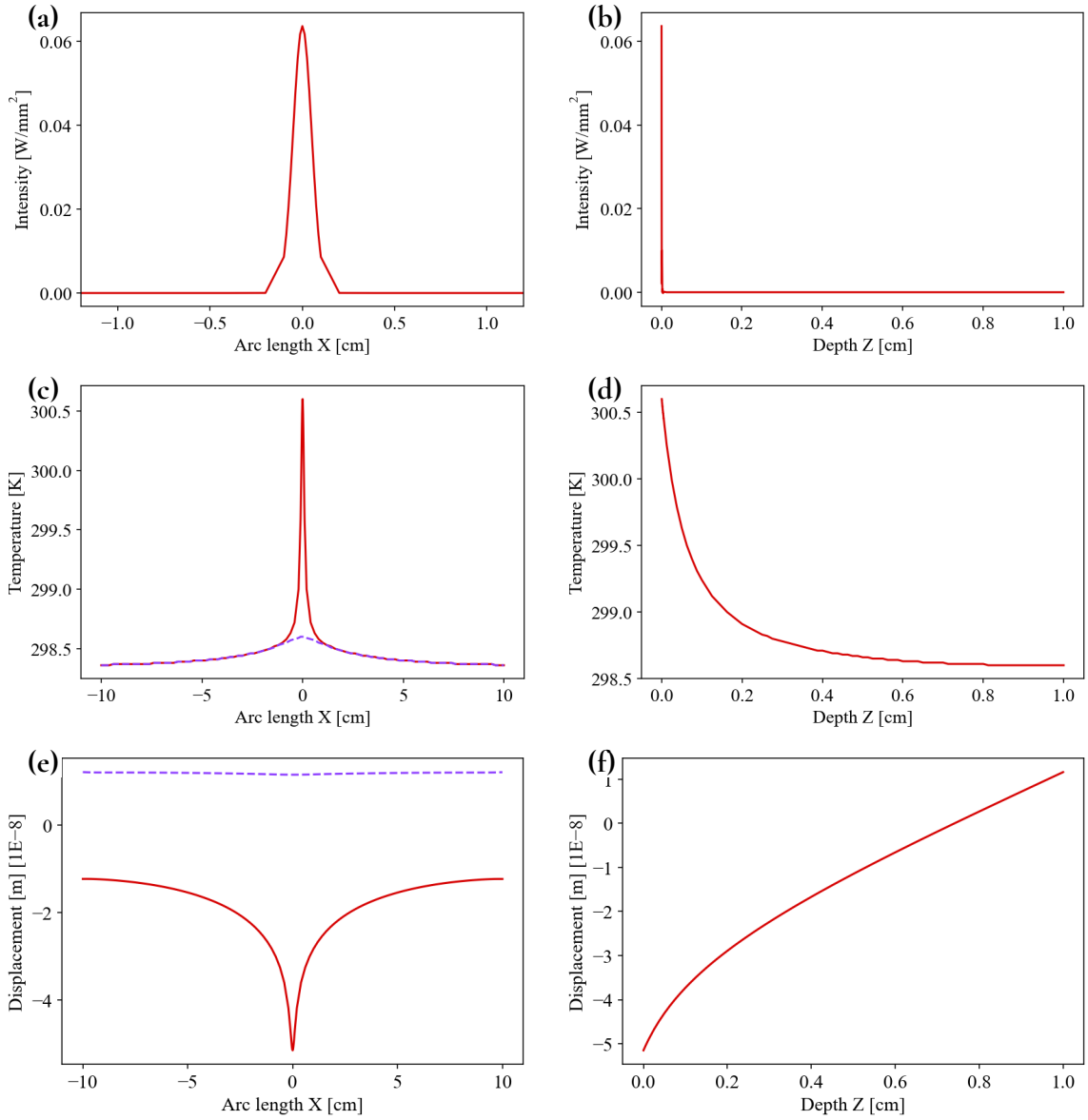

Figure B.16: The changes in Sapphire with 0.1 W of $10\mu m$ incident laser. The plots (a,c,e) on the left side show data for the front face of the material using the red curve, and the purple dashed curve shows data on the back face. The plots on the right (b,d,f) side show data along the thickness of the material. The first plot, showing Intensity along the radial arc (on the X axis, $Y = Z = 0$), shows the Gaussian beam incident on the centre of the plate. Following the heating due to the Gaussian beam, a change in temperature and displacement of the material are shown on the second and third rows, respectively.

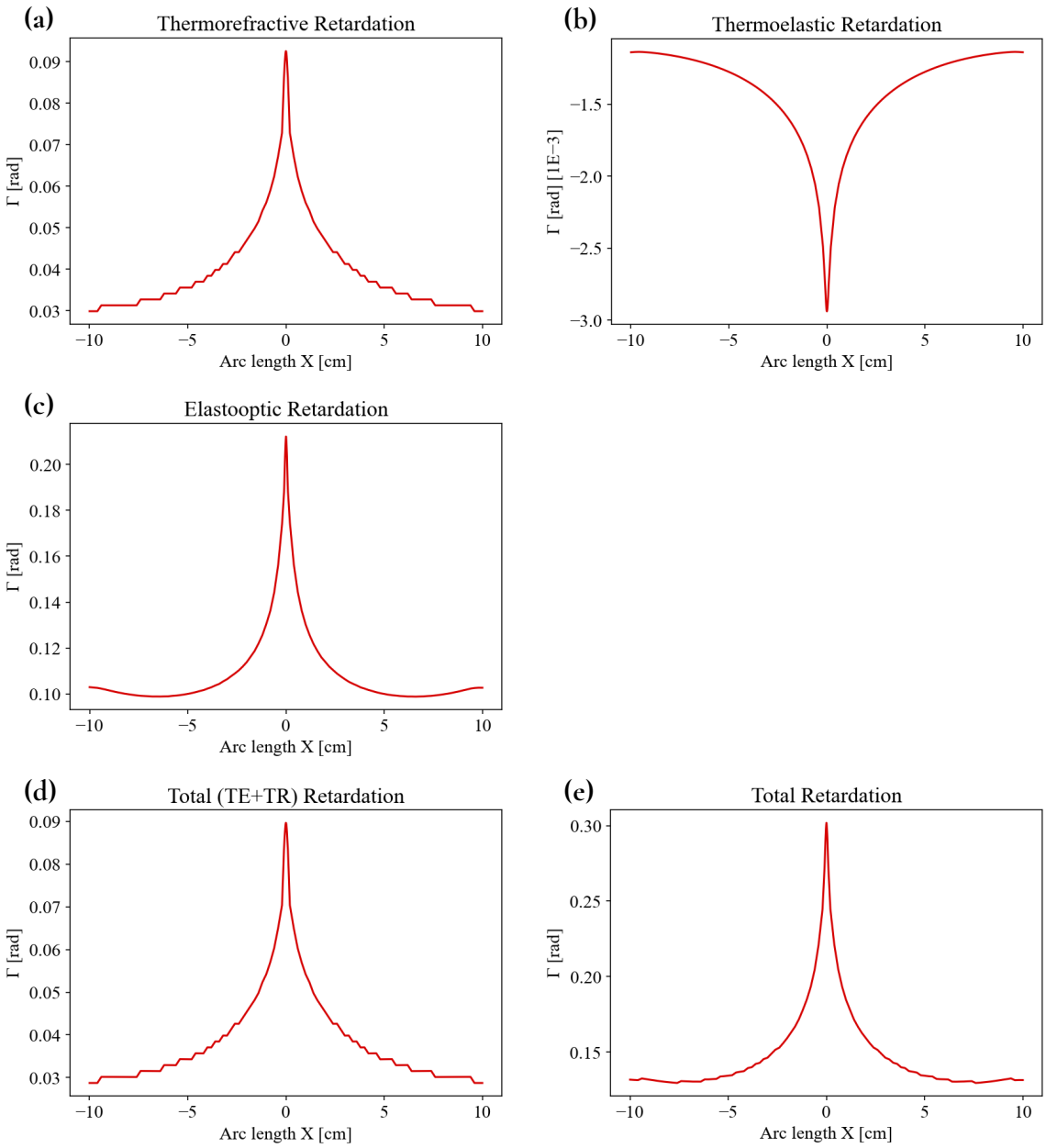

Figure B.17: The birefringence response at the central arc of Sapphire with 0.1 W of $10\mu m$ incident laser.

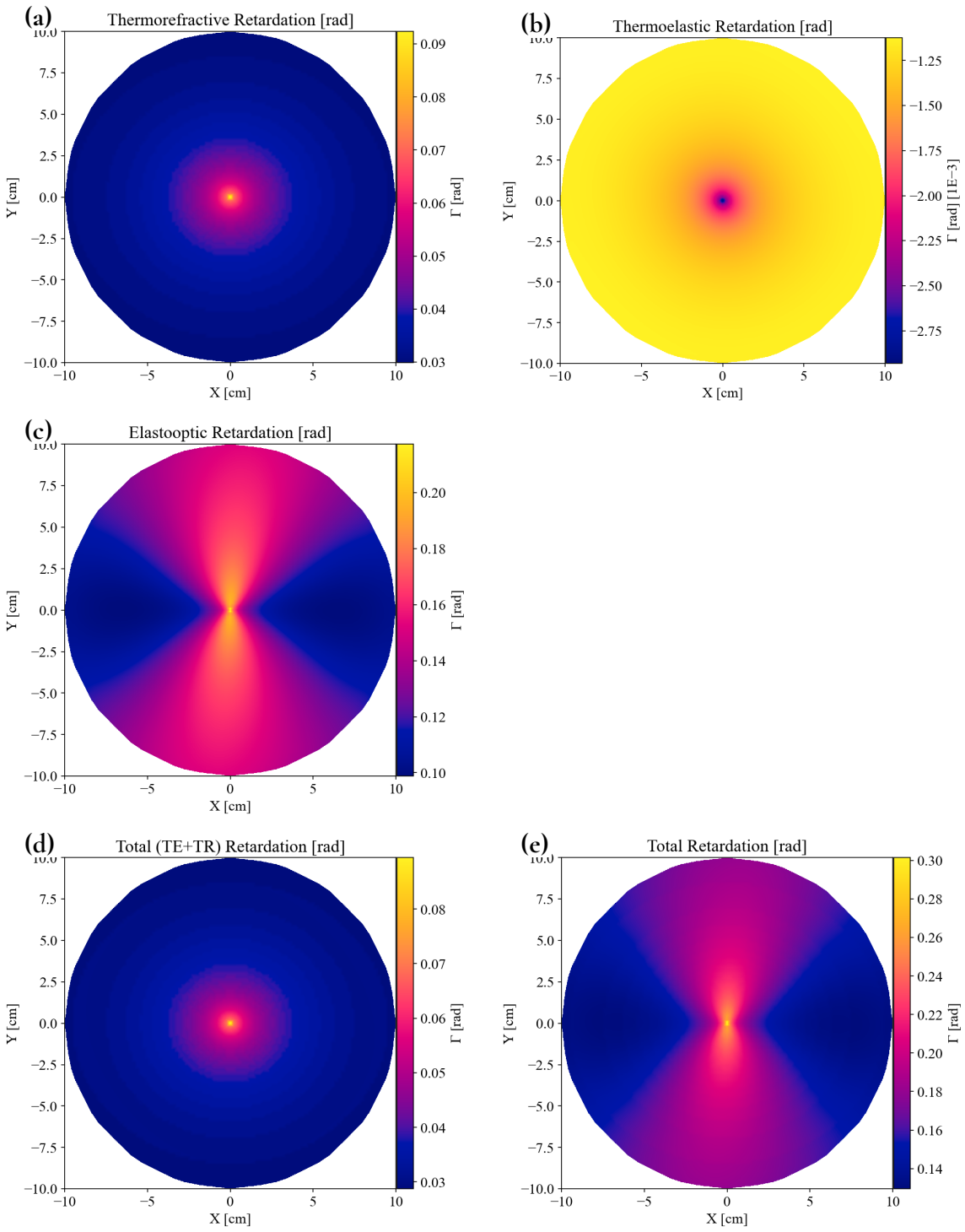

Figure B.18: Birefringence maps obtained of Sapphire with 0.1 W of 10μm incident laser.

Bibliography

[1] Albert Einstein. *The Meaning of Relativity*. 5th ed. Princeton: Princeton University Press, 1922.

[2] Charles W. Misner, Kip S. Thorne and John Archibald Wheeler. *Gravitation*. San Francisco: W. H. Freeman and Company, 1970.

[3] Michele Maggiore. *Gravitational Waves*. Online edn, Oxford Academic; accessed 2026-01-31. Oxford: Oxford University Press, 2008. ISBN: 9780198570745. DOI: 10.1093/acprof:oso/9780198570745.001.0001.

[4] LIGO Scientific Collaboration and Virgo Collaboration. 'GWTC-1: A Gravitational-Wave Transient Catalog of Compact Binary Mergers Observed by LIGO and Virgo during the First and Second Observing Runs'. In: *Physical Review X* 9 (Sept. 2019), p. 031040. DOI: 10.1103/PhysRevX.9.031040.

[5] B. P. *et al.* Abbott. 'Observation of Gravitational Waves from a Binary Black Hole Merger'. In: *Phys. Rev. Lett.* 116 (6 Feb. 2016), p. 061102. DOI: 10.1103/PhysRevLett.116.061102.

[6] LIGO Scientific Collaboration. 'Searches for Continuous Gravitational Waves from Nine Young Supernova Remnants'. In: *The Astrophysical Journal* 813 (Oct. 2015), p. 39. DOI: 10.1088/0004-637X/813/1/39.

[7] Nelson Christensen. 'Stochastic Gravitational Wave Backgrounds'. In: *Reports on Progress in Physics* 82 (Jan. 2019), p. 016903. DOI: 10.1088/1361-6633/aae6bb.

[8] Peter R. Saulson. *Fundamentals of Interferometric Gravitational Wave Detectors*. Singapore: World Scientific, 1994.

[9] Rana Adhikari. 'Sensitivity and Noise Analysis of 4 km Laser Interferometric Gravitational Wave Antennae'. Submitted to the Department of Physics on July 7, 2004. PhD thesis. Massachusetts Institute of Technology, July 2004. URL: https://gwic.science/assets/docs/theses/Adhikari_Thesis.pdf.

[10] D. R. Herriot and H. J. Schulte. 'Folded Optical Delay Lines'. In: *Applied Optics* 4.8 (1965), pp. 883–889.

[11] Rainer Weiss. *Electromagnetically Coupled Broadband Gravitational Antenna*. Tech. rep. Quarterly Progress Report 105. Cambridge, Massachusetts: Research Laboratory of Electronics, Massachusetts Institute of Technology, Apr. 1972.

[12] David Shoemaker, Reinhard Schilling, Lothar Schnupp, Walter Winkler, Karl Maischberger and Albrecht Rüdiger. 'Noise Behavior of the Garching 30-Meter Prototype Gravitational-Wave Detector'. In: *Physical Review D* 38.2 (July 1988), pp. 423–432.

[13] Ronald W. P. Drever. 'Interferometric Detectors of Gravitational Radiation'. In: *Gravitational Radiation*. Ed. by Nathalie Deruelle and Tsvi Piran. Les Houches, France: Centre de Physique des Houches, 1982, pp. 321–338.

[14] Peter K. Fritschel. 'Techniques for Laser Interferometer Gravitational Wave Detectors'. PhD thesis. Massachusetts Institute of Technology, Feb. 1992.

[15] D. Schnier, J. Mizuno, G. Heinzel, H. Lück, A. Rüdiger, R. Schilling, M. Schrempel, W. Winkler and K. Danzmann. 'Power Recycling in the Garching 30 m Prototype Interferometer for Gravitational-Wave Detection'. In: *Physics Letters A* 225 (1997), pp. 210–216.

[16] B. J. Meers. 'Recycling in laser-interferometric gravitational-wave detectors'. In: *Physical Review D* 38 (1988), pp. 2317–2326. DOI: 10.1103/PhysRevD.38.2317.

[17] Jun Mizuno. 'Comparison of Optical Configurations for Laser-Interferometric Gravitational-Wave Detectors'. PhD thesis. Universität Hannover, 1995.

[18] Robert L. Forward. 'Wideband Laser-Interferometer Gravitational-Radiation Experiment'. In: *Physical Review D* 17.2 (1978), pp. 379–390.

[19] Masaki Ando and the TAMA Collaboration. 'Stable Operation of a 300-m Laser Interferometer with Sufficient Sensitivity to Detect Gravitational-Wave Events within Our Galaxy'. In: *arXiv preprint* (2001). arXiv: astro-ph/0105473.

[20] GEO Collaboration. *GEO600: Status and Plans*. Tech. rep. P070043. LIGO Document Control Center, 2007. URL: https://dcc.ligo.org/public/0006/P070043/000/P070043-00.pdf.

[21] The LIGO Scientific Collaboration. 'LIGO: The Laser Interferometer Gravitational-Wave Observatory'. In: *Reports on Progress in Physics* 72.7 (2009), p. 076901. DOI: 10.1088/0034-4885/72/7/076901. arXiv: 0711.3041 [gr-qc].

[22] B. Caron *et al.* 'The Virgo interferometer'. In: *Classical and Quantum Gravity* 14.6 (1997), pp. 1461–1469. DOI: 10.1088/0264-9381/14/6/011.

[23] J. Aasi et al. 'Advanced LIGO'. In: *Classical and Quantum Gravity* 32.7 (2015), p. 074001. DOI: 10.1088/0264-9381/32/7/074001. arXiv: 1411.4547 [gr-qc].

[24] The Virgo Collaboration. 'Advanced Virgo: a second generation interferometric gravitational wave detector'. In: *Classical and Quantum Gravity* (2015). DOI: 10.48550/arXiv.1408.3978. arXiv: 1408.3978 [gr-qc].

[25] A. H. Nitz, S. Kumar, Y.-F. Wang, S. Kastha, S. Wu, M. Schäfer, R. Dhurkunde and C. D. Capano. '4-OGC: Catalog of Gravitational Waves from Compact Binary Mergers'. In: *arXiv e-prints* (2021). DOI: 10.48550/arXiv.2112.06878. arXiv: 2112.06878 [gr-qc].

[26] B. P. *et al.* Abbott. 'GW170817: Observation of Gravitational Waves from a Binary Neutron Star Inspiral'. In: *Phys. Rev. Lett.* 119 (16 Oct. 2017), p. 161101. DOI: 10.1103/PhysRevLett.119.161101.

[27] M. Bailes, B. K. Berger, P. R. Brady, M. Branchesi, K. Danzmann, M. Evans, K. Holley-Bockelmann, B. R. Iyer, T. Kajita, S. Katsanevas et al. 'Gravitational-wave Physics and Astronomy in the 2020s and 2030s'. In: *Nature Reviews Physics* 3 (2021), pp. 344–366. DOI: 10.1038/s42254-021-00303-8.

[28] ET Steering Committee. *ET Design Report Update 2020*. Accessed: 2022-04-02. 2020. URL: https://www.et-gw.eu/index.php/relevant-et-documents.

[29] T. Akutsu, M. Ando, K. Arai, Y. Arai, S. Araki, A. Araya, N. Aritomi, Y. Aso, S. Bae, Y. Bae et al. 'Overview of KAGRA: Detector Design and Construction History'. In: *Progress of Theoretical and Experimental Physics* 2021.05 (2021), 05A101. DOI: 10.1093/ptep/ptaa125. arXiv: 2005.05574 [physics.ins-det].

[30] M. Evans, R. X. Adhikari, C. Afle, S. W. Ballmer, S. Biscoveanu, S. Borhanian, D. A. Brown, Y. Chen, R. Eisenstein, A. Gruson et al. 'A Horizon Study for Cosmic Explorer: Science, Observatories, and Community'. In: *arXiv e-prints* (2021). DOI: 10.48550/arXiv.2109.09882. arXiv: 2109.09882 [gr-qc].

[31] Christopher J. Moore, Robert H. Cole and Christopher P. L. Berry. *Gravitational-Wave Detectors and Sources (GWplotter)*. https://gwplotter.com/. Accessed: 2026-01-29.

[32] J. Harms. 'Terrestrial gravity fluctuations'. In: *Living Reviews in Relativity* 18.3 (2015). DOI: 10.1007/lrr-2015-3.

[33] A. Buonanno and Y. Chen. 'Quantum Noise in Second Generation, Signal-Recycled Laser Interferometric Gravitational-Wave Detectors'. In: *Physical Review D* 64 (2001), p. 042006. DOI: 10.1103/PhysRevD.64.042006.

[34] A. Buonanno, Y. Chen and N. Mavalvala. 'Quantum Noise in Laser-Interferometer Gravitational-Wave Detectors with a Heterodyne Readout Scheme'. In: *Physical Review D* 67 (2003), p. 122005. DOI: 10.1103/PhysRevD.67.122005.

[35] L. McCuller, C. Whittle, D. Ganapathy, K. Komori, M. Tse, L. Barsotti, P. Fritschel, M. MacInnis, F. Matichard, K. Mason, N. Mavalvala, R. Mittleman, H. Yu and M. E. Zucker. 'Frequency-Dependent Squeezing for Advanced LIGO'. In: *Physical Review Letters* 124.171102 (2020). DOI: 10.1103/PhysRevLett.124.171102.

[36] G. González. 'Suspensions Thermal Noise in the LIGO Gravitational Wave Detector'. In: *Classical and Quantum Gravity* 17.21 (2000), pp. 4409–4432. DOI: 10.1088/0264-9381/17/21/301.

[37] Kentaro Komori. *KAGRA Logbook entry referencing the kagrapygwinc repository*. KAGRA Logbook. Accessed: 2026-01-29. URL: https://klog.icrr.u-tokyo.ac.jp/osl/?r=31984.

[38] R. Clark Jones. 'A New Calculus for the Treatment of Optical SystemsI. Description and Discussion of the Calculus'. In: *J. Opt. Soc. Am.* 31.7 (1941), pp. 488–493. DOI: 10.1364/JOSA.31.000488. URL: https://opg.optica.org/abstract.cfm?URI=josa-31-7-488.

[39] Russell A Chipman, Wai-Sze Tiffany Lam and Garam Young. *Polarized Light and Optical Systems (1st ed.)* CRC Press, 2018.

[40] D.H. Goldstein. *Polarized Light (3rd ed.)* CRC Press, 2011.

[41] J.F. Nye. *Physical Properties of crystals*. Oxford University Press, 1985. ISBN: 9780198511656.

[42] Garam Yun, Karlton Crabtree and Russell A. Chipman. 'Three-dimensional polarization ray-tracing calculus I: definition and diattenuation'. In: *Appl. Opt.* 50.18 (2011), pp. 2855–2865. DOI: 10.1364/AO.50.002855. URL: https://opg.optica.org/ao/abstract.cfm?URI=ao-50-18-2855.

[43] Garam Yun, Stephen C. McClain and Russell A. Chipman. 'Three-dimensional polarization ray-tracing calculus II: retardance'. In: *Appl. Opt.* 50.18 (2011), pp. 2866–2874. DOI: 10.1364/AO.50.002866.

[44] Simon Zeidler, Marc Eisenmann, Marco Bazzan, Pengbo Li and Matteo Leonardi. 'Correlation between birefringence and absorption mapping in large-size Sapphire substrates for gravitational-wave interferometry'. In: *Scientific Reports* 13.1 (2023), p. 21393. ISSN: 2045-2322. DOI: 10.1038/s41598-023-45928-0.

[45] Haoyu Wang, Yoichi Aso, Matteo Leonardi, Marc Eisenmann, Eiichi Hirose, GariLynn Billingsley, Keiko Kokeyama, Takafumi Ushiba, Masahide Tamaki and Yuta Michimura. 'Characterization of birefringence inhomogeneity of KAGRA sapphire mirrors from transmitted wavefront error measurements'. In: *Phys. Rev. D* 110 (8 2024), p. 082007. DOI: 10.1103/PhysRevD.110.082007. URL: https://link.aps.org/doi/10.1103/PhysRevD.110.082007.

[46] K. Somiya, E. Hirose and Y. Michimura. 'Influence of nonuniformity in sapphire substrates for a gravitational wave telescope'. In: *Phys. Rev. D* 100 (8 Oct. 2019), p. 082005. DOI: 10.1103/PhysRevD.100.082005. URL: https://link.aps.org/doi/10.1103/PhysRevD.100.082005.

[47] Eiichi Hirose, GariLynn Billingsley, Liyuan Zhang, Hiroaki Yamamoto, Laurent Pinard, Christoph Michel, Danièle Forest, Bill Reichman and Mark Gross. 'Characterization of Core Optics in Gravitational-Wave Detectors: Case Study of KAGRA Sapphire Mirrors'. In: *Phys. Rev. Appl.* 14 (1 July 2020), p. 014021. DOI: 10.1103/PhysRevApplied.14.014021. URL: https://link.aps.org/doi/10.1103/PhysRevApplied.14.014021.

[48] Yuta Michimura, Haoyu Wang, Francisco Salces-Carcoba, Christopher Wipf, Aidan Brooks, Koji Arai and Rana X. Adhikari. 'Effects of mirror birefringence and its fluctuations to laser interferometric gravitational wave detectors'. In: *Phys. Rev. D* 109 (2 2024), p. 022009. DOI: 10.1103/PhysRevD.109.022009.

[49] Baoliang Wang and Theodore C. Oakberg. 'A new instrument for measuring both the magnitude and angle of low level linear birefringence'. In: *Review of Scientific Instruments* 70.10 (1999), pp. 3847–3854. ISSN: 0034-6748. DOI: 10.1063/1.1150000.

[50] V. Jaberian Hamedan, A. Adam, C. Blair, L. Ju and C. Zhao. 'Precision mapping of a silicon test mass birefringence'. In: *Applied Physics Letters* 122.6 (2023), p. 064101. ISSN: 0003-6951. DOI: 10.1063/5.0136869.

[51] Thorlabs. *Half-Wave Liquid Crystal Retarders with Temperature Control*. URL: https://www.thorlabs.co.jp/half-wave-liquid-crystal-retarders-with-temperature-control?tabName=Overview.

[52] Thorlabs. *Polarimeter Systems with High Dynamic Range*. URL: https://www.thorlabs.com/newgrouppage9.cfm?objectgroup_id=1564.

[53] Shalika Singh, Marc Eisenmann, Yoichi Aso and Kentaro Somiya. 'Complete birefringence and Jones matrix characterization using arbitrary polarization'. In: *Optics Express* (2025). DOI: 10.1364/OE.558774.

[54] Shih-Yau Lu and Russell A. Chipman. 'Homogeneous and inhomogeneous Jones matrices'. In: *J. Opt. Soc. Am. A* 11.2 (1994), pp. 766–773. DOI: 10.1364/JOSAA.11.000766. URL: https://opg.optica.org/josaa/abstract.cfm?URI=josaa-11-2-766.

[55] Cynthia Whitney. 'Pauli-Algebraic Operators in Polarization Optics*'. In: *J. Opt. Soc. Am.* 61.9 (1971), pp. 1207–1213. DOI: 10.1364/JOSA.61.001207.

[56] Peter Lancaster and M. Tismenetsky. *The Theory of Matrices: With Applications*. Academic Press, 1985.

[57] Richard Barakat. 'Conditions for the Physical Realizability of Polarization Matrices Characterizing Passive Systems'. In: *Journal of Modern Optics* 34.12 (1987), pp. 1535–1544. DOI: 10.1080/09500348714551471.

[58] Julio C. Gutiérrez-Vega. 'How inhomogeneous can an inhomogeneous Jones matrix be?' In: *J. Opt. Soc. Am. A* 37.6 (2020), pp. 974–979. DOI: 10.1364/JOSAA.390127.

[59] Marc Eisenmann, Shalika Singh and Matteo Leonardi. 'Birefringence compensation method of test-mass substrates for gravitational wave detectors with arbitrary polarization states'. In: *Opt. Lett.* 49.12 (2024), pp. 3404–3407. DOI: 10.1364/OL.523753.

[60] Blair Hall and Joseph Borbely. *GUM Tree Calculator*. 2024. URL: https://doi.org/10.5281/zenodo.3982925.

[61] Harrison LaBollita, David Tanner and Guido Mueller. *Characterization of Mirror Birefringence for ALPS*. Tech. rep. Univeristy of Florida, 2017. URL: https://www.phys.ufl.edu/REU/2017/LaBollitaHarrison.pdf.

[62] Manuel Marchio. 'Development of an optical absorption measurement system to characterize KAGRA sapphire mirrors and new high-reflectivity crystalline coatings'. Ph.D. thesis. PhD thesis. University of Tokyo, 2018. DOI: 10.15083/0002001880.

[63] Junichi Kaneshiro, Tomonobu M. Watanabe, Hideaki Fujita and Taro Ichimura. 'Full control of polarization state with a pair of electro-optic modulators for polarization-resolved optical microscopy'. In: *Appl. Opt.* 55.5 (2016), pp. 1082–1089. DOI: 10.1364/AO.55.001082.

[64] Alba Peinado, Angel Lizana, Josep Vidal, Claudio Iemmi and Juan Campos. 'Optimization and performance criteria of a Stokes polarimeter based on two variable retarders'. In: *Opt. Express* 18.10 (2010), pp. 9815–9830. DOI: 10.1364/OE.18.009815.

[65] Thorlabs. *Electro-Optic Amplitude Modulator User Guide*. URL: blob:https://www.thorlabs.com/a22bf4d2-0b14-4899-8b8c-684387885920#EO-AM-NR-C2-Manual.pdf.

[66] Amnon Yariv and Pochi Albert Yeh. *Optical Waves in Crystals: Propagation and Control of Laser Radiation*. Wiley, 2002. ISBN: 978-0-471-43081-0.

[67] A. Méndez, A. García-Cabañes, E. Diéguez and J.M. Cabrera. 'Wavelength dependence of electro-optic coefficients in congruent and quasi-stoichiometric $LiNbO_3$'. In: *Electronics Letters* 35 (6 1999), pp. 498–499. DOI: 10.1049/el:19990345.

[68] David E. Zelmon, David L. Small and Dieter Jundt. 'Infrared corrected Sellmeier coefficients for congruently grown lithium niobate and 5 mol.% magnesium oxide–doped lithium niobate'. In: *J. Opt. Soc. Am. B* 14.12 (1997), pp. 3319–3322. DOI: 10.1364/JOSAB.14.003319. URL: https://opg.optica.org/josab/abstract.cfm?URI=josab-14-12-3319.

[69] Yariv Amnon. *Optical Electronics*. Saunders College Publishing, 1991. DOI: 10.7907/5r87-m275.

[70] *DR0608 Series Power Inductors*. Datasheet, Document 275-1, revised July 23, 2021. Coilcraft, Inc. 2021. URL: https://www.mouser.com/datasheet/3/995/1/dr0608.pdf.

[71] *OP27: Low Noise, Precision Operational Amplifier*. Datasheet, Rev. H. Analog Devices, Inc. 2015. URL: https://www.analog.com/media/en/technical-documentation/data-sheets/op27.pdf.

[72] *OP37: Low Noise, Precision, High Speed Operational Amplifier*. Datasheet, Rev. B. Analog Devices, Inc. 2002. URL: https://www.analog.com/media/en/technical-documentation/data-sheets/op37.pdf.

[73] *PA83: ±150 V Fully Protected Input, Low Bias Current Power Amplifier*. Datasheet. Apex Microtechnology Inc. n.d. URL: https://www.apexanalog.com/products/pa83.html.

[74] *BUF634: 250 mA High-Speed Buffer*. Datasheet, Rev. C. Texas Instruments Incorporated. 2024. URL: https://www.ti.com/lit/ds/symlink/buf634.pdf.

[75] *EL2099CT: High Speed Monolithic Operational Amplifier / Video Distribution Amplifier*. Datasheet. Elantec Semiconductor / Intersil Corporation. 1996. URL: https://www.alldatasheet.com/datasheet-pdf/pdf/59879/ELANTEC/EL2099CT.html.

[76] Miguel Vaca. *RF Toroid Calculator*. Accessed January 2026. 2025. URL: https://miguelvaca.github.io/vk3cpu/toroid.html.

[77] Mitchell Gordon Schiworski. 'Development and application of phase cameras for advanced gravitational wave detectors'. Accessed: 2026-01-07. Ph.D. Thesis. University of Adelaide, 2024. URL: https://inspirehep.net/literature/2933578.

[78] *TT25-1-X65+: RF Transformer, Plug-In, 50 , 0.02 – 30 MHz*. Datasheet. Mini-Circuits. 2021. URL: https://www.minicircuits.com/pdfs/TT25-1-X65%2B.pdf.

[79] *T-626-X65+: RF Transformer/Balun, 50 , 0.01 – 10 MHz*. Datasheet. Mini-Circuits. 2021. URL: https://www.minicircuits.com/pdfs/T-626-X65.pdf.

[80] R. Sobot. *Wireless Communication Electronics*. Boston, MA: Springer US, 2012. ISBN: 978-1-4614-1116-1, 978-1-4614-1117-8. DOI: 10.1007/978-1-4614-1117-8. URL: https://link.springer.com/10.1007/978-1-4614-1117-8 (retrieved 14/07/2020).

[81] John Ardizzoni. *A Practical Guide to High-Speed Printed-Circuit-Board Layout*. Technical Report. Available from Analog Devices (analog.com). Analog Devices, Inc., 2005. URL: https://www.analog.com/en/resources/analog-dialogue/articles/high-speed-printed-circuit-board-layout.html.

[82] RF-Microwave. *SPCW2R0 Welco Plus — Solid core silver plated copper wire, Ø 2 mm, AWG 12*. Online product page for SPCW2R0 solid core silver-plated copper wire (35m 1kg). RF-Microwave. 2026. URL: https://www.rf-microwave.com/en/welco-plus/spcw2r0/solid-core-silver-plated-copper-wire-2mm-awg-12/fra-2r0/ (retrieved 07/01/2026).

[83] Serge Y. Stroobandt. *RF inductance calculator for single-layer helical round-wire coils*. Accessed: 2026-01-05. Hamwaves. n.d. URL: https://hamwaves.com/inductance/en/.

[84] Kiwamu Izumi. *Triple Resonant Circuit for EOMs*. Tech. rep. Technical report. Department of Astronomy, University of Tokyo, Feb. 2012.

[85] AllElectroHub. *The Role of Copper Foil Thickness in PCB High Voltage Applications*. URL: https://www.allpcb.com/allelectrohub/the-role-of-copper-foil-thickness-in-pcb-high-voltage-applications.

[86] Altium. *PCB Trace Width vs. Current Table for High Power Designs*. URL: https://resources.altium.com/p/pcb-trace-width-vs-current-table-high-voltage-design.

[87] David M. Pozar. *Microwave Engineering*. 4th ed. Wiley, 2011. Chap. 2.

[88] EE Power. *Mica Capacitor | Capacitor Types | Capacitor Guide*. https://eepower.com/capacitor-guide/types/mica-capacitor/. Accessed: 2025-01-09. n.d. URL: https://eepower.com/capacitor-guide/types/mica-capacitor/.

[89] PJYFYM. *Mica Capacitors: Structure, Properties & Applications*. https://en.pjyfym.com/blog/mica-capacitors-structure-properties-applications.html. Published: 2025-08-13, Accessed: 2025-01-09. 2025. URL: https://en.pjyfym.com/blog/mica-capacitors-structure-properties-applications.html.

[90] Advantest Corporation. *R3754A/R3754B (Discontinued Product Catalog)*. Apr. 1998 Japanese catalog for R3754A and R3754B network analyzers. Advantest Corporation. 1998. URL: https://www.advantest.com/document/ja/customer-services/uptime/emi-discontinued/electronic-measuring/discontinued-product-catalog/pdf_Catalog_R3754A_R3754B_jp.pdf (retrieved 09/01/2026).

[91] A. P. Gregory. *Q-factor Measurement by Using a Vector Network Analyser*. NPL Report MAT 58. National Physical Laboratory, 2021. DOI: 10.47120/npl.MAT58. (retrieved 09/01/2026).

[92] scikit-rf team. *scikit-rf Documentation: skrf.qfactor.Qfactor.fit*. API reference for the Qfactor.fit method. scikit-rf. 2025. URL: https://scikit-rf.readthedocs.io/en/latest/api/generated/skrf.qfactor.Qfactor.fit.html (retrieved 09/01/2026).

[93] Knowles Voltronics. *AT40HV Trimmer Capacitor*. Product page on Digi-Key Japan. 1.5–40 pF, 1000 V PTFE trimmer capacitor. 2026. URL: https://www.digikey.jp/ja/products/detail/knowles-voltronics/AT40HV/6362736 (retrieved 09/01/2026).

[94] Satoshi Tanioka, Daniel Vander-Hyde, Garrett D. Cole, Steven D. Penn and Stefan W. Ballmer. 'Study on electro-optic noise in crystalline coatings toward future gravitational wave detectors'. In: *Phys. Rev. D* 107 (2 Jan. 2023), p. 022003. DOI: 10.1103/PhysRevD.107.022003.

[95] Anatoly Potemkin Efim Khazanov and Eugeny Katin. 'Compensating for birefringence in active elements of solid-state lasers: novel method'. In: *Journal of the Optical Society of America B* (2002). DOI: 10.1364/JOSAB.19.000667.

[96] Aidan F. Brooks, Benjamin Abbott, Muzammil A. Arain, Giacomo Ciani, Ayodele Cole et al. 'Overview of Advanced LIGO Adaptive Optics'. In: *arXiv:1608.02934* (2016). Preprint.

[97] Edward D. Palik. *Handbook of Optical Constants of Solids*. Elseiver, 1997. URL: https://www.sciencedirect.com/book/9780125444156/handbook-of-optical-constants-of-solids.

[98] Thorlabs. *Optical substrates, A comprehensive guide to optical glass used at Thorlabs*. URL: https://www.thorlabs.com/optical-substrates?tabName=a-BBO.

[99] Thorlabs. *Optical substrates, A comprehensive guide to optical glass used at Thorlabs*. URL: https://www.thorlabs.com/optical-substrates?tabName=Calcite.

[100] Thorlabs. *Optical substrates, A comprehensive guide to optical glass used at Thorlabs*. URL: https://www.thorlabs.com/optical-substrates?tabName=Sapphire.

[101] Newlight photonics. *Basic properties of quartz crystal*. URL: https://www.newlightphotonics.com/quartz-properties.html.

[102] Jonathan B. Pfeiffer, Yaniv Kaufman, Kelvin H. Wagner and Hassel Ledbetter. 'Complete Elastic Constants of α-BaB_2O_4: Resonant Ultrasound Spectroscopy versus Schaefer–Bergmann Diffraction'. In: *AIP Conference Proceedings*. Vol. 1600. 1. 2014, pp. 377–383. DOI: 10.1063/1.4879605.

[103] Louis Peselnick and Richard A. Robie. 'Elastic Constants of Calcite'. In: *Journal of Applied Physics* 34.8 (1963), pp. 2494–2495. ISSN: 0021-8979. DOI: 10.1063/1.1702777.

[104] Maarten de Jong, Wei Chen, Thomas Angsten, Anubhav Jain, Randy Notestine, Anthony Gamst, Marcel Sluiter, Chaitanya K. Ande, Sybrand van der Zwaag, Jose J. Plata, Cormac Toher, Stefano Curtarolo and Kristin A. Persson. 'Charting the complete elastic properties of inorganic crystalline compounds'. In: *Scientific Data* 2 (2015), p. 150009. DOI: 10.1038/sdata.2015.9. URL: https://doi.org/10.1038/sdata.2015.9.

[105] N. Nakamura, M. Sakamoto, H. Ogi and M. Hirao. 'Elastic constants of langasite and alpha quartz at high temperatures measured by antenna transmission acoustic resonance'. In: *Review of Scientific Instruments* 83.7 (2012), p. 073901. ISSN: 0034-6748. DOI: 10.1063/1.4731657.

[106] I. Martynyuk-Lototska, O. Mys, Ya. Dyachok, T. Dudok, V. Adamiv, Ya. Burak and R. Vlokh. 'Piezooptic Properties of β-BaB_2O_4 and $Li_2B_4O_7$ Crystals'. In: *arXiv preprint* arXiv:0709.0056 (2007). physics.optics. DOI: 10.3116/16091833/5/1/19/2004. URL: https://arxiv.org/abs/0709.0056.

[107] G. Ulian and G. Valdrè. 'Study of the variation of the optical properties of calcite with applied stress, useful for specific rock and material mechanics.' In: *Scientific Reports* (2022). DOI: 10.1038/s41598-021-04471-6.

[108] David L. Bradley. 'Photoelastic constants of synthetic sapphire'. Master of Science thesis. Master's thesis. East Lansing, MI: Michigan State University, 1963. DOI: 10.25335/xbjy-6557. URL: https://d.lib.msu.edu/etd/8251.

[109] T. S. Narasimhamurty. 'Photoelastic Constants of α Quartz'. In: *J. Opt. Soc. Am.* 59.6 (1969), pp. 682–686. DOI: 10.1364/JOSA.59.000682.

[110] Thorlabs. *Optical substrates, A comprehensive guide to optical glass used at Thorlabs*. URL: https://www.thorlabs.com/optical-substrates?tabName=YVO4.

[111] MolTech Gmbh. *INFRARED, PHOTOREFRACTIVE, MAGNETO-OPTICAL, MAGNETIC, PIEZOELECTRIC MATERIALS, WAFERS AND SUBSTRATES*. URL: https://www.mt-berlin.com/charts/chart_07.htm#IND10.

[112] Thorlabs. *Optical substrates, A comprehensive guide to optical glass used at Thorlabs*. URL: https://www.thorlabs.com/optical-substrates?tabName=Magnesium%2520Fluoride.

[113] Amin Mirzai, Aylin Ahadi and Solveig Melin. 'Photoelasticity of YVO4 through first-principles calculation'. In: *ECCOMAS Congress 2022 - 8th European Congress on Computational Methods in Applied Sciences and Engineering* (2022). DOI: 10.23967/eccomas.2022.220.

[114] D. Isaak, J. Carnes and O. Anderson. 'Elasticity of TiO2 rutile to 1800 K.' In: *Physics and Chemistry of Minerals* (1998). DOI: 10.1007/s002690050158.

[115] H. M. Kandil, J. D. Greiner, A. C. Ayers and J. F. Smith. 'Single-crystal elastic constants of MgF_2 in the temperature range 4.2-300 K'. In: *Journal of Applied Physics* 52.2 (1981), pp. 759–763. DOI: 10.1063/1.328759.

[116] M. H. Grimsditch and A. K. Ramdas. 'Elastic and elasto-optic constants of rutile from a Brillouin scattering study'. In: *Phys. Rev. B* 14 (4 1976), pp. 1670–1682. DOI: 10.1103/PhysRevB.14.1670.

[117] G. Swarna Kumari, N. Satyavathi and N. Rajeswara Rao. 'Evaluation of photoelastic constants from first-order Raman intensities of MgF_2'. In: *Pramana – Journal of Physics* 21.1 (1983), pp. 51–63. DOI: 10.1007/BF02846831.

[118] Neyco. *Single Crystal Substrates*. URL: https://www.neyco.fr/uploads/media/product/0001/08/Materials_J_Substrats%20Monocristallins_1649325676.pdf.

[119] National Institute of Standards and U.S. Department of Commerce Tehcnology. *NIST Chemistry WebBook, SRD 69*. URL: https://webbook.nist.gov/cgi/cbook.cgi?ID=C14808607&Type=JANAFS&Table=on.

[120] Jr. Chase M.W. 'NIST-JANAF Themochemical Tables, Fourth Edition'. In: *J. Phys. Chem. Ref. Data, Monograph 9* 1-1951 (1998).

[121] P. A. Popov, N. V. Moiseev, A. E. Kokh and K. A. Kokh. 'Thermal conductivity and heat capacity of α- and β-BaB_2O_4 single crystals'. In: *Inorganic Materials* 47.2 (2011), pp. 163–166. DOI: 10.1134/S0020168511020142.

[122] Eugene C. Robertson. *Thermal properties of rocks*. Open-File Report 88-441. Reston, VA: U.S. Geological Survey, 1988. DOI: 10.3133/ofr88441. URL: https://pubs.usgs.gov/of/1988/0441/report.pdf.

[123] Neutron. *α-BBO (BaB2O4) A novel UV-IR Birefringent Optical Crystal*. URL: https://www.thorlabs.com/optical-substrates?tabName=a-BBO.

[124] Guoqing Zhou, Jun Xu, Xingda Chen, Heyu Zhong, Siting Wang, Ke Xu, Peizhen Deng and Fuxi Gan. 'Growth and spectrum of a novel birefringent α-BaB_2O_4 crystal'. In: *Journal of Crystal Growth* 191.3 (1998), pp. 517–519. DOI: 10.1016/S0022-0248(98)00162-6.

[125] K. S. Gavrichev, M. A. Ryumin and A. V. Tyurin. 'Heat capacity and thermodynamic functions of YVO4 in the 13–347 K region'. In: *Russian Journal of Inorganic Chemistry* 55 (2010), pp. 1935–1939. DOI: 10.1134/S0036023610120181.

[126] Yoichi Sato and Takunori Taira. 'The studies of thermal conductivity in $GdVO_4$, YVO_4, and $Y_3Al_5O_{12}$ measured by quasi-one-dimensional flash method'. In: *Optics Express* 14.22 (2006), pp. 10528–10536. DOI: 10.1364/OE.14.010528. URL: https://opg.optica.org/oe/abstract.cfm?uri=oe-14-22-10528.

[127] Bo Fu, Guihua Tang and Alan J. H. McGaughey. 'Finite–temperature force constants are essential for accurately predicting the thermal conductivity of rutile TiO_2'. In: *Physical Review Materials* 6.015401 (2022), pp. 1–14. DOI: 10.1103/PhysRevMaterials.6.015401. URL: https://doi.org/10.1103/PhysRevMaterials.6.015401.

[128] W. R. Thurber and A. J. H. Mante. 'Thermal Conductivity and Thermoelectric Power of Rutile (TiO_2)'. In: *Physical Review* 139.A1655 (1965), A1655–A1660. DOI: 10.1103/PhysRev.139.A1655. URL: https://doi.org/10.1103/PhysRev.139.A1655.

[129] Impex High Tech GmbH. *MgF_2-Magnesium Fluoride Optical Material*. URL: https://www.impex-hightech.de/en/mgf2/.

[130] N. Ter-Gabrielyan, V. Fromzel and M. Dubinskii. 'Linear thermal expansion and thermo-optic coefficients of YVO_4 crystals in the 80–320 K temperature range'. In: *Optical Materials Express* 2.11 (2012), pp. 1624–1631. DOI: 10.1364/OME.2.001624.

[131] Roland Appel, Chris D. Dyer and John N. Lockwood. 'Design of a broadband UV–visible α-barium borate polarizer'. In: *Applied Optics* 41.13 (2002), pp. 2470–2480. DOI: 10.1364/AO.41.002470.

[132] G. Ghosh. 'Dispersion-equation coefficients for the refractive index and birefringence of calcite and quartz crystals'. In: *Optics Communications* 163.1–3 (1999), pp. 95–102. DOI: 10.1016/S0030-4018(99)00145-0. URL: https://doi.org/10.1016/S0030-4018(99)00145-0.

[133] I. H. Malitson and M. J. Dodge. 'Refractive Index and Birefringence of Synthetic Sapphire'. In: *Journal of the Optical Society of America* 62.12 (1972), pp. 1405–1409. DOI: 10.1364/JOSA.62.001405.

[134] Jingle Liu and X. C. Zhang. 'Birefringence and absorption coefficients of alpha barium borate in terahertz range'. In: *Journal of Applied Physics* 106.2 (2009), p. 023107. DOI: 10.1063/1.3176965. URL: https://doi.org/10.1063/1.3176965.

[135] Th. Posch, A. Baier, H. Mutschke and Th. Henning. 'Carbonates in space: the challenge of low-temperature data'. In: *The Astrophysical Journal* 668 (2007), pp. 993–1000. DOI: 10.1086/521390. URL: https://doi.org/10.1086/521390.

[136] V. E. Rogalin, I. A. Kaplunov, I. S. Tsenina, M. S. Andreeva and S. A. Filin. 'Optical properties of sapphire in its opacity range'. In: *Optics and Spectroscopy* 120 (2016), pp. 892–895. DOI: 10.1134/S0030400X16060175.

[137] W. G. Spitzer and D. A. Kleinman. 'Infrared Lattice Bands of Quartz'. In: *Physical Review* 121.5 (1961), pp. 1324–1335. DOI: 10.1103/PhysRev.121.1324.

[138] *Optical Constants*. Technical Report ADA158623. U.S. Department of Defense: Defense Technical Information Center (DTIC), 1985. URL: https://archive.org/details/DTIC_ADA158623.

[139] T. Aventin, A. Nehari, D. Forest, J. Degallaix, C. Dujardin, G. Cagnoli and K. Lebbou. 'Enabling cryogenic gravitational wave detectors: growth of sapphire crystals with record low absorption in the near infrared'. In: *CrystEngComm* 26.43 (2024), pp. 6172–6183. DOI: 10.1039/D4CE00519H. URL: https://doi.org/10.1039/D4CE00519H.

[140] Castech. *Yttrium Vanadate(YVO4) Crystal—Special crystal For Fiber Optics*. URL: https://www.castech-us.com/yvo4.htm.

[141] J. R. DeVore. 'Refractive Indices of Rutile and Sphalerite'. In: *Journal of the Optical Society of America* 41.6 (1951), pp. 416–419. DOI: 10.1364/JOSA.41.000416. URL: https://doi.org/10.1364/JOSA.41.000416.

[142] Marilyn J. Dodge. 'Refractive properties of magnesium fluoride'. In: *Applied Optics* 23.12 (1984), pp. 1980–1985. DOI: 10.1364/AO.23.001980.

[143] T. Siefke, S. Kroker, K. Pfeiffer, O. Puffky, K. Dietrich, D. Franta, I. Ohlídal, A. Szeghalmi, E.-B. Kley and A. Tünnermann. 'Materials pushing the application limits of wire grid polarizers further into the deep ultraviolet spectral range'. In: *Advanced Optical Materials* 4.11 (2016), pp. 1780–1786. DOI: 10.1002/adom.201600213. URL: https://doi.org/10.1002/adom.201600213.

[144] Thomas M. Cotter, Michael E. Thomas and William J. Tropf. 'Magnesium Fluoride (MgF_2)'. In: *Handbook of Optical Constants of Solids II*. Ed. by Edward D. Palik. Optical constants and refractive index data for MgF_2. San Diego, CA: Academic Press, 1991, pp. 897–917. ISBN: 978-0-12-544422-4.

[145] P. Wahyu, A. Chandra, J. Gunawan and S. Suprijadi. 'Universal dispersion model for characterization of optical thin films from far infrared to extreme ultraviolet'. In: *Optical Materials* 59 (2016), pp. 238–245. DOI: 10.1016/j.optmat.2016.02.030.

[146] COMSOL. *Radiative Beam in Absorbing Media Theory*. URL: https://doc.comsol.com/6.0/doc/com.comsol.help.heat/heat_ug_theory.07.60.html#751555.

[147] COMSOL. *Modeling of Material Heating via the Beer Lambert Law*. URL: https://www.comsol.jp/model/modeling-of-material-heating-via-the-beer-lambert-law-46701.

[148] COMSOL. *Modeling laser beam absorption in silica glass with Beer Lambert Law*. URL: https://www.comsol.jp/model/modeling-laser-beam-absorption-in-silica-glass-with-beer-lambert-law-56101.

[149] COMSOL. *Theory for Heat Transfer in Solids*. URL: https://doc.comsol.com/5.5/doc/com.comsol.help.heat/heat_ug_theory.07.07.html.

[150] COMSOL. *Thermal expansion for materials*. URL: https://doc.comsol.com/5.5/doc/com.comsol.help.sme/sme_ug_solid.07.22.html#3563189.

[151] COMSOL. *Linear Elastic Material*. URL: https://doc.comsol.com/5.5/doc/com.comsol.help.sme/sme_ug_solid.07.06.html#3511294.

[152] MIT OCW. *The concept of strain*. URL: https://ocw.mit.edu/courses/2-080j-structural-mechanics-fall-2013/71034688fba0ff26d25653a4bd236a4a_MIT2_080JF13_Lecture2.pdf.